EXPLOITING ISOTOPIC ENRICHMENT FOR A SOLID-STATE NMR INVESTIGATION OF "ADORABLE" ZEOLITES AND BREATHING METAL-ORGANIC FRAMEWORKS

Giulia Paola Maria Bignami

A Thesis Submitted for the Degree of PhD
at the
University of St Andrews

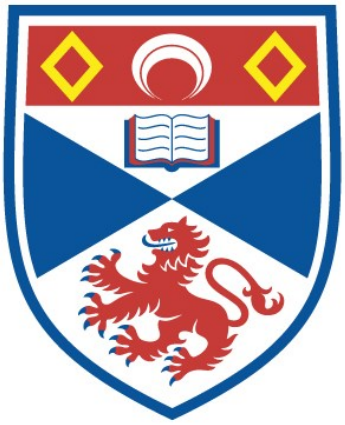

2018

Full metadata for this item is available in
St Andrews Research Repository
at:
http://research-repository.st-andrews.ac.uk/

Please use this identifier to cite or link to this item:
http://hdl.handle.net/10023/14202

This item is protected by original copyright

Exploiting Isotopic Enrichment for a Solid-State NMR Investigation of "ADORable" Zeolites and Breathing Metal-Organic Frameworks

Giulia Paola Maria Bignami

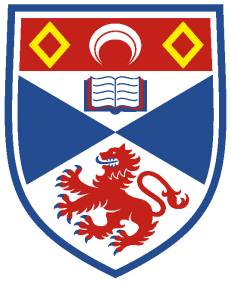

University of
St Andrews

This thesis is submitted in partial fulfilment for the degree of PhD
at the
University of St Andrews

January 2018

1. Candidate's declarations:

I, Giulia Paola Maria Bignami, hereby certify that this thesis, which is approximately 50,000 words in length, has been written by me, and that it is the record of work carried out by me, or principally by myself in collaboration with others as acknowledged, and that it has not been submitted in any previous application for a higher degree.

I was admitted as a research student in January 2014 and as a candidate for the degree of PhD in January 2015; the higher study for which this is a record was carried out in the University of St Andrews between 2014 and 2018.

Date Signature of candidate

2. Supervisor's declaration:

I hereby certify that the candidate has fulfilled the conditions of the Resolution and Regulations appropriate for the degree of PhD in the University of St Andrews and that the candidate is qualified to submit this thesis in application for that degree.

Date Signature of supervisor

Date Signature of supervisor

3. Permission for publication:

In submitting this thesis to the University of St Andrews I understand that I am giving permission for it to be made available for use in accordance with the regulations of the University Library for the time being in force, subject to any copyright vested in the work not being affected thereby. I also understand that the title and the abstract will be published, and that a copy of the work may be made and supplied to any bona fide library or research worker, that my thesis will be electronically accessible for personal or research use unless exempt by award of an embargo as requested below, and that the library has the right to migrate my thesis into new electronic forms as required to ensure continued access to the thesis. I have obtained any third-party copyright permissions that may be required in order to allow such access and migration, or have requested the appropriate embargo below.

The following is an agreed request by candidate and supervisors regarding the publication of this thesis:

PRINTED COPY
No embargo on print copy

ELECTRONIC COPY
No embargo on electronic copy

Date Signature of candidate

Date Signature of supervisor

Date Signature of supervisor

Acknowledgements

First and foremost I wish to thank my PhD supervisors, Sharon Ashbrook and Russell Morris, for giving me the opportunity of working on this joint project and for their constant support, advice and guidance throughout these four years. I would also like to thank Daniel Dawson for his help and support as well as for his patience, as Facility Manager, with my unfortunate travelling and being stranded in various airports over the past years.

A special thanks goes to the present and past members of the Ashbrook and Morris groups for their help and support, providing a great working atmosphere (and cakes) in both group offices. In particular, I would like to thank Valerie Seymour, Scott Sneddon, Paul Wheatley, Yuyang Tian and Marta Navarro for their help during my first year of NMR spectroscopy and zeolites synthesis; Matthew McPherson for his help with the surface area measurements of my zeolite samples; Samantha Russell for her help with the catalytic testing of many zeolites samples and her patience during very long SEM and EDX sessions; David McKay for his computational work on the MOFs project; Zachary Davis and Richard Parke for their work on the MOFs project as project students; Laura McCormick, Stewart Warrender and Morven Duncan for their help with the dehydration and (attempts of) loading of MOFs; Samuel Morris for his work on the refinement of the diffraction patterns obtained during the MOFs project and for his funny, frequently mismatched, socks; Daniel Firth for his support during these years, always making sure I was safe during zeolite conferences around the world; Michal Mazur and Vanessa Pimenta for cheering me up in the final months of writing-up.

Additional thanks go to Dinu Iuga at the UK 850 Solid-State NMR Facility (Warwick), Subhradip Paul at the DNP MAS NMR Facility (Nottigham) and John Craven at the NERC Ion Microprobe Facility (Edinburgh).

I also wish to thank the University of St Andrews, the EPSRC and ERC for funding.

Finally, my mother, grandmother and Simone who are such an important part of my life and always support me.

The UK 850 MHz solid-state NMR Facility used in this research was funded by EPSRC and BBSRC (contract reference PR140003), as well as the University of Warwick including via part funding through Birmingham Science City Advanced Materials Projects 1 and 2 supported by Advantage West Midlands (AWM) and the European Regional Development Fund (ERDF).

The University of Nottingham DNP MAS NMR Facility used in this research was funded by EPSRC and the University of Nottingham.

To my Father

Abstract

This thesis combines synthetic studies for isotopic enrichment with solid-state characterisation techniques to investigate two classes of microporous materials: zeolites and metal-organic frameworks (MOFs). These materials have a wide range of successful applications, from industrial catalysis to medicine, resulting in the increasing need for both a complete understanding of their unique structural features and synthetic methods to target new frameworks. Nuclear magnetic resonance (NMR) spectroscopy, thanks to its sensitivity to the local, atomic-scale, environment and its element specificity, is applied, in combination with powder X-ray diffraction (PXRD), electron microscopy, N_2 adsorption and mass spectrometry, to the study of these materials. Oxygen atoms play a crucial role in the structure and chemistry of zeolites and MOFs, making ^{17}O NMR an excellent tool for chemical and structural investigations. However, the low natural abundance of this isotope (0.037%) and the cost of ^{17}O-enriched reactants require the development of atom-efficient synthetic processes for isotopic enrichment. In the first part of this work, the unconventional assembly-disassembly-organisation-reassembly (ADOR) method is applied to the Ge-doped UTL framework and optimised in reduced-volume conditions for economic enrichment to obtain ^{17}O- and ^{29}Si-enriched UTL-derived zeolites. *In situ* and *ex situ* solid-state characterisation studies show that isotopic enrichment not only enables a more detailed spectroscopic investigation, but also provides new insights into the mechanism of the ADOR process and its sensitivity to experimental conditions. In the second part of this work, dry gel conversion synthesis and a novel steaming procedure are studied as cost-effective ^{17}O-enrichment pathways for Al, Ga and Sc mixed-metal terephthalate MOFs. ^{17}O solid-state NMR spectroscopy, in combination with PXRD and electron microscopy, is employed to investigate cation disorder and ^{17}O NMR spectra are shown to be sensitive to substitution of metal centers and conformational changes upon interaction with guest molecules.

Publications

Chapters 3 and 4 are based on work published in:

- G. P. M. Bignami, D. M. Dawson, V. R. Seymour, P. S. Wheatley, R. E. Morris and S. E. Ashbrook, *J. Am. Chem. Soc.*, 2017, **139**, 5140–5148.
- S. A. Morris, G. P. M. Bignami, Y. Tian, M. Navarro, D. S. Firth, J. Čejka, P. S. Wheatley, D. M. Dawson, W. A. Slawinski, D. S. Wragg, R. E. Morris and S. E. Ashbrook, *Nature Chem.*, 2017, **9**, 1012–1018.

Chapters 5 and 6 are based on work published in:

- G. P. M. Bignami, Z. H. Davis, D. M. Dawson, S. A. Morris, S. E. Russell, D. McKay, R. E. Parke, D. Iuga, R. E. Morris and S. E. Ashbrook, *Chem. Sci.*, 2018, **9**, 850–859.

Publications not related to this work:

- D. M. Dawson, Z. Ke, F. M. Mack, R. A. Doyle, G. P. M. Bignami, I. A. Smellie, M. Buhl and S. E. Ashbrook, *Chem. Commun.*, 2017, **53**, 10512–10515.
- M. Mazur, A. M. Arévalo-López, P. S. Wheatley, G. P. M. Bignami, S. E. Ashbrook, Á. Morales-García, P. Nachtigall, J. P. Attfield, J. Čejka and R. E. Morris, *J. Mater. Chem. A*, 2018, **6**, 5255–5259.
- A. Fernandes, R. F. Moran, S. Sneddon, D. M. Dawson, D. McKay, G. P. M. Bignami, F. Blanc, K. R. Whittle and S. E. Ashbrook, *RSC Adv.*, 2018, **8**, 7089–7101.

Table of contents

Introduction

Results and discussion

Introduction

1 Materials introduction

Microporous solids are materials defined as three-dimensional (3D) ordered structures containing pores ranging in diameter from 5 to 20 Å, with the ability of adsorbing molecules. Owing to their porous nature, these materials, depending on their chemical composition and structural features, have been widely employed in industry over the years.[1]

1.1 Introduction to zeolites

The term zeolite was originally introduced in 1756 by the Swedish mineralogist Baron Axel Fredrik Cronstedt, who first recorded a description of a zeolite mineral, stilbite.[2] He observed that, upon heating, this mineral evolved large amounts of steam from adsorbed water and thus called the material "zeolite", from the classical Greek ζέω (zeo, to boil) and λίθος (lithos, stone). About 20 new zeolite types were then reported in mineralogy texts over the following hundred years with an increasing rate of discovery from the middle of the 19th century up to the last 30 years reaching approximately 1 mineral, on average, every year. As well as being treated as mineralogical curiosities, zeolites attracted the attention of scientists for their peculiar chemical-physical properties related to their reversible dehydration behaviour, ion-exchange properties and selective adsorption of gases.[3] Structurally, zeolites are a class of tectosilicate minerals made up of corner-sharing aluminate and silicate tetrahedra fully crosslinked in 3D frameworks that are sufficiently open to reversibly adsorb molecules.[1] These materials, owing to their crystalline and highly porous structure, have high surface areas and a narrow range of pore sizes with molecular dimensions, that, in combination with their chemistry, lead to a great potential for catalytic activity and selectivity. Such a combination of structural features accounts for their vast range of successful applications, comprising the fields of industrial catalysis, adsorption, ion-exchange and medicine.[4-12] Zeolite frameworks are commonly described in terms of their structural units, referred to as

secondary building units (SBUs), that are made up of rings of alternating oxygens and tetrahedral cations. The number of cations in the ring and the shape of the unit formed define the name of the SBU, which might consist of single rings, e.g., a six-membered ring (6MR) contains six cations and six oxygens, or might be built up of two rings linked together, e.g., two four-membered rings (4MR) linked together form a double four-membered ring (D4R), as shown in Figure 1.1.[13]

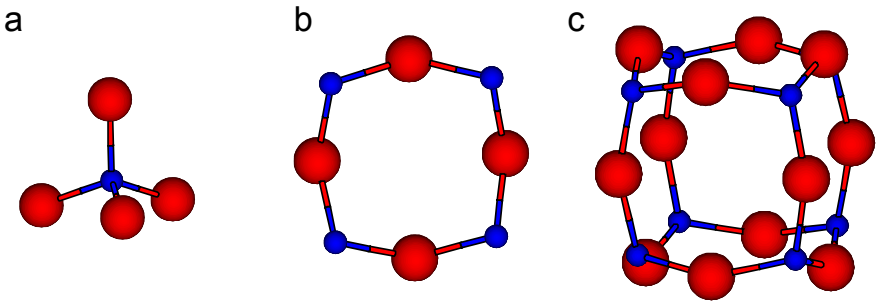

Figure 1.1 *Common building units in zeolites: (a) tetrahedral primary unit (b) 4MR and (c) D4R secondary building units. Si and O atoms are represented by blue and red spheres, respectively.*

Full details of all the 232 framework types unambiguously identified so far, each of which is given a unique three-letter code, are collected, refereed and published by the Structure Commission[14] of the International Zeolite Association (IZA). The main focus of this work will be the UTL (M**u**lhouse **t**we**l**ve)[14] framework, shown in Figure 1.2, a germanium-containing zeolite described independently as IM-12[15] and ITQ-15[16] in 2004 and consisting of the first example of a two-dimensional channel system formed by intersecting ultralarge 14MRs and 12MRs. The 3D structure can be described as stacked layers connected to each other by 4MR and thus forming D4R. Through structure determination and refinement it was possible to find that Ge atoms preferentially occupy the tetrahedral sites of the D4R unit.[15] Moreover, the incorporation of heteroatoms during or post synthesis in this thermally stable ultralarge pore framework with multidirectional channels has been shown to be possible. In particular, the ability to incorporate Al suggests this material could have catalytic applications with specific advantages over unidirectional frameworks to diffuse and react bulky molecules.[15-16]

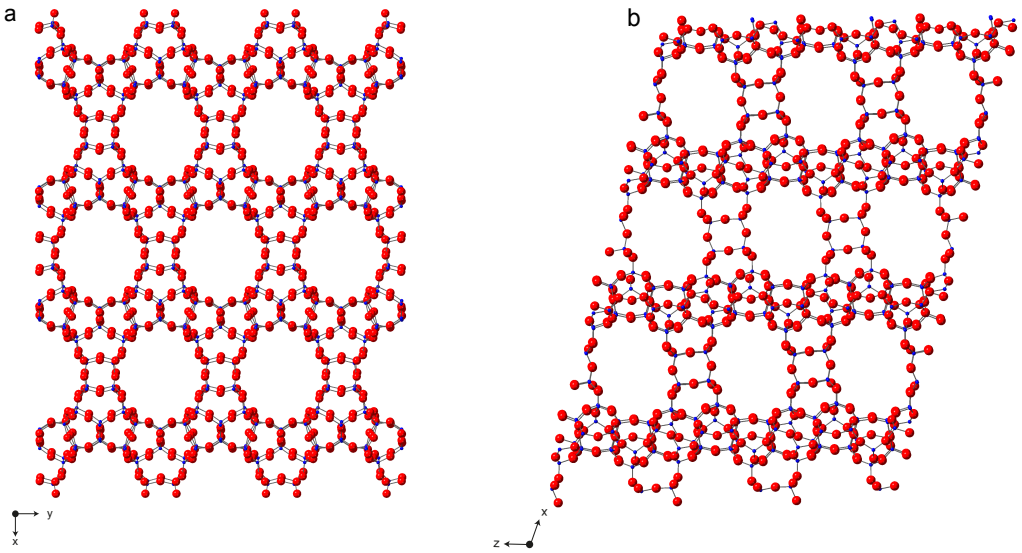

Figure 1.2 *UTL structure as viewed down (a) the z-axis and (b) the y-axis.*[14] *Si and O atoms are represented by blue and red spheres, respectively.*

Zeolite mineralogy and naturally occurring minerals have been the focus of research in the field of zeolite science, establishing its structural basis, until the beginning of the 1950s, with the first documented synthetic zeolite dating back to 1948.[17] With the development of zeolite chemistry, achieved as a result of large-scale synthesis under laboratory conditions,[1] interest moved towards synthetic products that offer many advantages over their naturally occurring counterparts. In particular, synthetic zeolites are more versatile, owing to their wider range of structures, are characterised by more open frameworks, more suitable for the adsorption of molecules and their transformation (catalysis), and can be obtained with constant chemical composition, which is an important requirement for many industrial applications.[3] The global market for synthetic zeolites reached 1.6 million tons in 2001 including 1.3 million tons in detergents, 120,000 tons in catalysis and 85,000 tons in desiccation and adsorbtion. Typically, zeolites A and X are widely used in detergents as water softeners, because of their ion-exchange properties, and in adsorbents for drying, chromatography and impurity removal. In catalysis, zeolite Y is the most commonly used, primarily in the petrochemical industry.[17]

1.1.1 Synthesis of zeolites

Typically, in most zeolite syntheses, a gel is initially prepared that contains a source of tetrahedral silicon atoms, which are the framework-building inorganic species available in reactive form, and structure-directing species, e.g., organic cations, in order to stabilise the open framework structures relative to denser phases with the same composition. The solvent medium has to enable the framework-forming species to come into solution, while not dissolving, or only moderately dissolving, the final crystalline product. Water is the most commonly employed solvent for this purpose, thanks to its polarity, which is appropriate for dissolution of ionic and partially ionic solids, and its acceptably low vapour pressure at the usual reaction temperatures (100-200 °C). Such synthesis is described as hydrothermal.[18-19] However, if non-aqueous solvent media are employed, syntheses are generally described as solvothermal[20-21] or ionothermal[22] when an ionic liquid, with the role of solvent and structure-directing agent, is used. Finally, the gel, whose pH has to be optimised for the solubility and speciation of its components, is heated at temperatures above 100 °C, consequently reaching pressures above atmospheric values, in Teflon-lined stainless steel autoclaves. The resulting solution, containing framework-forming species, reaches supersaturation and a thermodynamic driving force towards crystallisation arises, but nuclei of a critical size need to be formed before this can occur. Initial nuclei, agglomerated from particles in solution, will be unstable, due to their high surface area but, in supersaturation conditions, some of them might persist for a sufficient duration that they grow up to a critical size, where the contribution of the lattice energy outweighs the increasing surface-area free energy. Further addition of species from solution results in crystal growth, which ends when the species from the solution have been exhausted, as shown schematically in Figure 1.3.[13] This crystallisation process is considerably slower when solvothermal, rather than hydrothermal, conditions are used during synthesis because of the inherently low polarity of organic solvents. In these traditional pathways, synthesis proceeds through a reversible process of bond cleavage and formation, from low-density reaction gels to higher-density zeolitic structures

following a density gradient which can be identified as the traditional synthetic vector (TSV) and avoiding any high-energy configuration of the final structure.[24]

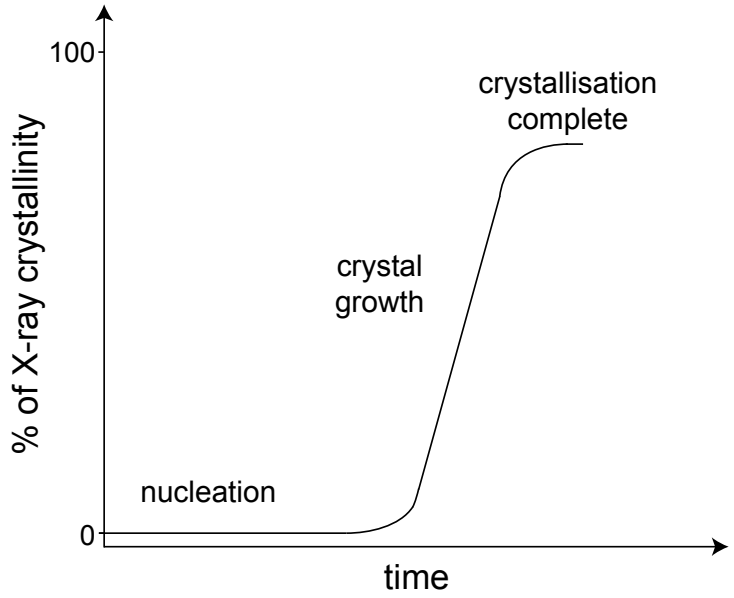

Figure 1.3 *Typical sigmoidal crystallisation curve for a hydrothermal synthesis with an initial stage of nucleation followed by crystal growth, which reaches completion when reactants are no longer available.*

During the synthetic process it is also possible to fine tune the chemistry of the resulting zeolite with the aim of obtaining different functionalities, by substituting other elements into the silicon-based materials. This can be achieved by doping the framework or introducing active sites. The former case applies to the introduction of GeO_2 into the synthetic gel to replace some of the silicon in the structure with dopant Ge^{4+} atoms that, without creating any charge imbalance, has been shown[25-27] to occupy preferential locations in zeolites and enable further transformation of the frameworks, as described in the following section. The latter case applies to the addition, for example, of a source of Al^{3+} atoms to the reaction gel replacing a small portion of Si^{4+} atoms and producing a negative charge in the framework. The Si/Al ratio can vary from infinite, for purely silica frameworks, to a minimum value of 1, below which it is impossible to avoid electrostatically unfavourable Al-O-Al linkages, according to Loewenstein's aluminium avoidance principle.[23] The overall negative charge of the framework can then be balanced by extra-framework cations which can also be replaced by protons after appropriate chemical conversions, thus

forming the acid sites needed for catalysis. In case the framework doesn't prove stable to the incorporation of extra elements in the reaction gel, this step can also be carried out post synthesis with the side effects of decreasing the efficiency of substitution and increasing the possibility of extra-framework localisation of the added element.[13]

1.1.2 The ADOR process

The structure of a zeolitic material determines both its properties and its potential applications and, in the last few years, the synthetic challenge has become the targeting of new specific architectures, with predetermined pore size.[24,28-35] There are more than 2 million ways to connect SiO_4 tetrahedra into zeolitic materials,[36] but there are only 232 zeolitic structures recognised so far by the IZA[14] and only about 50 of those are industrially relevant all- or high-silica zeolites, suggesting traditional synthetic methods have inherent limitations. Indeed, it has been reported[37] that most zeolites are inaccessible, "unfeasible", using traditional synthetic methods and that all currently prepared zeolites lie on the red line shown in Figure 1.4, a plot of energy *vs.* density of 300,000 computationally predicted hypothetical structures. This red line represents the limitations of traditional synthetic chemistry, leaving the "unfeasible" region, where many new zeolitic structures are located, out of reach. However, considering the very small number of zeolites actually synthesised compared to the proposed structures, the feasibility of synthesising computationally predicted frameworks has been questioned,[38] suggesting the need for further selection criteria, in addition to energy minimisation, to identify the most viable synthetic targets. Specifically, the necessary presence of structural flexibility windows, a range of densities within which the zeolitic units keep their ideal shape,[39] and criteria of local interatomic distances (LID),[40] very sensitive to unreasonable structures by focusing on local distortions, can be used to efficiently narrow the range of computationally predicted structures selecting the most realisable candidate frameworks.

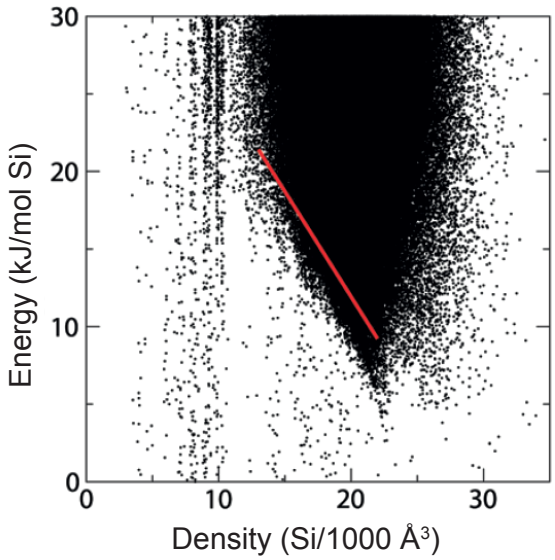

Figure 1.4 *Plot of energy (relative to quartz) vs. density for computationally predicted zeolite-like materials minimised by the Sanders-Leslie-Catlow (SLC) interatomic potential, showing the distributions of thermodynamically accessible structures. The linear fit of energy vs. density for the known zeolite structures is highlighted by the solid red line. Adapted from M.W. Deem et al., J. Phys. Chem. C, 2009.*[37]

In traditional synthetic methods, where zeolites condense from Si-rich solutions, the first accessible zeolitic structures to be encountered, as Si density increases during nucleation and growth, are located on the red line, the low-density edge of the distribution. Therefore, to obtain "unfeasible" zeolites new synthetic pathways have to be designed beyond the limitations of the TSV.[37] This is where the novelty of the Assembly - Disassembly - Organisation - Reassembly (ADOR) approach comes into play by engineering weakness into known materials so that they can then be used as starting points for new modified materials.[24,41-44] Following the ADOR process, solids with targeted structures can be obtained by selectively disassembling a pre-prepared parent zeolite and then reassembling the resulting products to form a new topology. The key feature required in the parent zeolite is the presence of a hydrolytically sensitive dopant element incorporated within the framework at specific sites, allowing the chemically selective removal of the dopant-containing units. Germanosilicates are ideal candidates for this process, as Ge has been suggested to preferentially occupy T-atom positions within D4Rs units.[25-27,45] The formation of such a key structural feature is related to the coordination flexibility of this element leading to Ge-O-Ge angles smaller than Si-O-Si angles, thus changing

the geometric constraints in the D4R units.[15,46] Moreover, Ge linkages have been shown to be much more sensitive to hydrolysis than silicate or aluminosilicate materials.[45,47-48] The Si/Ge ratios typically used are around values of ~4-6 to achieve the best efficiency and selectivity in the removal of D4R. Using the Ge-doped UTL framework as the parent zeolite, ADOR enabled the preparation of new zeolite materials, IPC-2 and IPC-4 (Institute of Physical Chemistry),[24,41,43] whose topologies have been approved by the IZA and given the three-letter codes OKO and PCR, respectively. As schematically represented in Figure 1.5, after the hydrothermal synthesis (assembly) of the parent zeolite, the initial disassembly is independent of the hydrolysis conditions yielding the poorly crystalline lamellar intermediate IPC-1P.[49] However, upon heating at 95 °C, the concentration of acid makes a significant difference to the structural organisation and the final reassembled material produced is dependent on two competing reactions, silica re-organisation and de-intercalation. Typically, IPC-4 is obtained via hydrolysis in slightly acidic conditions, whereas IPC-2 requires a hydrolytic process at very high acidity, e.g., 12 M HCl.[43] The difference between IPC-2 and IPC-4 is that the former contains single-four rings (S4Rs) between UTL-like layers, while IPC-4 has no silica subunits connecting the layers. Therefore, all the D4R units are removed from between the UTL layers in near neutral conditions, which favour de-intercalation and thus a reduction in the interlayer spacing. Alternatively, hydrolysis using 12 M HCl only removes half of the D4R units from between the layers, favouring a rearrangement process associated with an increase in the interlayer spacing. It is important to highlight that, unlike solvothermal methods, the final reassembly, after the organisation stage, is an irreversible entropy-driven stage.

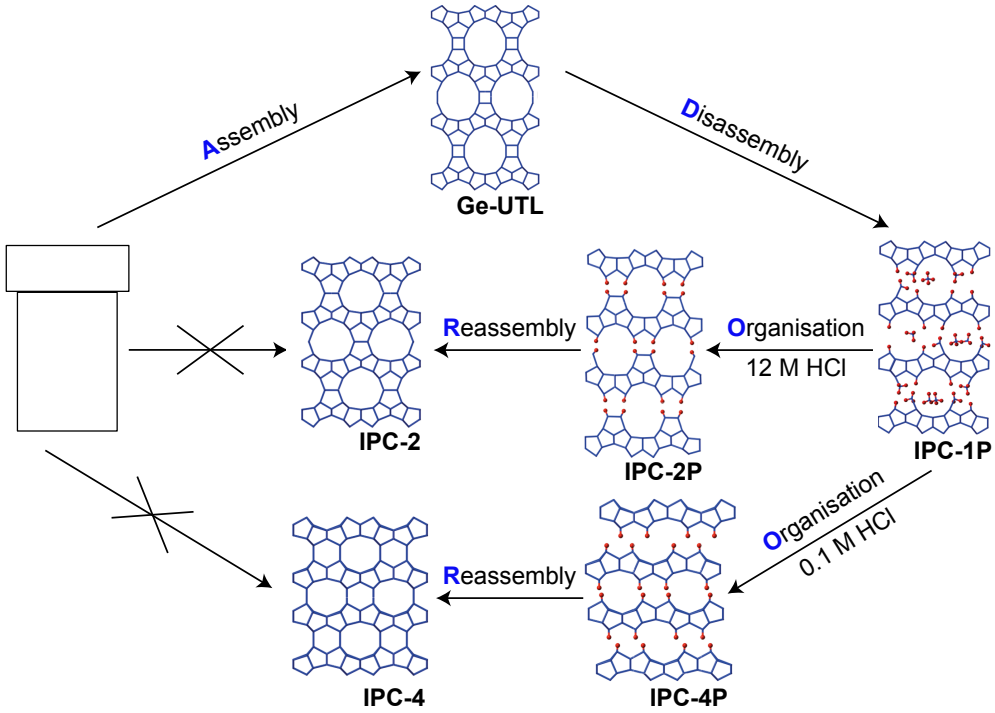

Figure 1.5 *Schematic representation of the ADOR process. For hydrolysed structures, O atoms on the surface are represented by red spheres.*

Following this unconventional synthetic method other new zeolites IPC-6, IPC-7, IPC-9 and IPC-10[42-43,50] have been synthesised, which are unlikely, if not even impossible, to be obtained through traditional hydrothermal methods. If the relative orientation of the layers is the same as in the original parent UTL structure, then the resulting reconnected zeolites follow the LID criteria and so can be described as a feasible zeolite regardless of the units reconnecting the layers. This is the case of IPC-2 (S4R connecting units) and IPC-4 (connecting oxygen bridges), as previously described, but also of IPC-6 (equal amounts of S4R connecting units and direct oxygen bridges) and IPC-7 (equal amounts of S4R and D4R connecting units) which are obtained in intermediate conditions between the two extreme acid concentrations (0.1-12 M HCl), by controlling the relative rates of the de-intercalation and rearrangement processes. On the other hand, if a geometric mismatch is introduced in the final reassembled layered zeolite, by using organic templates in the organisation stage,[24] structural strain and different energetic characteristics to the parent structures are produced. This results in "unfeasible" materials more likely to be located beyond

the red line shown in Figure 1.4, such as IPC-9 and IPC-10.[50] Consequently, by controlling the experimental conditions used during the organisation and rearrangement of the disassembled parent zeolite, different outcomes can be targeted and the porosity of the final material can be tuned over a wide range. Such control over pore volume and, subsequently, surface area cannot be achieved following traditional approaches to zeolite synthesis, underlining the notable advance brought by the development of the ADOR method.

1.1.3 Isotopic enrichment in the ADOR process

As a result of the different stages characterising the ADOR process, selective and successful isotopic enrichment has been experimentally achieved, see Chapter 3, for the two NMR-active nuclei of most interest in this material, ^{29}Si and ^{17}O, as described in Section 2.1.1. Oxygen plays a fundamental role in the structure of mineralogical compounds, such as zeolites, and ^{17}O NMR can, in principle, provide information about the interactions of oxygen atoms throughout the entire structure. However, while potentially very informative, ^{17}O NMR studies of solids have been hampered by the fact that, of the three stable oxygen isotopes, only ^{17}O is NMR active with a nuclear spin quantum number I = 5/2, but this isotope has the lowest natural abundance: ^{16}O, 99.76%, ^{17}O, 0.037% and ^{18}O, 0.2%. Thus, to record spectra within a reasonable timeframe isotopic enrichment is necessary, but also very expensive, requiring atom-efficient enrichment. For instance, in the case of the ^{17}O NMR spectra shown in this thesis, decades, if not centuries, of spectrometer time would have been needed for natural abundance samples to obtain spectra with the same level of signal to noise. Furthermore, a significant broadening affects the resonances of this nucleus, as a result of its quadrupolar nature (I = 5/2), as described in Section 2.4.2. Especially in zeolites and silicates, historically the first materials studied by ^{17}O NMR, relatively large quadrupolar interactions are usually present preventing the resolution of resonances from distinct oxygen sites, which also show a narrow shift range due to the similarity of the chemical environments in these materials.[51]

A wide range of methods for ^{17}O enrichment have now been experimentally implemented starting from the two readily available ^{17}O-labelled sources: O_2 gas and liquid H_2O, with enrichment levels ranging from 10 to 90%. The enrichment level chosen is usually a compromise between the required sensitivity and the cost of the enriched reactant which, depending on the enrichment level, will be in the range of 600-2000 €/g for liquid water. Typical enrichment methods for zeolites involve the direct hydrolysis with liquid ^{17}O-enriched water of the chloride $SiCl_4$ to produce SiO_2,[52] or post-synthetic gas exchange with ^{17}O-enriched O_2[53-54] or steaming in ^{17}O-enriched water.[55-58] These enrichment methods typically result in uniform labeling of the final materials unless experimental conditions are optimised to achieve a selective interaction of the labeled reactant with only certain oxygen sites, e.g., surface sites,[59] or if different oxygen sites are characterised by different exchange rates.[56] In this work, ^{17}O enrichment has been introduced in the ADOR process at the disassembly stage through the use of ^{17}O-enriched water, which plays the double role of enriching agent and reactant for the hydrolysis reaction. This enrichment method can, therefore, provide information about the interaction of the water molecules with the layers of the zeolites shedding light on the kinetics of the hydrolysis process and the dynamics of the oxygen sites within the layers. The resulting degree of enrichment uniformity or selectivity of the O sites of the hydrolysed zeolites will reflect the interactions established during the reaction path and will enable a better understanding of the mechanisms of the ADOR process.

^{29}Si, with a natural abundance of 4.67%, is one of the three stable silicon isotopes along with ^{28}Si at 92.23% and ^{30}Si at 3.1%, but is the only one that exhibits a non-zero nuclear spin quantum number (I = 1/2). The natural abundance of ^{29}Si still allows overnight spectral acquisition for zeolites, but for two-dimensional high-resolution correlation experiments enrichment in this isotope will be of crucial importance. In this work, ^{29}Si enrichment was introduced in the assembly step by synthesising Ge-UTL from a ^{29}Si-enriched precursor, tetraethoxysilane (TEOS). The ^{29}Si-enriched zeolite was then hydrolysed in ^{17}O-enriched water to obtain a doubly enriched product for which ^{17}O-^{29}Si correlation experiments were performed to gain further insight into the structural outcome of the hydrolytic process.

1.2 Introduction to MOFs

The field of metal-organic frameworks (MOFs) is considerably newer than that of zeolites, with the first reported use of the MOF classification appearing in 1995,[60] followed by an explosion in the synthesis and publication of new MOF structures over the past 20 years.[61] The ordered 3D structure of a MOF consists of nodes, taking the form of a single metal cation or a cluster of metal cations, interconnected by spacers, typically polydentate organic molecules, conferring on these materials a great structural variety. The final topology of the porous framework is determined by the coordination geometry at the metal nodes and the nature of the bridging organic linkers, resulting in a variety of structures with high surface area and tunable pore size for the interaction with guest molecules. Typical applications of MOFs are mainly related to their characteristic porous structures and include gas storage, sequestration and separation leading to uses in catalysis, medicine and environmental science.[62-66] The strength of the bond between the metal center and the organic linker determines the stability of the MOF structure at elevated temperatures and its ability to withstand adsorption and removal of guest molecules. In particular, the use of carboxylate ligands, as a result of the relatively strong M-OC bond, leads to highly thermally stable MOFs,[13] such as the terephthalate MOFs that will be discussed in the following sections.

1.2.1 Terephthalate MOFs

As already highlighted, some MOFs show, in general, a much greater structural flexibility compared to zeolites while maintaining their framework connectivity. Large changes in volume are observed in response to variations in temperature or pressure of guest molecules for many materials, that, subsequently, became known as “breathing” MOFs.[67] Among these, terephthalate MOFs represent an important class of materials, with examples, such as the MIL-53 framework, showing significant variations of cell volume, of approx. 40%, as a function of the adsorption or removal of guest molecules.[61] This is typically achieved because of the particular nature of the coordination environment, interconnecting the metal centers through flexible hinging linkers. Other materials, however, such as $Sc_2(O_2C\text{-}C_6H_4\text{-}$

$CO_2)_3$ (hereafter denoted as $Sc_2(BDC)_3$, BDC = 1,4-benzenedicarboxylate), don't show as much overall structural flexibility, with more rigid structures and smaller pores, but are still characterised by some dynamics of the linkers molecules changing the effective pore sizes.[68]

1.2.1.1 MIL-53

MIL-53 (Material Institut Lavoisier, Versailles) was synthesised in hydrothermal conditions in 2002 as the first 3D Cr^{3+} dicarboxylate MOF,[69] with general chemical formula $Cr^{3+}(OH)•\{O_2C\text{-}C_6H_4\text{-}CO_2\}•\{HO_2C\text{-}C_6H_4\text{-}CO_2H\}_x•H_2O_y$, and was subsequently prepared with Al^{3+}, Fe^{3+}, In^{3+}, Ga^{3+} and Sc^{3+} [70-74] as well as the vanadium analogue, MIL-47, isostructural but characterised by different properties due to the different oxidation states available and resulting changes in the coordination environment.[75-76] The as-synthesised Cr form, MIL-53as, is $Cr^{3+}(OH)•\{O_2C\text{-}C_6H_4\text{-}CO_2\}•\{HO_2C\text{-}C_6H_4\text{-}CO_2H\}_{0.75}$ and contains disordered excess linker that can be removed by calcination yielding the high temperature form, MIL-53ht, $Cr^{3+}(OH)•\{O_2C\text{-}C_6H_4\text{-}CO_2\}$ with large pores (lp). At room temperature, when exposed to air, MIL-53ht reversibly adsorbs atmospheric water leading to the low temperature form MIL-53lt, $Cr^{3+}(OH)•\{O_2C\text{-}C_6H_4\text{-}CO_2\}•H_2O$ characterised by narrow pores (np). A schematic breathing cycle from synthesis, through calcination to the hydration process is represented in Figure 1.6 for Al^{3+} MIL-53,[70] homologue of the Cr^{3+} containing MOF.

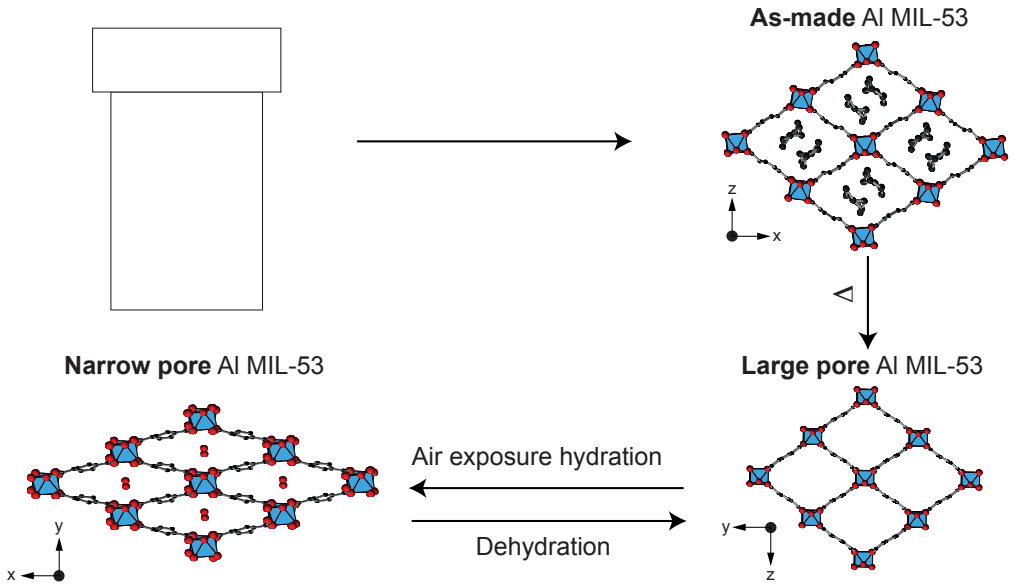

Figure 1.6 *Schematic breathing cycle for Al MIL-53, starting from its autoclave synthesis, leading to the as-made form with disordered linker molecules in the pores. After calcination the high temperature, large pore (lp), form is obtained, which, upon exposure to air at room temperature, undergoes reversible hydration resulting in the narrow pore form (np). AlO_6 are represented by blue octahedra, C atoms by black spheres and O atoms by red spheres. H atoms are omitted for clarity.*[70]

Characterisation of the structure using X-ray diffraction (XRD) was able to determine that this MOF is built from corner-sharing metal octahedra bridged by hydroxyl groups, as shown in Figure 1.7, and connected in layers by the bridging tetradentate terephthalate creating its characteristic 3D structure with an array of monodirectional large-pore channels. These channels can be filled with the free linker, terephthalic acid, or water, but when guest molecules are removed the solid is characterised by a surface area of approximately 1500 m^2g^{-1}. The adsorption of water molecules occurs through different schemes of hydrogen-bonding interactions leading to the presence of two inequivalent water molecules and two sets of channels in the hydrated structure.[77] These interactions, along with π-π stacking interactions of the benzyl groups from the linkers, yield MIL-53lt, which is characterised by a contraction and no accessible porosity as opposed to MIL-53ht which possesses large pores with a free aperture of approximately 8.5 × 8.5 $Å^2$.[70] The transition between the hydrated and anhydrous forms has been shown to be fully reversible and associated with a large breathing effect involving displacement of the MOF chains

by approximately 5 Å and a significant shrinkage of cell volume (by 40%) upon hydration.[70]

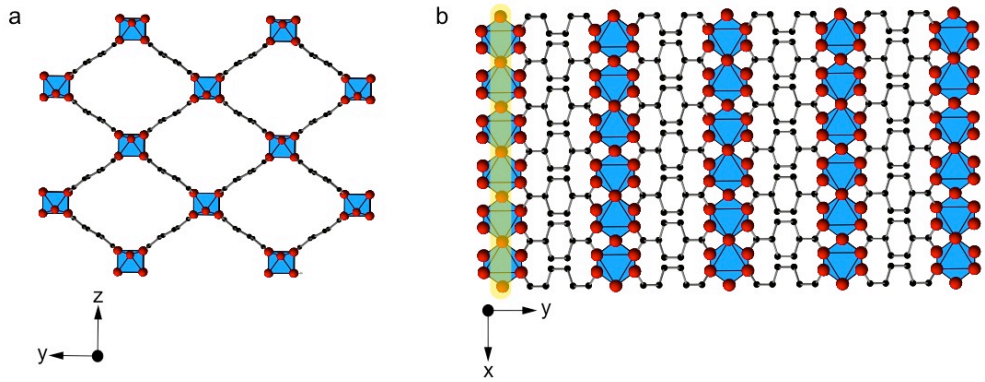

Figure 1.7 *Crystal structure of the large pore form of Al MIL-53, showing the AlO_6 octahedra (blue), oxygen (red) and the organic BDC spacer, containing carbon (black). (a) As viewed down the x-axis, highlighting the porous structure. (b) Rows of octahedra as viewed down the z-axis where the bridging hydroxyl groups can be seen, as highlighted for the first row. Hydrogen atoms have been omitted for clarity.*[70]

The breathing process induces adsorption selectivity when water is exchanged with other solvents. Indeed, these guest solvent molecules need to establish sufficiently strong hydrogen bonds with the framework in order to be adsorbed, e.g., acetone and ethanol are not exchangeable, whereas *N,N*-dimethylformamide (DMF) is.[61,78] The adsorption interaction and selectivity of this material have also been studied with different gases, such as N_2, CH_4, NO and CO_2, as well as with a wide range of alkylaromatic compounds for possible applications in industrial separation and environmental technology.[79-85] Furthermore, it has been shown that different metal nodes[86-91] alter the reversible breathing behaviour observed for the original Cr^{3+} and Al^{3+} MOFs,[69-70,92] as for example shown in Figure 1.8 for Sc MIL-53, recently opening viable synthetic pathways to optimise breathing behaviours for specific applications by mixing metal centers.[93-96]

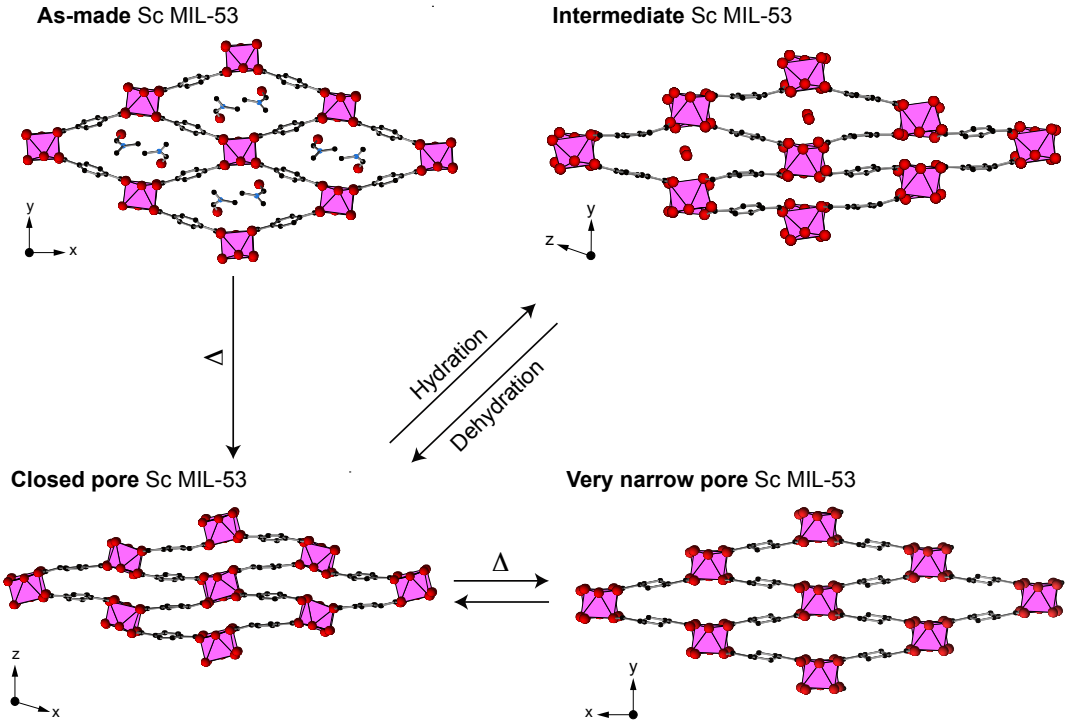

Figure 1.8 *Scheme showing the structural changes occurring to Sc MIL-53 starting from its as-made form containing N,N-dimethylformamide (DMF) in the pores. Subsequent calcination of this structure yields the closed pore (cp) structure, which, at room temperature, undergoes hydration leading to the intermediate form (int). Heating the cp form leads, reversibly, to a progressive expansion of the structure until the transition to the very narrow pore form (vnp) is produced. ScO_6 are represented by pink octahedra, C atoms by black spheres and O atoms by red spheres. H atoms are omitted for clarity.*[86]

1.2.1.2 $Sc_2(BDC)_3$

Scandium terephthalate, $Sc_2(BDC)_3$, is a small pore MOF made up of chains of ScO_6 octahedra interconnected by terephthalate linkers. The structure contains two crystallographically distinct terephthalate groups, as shown in Figure 1.9, in a ratio of 2:1. The framework includes small channels with triangular cross sections and a free pore diameter of about 4 Å, showing an adsorption capacity similar to that of most zeolites because of the absence of inaccessible pore volume. $Sc_2(BDC)_3$ displays very high thermal stability, owing to the lack of any easily removable coordinated species, and only weakly interacts with water molecules within its narrow pores which have phenyl groups making up the accessible pore walls.

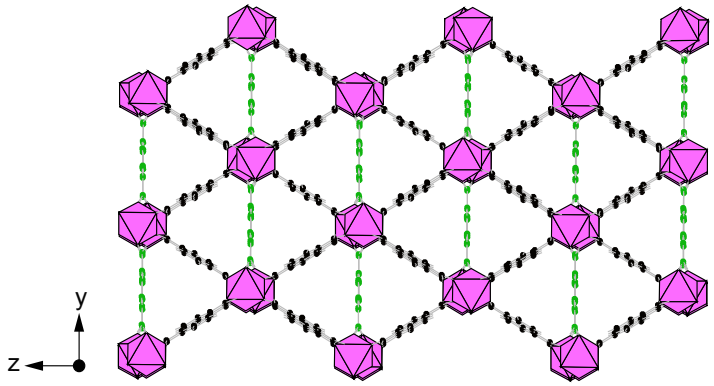

Figure 1.9 *Crystal structure of $Sc_2(BDC)_3$, showing the ScO_6 octahedra (pink) and the organic BDC spacer (with C atoms represented by black and green spheres for the two crystallographic distinct BDC spacers), as viewed down the x-axis, highlighting the porous structure and the full terephthalate coordination. H and O atoms have been omitted for clarity.*[97]

This framework has been investigated for its ability to adsorb small gas molecule through van der Waals interactions between the guest compounds and the phenyl rings of the spacer and, in particular, for its selectivity towards the adsorption of CO_2, which is strongly affected by the functionalisation of the linker.[98-99] This scandium terephthalate differs significantly from the other trivalent metal framework terephthalates, such as Al, Cr or Sc MIL-53, in the absence of bridging hydroxyl groups in the metal coordination environment, thus resulting in a more rigid structure that does not show any breathing behaviour.[68, 97,99]

1.2.2 Synthesis

The main difference between the synthetic procedures for MOFs and those used for zeolites is that the geometry of the metal-organic framework is, at least in part, predetermined by the use of a specific organic linker. The final topology will, subsequently, depend on the coordination of the metal nodes and the spacers used, without requiring the presence of template molecules in the reaction mixture. Typical syntheses are conducted at temperatures ranging from room temperature to 200 °C and involve mixing reactants in water or different organic solvents for a variable number of days depending on the reaction.[13] Quite commonly, in as-synthesised compounds excess solvent and linker molecules can be found in the pores of the

framework and can be removed by heating the sample under vacuum yielding the calcined form of the framework with empty pores. Once in this form, MOFs can also be gas loaded straight after calcination by exposing the sample to the gas of interest, allowing the gas molecules to interact with the binding sites in the pores of the framework. Unlike zeolites, it is important that the calcination process takes place either under vacuum or under inert gas flow to avoid decomposition of the organic linkers in general or any back-exchange in the case of isotopically enriched compounds. While the solvothermal approach[100] is most common for synthesising MOFs, it involves the use of large quantities of solvent (mL) and, therefore, doesn't represent a feasible pathway when expensive enriched reactants are used for enrichment purposes. In comparison, dry gel conversion (DGC) is a less common synthetic pathway, but has been used as an alternative for zeolite formation since 1990[101-104] and has been recently extended to MOFs.[105-106] This method involves the use of very small amounts of solvent (μL), compared to solvothermal synthesis, and has been shown to be a feasible cost-effective synthetic route to ^{17}O-enriched microporous materials[107] and MOFs in particular.[108] In this synthetic procedure, solid reagents are separated from the solvent within the autoclave, usually by placing a Teflon cup inside the Teflon liner of the autoclave, as shown in Figure 1.10. Once the autoclave is sealed and heated up to typical temperatures around 200 °C, water vapour is produced and is mixed with the reactants triggering the reaction and the formation of the final product.

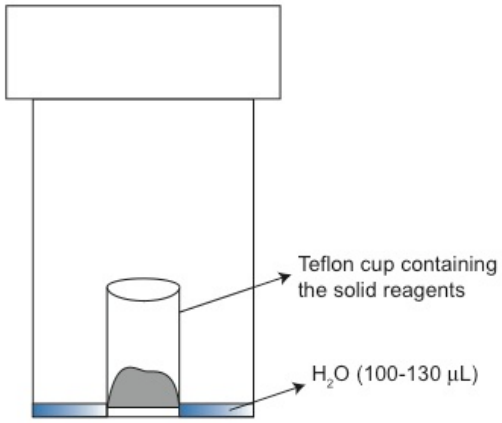

Figure 1.10 *Schematic dry gel conversion setup showing the Teflon cup containing the solid reactants and the solvent, water, at the bottom of the Teflon liner in the autoclave.*

However, this synthetic pathway might not be possible for all MOF topologies as some of them might require the presence of larger amounts of solvent to achieve a successful synthesis. For this reason, the development of a more general cost-effective enrichment procedure is required, allowing the investigation of a wider range of structures. Steaming of previously synthesised compounds in ^{17}O-enriched water vapour has been reported to successfully enable enrichment of inorganic salts and zeolites[109-111] and is investigated in this thesis as a more general enrichment pathway for terephthalate MOFs. The experimental setup for a steaming procedure is identical to that shown in Figure 1.10, but will involve the solvothermally pre-synthesised MOF instead of the starting reactants as the solid phase in the Teflon cup.

1.3 Thesis overview

Zeolites and MOFs, two classes of microporous solids, are investigated in this thesis, starting with the development of optimised pathways for the isotopic enrichment of these materials, with the aim of achieving a better understanding of the mechanisms involved in their synthesis and their structural behaviour. A complete solid-state characterisation is subsequently carried out primarily involving solid-state nuclear magnetic resonance (NMR) spectroscopy in combination with XRD, electron microscopy and mass spectrometry.

An introduction to the materials involved in this investigation, their structure, applications, synthesis and enrichment pathways is given in Chapter 1. Chapter 2 provides a background to the characterisation techniques used, in general, for zeolites and MOFs and the more specific background theory to XRD, NMR and dynamic nuclear polarisation (DNP).

The synthetic and characterisation results are presented and discussed in Chapter 3 to 6. Chapter 3 presents the synthetic procedures used for the UTL framework, the introduction of heteroatoms and the optimsation of enrichment pathways in ADOR hydrolyses. This chapter also includes the XRD and surface area characterisations carried out on hydrolysed and calcined "ADORable" zeolites. Chapter 4 presents a solid-state NMR investigation carried out on natural abundance and isotopically

enriched zeolites. *Ex situ* and *in situ* ^{29}Si and ^{17}O NMR characterisation of "ADORable" zeolites is described in this chapter, along with an ^{27}Al NMR investigation of aluminated zeolites tested for their catalytic performance. Chapter 5 presents the synthetic procedures used for the MOF frameworks introduced in Section 1.2.1 and the optimisation of different isotopic enrichment pathways. This chapter also includes the powder XRD characterisation of the synthesised MOFs, studies of morphology and composition using scanning electron microscopy (SEM)-energy dispersive X-ray (EDX) spectroscopy and the application of secondary ion mass spectrometry for the determination of enrichment levels. Chapter 6 presents the NMR results obtained on ^{17}O-enriched MIL-53 materials, containing single or mixed metals, Sc_2BDC_3 and mixed-phase compounds, as well as the DNP NMR preliminary studies of ^{17}O-enriched Al MIL-53 interacting with impregnating solvents of different polarity.

Chapter 7 summarises the conclusions from the work carried on the two classes of microporous materials investigated and outlines possible future work.

1.4 References

1 P. A. Wright, in *Microporous Framework Solids*, Royal Society of Chemistry Publishing, Cambridge, 2007, Chapter 1.

2 A. F. Cronstedt, *Akad. Handl.*, *Stockholm*, 1756, **17**, 20.

3 C. Colella, in *Studies in Surface Science and Catalysis*, Eds. J. Čejka and H. van Bekkum, Elsevier, 2005, **157**, pp. 13–40.

4 M.E. Davis, *Nature*, 2002, **417**, 813.

5 A. Primo and H. Garcia, *Chem. Soc. Rev.*, 2014, **43**, 7548–7561.

6 C. Martínez and A. Corma, *Coord. Chem. Rev.*, 2011, **255**, 1558–1580.

7 J. Gascon, F. Kapteijn, B. Zornoza, V. Sebastián, C. Casado and J. Coronas, *Chem. Mater.*, 2012, **24**, 2829–2844.

8 O. Cheung and N. Hedin, *RSC Adv.*, 2014, **4**, 14480–14494.

9 M. Moliner, *Dalton Trans.*, 2014, **43**, 4197–4208.

10 K. Li, J. Valla and J. Garcia-Martinez, *ChemCatChem*, 2013, **6**, 46–66.

11 M. P. Pina, R. Mallada, M. Arruebo, M. Urbiztondo, N. Navascués, O. de la Iglesia and J. Santamaria, *Micropor. Mesopor. Mater.*, 2011, **144**, 19–27.

12 A. Babaei, B. Khalilzadeh and M. Afrasiabi, *J. Appl. Electrochem.*, 2010, **40**, 1537–1543.

13 P. A. Wright, in *Microporous Framework Solids*, Royal Society of Chemistry Publishing, Cambridge, 2007, Chapters 2 and 5.

14 Ch. Baerlocher and L. B. McCusker, Database of Zeolite Structures: http://www.iza-structure.org/databases/

15 J. L. Paillaud, B. Harbuzaru, J. Patarin and N. Bats, *Science*, 2004, **304**, 990–992.

16 A. Corma, M. J. Díaz-Cabañas, F. Rey, S. Nicolopoulus and K. Boulahya, *Chem. Commun.*, 2004, 1356–1357.

17 F. Di Renzo and F. Fajula, in *Studies in Surface Science and Catalysis*, Eds. J. Čejka and H. van Bekkum, Elsevier, 2005, **157**, pp. 1–12.

18 C. S. Cundy and P. A. Cox, *Chem. Rev.*, 2003, **103**, 663–702.

19 C. S. Cundy and P. A. Cox, *Micropor. Mesopor. Mater.*, 2005, **82**, 1–78.

20 D. M. Bibby and M. P. Dale, *Nature*, 1985, **317**, 157–158.

21 A. Kuperman, S. Nadimi, S. Oliver, G. A. Ozin, J. M. Garcés and M. M. Olken, *Nature*, 1993, **365**, 239–242.

22 P. S. Wheatley, P. K. Allan, S. J. Teat, S. E. Ashbrook and R. E. Morris, *Chem. Sci.*, 2010, **1**, 483–487.

23 W. Loewenstein, *Am. Mineral.*, 1954, **39**, 92–96.

24 R. E. Morris and J. Čejka, *Nature Chem.*, 2015, **7**, 381–388.

25 T. Blasco, A. Corma, M. J. Díaz-Cabañas, F. Rey, J. A. Vidal-Moya and C. M. Zicovich-Wilson, *J. Phys. Chem. B*, 2002, **106**, 2634–2642.

26 J. Jiang, J. L. Jordá, M. J. Diaz-Cabanas, J. Yu and A. Corma, *Angew. Chem. Int. Ed.*, 2010, **49**, 4986–4988.

27 A. Corma, M. T. Navarro, F. Rey, J. Rius and S. Valencia, *Angew. Chem.*, 2001, **113**, 2337–2340.

28 J. Jiang, J. L. Jorda, J. Yu, L. A. Baumes, E. Mugnaioli, M. J. Diaz-Cabanas, U. Kolb and A. Corma, *Science*, 2011, **333**, 1131–1134.

29 C. Baerlocher, T. Weber, L. B. McCusker, L. Palatinus and S. I. Zones, *Science*, 2011, **333**, 1134–1137.

30 R. Simancas, D. Dari, N. Velamazán, M. T. Navarro, A. Cantín, J. L. Jordá, G. Sastre, A. Corma and F. Rey, *Science*, 2010, **330**, 1219–1222.

31 J. Sun, C. Bonneau, A. Cantín, A. Corma, M. J. Diaz-Cabanas, M. Moliner, D. Zhang, M. Li and X. Zou, *Nature*, 2009, **458**, 1154–1157.

32 M. Choi, K. Na, J. Kim, Y. Sakamoto, O. Terasaki and R. Ryoo, *Nature*, 2009, **461**, 246–249.

33 K. Na, M. Choi, W. Park, Y. Sakamoto, O. Terasaki and R. Ryoo, *J. Am. Chem. Soc.*, 2010, **132**, 4169–4177.

34 K. Varoon, X. Zhang, B. Elyassi, D. D. Brewer, M. Gettel, S. Kumar, J. A. Lee, S. Maheshwari, A. Mittal, C.-Y. Sung, M. Cococcioni, L. F. Francis, A. V. McCormick, K. A. Mkhoyan and M. Tsapatsis, *Science*, 2011, **334**, 72–75.

35 X. Zhang, D. Liu, D. Xu, S. Asahina, K. A. Cychosz, K. V. Agrawal, Y. Al Wahedi, A. Bhan, S. Al Hashimi, O. Terasaki, M. Thommes and M. Tsapatsis, *Science*, 2012, **336**, 1684–1687.

36 R. Pophale, P. A. Cheeseman and M. W. Deem, *Phys. Chem. Chem. Phys.*, 2011, **13**, 12407–12412.

37 M. W. Deem, R. Pophale, P. A. Cheeseman and D. J. Earl, *J. Phys. Chem. C*, 2009, **113**, 21353–21360.

38 M. D. Foster, A. Simperler, R. G. Bell, O. D. Friedrichs, F. A. A. Paz and J. Klinowski, *Nature Mater.*, 2004, **3**, 234–238.

39 A. Sartbaeva, S. A. Wells, M. M. J. Treacy and M. F. Thorpe, *Nature Mater.*, 2006, **5**, 962–965.

40 Y. Li, J. Yu and R. Xu, *Angew. Chem. Int. Ed.*, 2013, **52**, 1673–1677.

41 W. J. Roth, P. Nachtigall, R. E. Morris, P. S. Wheatley, V. R. Seymour, S. E. Ashbrook, P. Chlubná, L. Grajciar, M. Položij, A. Zukal, O. Shvets and J. Čejka, *Nature Chem.*, 2013, **5**, 628–633.

42 P. Eliášová, M. Opanasenko, P. S. Wheatley, M. Shamzhy, M. Mazur, P. Nachtigall, W. J. Roth, R. E. Morris and J. Cejka, *Chem. Soc. Rev.*, 2015, **44**, 7177–7206.

43 P. S. Wheatley, P. Chlubná-Eliášová, H. Greer, W. Zhou, V. R. Seymour, D. M. Dawson, S. E. Ashbrook, A. B. Pinar, L. B. McCusker, M. Opanasenko, J. Čejka and R. E. Morris, *Angew. Chem. Int. Ed.*, 2014, **53**, 13210–13214.

44 W. J. Roth, P. Nachtigall, R. E. Morris and J. Čejka, *Chem. Rev.*, 2014, **114**, 4807–4837.

45 E. Verheyen, L. Joos, K. Van Havenbergh, E. Breynaert, N. Kasian, E. Gobechiya, K. Houthoofd, C. Martineau, M. Hinterstein, F. Taulelle, V. Van Speybroeck, M. Waroquier, S. Bals, G. Van Tendeloo, C. E. A. Kirschhock and J. A. Martens, *Nature Mater.*, 2012, **11**, 1059–1064.

46 M. O'Keeffe and O. M. Yaghi, *Chem. Eur. J.*, 1999, **5**, 2796–2801.

47 W. J. Roth, O. V. Shvets, M. Shamzhy, P. Chlubná, M. Kubů, P. Nachtigall and J. Čejka, *J. Am. Chem. Soc.*, 2011, **133**, 6130–6133.

48 R. M. Ravenelle, F. Schüβler, A. D'Amico, N. Danilina, J. A. van Bokhoven, J. A. Lercher, C. W. Jones and C. Sievers, *J. Phys. Chem. C*, 2010, **114**, 19582–19595.

49 S. A. Morris, P. S. Wheatley, M. Položij, P. Nachtigall, P. Eliášová, J. Čejka, T. C. Lucas, J. A. Hriljac, A. B. Pinar and R. E. Morris, *Dalton Trans.*, 2016, **45**, 14124–14130.

50 M. Mazur, P. S. Wheatley, M. Navarro, W. J. Roth, M. Položij, A. Mayoral, P. Eliášová, P. Nachtigall, J. Čejka and R. E. Morris, *Nature Chem.*, 2015, **8**, 58–62.

51 K. J. D. MacKenzie and M. E. Smith, in *Multinuclear Solid-State NMR of Inorganic Materials*, Elsevier Science Ltd., 2002, Chapter 6.

52 A. E. Geissberger and P. J. Bray, *J. Non-Cryst. Solids*, 1983, **54**, 121–137.

53 J. E. Readman, N. Kim, M. Ziliox and C. P. Grey, *Chem. Commun.*, 2002, 2808–2809.

54 L. Peng, Y. Liu, N. Kim, J. E. Readman and C. P. Grey, *Nature Mater.*, 2005, **4**, 216–219.

55 X. Cheng, P. Zhao and J. F. Stebbins, *Am. Mineral.*, 2000, **85**, 1030–1037.

56 Z. Xu and J. F. Stebbins, *Geochim. Cosmochim. Acta*, 1998, **62**, 1803–1809.

57 T. Loeser, D. Freude, G. T. P. Mabande and W. Schwieger, *Chem. Phys. Lett.*, 2003, **370**, 32–38.

58 H. K. C. Timken, G. L. Turner, J. P. Gilson, L. B. Welsh and E. Oldfield, *J. Am. Chem. Soc.*, 1986, **108**, 7231–7235.

59 N. Merle, J. Trébosc, A. Baudouin, I. D. Rosal, L. Maron, K. Szeto, M. Genelot, A. Mortreux, M. Taoufik, L. Delevoye and R. M. Gauvin, *J. Am. Chem. Soc.*, 2012, **134**, 9263–9275.

60 O. M. Yaghi and H. Li, *J. Am. Chem. Soc.*, 1995, **117**, 10401–10402.

61 G. Férey, *Chem. Soc. Rev.*, 2008, **37**, 191–214.

62 J. Della Rocca, D. Liu and W. Lin, *Acc. Chem. Res.*, 2011, **44**, 957–968.

63 T. Baati, L. Njim, F. Neffati, A. Kerkeni, M. Bouttemi, R. Gref, M. F. Najjar, A. Zakhama, P. Couvreur, C. Serre and P. Horcajada, *Chem. Sci.*, 2013, **4**, 1597–1607.

64 L. Hamon, P. L. Llewellyn, T. Devic, A. Ghoufi, G. Clet, V. Guillerm, G. D. Pirngruber, G. Maurin, C. Serre, G. Driver, W. Van Beek, E. Jolimaître, A. Vimont, M. Daturi and G. Férey, *J. Am. Chem. Soc.*, 2009, **131**, 17490–17499.

65 J. Xiao, Y. Wu, M. Li, B. Liu, X. Huang and D. Li, *Chem. Eur. J.*, 2013, **19**, 1891–1895.

66 G. Zi, Z. Yan, Y. Wang, Y. Chen, Y. Guo, F. Yuan, W. Gao, Y. Wang and J. Wang, *Carbohydr. Polym.*, 2015, **115**, 146–151.

67 G. Férey and C. Serre, *Chem. Soc. Rev.*, 2009, **38**, 1380–1399.

68 J. P. S. Mowat, S. R. Miller, J. M. Griffin, V. R. Seymour, S. E. Ashbrook, S. P. Thompson, D. Fairen-Jimenez, A.-M. Banu, T. Düren and P. A. Wright, *Inorg. Chem.*, 2011, **50**, 10844–10858.

69 C. Serre, F. Millange, C. Thouvenot, M. Noguès, G. Marsolier, D. Louër and G. Férey, *J. Am. Chem. Soc.*, 2002, **124**, 13519–13526.

70 T. Loiseau, C. Serre, C. Huguenard, G. Fink, F. Taulelle, M. Henry, T. Bataille and G. Férey, *Chem. Eur. J.*, 2004, **10**, 1373–1382.

71 T. R. Whitfield, X. Wang, L. Liu and A. J. Jacobson, *Solid State Sci.*, 2005, **7**, 1096–1103.

72 E. V. Anokhina, M. Vougo-Zanda, X. Wang and A. J. Jacobson, *J. Am. Chem. Soc.*, 2005, **127**, 15000–15001.

73 M. Vougo-Zanda, J. Huang, E. Anokhina, X. Wang and A. J. Jacobson, *Inorg. Chem.*, 2008, **47**, 11535–11542.

74 J. P. S. Mowat, S. R. Miller, A. M. Z. Slawin, V. R. Seymour, S. E. Ashbrook and P. A. Wright, *Micropor. Mesopor. Mater.*, 2011, **142**, 322–333.

75 K. Barthelet, J. Marrot, D. Riou and G. Férey, *Angew. Chem. Int. Ed.*, 2002, **41**, 281–284.

76 S. Bourrelly, P. L. Llewellyn, C. Serre, F. Millange, T. Loiseau and G. Férey, *J. Am. Chem. Soc.*, 2005, **127**, 13519–13521.

77 G. Ortiz, G. Chaplais, J.-L. Paillaud, H. Nouali, J. Patarin, J. Raya and C. Marichal, *J. Phys. Chem. C*, 2014, **118**, 22021–22029.

78 G. W. P. Mounfield III and K. S. Walton, *J. Colloid Interface Sci.*, 2015, **447**, 33–39.

79 A. Boutin, F.-X. Coudert, M.-A. Springuel-Huet, A. V. Neimark, G. Férey and A. H. Fuchs, *J. Phys. Chem. C*, 2010, **114**, 22237–22244.

80 L. Alaerts, M. Maes, L. Giebeler, P. A. Jacobs, J. A. Martens, J. F. M. Denayer, C. E. A. Kirschhock and D. E. De Vos, *J. Am. Chem. Soc.*, 2008, **130**, 14170–14178.

81 B. Barth, M. Mendt, A. Pöppl and M. Hartmann, *Micropor. Mesopor. Mater.*, 2015, **216**, 97–110.

82 B. C. R. Camacho, R. P. P. L. Ribeiro, I. A. A. C. Esteves and J. P. B. Mota, *Sep. Purif. Technol.*, 2015, **141**, 150–159.

83 P. L. Llewellyn, S. Bourrelly, C. Serre, Y. Filinchuk and G. Férey, *Angew. Chem. Int. Ed.*, 2006, **45**, 7751–7754.

84 L. Hamon, P. L. Llewellyn, T. Devic, A. Ghoufi, G. Clet, V. Guillerm, G. D. Pirngruber, G. Maurin, C. Serre, G. Driver, W. V. Beek, E. Jolimaître, A. Vimont, M. Daturi and G. Férey, *J. Am. Chem. Soc.*, 2009, **131**, 17490–17499.

85 C. Serre, S. Bourrelly, A. Vimont, N. A. Ramsahye, G. Maurin, P. L. Llewellyn, M. Daturi, Y. Filinchuk, O. Leynaud, P. Barnes and G. Férey, *Adv. Mater.*, 2007, **19**, 2246–2251.

86 J. P. S. Mowat, V. R. Seymour, J. M. Griffin, S. P. Thompson, A. M. Z. Slawin, D. Fairen-Jimenez, T. Düren, S. E. Ashbrook and P. A. Wright, *Dalton Trans.*, 2012, **41**, 3937–3941.

87 L. Chen, J. P. S. Mowat, D. Fairen-Jimenez, C. A. Morrison, S. P. Thompson, P. A. Wright and T. Düren, *J. Am. Chem. Soc.*, 2013, **135**, 15763–15773.

88 F. Millange, N. Guillou, R. I. Walton, J.-M. Grenèche, I. Margiolaki and G. Férey, *Chem. Commun.*, 2008, 4732–4734.

89 F.-X. Coudert, A. U. Ortiz, V. Haigis, D. Bousquet, A. H. Fuchs, A. Ballandras, G. Weber, I. Bezverkhyy, N. Geoffroy, J.-P. Bellat, G. Ortiz, G. Chaplais, J. Patarin and A. Boutin, *J. Phys. Chem. C*, 2014, **118**, 5397–5405.

90 Y. Liu, D. Liu and C. Wang, *J. Solid State Chem.*, 2015, **223**, 84–94.

91 G. Xu, X. Zhang, P. Guo, C. Pan, H. Zhang and C. Wang, *J. Am. Chem. Soc.*, 2010, **132**, 3656–3657.

92 Y. Liu, J.-H. Her, A. Dailly, A. J. Ramirez-Cuesta, D. A. Neumann and C. M. Brown, *J. Am. Chem. Soc.*, 2008, **130**, 11813–11818.

93 O. Kozachuk, M. Meilikhov, K. Yusenko, A. Schneemann, B. Jee, A. V. Kuttatheyil, M. Bertmer, C. Sternemann, A. Pöppl and R. A. Fischer, *Eur. J. Inorg. Chem.*, 2013, **2013**, 4546–4557.

94 M. I. Breeze, G. Clet, B. C. Campo, A. Vimont, M. Daturi, J.-M. Grenèche, A. J. Dent, F. Millange and R. I. Walton, *Inorg. Chem.*, 2013, **52**, 8171–8182.

95 F. Nouar, T. Devic, H. Chevreau, N. Guillou, E. Gibson, G. Clet, M. Daturi, A. Vimont, J.-M. Grenèche, M. I. Breeze, R. I. Walton, P. L. Llewellyn and C. Serre, *Chem. Commun.*, 2012, **48**, 10237–10239.

96 I. Nevjestić, H. Depauw, K. Leus, V. Kalendra, I. Caretti, G. Jeschke, S. Van Doorslaer, F. Callens, P. Van Der Voort and H. Vrielinck, *ChemPhysChem*, 2015, **16**, 2968–2973.

97 S. R. Miller, P. A. Wright, C. Serre, T. Loiseau, J. Marrot and G. Férey, *Chem. Commun.*, 2005, 3850–3852.

98 R. S. Pillai, V. Benoit, A. Orsi, P. L. Llewellyn, P. A. Wright and G. Maurin, *J. Phys. Chem. C*, 2015, **119**, 23592–23598.

99 S. R. Miller, P. A. Wright, T. Devic, C. Serre, G. Férey, P. L. Llewellyn, R. Denoyel, L. Gaberova and Y. Filinchuk, *Langmuir*, 2009, **25**, 3618–3626.

100 Y.-R. Lee, J. Kim and W.-S. Ahn, *Korean J. Chem. Eng.*, 2013, **30**, 1667–1680.

101 W. Xu, J. Dong, J. Li, J. Li and F. Wu, *J. Chem. Soc., Chem. Commun.*, 1990, 755–756.

102 M. Matsukata, M. Ogura, T. Osaki, P. R. Hari Prasad Rao, M. Nomura and E. Kikuchi, *Top. Catal.*, 1999, **9**, 77–92.

103 D. Hu, Q. H. Xia, X. H. Lu, X. B. Luo and Z. M. Liu, *Mater. Res. Bull.*, 2008, **43**, 3553–3561.

104 S. Goergen, E. Guillon, J. Patarin and L. Rouleau, *Micropor. Mesopor. Mater.*, 2009, **126**, 283–290.

105 Q. Shi, Z. Chen, Z. Song, J. Li and J. Dong, *Angew. Chem. Int. Ed.*, 2010, **50**, 672–675.

106 I. Ahmed, J. Jeon, N. A. Khan and S. H. Jhung, *Cryst. Growth Des.*, 2012, **12**, 5878–5881.

107 B. Chen and Y. Huang, *J. Am. Chem. Soc.*, 2006, **128**, 6437–6446.

108 P. He, J. Xu, V. V. Terskikh, A. Sutrisno, H.-Y. Nie and Y. Huang, *J. Phys. Chem. C*, 2013, **117**, 16953–16960.

109 P. J. Dirken, S. C. Kohn, M. E. Smith and E. R. H. van Eck, *Chem. Phys. Lett.*, 1997, **266**, 568–574.

110 Z. Xu and J. F. Stebbins, *Geochim. Cosmochim. Acta*, 1998, **62**, 1803–1809.

111 X. Cheng, P. Zhao and J. F. Stebbins, *Am. Mineral.*, 2000, **85**, 1030–1037.

2 Introduction to characterisation techniques

2.1 Characterisation techniques for zeolites

The starting point to understand and exploit the properties and behaviour of zeolites is their structure and, depending on the experimental technique employed, distinct structural features can be identified and measured. On one hand, from diffraction-based experiments, the time- and space-averaged structure is obtained, while spectroscopy gives details of the local, atomic-scale structure. Therefore, the combination of these characterisation techniques, unveiling the overall framework structure as well as details of the local environment of atoms, is of fundamental importance for the study of zeolites. The common denominator in all the fields where zeolites are applied is their ability to selectively take up molecules, from the liquid or gas phase, within their porous framework. For this reason, experimental studies of adsorption, from which the internal surface area can be quantified, are also another important option for characterisation. In addition, SEM-EDX and catalytic characterisation studies prove very useful to better understand the topology, the incorporation of heteroatoms and potential catalytic applications of zeolites.

2.1.1 Solid-state NMR spectroscopy

The complementarity of solid-state NMR to XRD, along with its versatility in terms of the types of nuclei that can be studied and of the number of possible experiments that can be performed, have established it as an indispensable structural tool.[1-5] While ^{29}Si NMR spectroscopy has been widely investigated and has proven very useful in the characterisation of zeolites,[6-8] ^{17}O NMR spectroscopy, as described in Section 1.1.3, has been less commonly used and appears at first an unattractive nucleus to study owing to the anisotropic quadrupolar broadening of its spectral lineshapes, its very low natural abundance (0.037%) and moderate gyromagnetic ratio. Even with ^{17}O-enriched zeolites samples, high-resolution methods and high applied magnetic fields are often required to overcome the second-order quadrupolar broadening.[9-10] Early studies showed the sensitivity of ^{17}O quadrupolar parameters to

the local environment allowing the differentiation of Si-O-Al and Si-O-Si species.[11] However, resolution of the individual distinct Si-O-Al and Si-O-Si species proves difficult, even when high-resolution techniques are used, as a result of the high number of such oxygen sites and the large range of local environments present particularly in disordered frameworks. Only when the Si/Al ratio is either high or ~1, resulting in little disorder or ordering of the framework according to Loewensteins's rule (see Section 1.1.1), the range of local environments is reduced and resolution of different crystallographic sites has been shown to be possible with high-resolution techniques.[12-13] The catalytic properties of zeolites are determined by the presence of acid sites within their frameworks, typically Si-(OH)-Al Brønsted sites. The unambiguous identification of these hydroxyl resonances can often prove challenging, requiring high applied magnetic fields and a combination of spectral editing techniques.[14-15] Along with bulk Si-O-Si sites, hydroxyl sites, in the form of Si-OH species, are also normally present in silicate materials[16] as surface defects or in the interlayer region of layered materials. In the latter case dynamics, originating from adsorbed molecules in the interlayer region, can also hinder their detection.

To overcome the sensitivity issues related to the extremely low natural abundance of ^{17}O, DNP has been shown to provide significant gains in sensitivity[17] by microwave-induced transfer of polarisation from paramagnetic centers, in the form of radical solutions impregnating the sample and interacting with its surface,[18] directly or indirectly via ^{1}H to the nucleus of interest in the compounds analysed. While successfully applied, for example, to simple natural-abundance oxides and hydroxides[19] and hybrid functionalised mesoporous silica materials[20-21] by direct and indirect transfer to ^{17}O and ^{29}Si spins, respectively, the application of DNP to zeolites appears more difficult. Indeed, problems related to the efficiency of polarisation transfer[22] and the actual incorporation of the paramagnetic centers in the matrix containing the zeolite samples typically lead to moderate or non-existent signal enhancements, although this is an area of ongoing research.

The magnetic fields used in this investigation range from 9.4 T to 20.0 T and magic angle spinning (MAS) was always applied to average the orientational dependence of the anisotropic components of the dipolar coupling, chemical shielding, J coupling and first-order quadrupolar interactions. Both ^{17}O single-pulse and ^{17}O multiple-

quantum MAS (MQMAS) experiments have been carried out and, in the case of ^{29}Si, single-pulse and ^{1}H-^{29}Si cross-polarisation (CP) spectra have been recorded. In addition, ^{1}H-^{17}O cross-polarisation and two dimensional ^{17}O-^{29}Si correlation experiments have been performed. The theory of NMR and DNP NMR along with detailed descriptions of the experiments used will be separately introduced in Sections 2.4 and 2.5.

2.1.2 Powder X-ray diffraction

As many zeolitic materials are used in the form of powders, X-ray diffraction from microcrystalline powders (or powder X-ray diffraction, PXRD) is an extremely useful characterisation technique. This is routinely applied to identify products from syntheses, either matching peak positions and intensities with previously synthesised and known products or with patterns from diffraction databases. However, for the structure determination of novel phases, PXRD data, providing much less information then single-crystal XRD, generally needs to be integrated with the information from electron microscopy, solid-state NMR spectroscopy and computer simulation.

Owing to the layered structure of the zeolitic materials presented in this investigation, the primary use of the experimentally acquired PXRD patterns has been the determination of the spacing between layers, which is a uniquely identifying feature for a certain material.[23] Unless otherwise stated, PXRD data presented have been acquired with a PANalytical Empyrean instrument operated in reflection, Bragg-Brentano, θ-2θ mode and equipped with a Cu X-ray tube, a primary beam monochromator ($CuK_{\alpha 1}$) and X'celerator RTMS (Real Time Multiple Strip) detector. Typically, a 5-50° 2θ range was investigated in 1 h. For a few isotopically (^{17}O, ^{29}Si) enriched and post-synthesis aluminated samples data were collected on a STOE STADIP instrument operated in capillary Debye-Scherrer mode equipped with a Cu X-ray tube, a primary beam monochromator ($CuK_{\alpha 1}$) and a scintillation position-sensitive linear detector. Typically, 5-50° or 5-40° 2θ ranges were investigated in 1 h and 30 min or overnight. The theory behind XRD and the experimental geometries used will be separately introduced in Section 2.3.

2.1.3 N_2 adsorption

An adsorption isotherm shows the equilibrium uptake of a sorbate at a chosen constant temperature as a function of the concentration of the sorbate, which corresponds to a pressure for an adsorption from the gas phase.[24] Molecules can attach to a surface in two ways: either via physisorption or via chemisorption. The first phenomenon is mainly dominated by the long-range but weak van der Waals interactions between the adsorbate and the surface and typical values for the enthalpies involved are usually around −20 kJ mol^{-1}, insufficient to lead to bond breaking. Therefore, a physisorbed molecule retains its identity during this reversible process, even if it might be distorted by the presence of the surface. In the latter phenomenon, on the other hand, molecules form chemical bonds with the surface and the resulting enthalpy values are much greater, around −200 kJ mol^{-1}, with distances between the surface and the adsorbate typically shorter than physisorption.[25]

Physisorption of N_2 at 77 K is the most widely used method to measure surface areas of solids in general, and of crystalline microporous solids in particular. For this type of solid, the shape of the Type I isotherm, see Figure 2.1, is followed, even if not simply described by the Langmuir model, because of the inequivalence and non-uniformity of the surface sites, the absence of an open surface for adsorption and desorption and the presence of interactions between adsorbates. As shown in Figure 2.1, this type of isotherm is characterised by a high uptake at low pressures and a clear maximum level of uptake as the internal pores are filled, towards higher pressures.

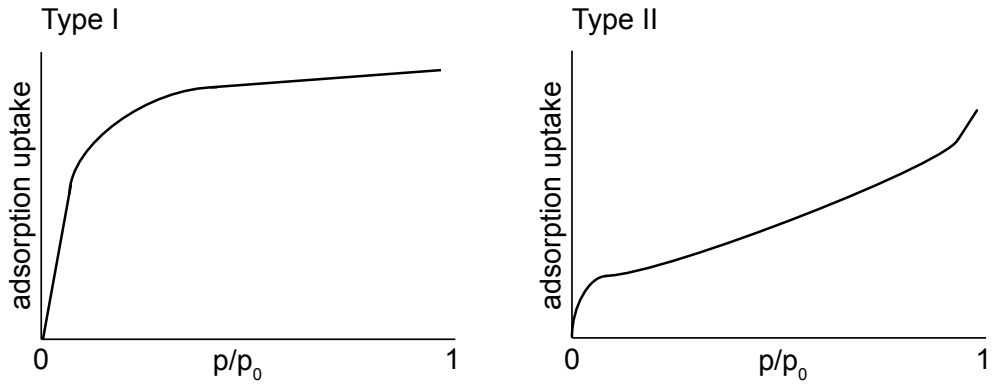

Figure 2.1 *Type I and Type II schematic isotherms according to Brunauer-Deming-Teller classification.[26] On the x axis, p indicates the adsorbate pressure, whereas p_0 indicates the saturated vapour pressure of the pure liquid adsorbate at the isotherm temperature.*

Such a maximum uptake level has been usefully converted in this investigation to a pore volume per unit mass by assuming the density of the adsorbed nitrogen to be equal to that of liquid nitrogen at that temperature. Surface area values of zeolite samples have been derived following the BET (Brunauer-Emmett-Teller) model, applicable to Type II isotherms, see Figure 2.1, even though not strictly valid because of the absence of open surface for multilayer formation[24]

$$\frac{V}{V_{mon}} = \frac{cz}{(1-z)\{1-(1-c)z\}}, \tag{2.1}$$

where V is the volume of adsorbate adsorbed, V_{mon} is the volume corresponding to monolayer coverage, $z = \frac{p}{p_0}$, with p indicating the adsorbate pressure and p_0 the saturated vapour pressure of the pure liquid adsorbate at the isotherm temperature, and c is a constant, which is large when the enthalpy of desorption from a monolayer is large compared to the enthalpy of vaporisation of the liquid adsorbate.

Equation 2.1 can be rearranged to

$$\frac{z}{(1-z)V} = \frac{1}{cV_{mon}} + \frac{(c-1)z}{cV_{mon}}, \tag{2.2}$$

obtaining $\frac{(c-1)}{cV_{mon}}$ from the slope and $\frac{1}{cV_{mon}}$ from the intercept of a plot of $\frac{z}{(1-z)V}$ against z, thus allowing the derivation of the surface area.[25]

Adsorption data presented in this investigation were acquired at −196 °C with a Tristar II 3020 instrument equipped with a volumetric system for the measurement of the amount of adsorption. Samples were degassed at 300 °C for 3 h. For these measurements, sample preparation and data collection was carried out in collaboration with Dr Matthew McPherson and data processing was performed in collaboration with Dr Paul Wheatley.

2.1.4 SEM-EDX analysis

To test potential applications of the zeolites synthesised, characterisation techniques aimed at better understanding catalytic activity, heteroatom incorporation and crystallite morphology have been carried out in collaboration with Samantha Russell. Mainly focusing on the UTL framework in which Al was post-synthetically exchanged, these investigations helped the understanding of the distribution and amount of heteroatoms incorporated and their possible role in a catalytic process.

SEM has been employed to acquire information on the topology of the samples analysed. A single beam of electrons is scanned over the surface of the sample and reflections from the sample are then collected by a detector. Upon entering a solid, accelerated electrons can be scattered both elastically, by electrostatic interactions with atomic nuclei, and inelastically by interaction with atomic electrons. Reflections coming from the sample can therefore be classified into two types: back scattering and secondary scattering. The former type of scattering occurs when the original electron is reflected by the sample with only a fractional loss of energy compared to the incoming electron beam (i.e., several keV) and in this case the intensity of the reflected signal, arising from several micrometers below the sample surface, is proportional to the atomic number of the specimen atoms involved. Owing to this, back scattering is commonly used to obtain SEM images with modulated intensities dependent on variations in the chemical composition of the sample. Secondary scattering, in contrast, occurs when electrons are emitted as a result of energy transfer from the incoming primary electron beam. Since the emitted electron has a higher probability of escaping the solid phase when located closer to the sample surface, secondary scattering, involving electrons with energies of less then 50 eV,

typically reflects the surface structure of the sample, thus providing information on surface topography.[27-28] All samples were placed in μg quantities on top of an adhesive carbon disk on the sample holder and gold-coated with a Quorum Q150R ES (dual sputtering and evaporation system) and studied on a Jeol JSM-5600 scanning electron microscope equipped with a secondary electron detector for topographic contrast imaging and a tungsten filament electron source. Measurements were carried out with a working distance of 20 mm, a spotsize of 40 and a voltage of 25 kV in the W filament. Gold sputter coating is achieved by exposing the target material (gold) to an energised plasma formed from a heavy inert gas, such as argon, leading to the ejection of target atoms which provide multidirectional coating on the specimen. Metal coating of non-conductive substrates is necessary to provide a thin (nm) layer of a conductive metal preventing the possibility of local potential build-up due to charging on the surface of the sample which could affect the detection of secondary electrons.[29] Figure 2.2 shows the basic components of a scanning electron microscope and the electron beam path from the gun to the sample. The electron beam is focused to a small spot projected on the sample by multiple lenses and can be deflected with the aid of scan coils to scan across the sample to provide a full image. While SEM provides valuable information about the morphology of a sample, it doesn't allow quantitative information about the composition of the sample to be obtained. For this purpose a signal highly dependent of the atomic number of the nucleus is needed, thus involving the electron-shell structure of the atom.

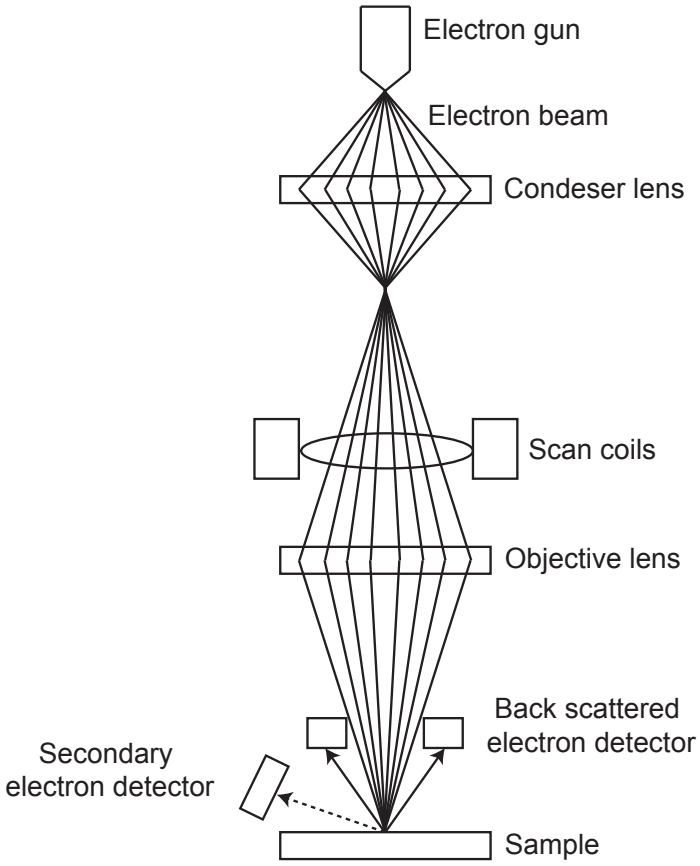

Figure 2.2 *General schematic setup of a scanning electron microscope showing the electron beam pathway.*

EDX spectroscopy is used to determine the chemical composition of the sample providing a spectrum of the characteristic X-rays emitted by specific elements. When an electron from the primary beam enters a sample, it has a low probability of being inelastically scattered by an inner-shell electron, which is excited and ejected from the shell, leaving the atom in an excited state with a vacancy in its inner shell. Within about 10^{-15} s one of the other electrons will fill this vacancy by making a transition from a higher energy level, resulting in the emission of a characteristic X-ray photon with an energy dependent on the atom and the energy levels involved. For these measurements a high-energy electron beam (typically 25 keV), penetrating several micrometers into the sample, is required to achieve the ejection of inner-shell electrons. Once X-rays are emitted, some form of dispersive device is needed to generate a spectrum, distinguishing X-ray photons on the basis of their energy. For this purpose, a semiconductor diode X-ray detector, cooled to about 140 K, is used to

convert X-rays into electronic signals, which are then processed to determine their energy. The characteristic X-rays and the resulting counts recorded provide information on the presence and relative ratios of specific elements in the sample. In theory, only peaks belonging to elements within the region of the sample analysed should be detected. In practice, however, spurious peaks will frequently appear typically from parts of the specimen holder or instrument components requiring caution when interpreting the significance of the recorded X-ray peaks.[30] An Oxford Inca EDX instrument, attached to the scanning electron microscope, was used for the compositional analyses reported. A specific technique related to EDX and known as "mapping" was used to better understand the distribution of Al on the surface of the zeolitic samples by superimposing the characteristic X-ray and the secondary electron images. The experimental variation for EDX measurements reported in this work has been evaluated by repeating experiments several times on the same area of some of the crystallites.

2.1.5 Catalytic testing

Catalytic tests have been carried out on zeolites where Al was incorporated to investigate the presence and potential activity of acid sites. In particular, the production of NO has been considered because of its known crucial role in the cardiovascular, nervous and immune systems.[31] Sodium nitrite ($NaNO_2$) is used as a substrate for this catalytic reaction and injected in the reaction vial, containing the zeolite suspended in water, shortly after the start of the run. The Al-containing zeolites are first exchanged with NH_4Cl solutions for varying lengths of time and at different temperatures to promote the formation of acid sites upon calcination, when NH_3 is released. The potential catalytic activity is then tested by monitoring the NO formation as a result of $NaNO_2$ injection, according to the following hypothesised pathway[32] shown in Equations 2.3-2.5

$$NO_2^- + H^+ \rightarrow HNO_2 \quad (2.3)$$

$$2HNO_2 \rightarrow N_2O_3 + H_2O \quad (2.4)$$

$$N_2O_3 \rightarrow NO + NO_2\,. \quad (2.5)$$

The resulting NO produced is monitored using a Sievers 280i nitric oxide analyser, as shown in Figure 2.3.

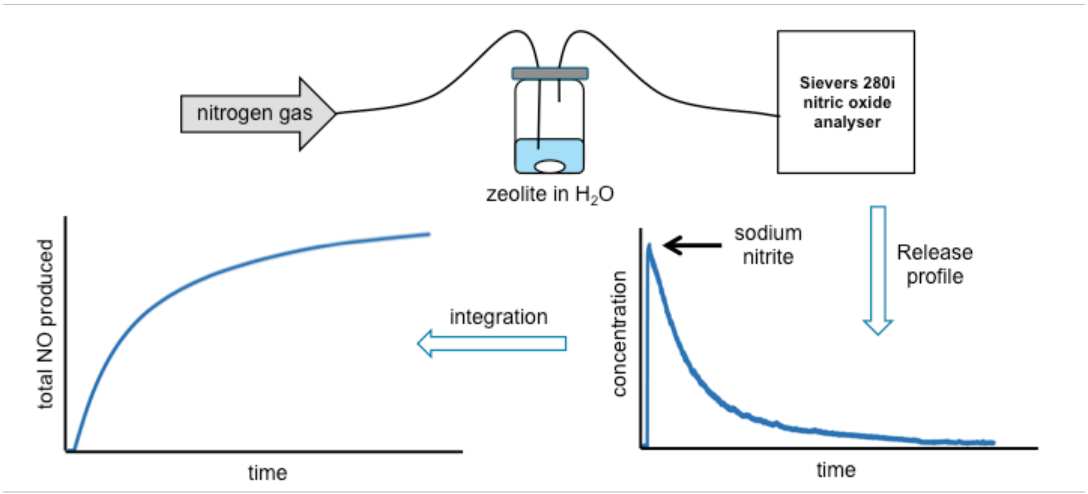

Figure 2.3 *Schematic setup for NO analysis with the resulting release and integrated profiles.*

A nitrogen supply is provided to the analyser passing through the reaction vial containing the sample as shown in Figure 2.3. The NO produced from the sample is then quantified by reaction with ozone, generated within the analyser from an oxygen supply, as described in Equations 2.6 and 2.7

$$NO + O_3 \rightarrow NO_2^* + O_2 \quad (2.6)$$

$$NO_2^* \rightarrow NO_2 + h\nu\,. \quad (2.7)$$

A photomultiplier subsequently measures the release of photons from the relaxation of the excited nitrogen dioxide, as shown in Equation 2.7. Calibrations using zero gas, which should not have NO content, and standard NO gas of known concentration are carried out to ensure accurate readings and allow the calculation of calibration constants for data processing.

2.2 Characterisation techniques for MOFs

Structure determination is key to understanding important properties of MOFs, such as their pore sizes, the nature of the interactions with potential guest molecules and changes occurring to the framework upon the variation of experimental conditions. All this information proves of fundamental importance when investigating the potential applications of these materials. Solid-state characterisation of these compounds usually combines local and space-averaged structure determination by spectroscopy and XRD, respectively. When dealing with disordered guest molecules present in loaded or as-made structures, in particular, the interpretation of data from XRD, a technique highly reliant on the presence of long-range order, can be problematic and requires additional spectroscopic investigation of atomic-level dynamics and disorder. Electron microscopy can be employed to acquire information on the crystallite morphology, potentially affected by the very low amounts of solvent used during the optimised enrichment syntheses, and cation distribution in mixed metal compounds. Moreover, to experimentally determine the amount of ^{17}O incorporated in the structures as a result of the DGC synthesis procedure, secondary ion mass spectrometry (SIMS) experiments have been carried out for some of the ^{17}O-enriched samples.

2.2.1 Solid-state NMR spectroscopy

A multinuclear solid-state NMR investigation is the typical approach for the characterisation of the local structure of a MOF. ^{13}C, in direct acquisition or by ^{1}H-^{13}C cross-polarisation experiments, and ^{1}H NMR spectra are acquired to obtain information on the nature of linker, possible decomposition of the structure, the presence of guest molecules in general and any hydration in particular. These investigations have been shown to help the determination of the behaviour of the framework as a function of different levels of hydration, the location of water molecules in hydrated structures and the presence of dynamics by deuteration studies.[33-35] Spectroscopy investigation of the metal centers, where possible (i.e., for non-paramagnetic compounds or those with favourable NMR properties), enables insight into the ordering of the structure and the resolution of inequivalent sites upon

interaction with guest molecules.[36-37] For the reasons outlined in Section 1.1.3, ^{17}O is a much less investigated nucleus notwithstanding its fundamental structural role. Indeed, oxygen atoms, in terephthalate-based and many other MOFs, directly connect the linker molecules to the metal centers potentially providing a wealth of information on the structural changes occurring when, for example, a substitution occurs at the metal center or the pore conformation changes as a result of an interaction with different types of guest molecules or heat treatments. For such ^{17}O NMR investigations to be possible within a reasonable timeframe, enrichment is necessary and has been shown to be possible[38] with the identification of chemically and crystallographically distinct spectral signatures of various oxygen species in representative MOFs, such as CPO-27, MIL-53 and UiO-66. DNP NMR experiments have also been shown to provide enhancements focusing on indirect polarisation transfer to ^{13}C or ^{15}N in the linker molecules[39] and to the metal centers, e.g., ^{27}Al, also allowing the acquisition of heteronuclear correlation experiments precluded under standard conditions.[40] In these cases, the choice of the size of the radical and resting time of the impregnated solid is of crucial importance to determine the possible diffusion of the radical species into the pores of the framework. Furthermore, the choice of the radical solution used is more critical than with other types of solids as MOFs can interact with solvent guest molecules, opening up the possibility of changes occurring to the framework conformation as a result of the type of solvent used.

The magnetic fields involved in this investigation range from 14.1 to 20.0 T and magic angle spinning (MAS) was always applied to average the orientational dependence of the anisotropic components of the dipolar coupling, chemical shielding, J-coupling and first-order quadrupolar interactions. A combination of ^{17}O, ^{1}H, ^{27}Al and ^{45}Sc single-pulse, ^{17}O and ^{1}H spin echo, ^{1}H-^{17}O and ^{1}H-^{13}C cross-polarisation, ^{17}O and ^{27}Al MQMAS and ^{17}O double rotation (DOR) experiments have been carried out on the range of MOFs synthesised. The theory of NMR and DNP NMR, along with detailed descriptions of the experimental conditions used, will be separately introduced in Sections 2.4-2.5.

2.2.2 Powder X-ray diffraction

All the investigated MOFs have been obtained in the form of microcrystalline powders and PXRD patterns have been mainly used to identify, by comparison to literature patterns, the terephthalate MOFs synthesised and the breathing behaviour of as-made, calcined, hydrated and dehydrated forms. Rietveld refinements and Pawley fits have been carried out in collaboration with Dr Samuel Morris to evaluate unit cell variations when the larger Ga^{3+} cation was introduced and to determine the actual Al:Ga ratios in the mixed-metal MIL-53 frameworks synthesised.

PXRD data were collected on a STOE STADIP instrument operated in capillary Debye-Scherrer mode equipped with a Cu X-ray tube, a primary beam monochromator ($CuK_{\alpha 1}$) and a scintillation position-sensitive linear detector. Typically, 3-50° ranges were investigated overnight. For calcined or dehydrated samples capillaries have been sealed to avoid exposure to air during acquisition. The theory behind XRD and the experimental geometries used will be separately introduced in Section 2.3.

2.2.3 SEM-EDX analysis

SEM analysis, as introduced in Section 2.1.4, enabled insight into the morphology of the MIL-53 samples obtained from the syntheses carried out in DGC conditions. Moreover, compositional analysis by EDX of single crystallites from mixed-metal MIL-53 samples has been carried out to better understand the cation distribution in these materials. For these latter experiments, powders have been sieved prior to analysis to obtain a better dispersion of the materials on the sample holders. Experimental conditions are the same as described in Section 2.1.4. The SEM-EDX characterisation has been carried out in collaboration with Samantha Russell.

2.2.4 Ion microprobe SIMS

Ion microprobe SIMS has been used for the determination of oxygen (^{16}O, ^{17}O and ^{18}O) isotopic ratios in some of the ^{17}O-enriched MOFs synthesised. This technique had been previously shown to achieve high-precision determination of

oxygen isotopic ratios in geological samples[41] and has been therefore investigated for its application to MOFs.

An ion microprobe consists of a primary column where the primary ion beam is generated, filtered, focused, shaped, positioned and rastered before reaching the sample. Typically the primary ion beam is composed of oxygen or cesium ions, with electropositive elements best analysed with an oxygen primary beam, either O^+ or O^-, and electronegative elements, such as oxygen, best analysed with cesium, only used as Cs^+. Secondary ions are formed as a result of erosion, or sputtering, of the sample surface from the primary beam and are extracted by holding the sample at a high potential usually of opposite polarity to the primary beam. To keep a constant secondary ion beam current major voltage changes have to be avoided and, for insulating materials, this can be achieved, at least in part, by gold coating the sample. The generated secondary ions, characterised by a wide range of energies, are transferred into the mass spectrometer and passed into an electrostatic energy analyser where they are dispersed with deflected paths dependent on their energies. A movable slit allows the selection of the desired portion of secondary ions that are passed into the magnetic analyser where ions are refocused as a function of their mass and energy and subsequently detected. In such a double-focusing mass spectrometer, the combined use of energy and mass analysers allows high mass resolution to be achieved. For insulating specimens charge build-up can occur at the sputter site as a result of the impact of Cs^+ ions and the emission of secondary electrons from the sample with insufficient electrons reaching the site from the conductive coating. In this case, the sample is bombarded with additional electrons from an electron flood gun. The instrument, schematically shown in Figure 2.4, has to be kept under ultra high vacuum for operation with the analysis chamber at 5×10^{-10} Torr to completely minimise the probability of a secondary ion hitting a gas molecule in its path.[42]

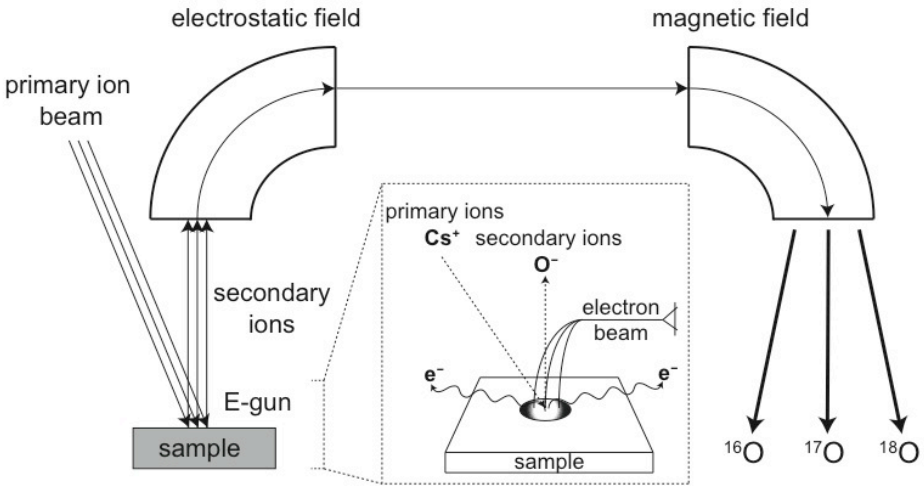

Figure 2.4 *Simplified scheme of a secondary ion double-focusing mass spectrometer with the inset showing in detail the generation of secondary ions and charge compensation occurring at the sputter site on the sample surface.*

The oxygen isotope data were acquired at the University of Edinburgh (in collaboration with Dr John Craven) using a Cameca IMS 1270 with a $^{133}Cs^{+}$ focused primary ion beam of ~4 nA rastered over an area of 25 μm^2. Secondary ions were extracted at 10 kV and ^{16}O, ^{17}O and ^{18}O were monitored at a mass resolution of ~6,000 using either a Faraday cup or an electron multiplier depending on the count rates of the isotope. Background, relative detector yield and dead-time corrections were applied to the count rates recorded. Each analysis involved a pre-sputtering time of 60 s, followed by automatic centering of the secondary ion beam into the field aperture (3,000 μm) and entrance slits (30 μm). Isotopic data was acquired in two blocks of ten cycles, amounting to a total count time of 80 seconds per isotope. Results were obtained with a standard error of the mean in the range 0.3-6% depending on the uniformity of the sample surface. Instrument calibration and alignment was checked by measuring the isotopic ratios of a reference mineral standard (Ilmenite) at natural abundance. For powdered samples, such as MOFs in their as-made and calcined forms, the packing stage, in order to obtain a flat and polished surface stable in vacuum for analysis, proved to be extremely challenging. Samples were prepared by embedding the MOF powders in indium (99.9995% purity

level) mounts using a hydraulic press (approx. 5 tons) and then covered with a gold coat about 30 nm thick.

2.3 X-ray diffraction

XRD is an experimental characterisation technique, primarily applied to crystalline materials, which provides structural information related to the position of atoms. This phenomenon originates from the interaction of atomic electrons in solids with X-rays which are characterised by wavelengths (of the order of 10^{-10} m) comparable to the separation of scattering centers, atoms or ions, in a solid.

2.3.1 Crystallography

All crystalline materials are characterised by a structure with a regular distribution of atoms in space and the simplest repeating portion of a structure that shows its full symmetry is defined as the unit cell. The unit cell can be thought as the smallest volume of space containing all the structural information, from which the entire structure can be reproduced by translational displacements. The unit cell is defined by angles and lengths, known as the cell parameters and shown for a general unit cell in Figure 2.5. By convention, the angle between a and b is γ, the angle between b and c is α and the angle between c and a is β.

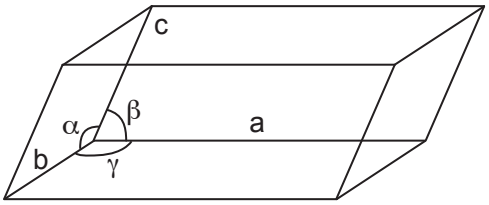

Figure 2.5 *General three dimensional unit cell with unit cell parameters.*

In Figure 2.5 the unit cell parameters can take any value as the cell has no definied symmetry, but, as the level of symmetry increases, relationships between the cell parameters can be established leading to the seven crystal systems summarised in Table 2.1.

Unit cell parameters		Crystal system
$a = b = c$	$\alpha=\beta=\gamma= 90°$	Cubic
$a = b \neq c$	$\alpha=\beta=\gamma= 90°$	Tetragonal
$a \neq b \neq c$	$\alpha=\beta=\gamma= 90°$	Orthorhombic
$a \neq b \neq c$	$\alpha=\gamma= 90° \beta\neq 90°$	Monoclinic
$a \neq b \neq c$	$\alpha\neq\beta\neq\gamma\neq 90°$	Triclinic
$a = b \neq c$	$\alpha=\beta= 90° \gamma= 120°$	Hexagonal
$a = b = c$	$\alpha=\beta=\gamma\neq 90°$	Trigonal

Table 2.1 *Unit cell parameters for the seven crystal systems.*

The position of atoms within the unit cell can be expressed in terms of fractional coordinates. Indeed, the position of an atom, displaced by x × a parallel to a, y × b parallel to b and x × c parallel to c from the origin, is described by the fractional coordinates (x,y,z). This method for the description of atomic positions can be applied to all the crystal systems and offers a clear way of visualising even complex structures, typically viewed in projection along one direction.

An array of equivalent points in one, two or three dimensions is termed a lattice, and shows the translational symmetry of the material. In crystal structures four different lattice types are found: primitive, body centered, face centered and side centered. For the primitive (P) lattice type, the only translational symmetry is that of the unit cell with lattice points located at the corners of the cell, whereas for the other lattice types there is additional symmetry within the unit cell. For the body centered (I) lattice type, lattice points can be found at the corners as well as at the center of the unit cell at fractional coordinates (1/2,1/2,1/2). When lattice points are at the center of the faces as well as at the corners of the unit cell, the lattice is known either as face centered (F), if lattice points are located at the center of all faces, or side centered (A, B or C) if the lattice points are located on only two opposite faces. Specifically, for the side centered notation, the C type lattice refers to the case when the additional lattice points are at the center of the faces determined by the ab plane and the A and B types refer to the cases where the lattice points are at the center of the bc and ac planes, respectively. The A and B centered descriptions are not, however, most

commonly used as a redefinition of the cell directions leads to the C centered description.

The combination of the four lattice types (P,I,F,C) with the seven crystal systems yields the Bravais lattices, 14 unique possibilities summarised in Table 2.2. It can be observed that not all combinations of lattice types and crystal systems result in a Bravais lattice, generally because an equivalent description can be found with one of the existing 14 lattices.

Crystal system	Bravais lattices
Cubic	P,I,F
Tetragonal	P,I
Orthorhombic	P,C,I,F
Monoclinic	P,C
Triclinic	P
Hexagonal	P
Trigonal	P

Table 2.2 *The 14 Bravais lattices.*

The type of lattice can also be used in conjunction with symmetry operations to indicate the space group of a crystallographic system, allowing a classification of the structures according to the symmetry elements they possess. Lattice points may be connected by planes in a three dimensional structure, resulting in a set of equally spaced parallel planes with each lattice point lying on one of the planes. Lattice planes are labelled using three conventional Miller indices h, k and l, which can be integers (positive or negative) or zero, and a set of Miller planes is normally identified with the notation {h,k,l}, whereas a single Miller plane is identified with the notation (h,k,l). Miller indices can be obtained from the reciprocals of the fractional intersection distances of the planes with each of the cell directions from the origin of the unit cell. For example, if the intercepts are 1/2 × a, 1 × b and 1/3 × c then the indices for this set of planes will be {2,1,3}. In the case of Miller planes that are parallel to one of the unit cell directions then there will be no intercept, or the intercept will be infinite, resulting in a Miller index of zero. Miller indices can be used to express the separation of planes, or d-spacing, in a structure, using the

notation d_{hkl}, as shown in Figure 2.6, and their relation to the unit cell parameters can be established as a function of the crystal system. For the case of a cubic unit cell, the d-spacing can be described in terms of the lattice parameters and Miller indices as shown in the following equation

$$\frac{1}{d^2_{hkl}} = \frac{h^2 + k^2 + l^2}{a^2}, \tag{2.8}$$

which can be generalised for an orthorhombic unit cell as

$$\frac{1}{d^2_{hkl}} = \frac{h^2}{a^2} + \frac{k^2}{b^2} + \frac{l^2}{c^2}. \tag{2.9}$$

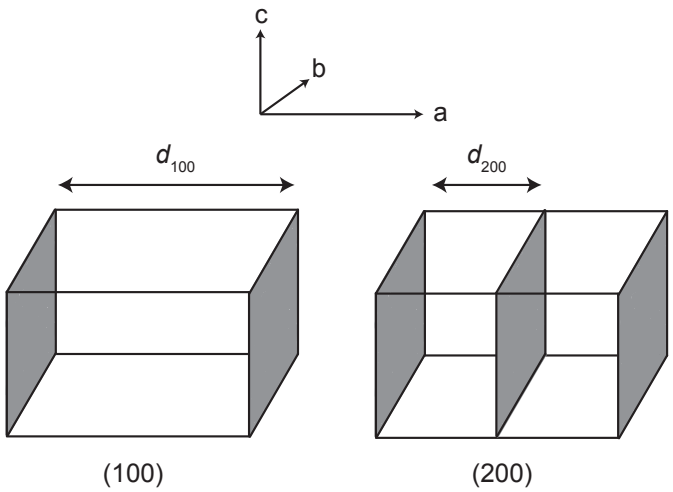

Figure 2.6 *(100) and (200) Miller planes along with the corresponding d-spacings.*

2.3.2 X-ray sources

X-rays are typically generated by bombardment of a metal target with a beam of high-energy electrons, which decelerate as they enter the metal generating radiation with a continuous range of wavelength, called Bremsstrahlung, from the German for "deceleration radiation". A few high intensity sharp peaks are superimposed on this continuum, as shown in Figure 2.7, for a typical spectrum obtained from a metal target. These peaks correspond to quantised electron transitions deriving from collisions of incoming electrons with inner-shell electrons. Such collisions expel electrons from inner shells resulting in higher-energy electrons filling the vacancy and emitting the excess energy as a X-ray photon. If the K shell is

involved, the X-rays are classified as K-radiation and distinct lines are labeled K_α and K_β, depending on the orbitals involved in the electronic transition. Lines can also be doublets, in this case termed $K_{\alpha 1}$ and $K_{\alpha 2}$, as a result of spin multiplicity in the orbitals.

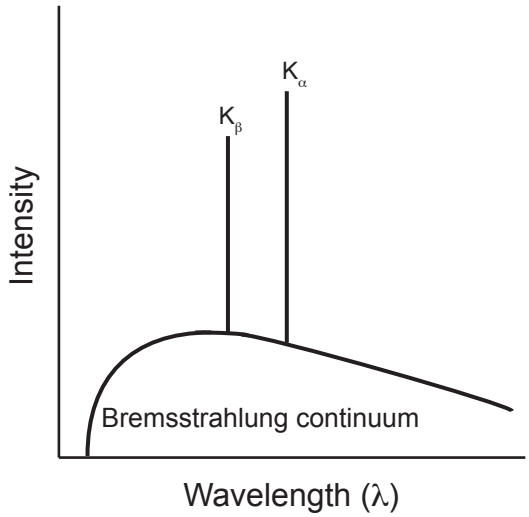

Figure 2.7 *Typical X-ray emission spectrum of a metal target.*

When a single crystal is analysed a broadband X-ray beam can be used since diffraction can be achieved for at least one of the wavelengths regardless of the orientation of the crystal. On the other hand, for powder diffraction experiments, single wavelength (monochromatic) X-ray radiation is desired and this can be achieved by a crystal monochromator or by a filter. In the former case, the X-ray beam emerging from the tube is passed through a crystal at a fixed orientation resulting in only one wavelength diffracted, according to Bragg's law (see following section). By adjusting the orientation of this crystal, a certain wavelength can be selected, normally the one with the most intense emission. The filter method involves a foil of metal with an atomic number one or two below that of the metal used as a target. In this way, lower energy lines and the Bremsstrahlung radiation can be removed by adsorption from the filter and the X-ray radiation emerging from the filter is almost monochromatic.

When sensitivity enhancements or faster data acquisition are required for small and weakly diffracting crystals or complex experiments, radiation of higher intensity and

brightness is desirable and, for this reason, radiation available from synchrotron sources is used. The general structure of a synchrotron facility consists of a central storage ring in ultra-high vacuum where electrons are injected and where they circulate at speeds close to that of light. A series of magnets ensures the circular trajectories of the electrons as well as the emission of electromagnetic waves by forcing electrons to follow deflected paths. Tangential straight tubes from the storage ring are called beamlines where the emitted synchrotron light is collected and channeled to experimental chambers where powder and single-crystal diffraction experiments are carried out in a wide range of experimental conditions.[43-46]

2.3.3 Bragg's law

Peaks in XRD patterns are called reflections and they derive from the constructive interference of X-ray beams diffracted by electrons in atoms. In the case of two adjacent planes of a lattice irradiated with two parallel rays of the same wavelength, as shown in Figure 2.8, constructive interference and thus diffraction can be observed only if the path-length difference of the two parallel incoming rays between the two adjacent lattice planes equals an integer number of wavelengths, satisfying Bragg's law

$$n\lambda = 2d \sin\theta , \tag{2.10}$$

where λ is the wavelength experimentally used, d is the spacing between two adjacent lattice planes, θ is the incident angle and n is an integer number, usually taken as unity since higher order diffraction maxima can be represented by diffraction from a set of planes with 1/n separation.

In a crystalline material, each of the d-spacings, obtained from a set of lattice parameters and h, k and l indices, as, for example, shown in Equations 2.8 and 2.9, can be combined with Bragg's law resulting in diffraction peaks at specific diffraction angles. The position of these peaks in an experimental diffraction pattern will then be related to the lattice parameters, Miller indices and experimental X-ray wavelength, providing information about the size of the repeat unit, the d-spacings, of the system analysed.[45-46]

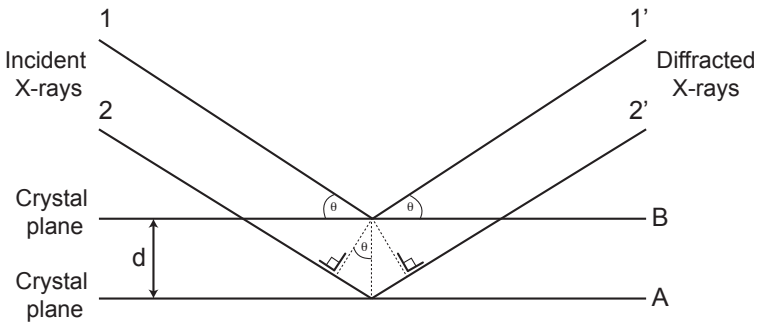

Figure 2.8 *Derivation of Bragg's law.*

2.3.4 Powder X-ray diffraction

Generally, the basic components for a XRD experiment are: a monochromatic source of X-ray radiation, the sample under investigation and a detector to collect the diffracted X-rays. Experimentally, XRD patterns can be acquired with different geometries both on single-crystal samples and powder samples. In this thesis, only powder samples have been analysed and the specific experimental geometries used for the characterisation of zeolite and MOF powders are described in this section.

In a powder sample for X-ray characterisation an infinite number of randomly oriented crystals are present with lattice planes equally randomly oriented. Some crystallites, for each set of lattice planes, will therefore be oriented at the Bragg angle with respect to the incident beam resulting in diffracted X-rays, which can be subsequently detected. PXRD experiments can be carried out in reflection or transmission, requiring different geometries and resulting in different experimental advantages and disadvantages. Transmission PXRD experiments can be acquired using the Debye-Scherrer geometry, as shown in Figure 2.9, where the generated X-ray radiation is applied perpendicular to the powder sample, which is packed in a capillary and rotated to avoid any preferential orientation of the crystallites. Given the random orientations of all the crystallites in the sample, it is possible that some of these will be correctly oriented to satisfy Bragg's law for a set of crystal planes with, for example, a d_1 spacing.

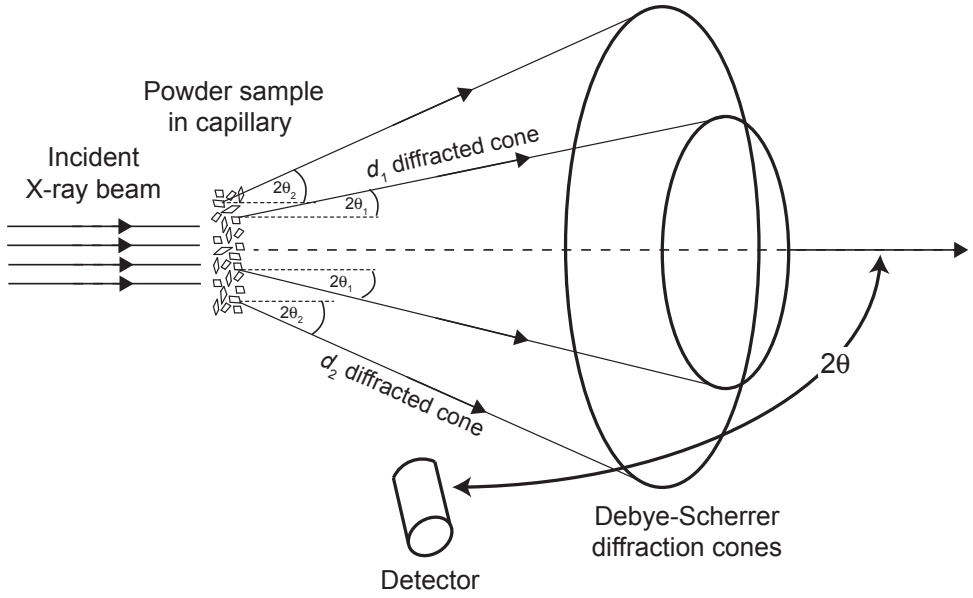

Figure 2.9 *Debye-Scherrer geometry for transmission experiments showing the incoming X-ray beam perpendicularly incident upon the randomly oriented crystallites present in the sample packed in the rotating capillary. Diffracted cones are then detected by a movable detector as a function of 2θ with respect to the incoming X-ray beam.*

Two such crystallites are schematically illustrated in Figure 2.9 and, considering the whole sample, a cone of rays is diffracted at a $2\theta_1$ angle with respect to the incoming X-ray radiation. At the same time, other crystallites will also be in the correct orientation to satisfy Bragg's law, and hence to diffract, for a number of different d-spacings, such as the d_2 spacing shown for another couple of crystallites in Figure 2.9, and the diffracted cones produced are then detected. The advantages of this technique are that very limited amounts of sample are needed and air- or moisture-sensitive samples can be easily analysed by sealing the capillary to avoid any contact with air or water during data acquisition. However, the small amounts of sample used result in low sensitivity and for some samples the packing stage can prove challenging.

Reflection PXRD experiments have been acquired using the Bragg-Brentano geometry where large amounts of sample are packed in a disk with X-ray radiation incident on the sample surface at an angle θ, as shown in Figure 2.10. The resulting

diffracted beams are then detected by a movable detector as a function of 2θ with respect to the incoming X-ray beam. Scanning of the desired 2θ range can be achieved either by moving at the same time the X-ray tube and the detector by θ with a static sample holder or by keeping the X-ray generation tube stationary and turning the sample holder in sync with the detector by θ and 2θ, respectively. The packing of the powder in the disk requires more sample compared to the capillary described above and could result in unwanted preferential orientation of the crystallites, which can be, at least partially, removed by rotating the disk. As a result of the greater amount of solid used, this technique usually yields patterns characterised by higher intensities and better signal-to-noise ratios compared to the transmission capillary setup, for equivalent amounts of acquisition time.[44,46-48]

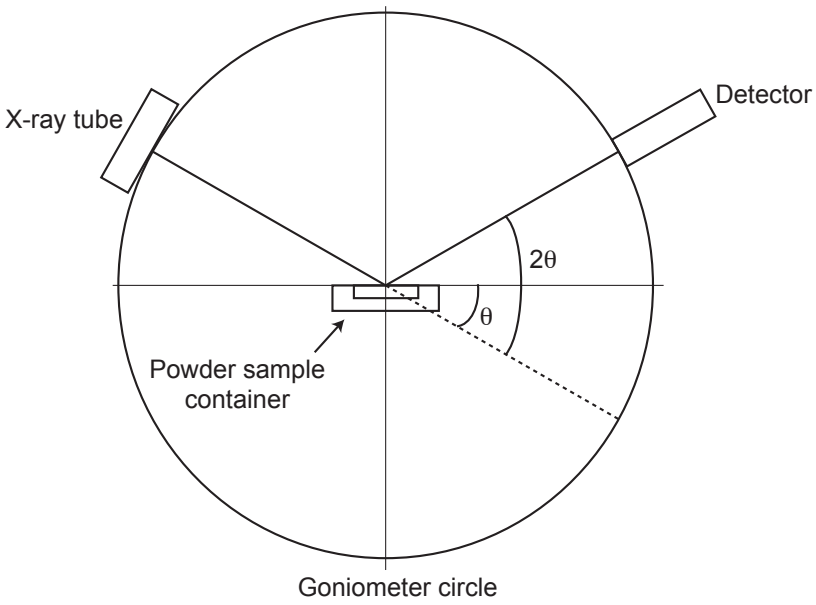

Figure 2.10 *Bragg-Brentano geometry for reflection experiments showing the incoming X-ray beam incident at angle θ upon the randomly oriented crystallites present in the sample packed in the rotating disk. Diffracted X-rays are then detected by a movable detector as a function of 2θ. In the schematic setup shown the scan over the selected 2θ range is achieved by moving the X-ray tube and the detector at the same time by θ.*

2.3.5 Rietveld and Pawley refinements

A powder pattern represents the fingerprint of a crystalline material since the position and intensity of the recorded peaks are related to the size and shape of the unit cell and the position and number of electrons of the atoms in the cell, respectively. Diffraction data provide, therefore, a wealth of crystallographic information ranging from routine identification of materials, analyses of mixtures and phases, determination of lattice parameters up to, where possible, full structure resolution. For this last purpose atomic positions need to be determined and so peak intensities need to be considered using different methods depending on the starting degree of knowledge of the structure. In this thesis, Rietveld and Pawley refinements from powder diffraction data have been carried out in collaboration with Dr Samuel Morris for the determination of cation ratios and unit cell variations during the breathing cycle in MIL-53 MOFs.

The Rietveld approach was introduced[49] in the middle of the 1960s by the Dutch physicist Hugo M. Rietveld for the accurate determination of crystal structures from neutron diffraction data, and later X-ray data, and is the most widely used full profile refinement technique today. The basis of the Rietveld approach is that all structural and experimental parameters are refined with the non-linear least squares method by fitting the observed data to a calculated profile deriving from an adequate structural model. Therefore, in this method, intensities are treated in all calculations as functions of the geometrical and structural parameters of the compound under analysis, as opposed to the Pawley method described later in this section, where intensities are treated as free least squares variables. This basic idea should result in a fully refined structure yielding a calculated diffraction pattern characterised by little, or ideally no, difference with the experimental pattern. The Rietveld method can thus be considered a powerful structural optimisation technique, requiring, however, an approximate initial knowledge of the structure. During a refinement the function Φ is minimised using the non-linear least squares method:

$$\Phi = \sum_{i=1}^{n} w_i \left(Y_i^{obs} - Y_i^{calc} \right)^2 , \tag{2.11}$$

where n is the total number of experimental points in the powder diffractogram and Y_i^{obs} and Y_i^{calc} are the observed and calculated intensities, respectively, of the i^{th} data point. The weight, w_i, of the i^{th} data point, assuming that the recorded intensity is only affected by statistical errors without interference from the background, can be given as:

$$w_i = \left[Y_i^{obs}\right]^{-1} . \tag{2.12}$$

The Pawley method,[50] also based on non-linear least squares minimisation of the difference between the observed and the calculated profile, is a refinement procedure introduced by Pawley in 1981 to obtain the best possible unit cell from a powder diffraction pattern starting from suggested parameters obtained from a unit cell analysis program. In this method, knowledge of the crystal structure is not required and, for this reason, each reflection peak in the diffraction pattern has a variable intensity, not being constrained by the crystal structure. If a complete structure solution is desired, the relevant structural and experimental parameters obtained through this method can then be used as initial approximate values for a Rietveld refinement.

In both methods, the least squares solution can be considered found when the best fit between the calculated Y_i^{calc} and experimental Y_i^{obs} intensities is obtained. Therefore, to quantify the quality of the fits the following factors have been introduced:

- the residual factor R_p

$$R_p = \frac{\sum_{i=1}^{n}\left|Y_i^{obs} - Y_i^{calc}\right|}{\sum_{i=1}^{n} Y_i^{obs}} \times 100\% , \tag{2.13}$$

- the weighted profile residual R_{wp}

$$R_{wp} = \left[\frac{\sum_{i=1}^{n} w_i\left(Y_i^{obs} - Y_i^{calc}\right)^2}{\sum_{i=1}^{n} w_i\left(Y_i^{obs}\right)^2}\right]^{1/2} \times 100\% , \tag{2.14}$$

- the expected profile residual R_{exp}

$$R_{exp} = \left[\frac{n - p}{\sum_{i=1}^{n} w_i\left(Y_i^{obs}\right)^2}\right]^{1/2} \times 100\% , \tag{2.15}$$

- the goodness of the fit χ^2

$$\chi^2 = \frac{\sum_{i=1}^{n} w_i\left(Y_i^{obs} - Y_i^{calc}\right)^2}{n - p} = \left[\frac{R_{wp}}{R_{exp}}\right]^2 , \tag{2.16}$$

where n is the total number of experimental points in the powder diffractogram, Y_i^{obs} and Y_i^{calc} are the observed and calculated intensities, respectively, of the i^{th} data point, w_i is the weight of the i^{th} data point and p is the number of free least squares parameters. In general, a better fit is related to lower values of all residuals, but there aren't exact numerical values to define the acceptability of the fit and the relation between R_{wp} and R_{exp}, established in the goodness of the fit, is probably the best evaluation method of the quality of the fit. Since the expected residual, R_{exp}, involves an ideal model defined and limited by the quality of the data, the value of R_{wp} in the best fit should tend to R_{exp}, and therefore χ^2 should approach unity.[47,51-52]

2.4 Nuclear magnetic resonance spectroscopy

NMR spectroscopy is one of the most powerful, versatile and widely applied analytical techniques for local, atomic-level structure determination and the study of dynamics. It is element specific, with almost all elements having accessible spin-active isotopes, and can be applied to a vast range of samples, both in the solid and liquid state, without any requirement for long- or short-range order. However, NMR spectroscopy of materials in the solid state has been characterised, until relatively recently, by a slower development compared to its solution-state counterpart. The reason for this slower progress lies in the inherently restricted molecular mobility characteristic of the solid state, where anisotropic interactions are not averaged to their isotropic values, as in solution. Therefore, NMR interactions, normally ignored in solution state, need to be taken into consideration, affecting the acquisition, resolution and interpretation of solid-state NMR spectra. However, owing to these interactions, NMR spectra of solids provide a wealth of information about structure and bonding that is otherwise lost in solution as a result of the tumbling motion of molecules.

2.4.1 NMR theory

The nuclear spin quantum number I, which may correspond to any positive integer or half-integer value, describes the intrinsic spin angular momentum, denoted by the vector **I**. The projection of **I** on an arbitrary z-axis is quantised in units of $m_I\hbar$, where m_I is the magnetic quantum number and can take values from +I to –I in integer steps, resulting in 2I+1 degenerate spin states. When nuclei possess spin I > 0, a magnetic dipole moment, $\boldsymbol{\mu}$, related to **I** by the gyromagnetic ratio, γ, specific for each nuclide, arises, thus leading to its quantisation on the z-axis in units of $\gamma m_I\hbar$. As Figure 2.11 shows, when an external magnetic field, B_0, is applied the axis of quantisation is defined and the degeneracy of the nuclear spin states is removed.

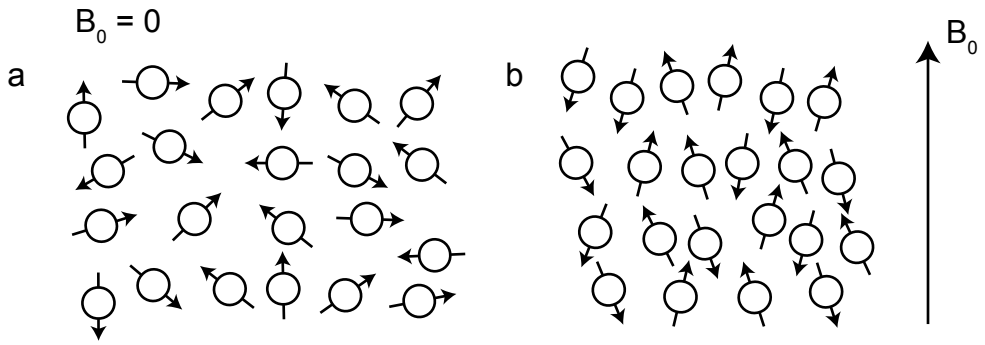

Figure 2.11 *(a) In the absence of external magnetic field, all orientations of the nuclear magnetic moment are degenerate. (b) An external magnetic field, B_0, aligns nuclear spins removing the degeneracy of the nuclear spin energy levels. For a nucleus with spin quantum number I (in this case I = 1/2) this results in 2I+1 spin states.*

This field-induced splitting of nuclear energy levels is known as the Zeeman interaction, with the Zeeman energy of a state, m_I, given by:

$$E_{m_I} = -\gamma m_I \hbar B_0 \,. \tag{2.17}$$

Only transitions with $\Delta m_I = \pm 1$ can be directly observed in NMR spectroscopy and, for this reason, all the observable transitions are degenerate with a frequency:

$$\omega_0 = -\gamma B_0 \,, \tag{2.18}$$

where ω_0 (rad s^{-1}) is the Larmor frequency.

If, for simplicity, a nucleus with I = 1/2 is considered (as in Figure 2.11), then two resulting states are obtained, α and β, aligned and opposed to the external field,

respectively. In an NMR sample, an ensemble of nuclear spins is present and the population of nuclear spins in each state can be indicated as p_α and p_β. At conditions of thermal equilibrium, nuclei occupy energy levels following the Boltzmann distribution

$$\frac{p_\beta}{p_\alpha} = e^{\frac{-h\nu_0}{kT}}, \tag{2.19}$$

where $\nu_0 = \omega_0/2\pi$, k is the Boltzmann constant and T is the absolute temperature. The resulting population difference yields a bulk nuclear magnetisation, which can be represented by a vector, **M**, aligned with the field, as shown in Figure 2.12a. The magnitude of **M** is exponentially dependent on ω_0, so that, according to Equation 2.18, at a given field strength, **M** is larger for nuclei with higher γ and, for a given nucleus, **M** increases with field strength.

When recording an NMR spectrum, in the simplest possible case, a short intense pulse of monochromatic radiofrequency (rf) electromagnetic radiation is applied to the sample at the transmitter frequency, ω_{rf}, set close to the nuclear Larmor frequency, ω_0. Despite the fact that all NMR experiments are carried out in the static or "laboratory" frame, it is convenient to see the effects of a pulse in the rotating frame, where the z-axis remains aligned with B_0 and the xy-plane rotates around this at a frequency of ω_{rf}. In such a coordinate system, the pulse appears to consist of two components, a static one, which actually interacts with nuclear spins, and a second one rotating at $-2\omega_{rf}$, which has no effect. The static field, with magnitude B_1, associated with the pulse causes nutation of **M** about the field at a frequency $\omega_1 = -\gamma B_1$ for the duration of the pulse, τ_p. Pulses are generally described by a flip angle, $\beta = \omega_1\tau_p$, the angle through which **M** nutates during the pulse, and a phase, ϕ, the direction along which B_1 lies in the rotating frame. A crucial feature of the pulse also involves the simultaneous and uniform excitation of the spins in the full range of nuclear resonance frequencies, resulting in the need for appropriate pulse strengths ($-\gamma B_1$) to ensure the nutation of all the spins. A typical single-pulse NMR experiment begins by applying a 90° pulse, creating magnetisation in the transverse xy-plane, as shown in Figure 2.12b.

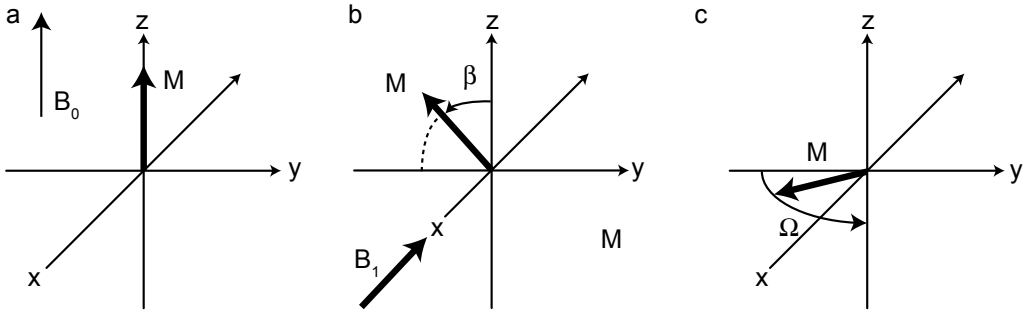

Figure 2.12 *(a) Vector model representation of the bulk magnetisation vector,* ***M****, aligned along the z-axis in the rotating frame. (b) Nutation of* ***M*** *in the yz-plane caused by a pulse applied along the x-axis. (c)* ***M*** *undergoing free precession in the xy-plane at a frequency Ω.*

Following a pulse, the return of magnetisation to equilibrium, known as relaxation, usually occurs as a result of two main processes: the spin-lattice or longitudinal relaxation, described by the time constant T_1, and the spin-spin or transverse relaxation, described by the time constant T_2. The former relaxation time constant describes the process of the return to equilibrium of the z component of **M**, i.e., along B_0, following a perturbation as described by the following equation

$$M_z(t) - M_0 = [M_z(0) - M_0]e^{-\frac{t}{T_1}}, \tag{2.20}$$

where M_0 is the equilibrium magnetisation and $M_z(0)$ is the magnetisation in the z direction after the perturbation. T_1 relaxation time constants of typically a few seconds, but up to many minutes even hours, are characteristic of the solid state, often making the acquisition of NMR spectra of solids a very time-consuming process. The spin-spin relaxation process relates to the decay of the xy component of **M**, i.e., perpendicular to B_0, which is zero at equilibrium, but becomes non-zero as a result of applying rf pulses. Moreover, transverse relaxation can affect the shape, in terms of distribution of frequencies, and the width of the line observed in the spectrum. Generally, in solids $T_1 \gg T_2$, with the latter time constant typically on the timescale of milliseconds. An additional third relaxation mechanism is known as spin-lattice relaxation in the rotating frame, $T_{1\rho}$, and describes the return to equilibrium of transverse magnetisation while an rf magnetic field, B_1, is applied in the same direction. Under these conditions magnetisation is spin-locked and $T_{1\rho}$ values are of particular importance during cross-polarisation experiments. Overall,

relaxation mechanisms typically occur through time-dependent nuclear spins interactions, such as shielding, dipolar and quadrupolar interactions (see following section), with larger interactions leading to more efficient relaxation mechanisms. Unpaired electrons, if present, also represent an efficient source of relaxation, given their magnetic moment is much greater than that of protons. Moreover, measurements of relaxation times, especially if carried out at variable temperatures, can give information about dynamics, since time dependency is related to motion at a molecular level.

Following a pulse, the precession of **M** about the z-axis with a frequency $\Omega = \omega_0 - \omega_{rf}$, see Figure 2.12c, produces a signal, deriving from decaying transverse magnetisation, recorded in the xy-plane, known as free induction decay (FID). The FID contains all the information needed to obtain an NMR spectrum and is a complex time-dependent signal, S(t), affected by relaxation, which can be expressed as

$$S(t) = e^{i\Omega t} e^{-\frac{t}{T_2}}. \tag{2.21}$$

Quadrature detection, involving two different receiver phases shifted by 90°, is employed to record the real and imaginary parts of the precessing magnetisation.

This signal can be then Fourier-transformed,[53] as schematically shown in Figure 2.13, to yield a complex frequency-domain signal, S(ω), or spectrum

$$S(\omega) = \int_0^\infty S(t) e^{i\omega t} dt, \tag{2.22}$$

where the complex time-domain function is multiplied by the complex exponential $e^{i\omega t}$ and integration is subsequently carried out over time. While in theory the upper time limit of the integral is infinite, in practice it is only necessary to calculate the integral from zero up to where the FID intensity is negligible compared to experimental noise, as the FID eventually decays to zero. The time domain signal is sensitive to the sign of the offset resonance, Ω, and, upon Fourier transformation, this leads to an unambiguous spectrum with frequency discrimination.

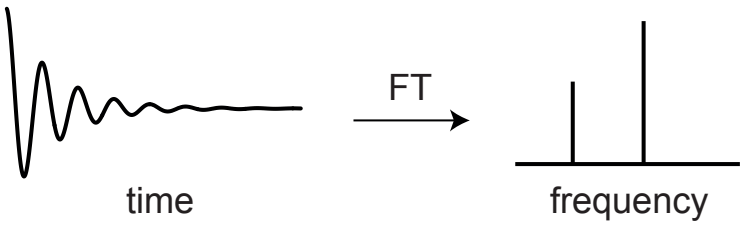

Figure 2.13 *Schematic representation of the free induction decay signal in the time domain (left) converted to the frequency domain by Fourier transformation (right).*

The complex frequency-domain signal can be expressed as

$$S(\omega) = A(\Delta\omega) + iD(\Delta\omega)\,, \tag{2.23}$$

where $A(\Delta\omega)$ is the real absorptive component, $D(\Delta\omega)$ is the imaginary dispersive component and $\Delta\omega = \omega - \Omega$, see Figure 2.14. In general, the real and imaginary parts of a spectrum contain a mixture of absorptive and dispersive lineshapes, but ideally the real part of the spectrum should have an absorptive lineshape. To achieve this, the phase of $S(\omega)$ is altered to obtain a purely absorptive real component and a purely dispersive imaginary component.

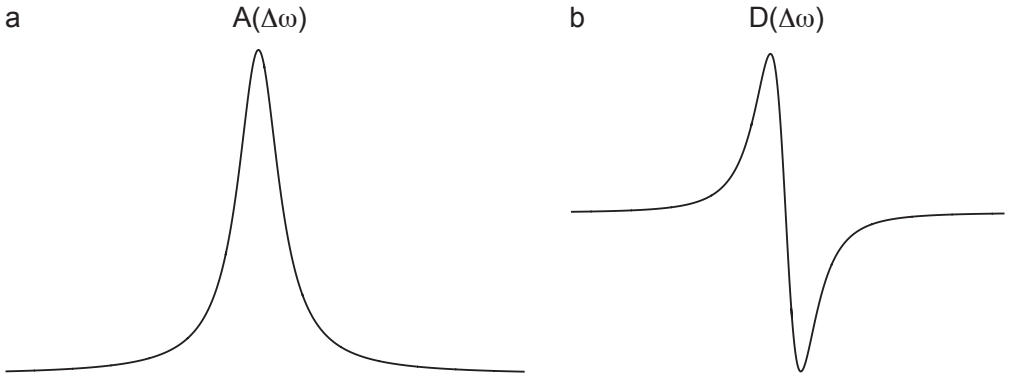

Figure 2.14 *The real and imaginary parts of the complex frequency-domain signal characterised by absorptive (a) and dispersive (b) Lorentzian linshapes, respectively.*

In most cases, in order to improve the signal-to-noise-ratio (SNR) of the final spectrum, the same experiment is repeated N times with NMR signals increasing linearly with N and random noise increasing more slowly by √N, giving a √N increase in the SNR. During this procedure of signal averaging, since successive FIDs are acquired, the nuclear spin population should reach thermal equilibrium by the time a new spectrum is recorded.[9,54-56] This can be achieved by leaving a time of ~5 T_1 between successive transients.

2.4.2 Interactions in NMR

Nuclear spins are affected by a variety of interactions, originating either between two spins or between the spin and its local environment, in addition to the Zeeman interaction discussed above.

2.4.2.1 The chemical shift interaction

In particular, owing to the circulation of electrons in molecules, a magnetic field, B', proportional to B_0, is created and the effective magnetic field, B_{eff}, experienced by a nucleus is then given by:

$$B_{eff} = B_0 - B' = B_0(1 - \sigma)\,, \tag{2.24}$$

where σ is a field-independent shielding constant. The observed precession frequency of a spin, ω_{obs}, is altered by this local field, giving different resonances for magnetically inequivalent nuclei, according to

$$\omega_{obs} = -\gamma B_{eff} = -\gamma B_0(1 - \sigma)\,. \tag{2.25}$$

However, considering the difficulties in the measurement of the absolute value of σ, in practice a chemical shift, δ, a deshielding parameter, is measured on the basis of the difference between the observed resonance frequency for the nucleus of interest, ω_{obs}, and the known frequency of a reference compound, ω_{ref},

$$\delta = 10^6 \frac{(\omega_{obs} - \omega_{ref})}{\omega_{ref}}. \tag{2.26}$$

δ is usually reported in *parts per million* (ppm). The relation between σ and δ can be expressed according to the following equation

$$\delta = 10^6 \frac{(\sigma_{ref} - \sigma)}{(1 - \sigma_{ref})} \approx 10^6(\sigma_{ref} - \sigma)\,, \tag{2.27}$$

where the approximation $\sigma_{ref} \ll 1$ has been used. It is clear from Equation 2.27 that a greater value of σ, a greater shielding, results in a decreased value of δ.[57]

Since the electron distribution around a nucleus is rarely perfectly spherical, a chemical shift anisotropy (CSA) arises. For this reason, rather than using the scalar constants σ and δ, a shielding, $\boldsymbol{\sigma}$, and a corresponding shift, $\boldsymbol{\delta}$, tensor have to be introduced to properly describe the shielding. It is possible to define an axis system with respect to which the tensor for the interaction of interest is diagonal. This axis

$$\boldsymbol{\sigma}^{PAS} = \begin{pmatrix} \sigma_{11} & 0 & 0 \\ 0 & \sigma_{22} & 0 \\ 0 & 0 & \sigma_{33} \end{pmatrix}. \tag{2.28}$$

system is called the principal axis system (PAS) and the values on the resulting diagonal of the interaction tensor are its principal components. So, for the shielding tensor in the principal axis system, $\boldsymbol{\sigma}^{PAS}$, the three principal components are σ_{11}, σ_{22} and σ_{33}

The orientation of the principal axis system is, in general, determined by the local environment of the nucleus of interest. For the specific case of the shielding tensor, the orientation of the principal axis system is determined by the electronic structure of the molecule containing the nucleus of interest. The shielding tensor can be then represented by an ellipsoid whose principal axes coincide with the principal axis system of the shielding tensor. The lengths of the principal axes of the ellipsoid are proportional to the value of the principal components of the shielding tensor,[58] as shown in Figure 2.15.

The correspondent principal components of the chemical shift tensor in the principal axis system, $\boldsymbol{\delta}^{PAS}$, are δ_{11}, δ_{22} and δ_{33} and the chemical shift, δ, observed for a resonance can be shown to be:

$$\delta = \delta_{11}\sin^2\theta\cos^2\phi + \delta_{22}\sin^2\theta\sin^2\phi + \delta_{33}\cos^2\theta\,, \tag{2.29}$$

where the angles θ and ϕ describe the orientation of the tensor relative to the external field, B_0, as shown in Figure 2.15.

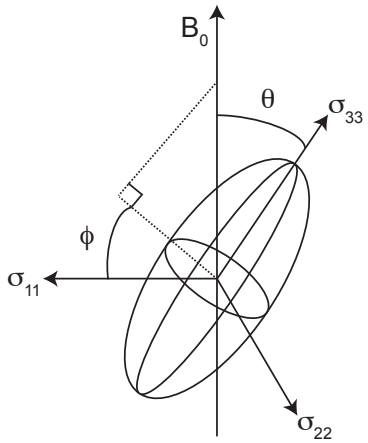

Figure 2.15 *The shielding tensor ellipsoid with principal axes coinciding with the principal axis system and proportional to the value of the principal components of the tensor. The angles θ and ϕ indicate the orientation of the tensor with respect to the external magnetic field, B_0.*

According to the Haeberlen convention,[59] δ_{iso}, $\Delta\delta_{cs}$, η_{cs} can be used to parameterise the chemical shielding, with $|\delta_{33}-\delta_{iso}| \geq |\delta_{11}-\delta_{iso}| \geq |\delta_{22}-\delta_{iso}|$. The isotropic chemical shift, δ_{iso}, is given by the average of the three principal components

$$\delta_{iso} = \frac{\delta_{11} + \delta_{22} + \delta_{33}}{3}. \tag{2.30}$$

The chemical shielding anisotropy, $\Delta\delta_{cs}$, is given by

$$\Delta\delta_{cs} = (\delta_{33} - \delta_{iso}), \tag{2.31}$$

and the asymmetry is

$$\eta_{cs} = \frac{(\delta_{22} - \delta_{11})}{(\delta_{33} - \delta_{iso})}, \tag{2.32}$$

where $0<\eta_{cs}<1$.

Equation 2.29 can be thus rewritten as

$$\delta = \delta_{iso} + \left(\frac{\Delta\delta_{cs}}{2}\right)[(3\cos^2\theta - 1) + \eta_{cs}(\sin^2\theta \cos 2\phi)], \tag{2.33}$$

highlighting that the chemical shift contains both an orientation-independent, isotropic, and an orientation-dependent, anisotropic, term. In a powdered sample, crystallites with many different orientations to the external magnetic field will be present resulting in a broad lineshape with associated values of $\Delta\delta_{cs}$ and η_{cs}, as exemplified in Figure 2.16.[9]

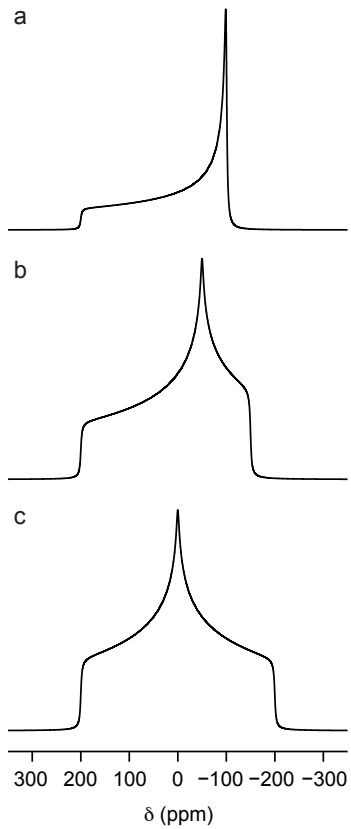

Figure 2.16 *Static powder lineshapes (simulated using Topspin) for a spin I = 1/2 nucleus with* $\delta_{iso} = 0$, $\Delta\delta_{cs} = 200$ *ppm and* $\eta_{cs} = 0$ *(a), 0.5 (b) and 1 (c) at 9.4 T.*

2.4.2.2 Dipolar coupling

The position of resonances in the spectra is also affected by interactions with other nuclei: indeed, nuclear dipole moments can couple either directly through space, i.e., the dipolar interaction, or indirectly, through regions of shared electron density, i.e., J coupling. In the latter case, the spin-spin coupling operates through bonds and can therefore provide valuable information on the molecular-level conformation and connectivity. This coupling, described by the tensor **J** with isotropic value J_{iso}, is highly important in solution-state NMR, but is only rarely directly observed in solid-state NMR, being the smallest interaction in magnitude, typically less than 1 kHz, but, for some heavy elements, in the region of 10 kHz.[54] The dipolar interaction, where one spin is affected by the small, localised field resulting from another spin, is described by the axially symmetric tensor $\mathbf{D}^{PAS}$ and

results in an orientation-dependent splitting, which, for an isolated spin pair, is proportional to

$$\omega_D = -\omega_D^{PAS}\frac{1}{2}(3\cos^2\theta - 1), \tag{2.34}$$

where

$$\omega_D^{PAS} = \frac{\mu_0}{4\pi}\frac{\gamma_I\gamma_S\hbar}{r_{IS}^3}. \tag{2.35}$$

In Equation 2.35 ω_D^{PAS} is the dipolar-coupling constant in the principal axis system in units of rad s^{-1}, r_{IS} is the internuclear distance between spins I and S, and θ is the angle between the internuclear vector and the external magnetic field, as shown in Figure 2.17.[9,60] For ^{29}Si-^{17}O, typical dipolar couplings are expected to be in the range 0.5-1.5 kHz.

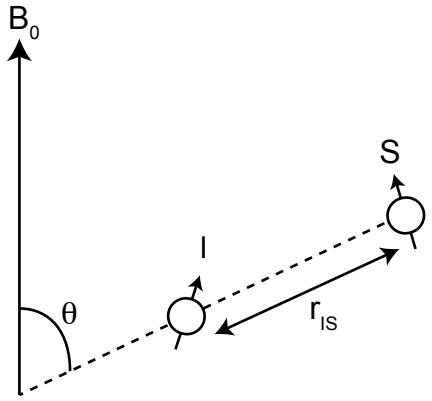

Figure 2.17 *Schematic representation of the dipolar interaction between two spins, I = 1/2 and S = 1/2, in an external magnetic field, B_0. The angle between the internuclear distance, r_{IS}, and B_0 is indicated by θ.*

For a single crystallite containing an isolated pair of spin I = 1/2 nuclei the spectrum will be a doublet of separation ω_D, for a heteronuclear spin system, or 3/2 ω_D, for a homonuclear spin system. In a polycrystalline powder a distribution of orientations of the internuclear vector with respect to the external magnetic field will be present and, considering the orientational dependence of ω_D, a Pake Doublet[61] is obtained for an isolated pair of spins 1/2 with a peak separation of ω_D^{PAS} in case of heteronuclear coupling, as shown in Figure 2.18a, and 3/2 ω_D^{PAS} in case of homonuclear coupling. Since in most solids there are virtually infinite I–S dipolar interactions, the orientation and distance dependence of ω_D, whose magnitude increases when high-γ

nuclei close in space are involved, typically leads to a Gaussian-like broadening of the spectrum, as shown in Figure 2.18b.[54]

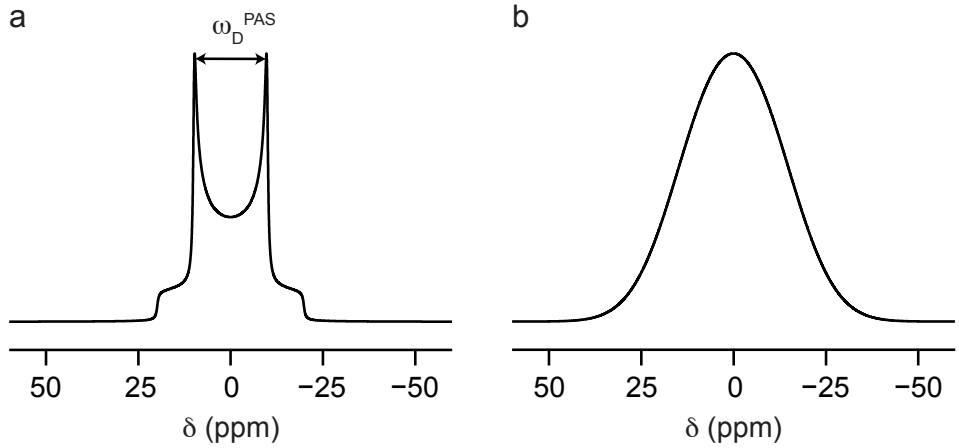

Figure 2.18 *Schematic spectra (simulated using Topspin) of spin I = 1/2 (a) with a dipolar coupling of 3 kHz to spin S = 1/2 (b) with many different dipolar interactions.*

2.4.2.3 The quadrupolar interaction

Owing to the quadrupolar nature (i.e., I > 1/2) of around 75% of NMR-active nuclei (e.g., ^{27}Al, ^{45}Sc, ^{17}O etc.), an additional spectral broadening has to be taken into consideration: the anisotropic interaction of the nuclear electric quadrupole moment, Q, with the surrounding electric field gradient (EFG). The quadrupole moment and EFG originate from the non-spherical distribution of charge in the nucleus and the non-spherical distribution of the nearby electrons and nuclei in the structure, respectively. The interaction between Q and EFG can, therefore, provide information on the coordination environment, symmetry and distortions, when accurately measured. The EFG is described by a tensor, **V**, diagonalised in the PAS to give

$$\mathbf{V}^{\mathrm{PAS}} = \begin{pmatrix} V_{XX} & 0 & 0 \\ 0 & V_{YY} & 0 \\ 0 & 0 & V_{ZZ} \end{pmatrix}, \tag{2.36}$$

with $|V_{zz}| \geq |V_{yy}| \geq |V_{xx}|$. The quadrupolar interaction is usually described by its magnitude

$$C_Q = \frac{eQV_{zz}}{h}, \tag{2.37}$$

expressed in frequency units, where e is the electric charge, and its asymmetry

$$\eta_Q = \frac{V_{xx} - V_{yy}}{V_{zz}}, \tag{2.38}$$

dimensionless ($0 \leq \eta_Q \leq 1$). The resulting quadrupolar product, P_Q, can be defined as

$$P_Q = C_Q \sqrt{\left(1 + \frac{\eta_Q^2}{3}\right)}. \tag{2.39}$$

Even though the quadrupolar interaction can in some cases be very large (e.g., many MHz in magnitude), in most practically relevant cases its effect can be treated as a perturbation to the Zeeman energy levels. As shown in Figure 2.19, a spin I = 5/2 nucleus has six, (2I + 1), allowed orientations of the nuclear magnetic moment with respect to B_0, resulting in six Zeeman energy levels and five, (2I), degenerate transitions at the Larmor frequency, ω_0. To a first-order approximation, the effect of the quadrupolar interaction is to perturb the degeneracy of the transitions, yielding, in the case of nuclei with half-integer spin quantum number, a central transition (CT), unaffected by the quadrupolar interaction, and satellite transitions (STs), whose frequencies depend on the quadrupolar splitting parameter:

$$\omega_Q = \frac{\omega_Q^{PAS}}{2}\left[(3\cos^2\beta - 1) + \eta_Q(\sin^2\beta)\cos 2\gamma\right], \tag{2.40}$$

where β and γ are two of the Euler angles relating the PAS of the EFG to the laboratory frame and ω_Q^{PAS}, in rad s^{-1}, is given by:

$$\omega_Q^{PAS} = 3\pi \frac{C_Q}{2I(2I-1)}. \tag{2.41}$$

Therefore, the spectrum for a single crystal is composed of five, (2I), resonances: four STs, which, in the case of a powdered sample, produce a broadened lineshape and one CT, unaffected by changes in the physical state of the sample, as shown in Figure 2.20. For integer spins, there is no CT and all transitions are affected by the first-order quadrupolar interaction, as shown in Figure 2.21. However, when larger EFGs are involved, a more complex second-order perturbation, much smaller than that to first order, but affecting all the transitions in the spectrum, has to be taken into account, resulting in the anisotropic broadening of the CT, as shown in Figures 2.19-2.20.

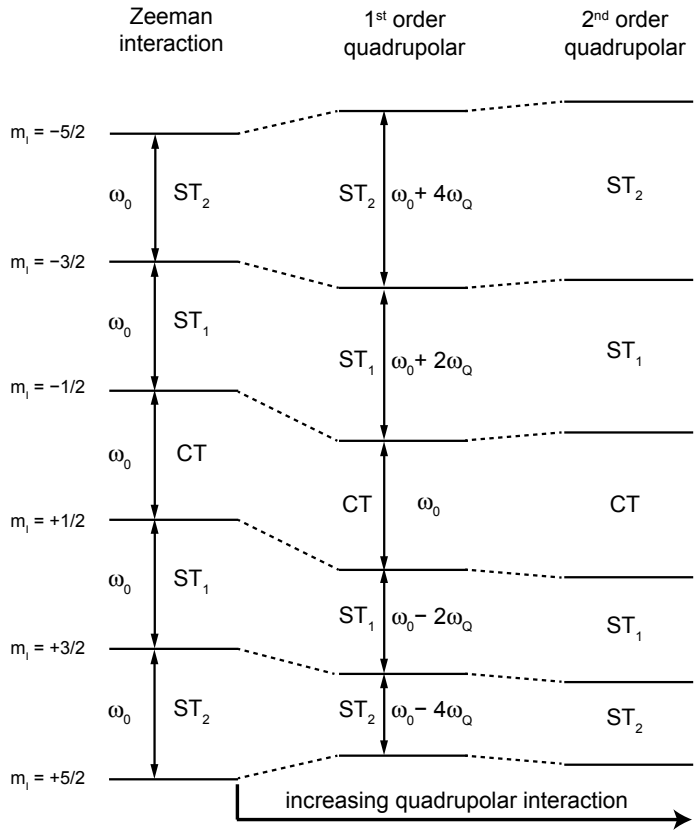

Figure 2.19 *Schematic of the quadrupolar interaction affecting the Zeeman energy levels of a spin I = 5/2 nucleus showing the first-order quadrupolar interaction affecting the satellite transitions and the second-order quadrupolar interaction affecting all transitions.*

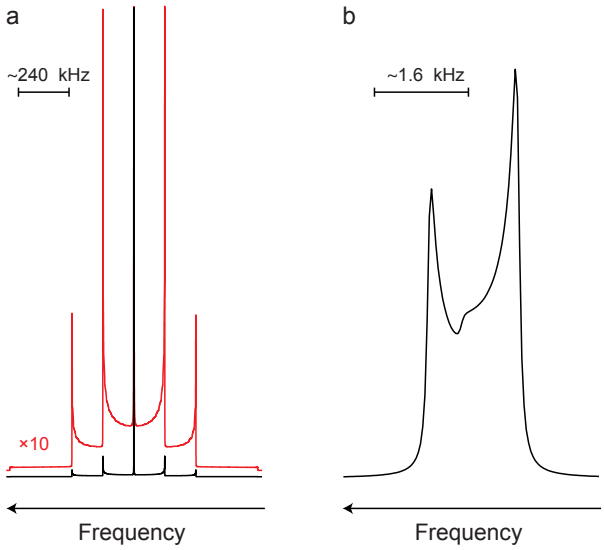

Figure 2.20 *Schematic spectra (simulated using Topspin) showing the effect of the first-order quadrupolar interaction for a spin I = 5/2 on a powdered sample (a). (b) Anisotropic broadening of the CT by the second-order quadrupolar interaction.* C_Q *= 2.2 MHz,* η_Q *= 0,* B_0 *= 14.1 T.*

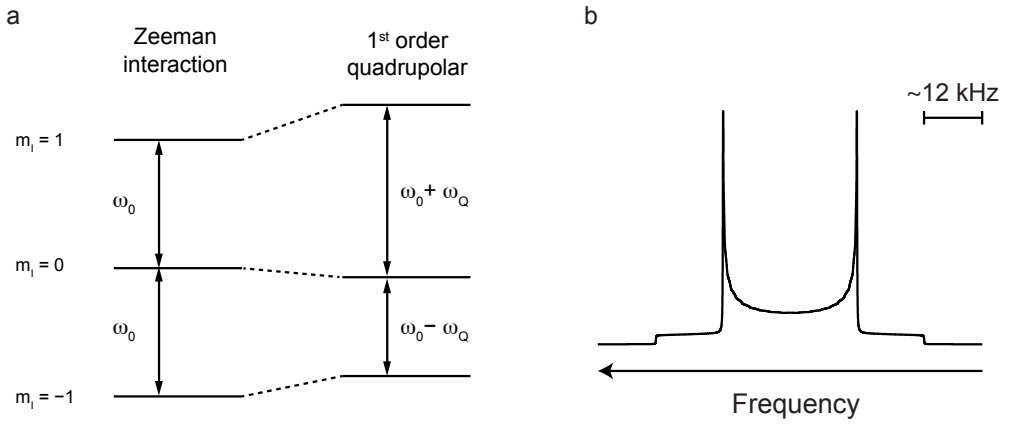

Figure 2.21 *(a) Quadrupolar interaction affecting the Zeeman energy levels of a spin I = 1. (b) Schematic spectrum (simulated using Topspin) showing the effect of first-order quadrupolar interaction for a powdered sample (C_Q = 40 kHz, η_Q = 0, B_0 = 9.4 T).*

The second-order perturbation of a single energy level is

$$E_i^{(2)} = \frac{\left(\omega_Q^{PAS}\right)^2}{2\omega_0} \times \left(A_{I,m_i}^{(0)} B^{(0)} + A_{I,m_i}^{(2)} B^{(2)}(\beta,\gamma) + A_{I,m_i}^{(4)} B^{(4)}(\beta,\gamma)\right), \tag{2.42}$$

where β and γ are Euler angles, the spin and magnetic quantum number-dependent coefficients, $A_{I,m_i}^{(l)}$, are summarised in Table 2.3 for spins I = 3/2 and 5/2, and the orientation-dependent coefficients are

$$B^{(0)} = \left(1 + \frac{\eta_Q^2}{3}\right), \tag{2.43}$$

$$B^{(2)}(\beta,\gamma) = \left(1 - \frac{\eta_Q^2}{3}\right) d_{0,0}^2(\beta) - \frac{2\sqrt{2}}{\sqrt{3}} \eta_Q d_{2,0}^2(\beta) \cos 2\gamma\,, \tag{2.44}$$

$$\begin{aligned} B^{(4)}(\beta,\gamma) = &\left(1 + \frac{\eta_Q^2}{18}\right) d_{0,0}^4(\beta) + \frac{\sqrt{10}}{3} \eta_Q d_{2,0}^4(\beta) \cos 2\gamma \\ &+ \frac{35}{9\sqrt{70}} \eta_Q^2 d_{4,0}^4(\beta) \cos 4\gamma\,, \end{aligned} \tag{2.45}$$

where $d_{m',m}^l(\beta)$ is a reduced Wigner rotation matrix element.[62]

	$A^{(0)}_{I,m_i}$	$A^{(2)}_{I,m_i}$	$A^{(4)}_{I,m_i}$
Spin I = 3/2			
$m_I = +3/2$	6/5	0	−6/5
$m_I = +1/2$	−2/5	−8/7	54/35
Spin I = 5/2			
$m_I = +5/2$	20/3	40/21	−60/7
$m_I = +3/2$	−4/5	−40/7	228/35
$m_I = +1/2$	−16/15	−64/21	144/35

Table 2.3 *Spin and magnetic quantum number dependent coefficients for spin I = 3/2 and I = 5/2.*[62] *For the corresponding negative values of m_I the sign of the coefficients is reversed.*

Once the second-order quadrupolar interaction is included, two main effects can be noticed: the broadening of the central transition of a half-integer quadrupolar spin and the shift of its center of mass, or quadrupolar isotropic shift, δ_Q, by an amount proportional to A^0.

In case of a significant second-order broadening of the CT (more than a few kHz), the observation of the STs can be challenging and normally only the CT is experimentally observed.

2.4.3 Dynamic nuclear polarisation

Solid-state DNP NMR experiments have been carried out on the two classes of microporous compounds investigated in this work, zeolites and MOFs, to better understand their surface interactions and evaluate potential spectroscopic enhancement for challenging nuclei, such as ^{17}O.

Solid-state NMR characterisation of surface sites, while of fundamental importance for the development of new materials with porous and catalytic properties, is affected by sensitivity problems related to the very small concentration of surface sites compared to bulk sites. The introduction of DNP helped to overcome these problems with the transfer of polarisation from unpaired electrons, intrinsic to samples or from exogenous radical solutions, to the nucleus of interest in the sample, by microwave

irradiation at the electron paramagnetic resonance (EPR) frequency. The resulting theoretical enhancements (ε) are dependent on the ratio of the gyromagnetic ratios of the electron (e) and the polarised nucleus (x), γ_e/γ_x. Theoretically developed in the 1950s by Overhauser,[63] DNP was experimentally observed in 1953[64] and then further investigated over the following decades with experimental applications to thin films of diamonds with intrinsic polarisation sources in the 1990s.[65] The introduction of high-power microwave sources, gyrotrons,[66] cryogenic MAS probes for experiments at 100 K[67] and external polarisation sources in the form of efficient biradicals[68] subsequently opened the way for DNP experiments to achieve high enhancements. Indeed, as a result of the better saturation of the EPR transitions, more efficient polarisation mechanisms and with no magnetic field strength limitation, the range of applications was widened to challenging systems, including those of biological origin.

If the materials under analysis are characterised by the absence of intrinsic sources of polarisation, radical molecules need to be introduced in solution without diluting the sample or affecting its chemistry. This has been achieved in this work using optimised stable biradicals, as shown in Figure 2.22, in water-based solutions, e.g. TOTAPOL and AMUPOL, or organic-based solutions, e.g. TEKPol in 1,1,2,2-tetrachloroethane (TCE), depending on the chemistry of the sample. The simplest method used to impregnate porous materials is known as the incipient wetness impregnation (IWI) technique[69] and typically involves the use of ~10 μl of radical solutions (~15-20 mM) mixed with 10-20 mg of porous sample.

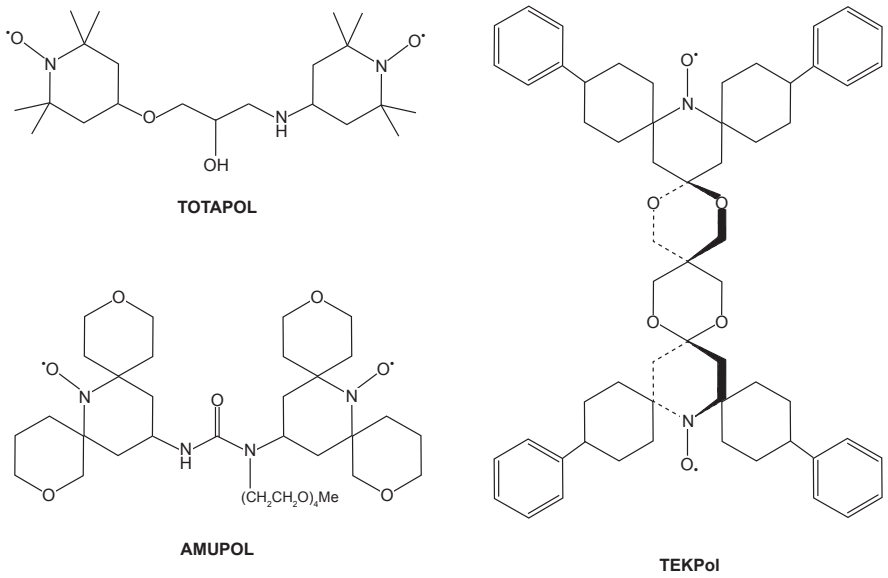

Figure 2.22 *Biradical molecules used as polarising agents in DNP experiments carried out in this work. TOTAPOL and AMUPOL are used in water-based solution, whereas TEKPol is employed in TCE solutions.*

The two main types of mechanisms in DNP experiments of insulating solids are the solid effect (SE), involving one electron and one nuclear spin, and the cross effect (CE), involving a pair of electrons, as in the biradicals shown in Figure 2.22, and a nuclear spin. A third mechanism known as thermal mixing involves multiple dipolar coupled electrons and is not commonly observed as it would experimentally require high radical concentrations. Depending on the homogenous linewidth, δ_{EPR}, and the inhomogenous breadth, Δ_{EPR}, of the EPR spectrum of the radical compared to the nuclear Larmor frequency, ω_{0I}, DNP occurs through the solid effect, if $\delta_{EPR}, \Delta_{EPR} < \omega_{0I}$, or the cross effect, if $\delta_{EPR} < \omega_{0I} < \Delta_{EPR}$. The solid effect is less efficient at high magnetic field since it relies on one electron and one nucleus interacting through electron-nuclear coupling and subsequent mixing of nuclear states with microwave irradiation ($\omega_{\mu W}$) of forbidden transitions at

$$\omega_{\mu W} = \omega_{0S} \pm \omega_{0I} \,, \tag{2.46}$$

where ω_{0S} and ω_{0I} are the electron and nuclear Larmor frequencies. The applicability of this mechanism is also restricted by the fact that it requires a relatively narrow EPR spectrum of the polarising agent. The cross effect can be

treated as a three-spin system with two dipolar coupled interacting electrons and a nuclear spin achieving maximum polarisation transfer when the Larmor frequency separation of the electrons satisfies the relation

$$\left|\omega_{0S_1} - \omega_{0S_2}\right| = \omega_{0I}\,, \tag{2.47}$$

where ω_{0S_1} and ω_{0S_2} are the Larmor frequencies of the dipolar coupled electrons, S_1 and S_2, and ω_{0I} is the Larmor frequency of the nucleus I. With this mechanism the best enhancements are obtained using biradical molecules, such as TOTAPOL, with the possibility of fine tuning the electron-electron dipolar coupling on the basis of the length of the alkyl chain of the radical.[70-72]

Typical experimental temperatures for DNP experiments are in the range of 90-100 K, leading to the freezing of the impregnated solid sample. Polarisation disperses in the bulk of the frozen matrix, containing the radical solution and the sample, through spin diffusion and can either be transferred directly ($e^- \rightarrow {}^{13}C/{}^{17}O$) or more usually indirectly ($e^- \rightarrow {}^{1}H \rightarrow {}^{13}C/{}^{17}O$) to the nucleus of interest in the sample. In the latter case, polarisation transfer relies on ^1H spin diffusion across the frozen matrix and is transferred to the sample through cross-polarisation (CP), as schematically shown in Figure 2.23 for a MOF sample. Results obtained from the DNP NMR investigation carried out for Al MIL-53 samples will be presented in Section 6.4.

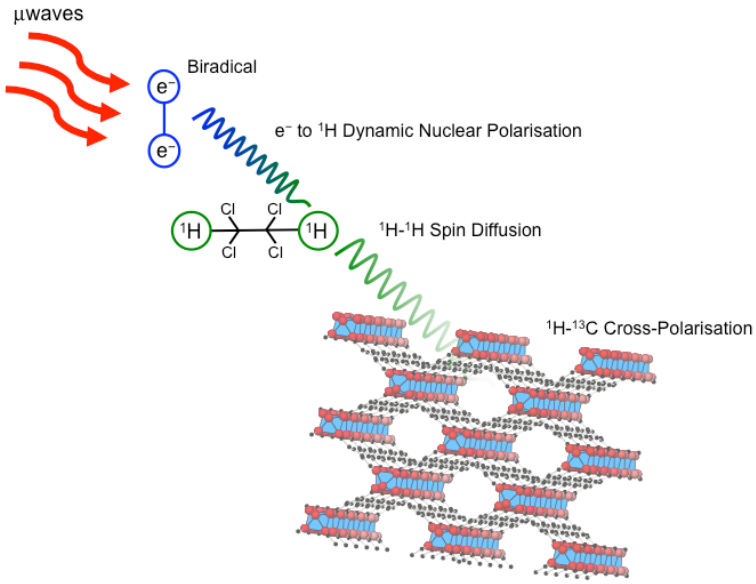

Figure 2.23 *Schematic showing the polarisation transfer pathway from the biradical, across the frozen matrix containing the solvent and the sample through ^1H spin diffusion and up to ^{13}C atoms in the MOF by ^1H-^{13}C cross-polarisation.*

The success of this experiment strongly depends on the efficiency of the polarisation transfer in the final CP step, but has the advantage of relying on the ^{1}H fast polarisation build-up times, characterised by an efficient spin diffusion process. In case polarisation is transferred directly to nuclei (^{13}C,^{17}O) other than ^{1}H, higher enhancements can be potentially obtained, as a result of the higher theoretical γ_e/γ_x ratios, and the spectrum obtained is not edited by proximity to ^{1}H. However, a significant disadvantage of this last method is that polarisation build-up times become much longer because of a much less efficient spin diffusion process. This results from the lower gyromagnetic ratios and concentrations of nuclei such as ^{13}C or ^{17}O compared to ^{1}H, and hence a smaller dipolar coupling mediating the process.[73]

The observed enhancement resulting from DNP experiments can be directly evaluated by comparison of the intensities of spectra recorded with and without microwave irradiation ($\varepsilon_{on/off}$). However, this comparison does not take into account other experimental conditions, such as the presence of radical species and the cryogenic temperatures involved, to quantify DNP gains in sensitivity compared to room temperature experiments. Indeed, reduction or quenching of the signal, resulting from the presence of paramagnetic species, and changes in the longitudinal proton relaxation times, determined by thermal and paramagnetic effects, need to be taken into account, as well as a thermal enhancement factor at the typical experimental temperatures (100 K), to determine the overall sensitivity enhancement.[74-75]

The instrumentation required for the implementation of DNP experiments includes, in addition to the NMR spectrometer, a stable microwave source and a waveguide for the transmission of microwaves to the NMR probe. Considering the microwave power requirements of DNP experiments, gyrotron sources are typically used. A gyrotron is an electronic device that operates under vacuum in static magnetic field and is able to generate high microwave power at high frequencies. Electrons are emitted from an electron gun, accelerated by high voltage and, in the presence of an external magnetic field, they start to gyrate following the magnetic field lines with increasing rotational energy as the magnetic field gets stronger until they reach the cavity region, where emission of microwave radiation occurs by conversion of the electron kinetic energy. Microwaves emitted are then directed to the NMR sample

through the waveguide and the spent electrons are collected within the gyrotron. Probes need to be connected to the waveguide to allow irradiation of the sample and are designed to achieve MAS conditions at temperatures of ~100 K, since DNP processes are most efficient at these low temperatures. An example of DNP instrumentation is shown in Figure 2.24. Moreover, a sweep coil is normally added to the magnet since, to achieve conditions of maximum enhancement, the frequency of the microwave source or the magnetic field need to be adjusted, but gyrotrons typically operate at fixed frequencies.[72,76]

Figure 2.24 *Picture of the UK DNP MAS NMR Facility at the University of Nottingham, where the DNP measurements reported in this work have been carried out.*

2.5 Solid-state NMR experimental techniques

2.5.1 General solid-state NMR experimental details

Solid-state NMR experiments at St Andrews were carried out using Avance III spectrometers equipped with 9.4 and 14.1 T widebore superconducting magnets and conventional MAS probes. Depending on the amount of sample available and the desired spin rates, powdered samples were packed in conventional 4 and 3.2 mm zirconia rotors reaching MAS rates in the range 10-20 kHz. For *in situ* experiments, disposable PTFE "HR-MAS" Bruker inserts, containing the sample and the hydrolysing solutions, were packed inside conventional 4 mm zirconia rotors, achieving a safe spinning speed of 5 kHz. High-field NMR spectra were recorded at the UK 850 MHz Facility at the University of Warwick, with assistance from Dr Dinu Iuga, using an Avance III spectrometer equipped with a 20.0 T widebore superconducting magnet. Samples were packed in conventional 3.2 mm zirconia rotors with typical MAS rates of 16-20 kHz. DOR experiments were also carried out at the Facility with 9.3 and 3.4 mm outer and inner rotors, respectively. DNP experiments were carried out at the UK DNP MAS NMR Facility at the University of Nottingham with assistance from Dr Subhradip Paul using an Ascend widebore 14.09 T cryo-magnet. The experimental techniques and pulse sequences used for DNP experiments are introduced in the following general sections for solid-state NMR. The impregnated solids, as described in Section 2.4.3, were packed in zirconia or sapphire 3.2 mm rotors with typical MAS rates of 12.5 and 20 kHz in low- (~100 K) and room-temperature conditions, respectively. Further experimental details will be provided in the relevant chapters and in figure captions. Fitting and spectral analysis has been performed with Topspin 2.1 (Bruker) and Dmfit.[77]

2.5.2 Experimental techniques

A wide range of solid-state NMR experiments have been carried out to obtain a complete and high-resolution characterisation of the microporous compounds synthesised. Thanks to these experimental techniques, it has been possible to remove the broadening resulting from anisotropic interactions and obtain valuable information about the materials analysed.

2.5.2.1 Magic angle spinning

Whereas all the anisotropic interactions discussed in Section 2.4.2 are averaged to their isotropic values by the rapid tumbling of molecules in solution, solid-state NMR spectra of polycrystalline samples contain both the isotropic and anisotropic components of all the interactions present, providing plenty of valuable information. However, such a wealth of information poses, at the same time, significant challenges in the interpretation and analysis of solid-state NMR spectra, due to the presence of broadened and often overlapping resonances. For this reason, a widely applied approach used to improve spectral sensitivity and resolution is to mimic the orientational averaging occurring in solution. Since the anisotropic parts of the chemical shielding (Equation 2.33), dipolar (Equation 2.34), J coupling and first-order quadrupolar (Equation 2.40) interactions all have a similar orientational dependence of the form $(3\cos^2\theta - 1)/2$, their magnitudes will drop to zero when $\theta = 54.736°$. This condition can be fulfilled by physically rotating the sample about an axis inclined at the "magic" angle, χ, of 54.736° to B_0 in a technique called magic angle spinning (MAS),[78-80] as shown in Figure 2.25, thus ensuring an average orientation of 54.736° to the external magnetic field for all the crystallites simultaneously. Experimentally, MAS is carried out by packing the sample into ZrO_2 holders, or "rotors", schematically represented in Figure 2.25a, of various diameters, which can then be rotated at increasing rates of up to 110 kHz, as the rotor diameter, and subsequently sample volume, decreases. The significant effect of MAS on the ^1H spectrum of alanine can also be observed comparing Figure 2.25b and Figure 2.25c.

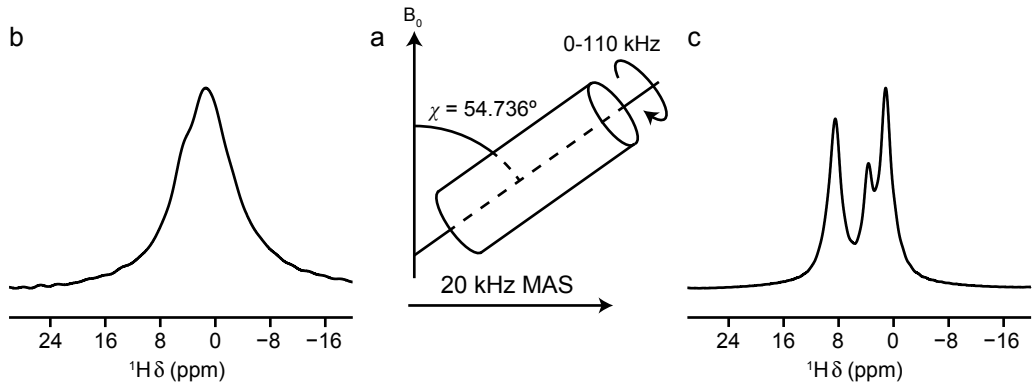

Figure 2.25 *Schematic representation of a MAS experiment, where a polycrystalline sample, packed in a rotor, is spun about an axis inclined at the magic angle, χ, of 54.736° to B_0 (a). (c) shows the effect of MAS, at a rate of 20 kHz, on the ^1H spectrum of alanine, resolving its three different environments, compared to the static spectrum in (b), at 14.1 T.*

In order to efficiently remove the anisotropic interactions, the rotation must be sufficiently fast, relatively to the magnitude of the interaction to be removed. Otherwise, the powder-pattern lineshape is broken into a series of "spinning sidebands" (SSBs), separated by integer multiples of the spinning rate, ν_R, from the isotropic peak.[9] The effect of increasing MAS on a typical CSA lineshape, as shown in Figure 2.16, is represented in Figure 2.26. At slow rates of MAS the intensities resulting from the spinning sideband manifold reproduce the shape of the powder-pattern static lineshape, see Figure 2.26b. As the MAS rate increases, it is possible to observe more clearly the intense resonance at the isotropic chemical shift, as in Figures 2.26c-d. In the case of quadrupolar nuclei, MAS can only partially remove the quadrupolar interaction, since the second-order quadrupolar broadening has a more complex angular dependence, see Equation 2.42. As shown by the simulated lineshapes in Figure 2.27 and experimental results in Figure 2.28, the ^{27}Al lineshape narrows under MAS conditions but a second-order quadrupolar broadening is still present.

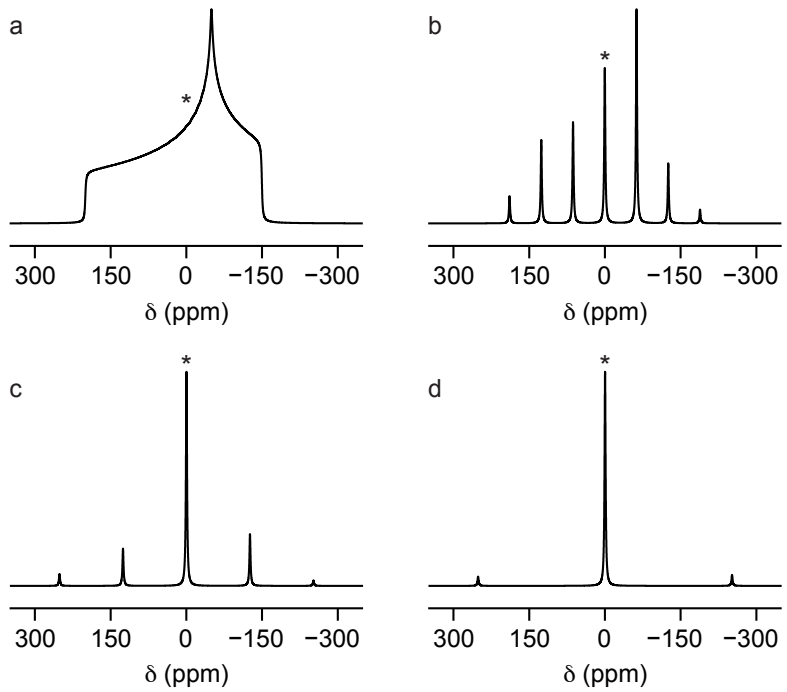

Figure 2.26 *Static and MAS NMR lineshapes, simulated using Topspin, for a spin ½ nucleus with $\Delta\delta_{cs}$ = 200 ppm and η_{cs} = 0.5 with MAS rates of (a) 0, (b) 5, (c) 10 and (d) 20 kHz at 9.4 T. The isotropic resonance position is indicated by an asterisk.*

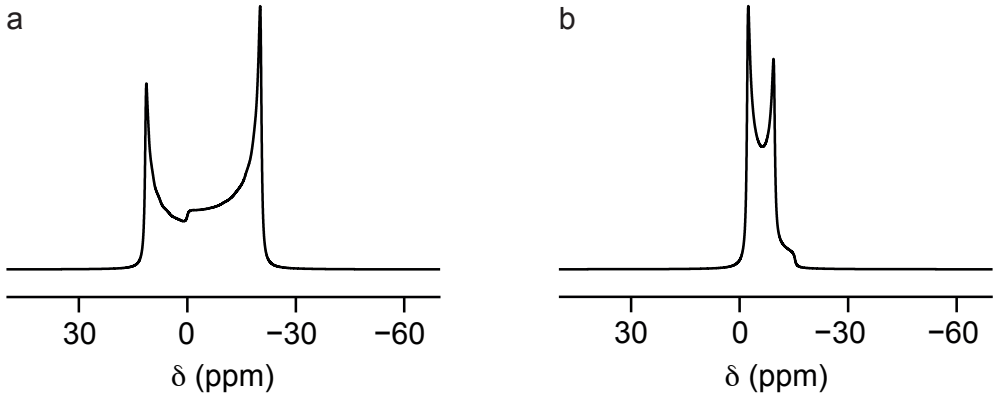

Figure 2.27 *^{27}Al NMR spectra, simulated using Topspin, (a) static and (b) at a MAS rate of 16 kHz with C_Q = 5 MHz and η_Q = 0, at 14.1 T.*

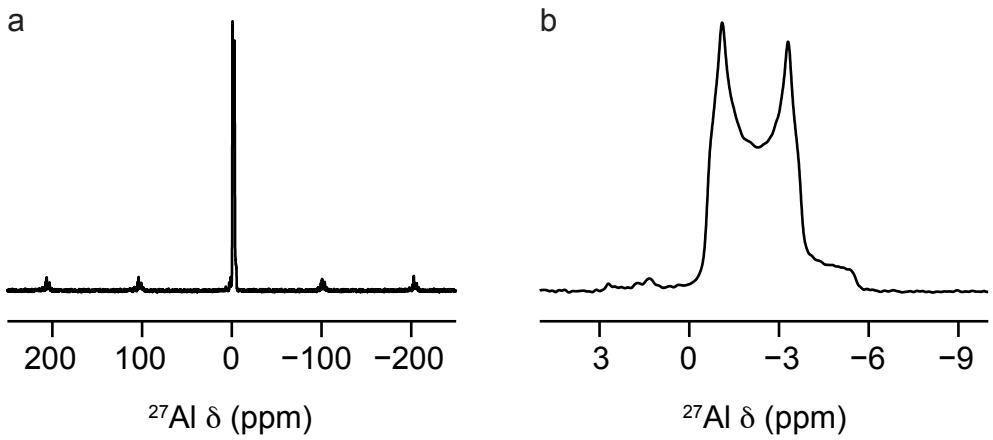

Figure 2.28 *(a) ^{27}Al (14.1 T, 16 kHz) MAS NMR spectrum of aluminium acetylacetonate, $Al(acac)_3$, and shown expanded in (b).*

Under MAS conditions, if we assume the MAS rate is faster than $\frac{\left(\omega_Q^{PAS}\right)^2}{\omega_0}$, the MAS-averaged second-order correction to the energy can be obtained from Equation 2.42 as

$$\langle E_i^{(2)} \rangle_{MAS} = \frac{\left(\omega_Q^{PAS}\right)^2}{2\omega_0} \times \left(A_{I,m_i}^{(0)} B^{(0)} - \frac{7}{18} A_{I,m_i}^{(4)} B^{(4)}(\beta', \gamma') \right), \qquad (2.48)$$

where β' and γ' are Euler angles relating the PAS of the EFG tensor to the rotor frame with z corresponding to the MAS axis. Equation 2.48 shows that part of second-order broadening survives MAS, since the second-rank term is averaged out, but the forth-rank term is only scaled.

Notwithstanding the remaining quadrupolar broadening, it is possible to extract useful information from quadrupolar lineshapes in the form of the quadrupolar parameters, C_Q and η_Q, as shown in Figure 2.29.

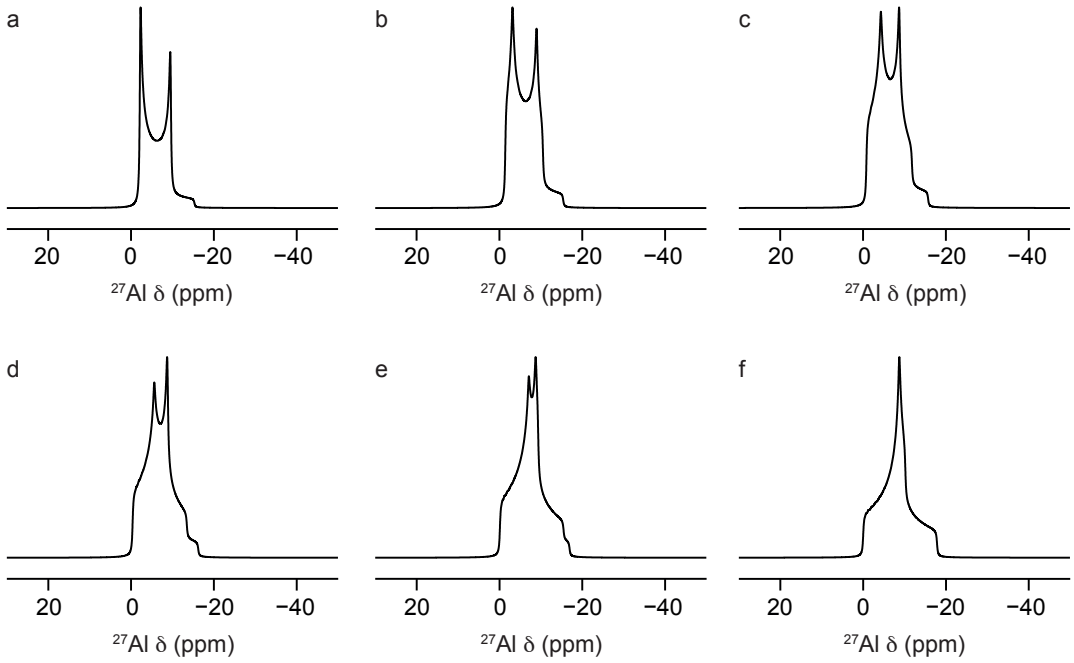

Figure 2.29 *Second-order broadened CT quadrupolar lineshapes, simulated using Topspin, for ^{27}Al at 14.1 T with C_Q = 5 MHz and η_Q of (a) 0, (b), 0.2, (c) 0.4, (d) 0.6, (e) 0.8, (f) 1, using a MAS rate of 10 kHz.*

2.5.2.2 Double rotation

Double rotation (DOR)[81] experiments can be used to obtain high-resolution spectra of quadrupolar nuclei affected by second-order quadrupolar broadening. This technique works by overcoming the limits of MAS, which, as shown in Equation 2.48, is unable to remove entirely the second-order quadrupolar broadening. The second-order contribution to quadrupolar broadening can be averaged to zero by spinning the sample at two specific angles. This is experimentally achieved with two rotors, one embedded in the other, each spinning at a different angle to the external magnetic field: the spinning axis of the outer rotor forms an angle θ_o of 54.736° to the direction of the external magnetic field and the axis of the inner rotor is inclined at an angle θ_i of either 30.56° or 70.12° with respect to the outer rotor axis, as shown in Figure 2.30. In this way, both the second- and fourth-rank terms of the second-order quadrupolar broadening, see Equation 2.42, are averaged to zero, in addition to all the interactions that would be removed by MAS, and truly high-resolution spectra can be acquired. DOR experiments are, however, quite complex to implement,

requiring expensive and specialist equipment. Moreover, this experiment is technically limited by the slow MAS rates that can be achieved (up to ~8 kHz for the inner rotor and ~2 kHz for the outer), resulting in the presence of many spinning sidebands in the final spectrum. Therefore, the identification of isotropic resonances can be challenging, especially when multiple sites are present in a sample. This can be overcome to some extent by using spinning sideband suppression[82] sequences and by repeating the same experiment at different MAS rates so that spinning sidebands will appear to move while the position of the isotropic peak will remain unchanged.

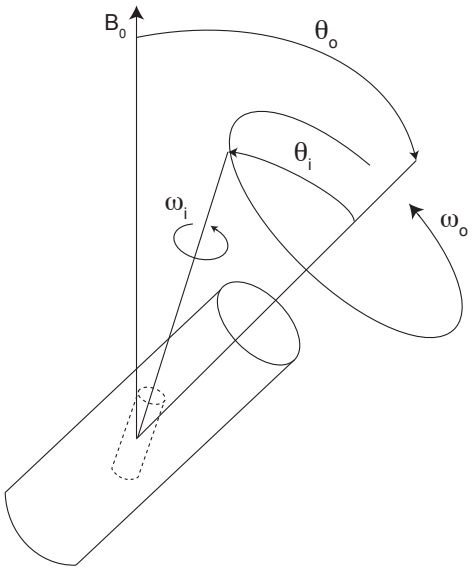

Figure 2.30 *Schematic representation of DOR experimental configuration, showing the two different angles, θ_i and θ_o, and the related spinning frequencies, ω_i and ω_o, of the two (inner and outer) rotors.*

2.5.2.3 Direct polarisation single-pulse and spin echo

The single-pulse experiment is the simplest NMR experiment, where, as shown in Figure 2.31, a 90° pulse is applied to the sample and the resulting signal is subsequently recorded. In order to allow the equilibrium conditions to be restored, it is generally best to wait approximately 5 T_1 between the acquisition of successive FIDs.[9]

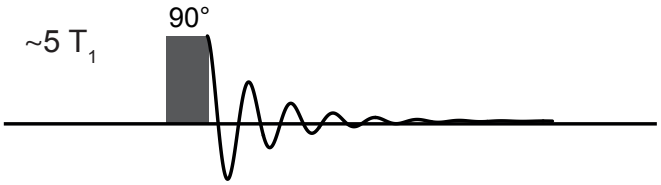

Figure 2.31 *Pulse sequence for a single-pulse experiment.*

In case of very short T_2, i.e. very rapid transverse relaxation, the intensity of the FID may quickly decay to zero by the time signal acquisition starts. This happens because a small dead time is required before signal acquisition to avoid possible distortions deriving from the effects of the rf pulse on the probe, known as "probe ringing". To overcome this problem, a spin echo experiment[83] can be used, as shown in Figure 2.32. In a spin echo experiment, after a time τ, known as the echo duration, from the initial 90° pulse, a 180° pulse is applied, refocusing magnetisation in the xy plane and allowing spectra to be acquired without distortions.[84]

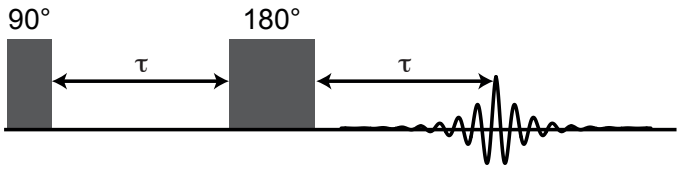

Figure 2.32 *Pulse sequence for a spin echo experiment.*

2.5.2.4 Heteronuclear decoupling

Broadening contributions deriving from spin-spin interactions (e.g., dipolar and isotropic J terms) often cannot be completely averaged to zero by MAS leading to a loss of resolution in NMR spectra. These broadening effects result from interactions between spins where the resonant frequency of one spin, I, is affected by the state of another spin, S. In these cases, to increase the resolution of NMR spectra heteronuclear decoupling can be used. Decoupling works by irradiating spin S while acquiring the spectrum of spin I, thus constantly changing the state of S and averaging to zero the resulting heteronuclear I-S dipolar coupling. The original and

simplest method of decoupling is continuous wave (CW) decoupling where a continuous irradiation is applied, but more complex pulse sequences with variations in duration, strength and phase of the decoupling pulses, such as two-pulse phase modulation (TPPM)[85] and SPINAL[86], are now typically used to achieve a more efficient averaging of the dipolar interaction. TPPM, in particular, has been extensively used in this work and involves a train of pulses with alternating phases ϕ and $-\phi$, typically indicated as TPPM-ϕ.

2.5.2.5 Cross-polarisation

After MAS, cross-polarisation (CP)[87] is one of the most widely used techniques in solid-state NMR. However, unlike MAS, its main aim is not to improve resolution, but to improve sensitivity, hence it is mainly applied to assist in observing dilute spins, e.g., ^{29}Si, whose natural abundance is approx. 4.7%. Observing such dilute spins poses a number of problems in NMR spectroscopy, since the SNR is inevitably poor for low abundance nuclei, which also tend to have very long relaxation times as a result of the absence of relaxation-stimulating strong homonuclear dipolar interactions.[88] In order to overcome these problems, the CP approach not only involves the transfer of magnetisation from the highly abundant, high-γ spin I (typically ^{1}H) to the lower γ and lower abundance spin S (e.g., ^{29}Si, ^{13}C), with a maximum gain of a factor of γ_I/γ_S, but also allows the experiment to be repeated more rapidly, as T_1 is generally shorter for the highly abundant and high-γ spins.

As shown in Figure 2.33, after an initial 90° pulse on spin I, the resulting magnetisation is transferred to spin S in a contact time, during which pulses are applied to both spins to lock the magnetisation while transfer takes place. Optimisation of the contact time length is required to maximise the transferred signal, whose intensity depends on the build-up rate, proportional to the dipolar coupling between spins, and the rotating frame spin-lattice relaxation, $T_{1\rho}$. The spin-lattice relaxation in the rotating frame concerns the loss of transverse magnetisation in the presence of a rf magnetic field, B_1, in the same direction and can be measured using the pulse sequence shown in Figure 2.34.[89]

After the contact time, the S spin FID is acquired usually decoupling I to improve the resolution of the final spectrum. Moreover, since magnetisation is transferred through the heteronuclear dipolar coupling, the spectrum is edited by proximity to the nuclei involved in the magnetisation transfer, providing structural information. However, owing to such a dependence on the dipolar coupling, quantitative spectra can't be obtained from this technique. Therefore, the relative intensities in CP spectra must be treated with caution, as shown in Figure 2.35 for ^{1}H-^{13}C cross-polarised and ^{13}C directly acquired spectra of alanine, where the three ^{13}C sites have different relative intensities in the two experiments.

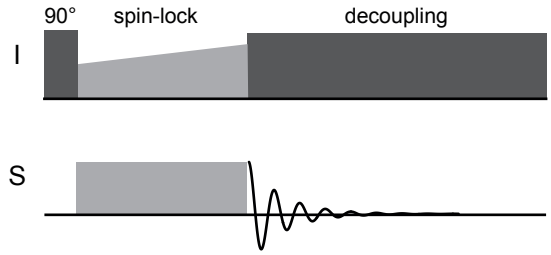

Figure 2.33 *Pulse sequence for a cross-polarisation experiment with a ramped pulse for I. Decoupling of I is applied while recording the FID of S.*

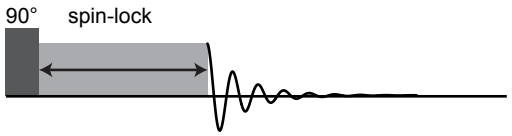

Figure 2.34 *Pulse sequence for a $T_{1\rho}$ experiment.*

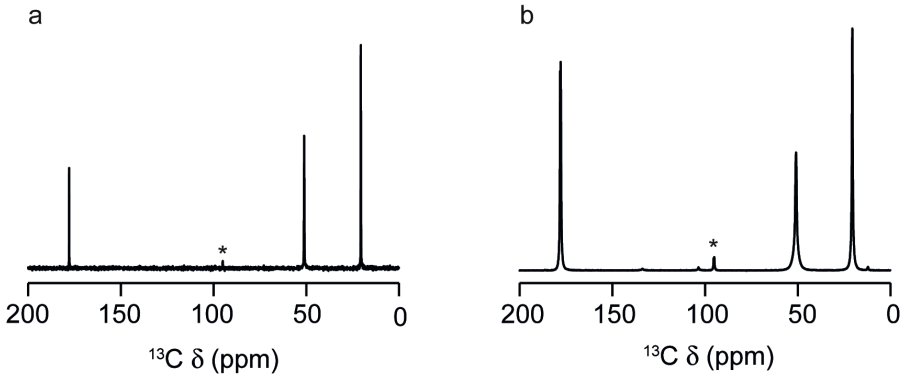

Figure 2.35 *(a) ^{1}H-^{13}C CP and (b) ^{13}C MAS NMR spectra (14.1 T, 12.5 kHz) of (a) natural abundance and (b) ^{13}C-enriched alanine. For both spectra 8 transients were averaged with a recycle delay of (a) 3 s and (b) 360 s. Spinning sidebands are denoted by asterisks.*

In a static CP experiment, magnetisation transfer can only be achieved if the rf fields applied during the contact time fulfill the Hartmann-Hahn[87] condition

$$\gamma_I B_{1I} = \gamma_S B_{1S} . \quad (2.49)$$

Since all the experiments in this work have been carried out under MAS conditions,[90-91] Equation 2.49 has to be modified to give

$$\gamma_I B_{1I} = \gamma_S B_{1S} \pm n\omega_R , \quad (2.50)$$

where ω_R is the MAS rate and n is an integer (typically 1 or 2). In practice, while any rf fulfilling these conditions could be chosen, lower powers are preferred to minimise possible detrimental effects on the probe hardware.[9] A variable amplitude contact pulse, typically ramped,[92] can be used to increase the efficiency of polarisation transfer in CP MAS experiments, by satisfying the match conditions for more crystallites.

Cross-polarisation can be a very useful experiment when attempting to resolve and better understand the broad and multi-component spectra recorded for quadrupolar nuclei, such as ^{17}O and ^{27}Al. However, CP experiments become complicated when a quadrupolar nucleus is involved, requiring the use of model samples specifically synthesised to assist with the optimisation of the pulse sequence. Firstly, this results in a modification of the Hartmann-Hahn matching conditions. In the limit of large quadrupolar couplings, in principle it is possible to cross-polarise selectively to the central transition at

$$\gamma_I B_{1I} = (S + 1/2)\gamma_S B_{1S} \pm n\omega_R. \quad (2.51)$$

However, in practice, particularly for a powder distribution of crystallites, this weak field limit is no longer applicable resulting in more complex matching behaviour.[93-94] Secondly, depending on the relative magnitudes of the quadrupolar splitting parameter, ω_Q^{PAS}, the radiofrequency field strength applied, ω_1, and, under MAS conditions, the spinning rate, ω_R, a different behaviour during spin-locking is observed, described by introducing an adiabaticity parameter [95-96]

$$\alpha = \frac{\omega_1^2}{2\omega_Q^{PAS}\omega_R} . \quad (2.52)$$

In the sudden limit, where $\alpha \ll 1$, the signal amplitude, after an initial drop in intensity, owing to initial dephasing of terms that do not commute with the spin-locking Hamiltonian,[95-96] remains unchanged by MAS as a function of the spin-

locking time. In contrast, for spin-locking in the adiabatic limit, where $\alpha \gg 1$, a time dependence is introduced in the spin-locked state, resulting in oscillatory behaviour (with the rotor period) of the signal amplitude as function of spin-locking time.[96] Therefore, for the purposes of a CP experiment involving a quadrupolar nucleus the spin-locking behaviour has to be investigated through spin-lock measurements where after an initial 90° pulse, experiments with variable spin-locking durations are performed. The resulting signal intensity is plotted as a function of spin-locking time providing valuable information to understand the behaviour of the system in terms of Equation 2.52. In this way, it is possible to avoid the intermediate regime, where $\alpha \approx 0$ and fast decrease in the signal amplitude is observed during spin-locking leading to a failure in the transfer of magnetisation. Experiments showing different spin-locking regimes, as in Figure 2.36, have been carried out on amorphous ^{17}O-enriched SiO_2. This model sample (synthesised and ^{17}O enriched, as described in Section 3.4.2) was used for the optimisation of ^{1}H-^{17}O CP conditions for experiments on zeolites samples, given the similarity of the oxygen environments between the two samples. In Figure 2.36a, after a sharp drop in signal intensity, a reasonable spin-locking efficiency is observed. This behaviour is characteristic of the sudden limit, with $\alpha = 4.3 \times 10^{-3}$. If a higher rf field is applied during spin-locking, a much more significant drop in signal intensity can be observed in Figure 2.36b and an oscillation with the rotor period confirms the system is between the intermediate and the adiabatic regimes, with $\alpha \approx 0.127$. As a result of the information obtained from these experiments, the best experimental conditions can be chosen for the maximum efficiency of the cross-polarisation experiment.

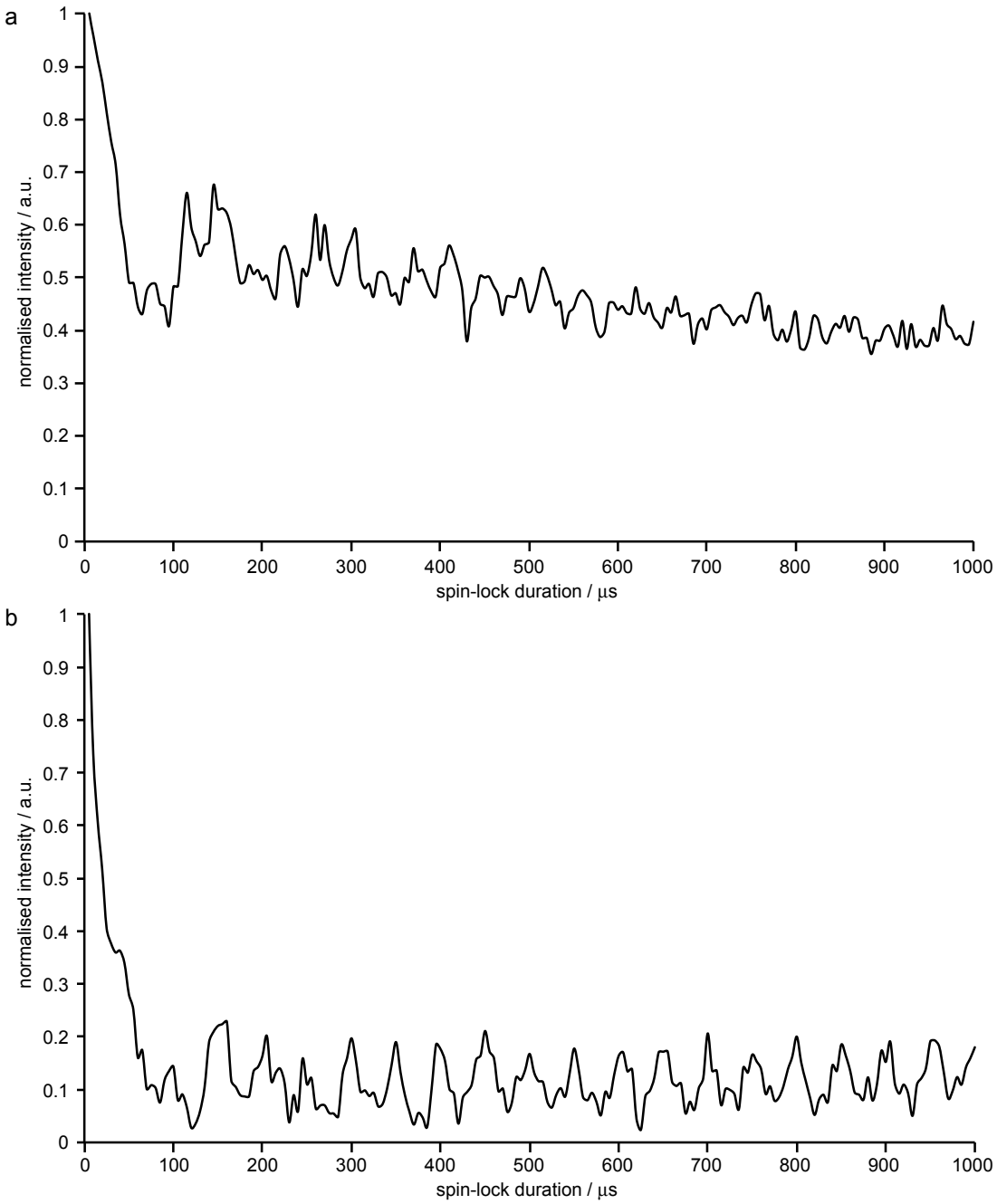

Figure 2.36 *Normalised plots showing ^{17}O (14.1 T, 20 kHz MAS) spin-locking signal intensity as a function of the spin-lock duration for amorphous ^{17}O-enriched SiO_2. Spin-lock pulses are applied with rf fields of (a) 8 kHz and (b) 45 kHz.*

2.5.2.6 Inversion and saturation recovery

The pulse sequence used to measure T_1 relaxation in inversion recovery experiments is shown in Figure 2.37. The experiment starts with the magnetisation **M** aligned along the z-axis at thermal equilibrium. After the first 180° pulse, **M** is inverted and during the recovery delay, τ_{rec}, the magnetisation returns to equilibrium at a rate of $e^{\frac{-\tau_{rec}}{T_1}}$. After τ_{rec}, a second 90° pulse generates transverse magnetisation with a corresponding signal intensity proportional to $S(\tau_{rec})$. The signal recovery, recorded by increasing τ_{rec} from 0 to >5 T_1, is then fitted to

$$S(\tau_{rec}) = S_0\left(1 - 2e^{\frac{-\tau_{rec}}{T_1}}\right), \tag{2.53}$$

where $S(\tau_{rec})$ is the signal intensity measured at a recovery time τ_{rec} and S_0 is the signal intensity when $\tau_{rec} = \infty$, allowing, in the appropriate experimental conditions, an accurate measurement of T_1. It is also possible to get an estimate of T_1 from the τ_{rec} at which the signal is zero: $S(\tau_{rec}) = 0$ when $\tau_{rec} = \ln(2)\,T_1 = 0.693\,T_1$. However, inversion recovery experiments have the disadvantage that the recycle interval must be at least 5 T_1 to allow the system to fully relax between successive repeated experiments, for accurate measurements to be possible.[89] To avoid such a disadvantage, it is possible to use a saturation recovery pulse sequence, which, starting by saturating the spins, doesn't require the system to return to equilibrium after acquisition, as shown in Figure 2.38.[89] Signal recovery in this case can be fitted to

$$S(\tau_{rec}) = S_0\left(1 - e^{\frac{-\tau_{rec}}{T_1}}\right). \tag{2.54}$$

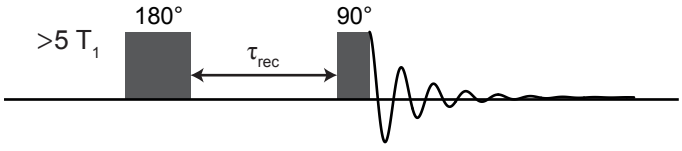

Figure 2.37 *Pulse sequence for an inversion recovery experiment.*

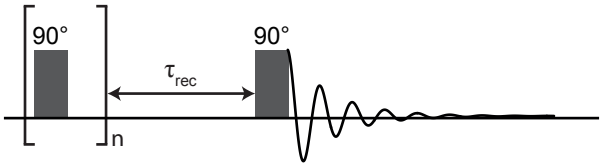

Figure 2.38 *Pulse sequence for a saturation recovery experiment.*

2.5.2.7 Heteronuclear correlation

In order to gain greater insights and more details about a system, it is often necessary to go beyond conventional 1D spectra by exploiting the interactions between the nuclear spins in two-dimensional correlation experiments. In a general 2D experiment, the magnetisation, created in a preparation step either by a single pulse or a combination of pulses, evolves during a time t_1. After this time, a second pulse or combination of pulses is applied in a mixing step, where the magnetisation, that has evolved on one spin during t_1, is transferred to another spin, before the FID is acquired in a time t_2. As a result of this general pulse sequence, shown in Figure 2.39, the amplitude of the FID directly recorded in t_2 is modulated by the evolution, observed indirectly, in t_1, which can be systematically increased in a series of experiments.

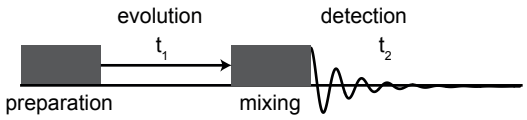

Figure 2.39 *General scheme for a 2D NMR experiment.*

Double Fourier transformation of a 2D data set leads to a 2D spectrum showing between which spins magnetisation was transferred. The power of 2D NMR lies in the flexibility of the general scheme described above, which can be adapted depending on the system analysed and the interaction probed. Correlation experiments can be heteronuclear (i.e., between two different nuclear species, requiring the application of pulses to both species) or homonuclear (i.e., between nuclear species of the same type) and can be designed, depending on the choice of pulses applied, to obtain the magnetisation transfer via either the through-bond J

coupling or the through-space dipolar interaction. The resulting cross peaks will then demonstrate that two spins are either connected by covalent bonds or are close in space, respectively.[9] Heteronuclear correlation via the dipolar interaction can be achieved through a magnetisation transfer step, for example, involving a cross-polarisation (CP HETCOR) experiment, as shown in Figure 2.40. In this case, an evolution period is added on the ^{1}H spins and heteronuclear decoupling is usually applied during acquisition, after the magnetisation transfer stage. If an increase in the resolution of the ^{1}H dimension is needed, homonuclear decoupling sequences can also be applied on the ^{1}H during the evolution time.[97]

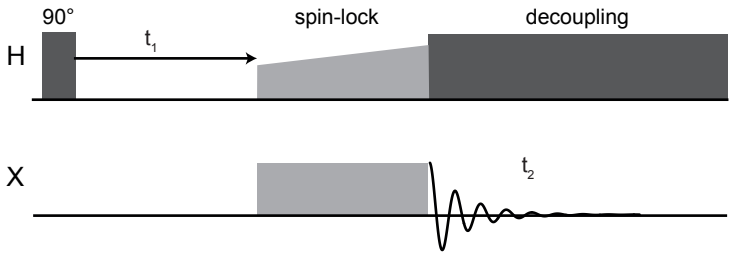

Figure 2.40 *Pulse sequence for a 2D CP HETCOR experiment.*

Dipolar interactions can also be studied in a different type of 2D experiment, heteronuclear multiple-quantum correlation (D-HMQC), where recoupling of these interactions occurs by different possible heteronuclear dipolar recoupling sequences.[98] This experiment has been specifically applied on doubly enriched zeolites for ^{17}O-^{29}Si correlation experiments at high field using the SR 4_1^2 heteronuclear recoupling sequence,[99] as shown in Figure 2.41. The step-by-step analysis of the pulse sequence is as follows:[100]

1- ^{17}O equilibrium magnetisation is excited with a soft, CT selective, "90°" pulse and becomes anti-phase during τ while suspending the averaging of the dipolar couplings by MAS over a defined time interval with the SR 4_1^2 heteronuclear recoupling sequence. Such a pulse sequence, applied to ^{29}Si, recouples heteronuclear dipolar interactions and simultaneously decouples homonuclear dipolar interactions. However, unless the 2D spectrum of a ^{29}Si-enriched sample is being recorded, this latter decoupling of homonuclear dipolar interactions does not have a significant effect owing to the low natural abundance (4.7%) of ^{29}Si.

2- As a result of the first 90° pulse on ^{29}Si, the anti-phase magnetisation is converted into heteronuclear multiple-quantum coherence, which then evolves for t_1. At the same time, a selective "180°" pulse, applied to ^{17}O and placed at the center of t_1, creates a spin echo from the first pulse to the start of acquisition, as indicated in Figure 2.41 by the dashed double-headed arrow.

3- The heteronuclear multiple-quantum coherence is converted back, by the second 90° pulse applied to ^{29}Si, into observable magnetisation on ^{17}O and the coupling is allowed to refocus during a second τ period, while again applying the $SR4_1^2$ heteronuclear recoupling sequence to ^{29}Si, before acquiring the signal.

The result of this experiment is a 2D spectrum with an ^{17}O spectrum in the direct dimension and a ^{29}Si spectrum in the second, indirect, dimension, with cross peaks providing valuable information on spins that are close in space as a function of the length of the recoupling applied.

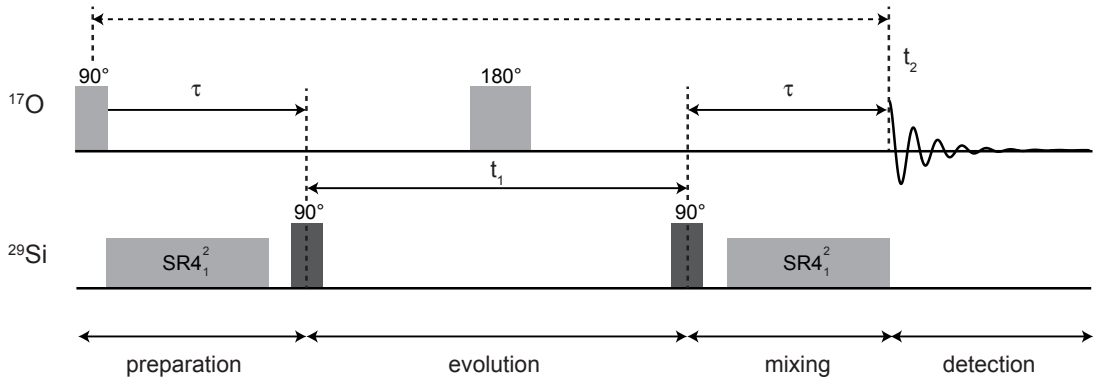

Figure 2.41 *HMQC pulse sequence with SR$\mathbf{4_1^2}$ heteronuclear recoupling. At the bottom, the basic scheme of a general 2D NMR experiment is highlighted.*

2.5.2.8 MQMAS

As previously discussed, the orientation dependence of the first-order quadrupolar interaction, being similar to that of the chemical shielding anisotropy or dipolar coupling, can in theory be removed by MAS. However, the second-order quadrupolar interaction, which broadens the CT lineshape, has a more complex angular dependence and cannot be completely removed by MAS. Frequently, 1D spectra of quadrupolar nuclei, such as ^{27}Al or ^{17}O, are characterised by broad overlapping peaks, without enough resolution for the assignment of resonances and subsequent extraction of parameters for specific sites in the material analysed. In order to fully remove quadrupolar broadening and obtain high-resolution spectra for half-integer quadrupolar nuclei, DOR, as described in Section 2.5.2.2, or two-dimensional multiple-quantum magic angle spinning (MQMAS) experiments can be used. This latter approach has seen widespread application in recent years and now represents the most popular method of studying quadrupolar nuclei, providing more information than one-dimensional MAS spectra. In addition, this method does not require the use of specialist hardware, such as DOR probes, and is therefore more experimentally accessible using conventional MAS probeheads.

Originally introduced by Frydman and Harwood in 1995,[101] the MQMAS pulse sequence has since been modified to obtain experiments with better sensitivity and pure phase lineshapes, becoming a routine method for the spectroscopic investigation of quadrupolar nuclei.[102] MQMAS is a 2D experiment in which a CT spectrum, acquired during t_2, is correlated with a multiple-quantum, usually triple-quantum, spectrum acquired indirectly in t_1. As usual for two-dimensional experiments, FIDs are collected over a time t_2 for various values (increments) of t_1 to produce a 2D dataset involving two time variables. Double Fourier transformation yields a 2D plot in the frequency domain containing ridge-like lineshapes usually lying parallel to the direct dimension, δ_2, as a result of appropriate processing or specific pulse sequences applied during acquisition, and an isotropic, high-resolution spectrum without quadrupolar broadening in the indirect dimension, δ_1. Therefore, lineshapes that appear broadened and overlapping in 1D MAS spectra can potentially be resolved in such a 2D spectrum. Moreover, it is also possible, by extracting cross sections

parallel to δ_2, to individually study each quadrupolar lineshape, which can then be fitted to extract the relevant NMR parameters, δ_{iso}, C_Q and η_Q. Information on the quadrupolar interaction and isotropic chemical shift can also be derived from the position of the center of gravity of the lineshapes in the 2D spectrum.

The original pulse sequence for triple-quantum MAS experiments involved the use of two pulses for the generation of the triple-quantum coherences, but it was later shown that the efficiency of this can be increased by the use of one long pulse,[103] as shown in Figure 2.42. After an evolution time t_1, multiple-quantum coherences are converted back to observable single-quantum coherences and the coherence pathway followed depends on the ratio, R,[104] of the fourth-rank terms, $A^{(4)}_{I,m_i}$, for the single- and multiple-quantum transitions studied. The ratio will be different for different spin systems and coherence orders, as shown in Table 2.4, and in this work triple-quantum experiments of I = 5/2 nuclei will be described.

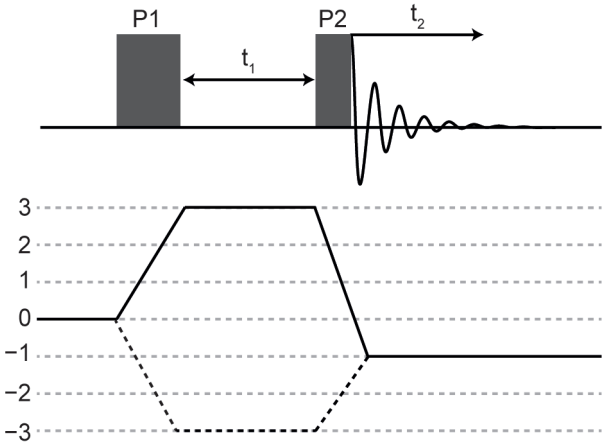

Figure 2.42 *Pulse sequence and coherence transfer pathway for the two-pulse 3QMAS NMR experiment adapted from the original sequence.[101] The bold and dashed lines denote the coherence transfer pathway for nuclei with I > 3/2 and I = 3/2, respectively, corresponding to positive or negative values in Table 2.4.*

I	3Q	5Q	7Q	9Q
3/2	−7/9			
5/2	19/12	−25/12		
7/2	101/45	11/9	−161/45	
9/2	91/36	95/36	7/18	−31/6

Table 2.4 *MQMAS ratios, R, ($A^{(4)}_{I,m_i}/A^{(4)}_{I,1/2}$) for nuclei with half-integer spins.*

The original experiment has been subsequently modified to include amplitude-modulated z-filtered[105] and phase-modulated shifted-echo[106] experiments, to obtain pure absorption lineshapes.

The amplitude-modulated pulse sequence selects two symmetrical coherence pathways (0⟶±p⟶0⟶−1) and is normally combined with a z filter, as shown in Figure 2.43. The contributions from the symmetric coherence pathways are equal in amplitude in this pulse sequence, leading to a 2D spectrum with purely absorptive lineshapes.

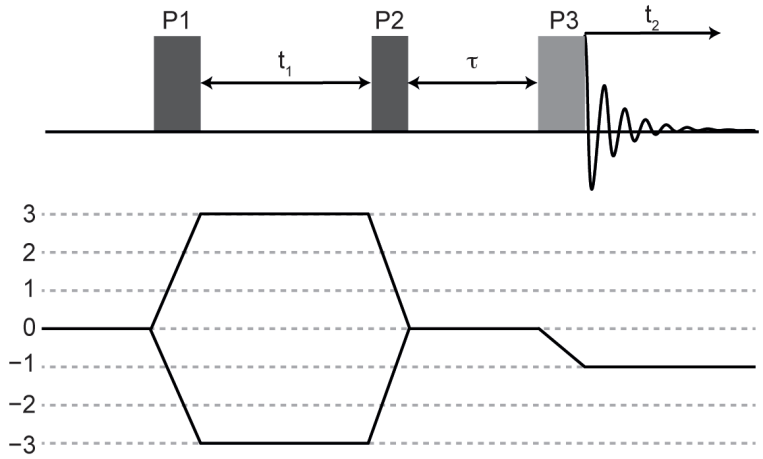

Figure 2.43 *Pulse sequence and coherence transfer pathway for an amplitude-modulated z-filtered 3QMAS NMR experiment. Pulses with reduced power are shown in grey.*

The z filter consists of a short delay, τ, during which magnetisation is stored along B_0, allowing unwanted coherences in the transverse plane to dephase, and then transferred to observable CT coherences. This type of MQMAS experiment is amplitude modulated during t_1 and is very robust and easy to optimise. To maximise the efficiency of the experiment the excitation and conversion pulses should use high rf and the third pulse should be a CT selective $\pi/2$ pulse. The rf field strength of this last pulse should be chosen as a compromise between the complete and the selective irradiation of the central transition. If needed, ^{1}H decoupling can be applied during the pulse sequence to increase the resolution of the final spectrum. MQMAS spectra acquired with this pulse sequence contain ridge lineshapes aligned along a gradient determined by the MQMAS ratio, R, for the specific multiple-quantum transition and nuclear spin system, as in Table 2.4. For a more convenient analysis, a shearing transformation[102] is carried out to obtain a spectrum with ridges parallel to δ_2, with the isotropic spectrum in δ_1, as schematically shown in Figure 2.44.

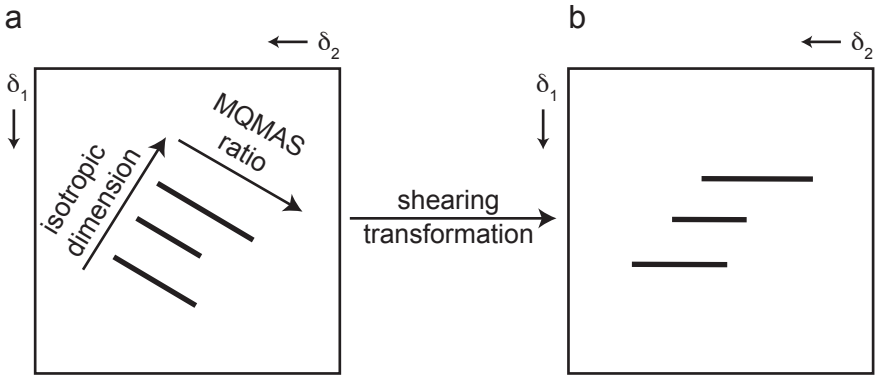

Figure 2.44 *Schematic representation of shearing transformation for MQMAS spectra. (a) The set of ridges is aligned along a gradient determined by the MQMAS ratio, R. (b) The set of ridges is now parallel to δ_2 with the isotropic spectrum in δ_1.*

Alternatively, a shifted-echo approach can be used, where one coherence pathway is followed and the whole echo is acquired, thus generating pure phase spectra. In this approach the coherence transfer pathway chosen will depend on the sign of the MQMAS ratio, the signal is phase modulated during t_1 and a final CT selective π pulse is added, after a time τ, at the end of the first two pulses, as shown in Figure 2.45. The resulting spectrum, similarly to the amplitude-modulated z-filtered experiment already described, will require shearing to obtain ridges parallel to δ_2.

However, due to the time needed for the acquisition of the whole echo, this type of experiment is not suitable for those materials where T_2 relaxation can cause problems of signal loss and, in these cases, the amplitude-modulated z-filtered experiment is preferred.

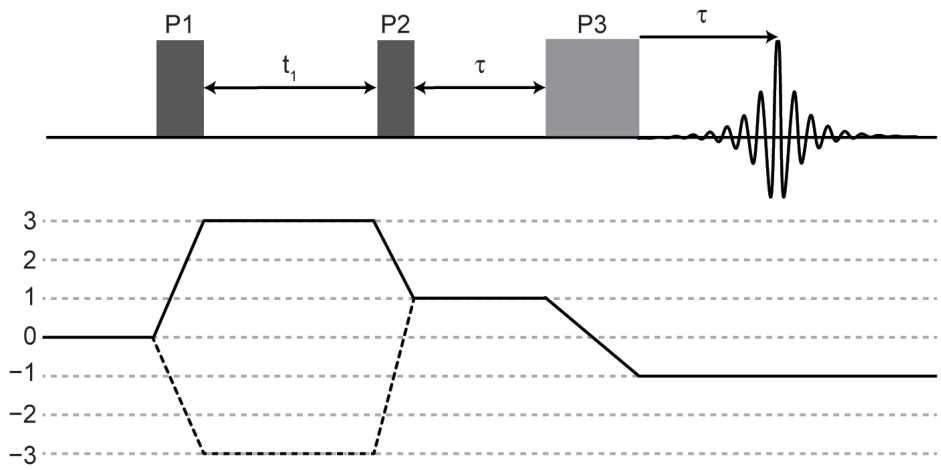

Figure 2.45 *Pulse sequence and coherence transfer pathway for the phase-modulated shifted-echo 3QMAS NMR experiment. The bold and dashed lines denote the coherence transfer pathway for nuclei with I > 3/2 and I = 3/2, respectively. Pulses with reduced power are shown in grey.*

A split-t_1 experiment,[102] which can be applied to both phase- or amplitude-modulated experiments, has the major advantage of not requiring the shearing transformation, which can potentially result in distorted lineshapes. This method of data acquisition relies on the splitting of the t_1 duration into the desired multiple-quantum ($k\ t_1$) and single-quantum ($k'\ t_1$) evolution periods, where k and k′ are related to the MQMAS ratio.[107] In the split-t_1 shifted-echo approach, as shown in Figure 2.46, one coherence pathway is followed, the experiment is phase modulated and the whole echo is acquired, yielding a pure absorptive lineshape. The triple-quantum phase-modulated split-t_1 pulse sequence, shown in Figure 2.46, consists of a triple-quantum (3Q) excitation, followed by a fraction of t_1, and then a p=+3⟶p=+1 conversion pulse, followed by an echo delay, τ. The third pulse is a CT selective inversion pulse applied before the remaining fraction of t_1 for I > 3/2 or after for I = 3/2. Owing to the split of t_1 between multiple- and single-quantum evolution, the second-order quadrupolar broadening is refocused at the end of t_1 and the resulting spectrum is characterised by ridges parallel to δ_2 and the isotropic spectrum in δ_1.

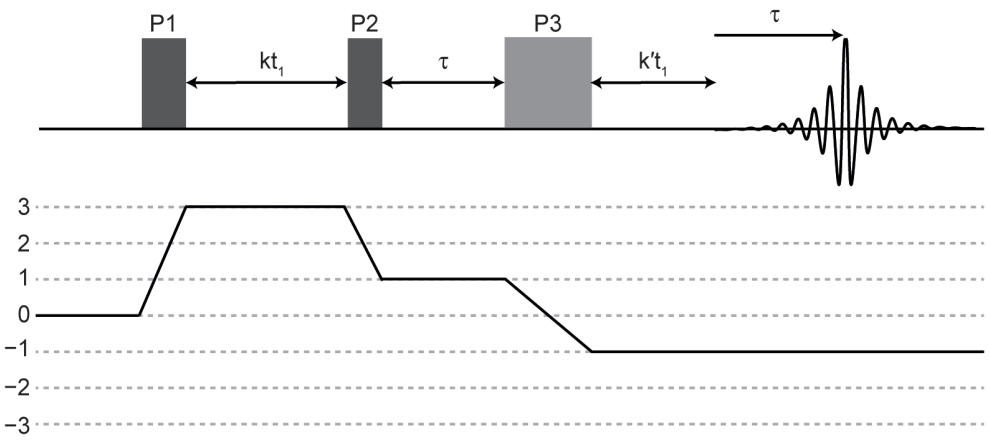

Figure 2.46 *Pulse sequence and coherence transfer pathway for the split-t_1 phase-modulated shifted-echo 3QMAS NMR experiment for I > 3/2. Pulses with reduced power are shown in grey.*

MQMAS z-filtered spectra are shown in this work after a shearing transformation[102] and the indirect dimension of split-t_1/sheared spectra is scaled and referenced according to the convention described in Pike *et al.*[108]

Perhaps the greatest disadvantage of the MQMAS technique resides in the low efficiency of filtration, since the direct excitation and conversion of multiple-quantum magnetisation is formally forbidden by the NMR selection rule.[9] Therefore, several approaches have been developed to improve the overall efficiency of the experiment. In some of the experiments carried out in this work different sequences of composite pulses have been used to improve the conversion efficiency of triple- to single-quantum coherences: soft pulse added mixing (SPAM),[109] fast amplitude modulated (FAM)[110] pulses or double frequency sweep (DFS).[111-112]

When samples are ordered and have sharp lineshapes it is frequently possible to extract NMR parameters (δ_{iso}, C_Q and η_Q) fitting well-defined cross sections extracted along the ridges parallel to the δ_2 dimension in a split-t_1 or sheared spectrum. When disorder is present, however, broadened or overlapping lineshapes are observed and in these cases average parameters $\langle\delta_{iso}\rangle$ and $\langle P_Q\rangle$, as previously introduced in Equation 2.39, are normally obtained from the position of the center of gravity (δ_1,δ_2) of the ridges. The equations involved depend on the nuclear spin, the coherence pathway and type of experiment.[108,113-114] In particular, for a split-t_1 or

sheared 3QMAS experiment involving a spin I = 5/2 nucleus, such as ^{17}O or ^{27}Al, the relation of δ_1 and δ_2 with δ_{iso} and δ_Q is

$$\delta_1 = \frac{17}{31}\delta_{iso} + \frac{32}{93}\delta_Q \quad (2.55)$$

$$\delta_2 = \delta_{iso} - \frac{16}{15}\delta_Q, \quad (2.56)$$

where

$$\delta_Q = \left(\frac{75P_Q}{\nu_0}\right)^2. \quad (2.57)$$

An example of the resolution achieved by MQMAS and the information that can be obtained by extracting quadrupolar parameters is shown in Figure 2.47 for the ^{17}O MQMAS of 75% ^{17}O-enriched orthoenstatite. This mineral is one of the polymorphs of $MgSiO_3$ and is present in the upper mantle (to a depth of 410 km) of the Earth. It is a chain silicate with a structure of corner-sharing SiO_4 tetrahedra linked by Mg^{2+} cations. In each chain there are two non-bridging oxygen species (i.e., those bonded only to a single Si) and one bridging oxygen (i.e., Si-O-Si) linking the tetrahedra. As two slightly different chains are present, the structure is characterised by a total of six different oxygen sites. The ^{17}O MAS NMR spectrum in Figure 2.47a shows a composite resonance with broad overlapping lineshapes which are resolved in the amplitude-modulated z-filtered 3QMAS experiment, shown, after a shearing transformation, in Figure 2.47b, with six resonances observed in the isotropic dimension. Figures 2.47c-h show, in order of increasing δ_1 shifts, cross sections parallel to δ_2 through the six ridge lineshapes overlaid on the corresponding fits with the resulting quadrupolar parameters reported in Table 2.5. The four resonances at lower δ_1 correspond to non-bridging oxygens, whereas the two resonances at higher δ_1, with higher values of C_Q, correspond to bridging oxygen species. The four non-bridging oxygen species have very similar C_Q values, but differences in chemical shift enable the distinct oxygen crystallographic sites to be assigned. The two bridging oxygen species can also be identified on the basis of the difference in their C_Q values.[113]

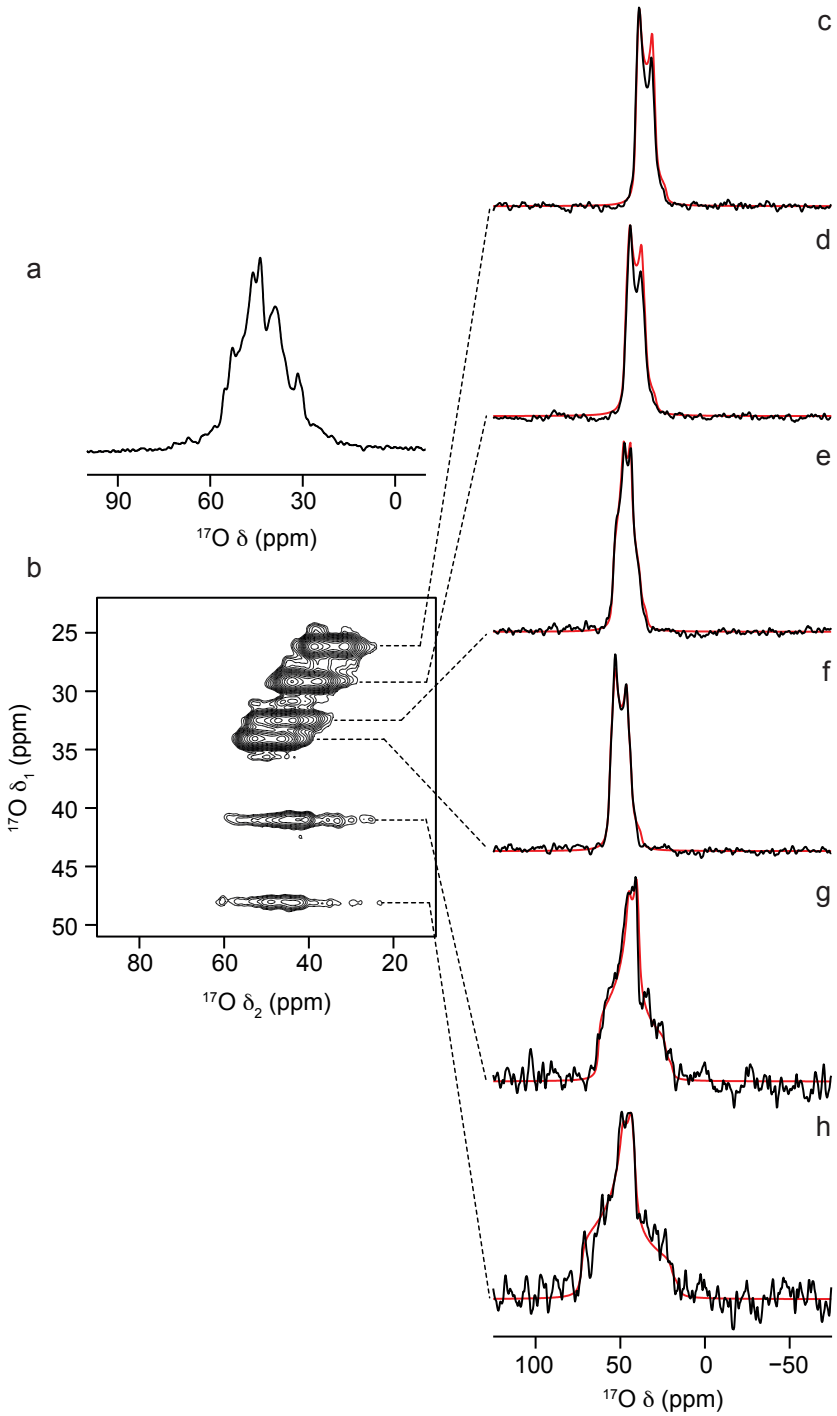

Figure 2.47 *^{17}O (a) MAS and (b) amplitude-modulated z-filtered 3QMAS (shown after a shearing transformation) NMR spectra (14.1 T, 14 kHz MAS) of 75% ^{17}O-enriched orthoenstatite. (c)-(h) cross sections (black), extracted parallel to δ_2 from the 3QMAS experiment in (b), in order of increasing δ_1 values and corresponding fits (red) using the parameters reported in Table 2.5.*

δ_1 (ppm), 14.1 T	δ_{iso} (ppm)	P_Q / MHz	C_Q / MHz	η_Q
26(1)	43(2)	3.0(2)	3.0(2)	0.18(5)
29(1)	49(2)	3.0(2)	3.0(2)	0.25(5)
32(1)	55(2)	3.1(2)	3.0(2)	0.57(5)
34(1)	58(2)	3.0(2)	3.0(2)	0.29(5)
41(1)	63(3)	4.7(3)	4.2(2)	0.78(5)
48(1)	73(3)	5.3(3)	4.8(2)	0.85(5)

Table 2.5 *Quadrupolar parameters obtained from the ^{17}O 3QMAS NMR spectrum shown in Figure 2.47b for 75% ^{17}O-enriched orthoenstatite.*

2.6 References

1 S. E. Ashbrook, D. M. Dawson and V. R. Seymour, *Phys. Chem. Chem. Phys.*, 2014, **16**, 8223–8242.

2 L. Mafra and J. Klinowski, eMagRes, 2013, DOI: 10.1002/9780470034590.emrstm1325.

3 L. Mafra and J. Klinowski, eMagRes, 2013, DOI: 10.1002/9780470034590.emrstm1307.

4 M. Hunger, *Catal. Rev.- Sci. Eng.*, 1997, **39**, 345–393.

5 W. Zhang, S. Xu, X. Han and X. Bao, *Chem. Soc. Rev.*, 2012, **41**, 192–210.

6 Y. Jiang, J. Huang, W. Dai and M. Hunger, *Solid State Nucl. Magn. Reson.*, 2011, **39**, 116–141.

7 J. Van Aelst, M. Haouas, E. Gobechiya, K. Houthoofd, A. Philippaerts, S. P. Sree, C. E. A. Kirschhock, P. Jacobs, J. A. Martens, B. F. Sels and F. Taulelle, *J. Phys. Chem. C*, 2014, **118**, 22573–22582.

8 W. Lutz, W. Wieker, D. Müller, M. Schneider, C. H. Rüscher and J. C. Buhl, *Z. Anorg. Allg. Chem.*, 2000, **626**, 1460–1467.

9 S. E. Ashbrook, D. M. Dawson and J. M. Griffin, in *Local Structure Characterisation*, Eds. D. W. Bruce, D. O'Hare and R. I. Walton, John Wiley & Sons, 2014, Chapter 1.

10 S. E. Ashbrook and S. Sneddon, *J. Am. Chem. Soc.*, 2014, **136**, 15440–15456.

11 H. K. C. Timken, G. L. Turner, J. P. Gilson, L. B. Welsh and E. Oldfield, *J. Am. Chem. Soc.*, 1986, **108**, 7231–7235.

12 U. T. Pingel, J. P. Amoureux, T. Anupõld, F. Bauer, H. Ernst, C. Fernandez, D. Freude and A. Samoson, *Chem. Phys. Lett.*, 1998, **294**, 345–350.

13 L. M. Bull, B. Bussemer, T. Anupõld, A. Reinhold, A. Samoson, J. Sauer, A. K. Cheetham and R. Dupree, *J. Am. Chem. Soc.*, 2000, **122**, 4948–4958.

14 L. Peng, Y. Liu, N. Kim, J. E. Readman and C. P. Grey, *Nature Mater.*, 2005, **4**, 216–219.

15 R. E. Wasylishen, S. E. Ashbrook and S. Wimperis, Eds., in *NMR of Quadrupolar Nuclei in Solid Materials*, Wiley, 2012, Chapter 18.

16 E. R. H. van Eck, M. E. Smith and S. C. Kohn, *Solid State Nucl. Magn. Reson.*, 1999, **15**, 181–188.

17 V. K. Michaelis, E. Markhasin, E. Daviso, J. Herzfeld and R. G. Griffin, *J. Phys. Chem. Lett.*, 2012, **3**, 2030–2034.

18 A. Lesage, M. Lelli, D. Gajan, M. A. Caporini, V. Vitzthum, P. Miéville, J. Alauzun, A. Roussey, C. Thieuleux, A. Mehdi, G. Bodenhausen, C. Copéret and L. Emsley, *J. Am. Chem. Soc.*, 2010, **132**, 15459–15461.

19 F. Blanc, L. Sperrin, D. A. Jefferson, S. Pawsey, M. Rosay and C. P. Grey, *J. Am. Chem. Soc.*, 2013, **135**, 2975–2978.

20 M. Lelli, D. Gajan, A. Lesage, M. A. Caporini, V. Vitzthum, P. Miéville, F. Héroguel, F. Rascón, A. Roussey, C. Thieuleux, M. Boualleg, L. Veyre, G. Bodenhausen, C. Copéret and L. Emsley, *J. Am. Chem. Soc.*, 2011, **133**, 2104–2107.

21 A. S. Lilly Thankamony, O. Lafon, X. Lu, F. Aussenac, M. Rosay, J. Trébosc, H. Vezin and J.-P. Amoureux, *Appl. Magn. Reson.*, 2012, **43**, 237–250.

22 F. A. Perras, T. Kobayashi and M. Pruski, *J. Am. Chem. Soc.*, 2015, **137**, 8336–8339.

23 P. S. Wheatley, P. Chlubná-Eliášová, H. Greer, W. Zhou, V. R. Seymour, D. M. Dawson, S. E. Ashbrook, A. B. Pinar, L. B. McCusker, M. Opanasenko, J. Čejka and R. E. Morris, *Angew. Chem. Int. Ed.*, 2014, **53**, 13210–13214.

24 P. A. Wright, in *Microporous Framework Solids*, Royal Society of Chemistry Publishing, Cambridge, 2007, Chapter 7.

25 P. Atkins and J. De Paula, in *Atkins' Physical Chemistry*, Oxford University Press, 2010, Chapter 23.

26 S. Brunauer, L. S. Deming, W. E. Deming and E. Teller, *J. Am. Chem. Soc.*, 1940, **62**, 1723–1732.

27 R. F. Egerton, in *Physical Principles of Electron Microscopy*, Springer US, Boston, MA, 2005, Chapter 5.

28 P. Echlin, in *Handbook of Sample Preparation for Scanning Electron Microscopy and X-Ray Microanalysis*, Springer US, Boston, MA, 2009, Chapter 8.

29 P. Echlin, in *Handbook of Sample Preparation for Scanning Electron Microscopy and X-Ray Microanalysis*, Springer US, Boston, MA, 2009, Chapter 11.

30 R. F. Egerton, in *Physical Principles of Electron Microscopy*, Springer US, Boston, MA, 2005, Chapter 6.

31 P. S. Wheatley, A. R. Butler, M. S. Crane, S. Fox, B. Xiao, A. G. Rossi, I. L. Megson and R. E. Morris, *J. Am. Chem. Soc.*, 2006, **128**, 502–509.

32 M. Mowbray, X. Tan, P. S. Wheatley, R. E. Morris and R. B. Weller, *J. Invest. Dermatol.*, 2008, **128**, 352–360.

33 J. P. S. Mowat, S. R. Miller, J. M. Griffin, V. R. Seymour, S. E. Ashbrook, S. P. Thompson, D. Fairen-Jimenez, A.-M. Banu, T. Düren and P. A. Wright, *Inorg. Chem.*, 2011, **50**, 10844–10858.

34 T. Loiseau, C. Serre, C. Huguenard, G. Fink, F. Taulelle, M. Henry, T. Bataille and G. Férey, *Chem. Eur. J.*, 2004, **10**, 1373–1382.

35 G. Ortiz, G. Chaplais, J.-L. Paillaud, H. Nouali, J. Patarin, J. Raya and C. Marichal, *J. Phys. Chem. C*, 2014, **118**, 22021–22029.

36 J. P. S. Mowat, S. R. Miller, A. M. Z. Slawin, V. R. Seymour, S. E. Ashbrook and P. A. Wright, *Micropor. Mesopor. Mater.*, 2011, **142**, 322–333.

37 J. P. S. Mowat, V. R. Seymour, J. M. Griffin, S. P. Thompson, A. M. Z. Slawin, D. Fairen-Jimenez, T. Düren, S. E. Ashbrook and P. A. Wright, *Dalton Trans.*, 2012, **41**, 3937–3941.

38 P. He, J. Xu, V. V. Terskikh, A. Sutrisno, H.-Y. Nie and Y. Huang, *J. Phys. Chem. C*, 2013, **117**, 16953–16960.

39 A. J. Rossini, A. Zagdoun, M. Lelli, J. Canivet, S. Aguado, O. Ouari, P. Tordo, M. Rosay, W. E. Maas, C. Copéret, D. Farrusseng, L. Emsley and A. Lesage, *Angew. Chem. Int. Ed.*, 2011, **51**, 123–127.

40 F. Pourpoint, A. S. L. Thankamony, C. Volkringer, T. Loiseau, J. Trébosc, F. Aussenac, D. Carnevale, G. Bodenhausen, H. Vezin, O. Lafon and J.-P. Amoureux, *Chem. Commun.*, 2014, **50**, 933–935.

41 N. T. Kita, J. M. Huberty, R. Kozdon, B. L. Beard and J. W. Valley, *Surf. Interface Anal.*, 2010, **43**, 427–431.

42 T. R. Ireland, in *Handbook of Stable Isotope Analytical Techniques*, Ed. P. A. de Groot, Elsevier, 2004, Chapter 30.

43 G. Margaritondo, in *Elements of Synchrotron Light for Biology, Chemistry and Medical Research*, Oxford University Press, 2002, Chapter 1.

44 A. R. West, in *Solid State Chemistry and Its Applications*, Wiley, 2014, Chapter 5.

45 P. Atkins and J. De Paula, in *Atkins' Physical Chemistry*, Oxford University Press, 2010, Chapter 19.

46 M. T. Weller, in *Inorganic Materials Chemistry*, Oxford University Press, 2001, Chapter 1.

47 A. K. Cheetham and P. Day, Eds., in *Solid State Chemistry Techniques*, Clarendon Press Oxford, 1995, Chapter 2.

48 V. K. Pecharsky and P. Y. Zavalij, in *Fundamentals of Powder Diffraction and Structural Characterisation of Materials*, Springer, 2005, Chapter 3.

49 H. M. Rietveld, *Acta Cryst.,* 1967, **22**, 151–152.

50 G. S. Pawley, *J. Appl. Crystallogr.*, 1981, **14**, 357–361.

51 B. H. Toby, *Powder Diffr.*, 2012, **21**, 67–70.

52 V. K. Pecharsky and P. Y. Zavalij, in *Fundamentals of Powder Diffraction and Structural Characterisation of Materials*, Springer, 2005, Chapters 6-7.

53 R. R. Ernst and W. A. Anderson, *Rev. Sci. Instrum.*, 1966, **37**, 93–102.

54 D. C. Apperley, R. K. Harris and P. Hodgkinson, in *Solid State NMR Basic Principles & Practice*, Momentum Press, 2012, Chapters 1-2.

55 P. J. Hore, in *Nuclear Magnetic Resonance*, Oxford Science Publications, 1995, Chapter 6.

56 J. Keeler, in *Understanding NMR Spectroscopy,* Wiley, 2005, Chapters 5, 9, 12.

57 P. J. Hore, in *Nuclear Magnetic Resonance*, Oxford Science Publications, 1995, Chapter 2.

58 M. J. Duer, in *Introduction to Solid-State NMR Spectroscopy*, Blackwell Publishing, 2004, Chapter 1.

59 U. Haeberlen, in *Advances in Magnetic Resonance*, Academic Press, New York, 1976.

60 M. J. Duer, in *Introduction to Solid-State NMR Spectroscopy*, Blackwell Publishing, 2004, Chapter 4.

61 G. E. Pake, *J. Chem. Phys.*, 1948, **16**, 327–336.

62 S. E. Ashbrook and S. Wimperis, in *Quadrupolar Coupling: An Introduction and Crystallographic Aspects*, eMagRes., 2009.

63 A. W. Overhauser, *Phys. Rev.*, 1953, **92**, 411–415.

64 T. R. Carver and C. P. Slichter, *Phys. Rev.*, 1953, **92**, 212–213.

65 H. Lock, G. E. Maciel and C. E. Johnson, *J. Mater. Res.*, 2011, **7**, 2791–2797.

66 L. R. Becerra, G. J. Gerfen, R. J. Temkin, D. J. Singel and R. G. Griffin, *Phys. Rev. Lett.*, 1993, **71**, 3561–3564.

67 D. A. Hall, D. C. Maus, G. J. Gerfen, S. J. Inati, L. R. Becerra, F. W. Dahlquist and R. G. Griffin, *Science*, 1997, **276**, 930–932.

68 C. Song, K.-N. Hu, C.-G. Joo, T. M. Swager and R. G. Griffin, *J. Am. Chem. Soc.*, 2006, **128**, 11385–11390.

69 J. Haber, J. H. Block and B. Delmon, *Pure Appl. Chem.*, 2004, **67**, 1–50.

70 Q. Z. Ni, E. Daviso, T. V. Can, E. Markhasin, S. K. Jawla, T. M. Swager, R. J. Temkin, J. Herzfeld and R. G. Griffin, *Acc. Chem. Res.*, 2013, **46**, 1933–1941.

71 S. A. Walker, D. T. Edwards, T. A. Siaw, B. D. Armstrong and S. Han, *Phys. Chem. Chem. Phys.*, 2013, **15**, 15106–15120.

72 T. Maly, G. T. Debelouchina, V. S. Bajaj, K.-N. Hu, C.-G. Joo, M. L. Mak Jurkauskas, J. R. Sirigiri, P. C. A. van der Wel, J. Herzfeld, R. J. Temkin and R. G. Griffin, *J. Chem. Phys.*, 2008, **128**, 052211-052249.

73 T. Maly, A.-F. Miller and R. G. Griffin, *ChemPhysChem*, 2010, **11**, 999–1001.

74 A. J. Rossini, A. Zagdoun, M. Lelli, D. Gajan, F. Rascón, M. Rosay, W. E. Maas, C. Copéret, A. Lesage and L. Emsley, *Chem. Sci.*, 2012, **3**, 108–115.

75 A. J. Rossini, A. Zagdoun, M. Lelli, A. Lesage, C. Copéret and L. Emsley, *Acc. Chem. Res.*, 2013, **46**, 1942–1951.

76 A. B. Barnes, G. De Paëpe, P. C. A. van der Wel, K.-N. Hu, C.-G. Joo, V. S. Bajaj, M. L. Mak-Jurkauskas, J. R. Sirigiri, J. Herzfeld, R. J. Temkin and R. G. Griffin, *Appl. Magn. Reson.*, 2008, **34**, 237–263.

77 D. Massiot, F. Fayon, M. Capron, I. King, S. Le Calvé, B. Alonso, J.-O. Durand, B. Bujoli, Z. Gan and G. Hoatson, *Magn. Reson. Chem.*, 2002, **40**, 70–76.

78 E. R. Andrew, A. Bradbury and R. G. Eades, *Nature*, 1958, **182**, 1659.

79 E. R. Andrew, A. Bradbury and R. G. Eades, *Nature*, 1959, **183**, 1802–1803.

80 I. J. Lowe, *Phys. Rev. Lett.*, 1959, **2**, 285–287.

81 A. Samoson and A. Pines, *Rev. Sci. Instrum.*, 1989, **60**, 3239–3241.

82 A. Samoson and J. Tegenfeldt, *J. Magn. Reson., Ser. A*, 1994, **110**, 238–244.

83 E. L. Hahn, *Phys. Rev.*, 1950, **80**, 580–594.

84 D. C. Apperley, R. K. Harris and P. Hodgkinson, in *Solid State NMR Basic Principles & Practice*, Momentum Press, 2012, Chapter 4.

85 A. E. Bennett, C. M. Rienstra, M. Auger, K. V. Lakshmi and R. G. Griffin, *J. Chem. Phys.*, 1995, **103**, 6951–6958.

86 B. M. Fung, A. K. Khitrin and K. Ermolaev, *J. Magn. Reson.*, 2000, **142**, 97–101.

87 S. R. Hartmann and E. L. Hahn, *Phys. Rev.*, 1962, **128**, 2042–2053.

88 M. J. Duer, in *Introduction to Solid-State NMR Spectroscopy*, Blackwell Publishing, 2004, Chapter 2.

89 D. C. Apperley, R. K. Harris and P. Hodgkinson, in *Solid State NMR Basic Principles & Practice*, Momentum Press, 2012, Chapter 7.

90 E. O. Stejskal, J. Schaefer and J. S. Waugh, *J. Magn. Reson. (1969)*, 1977, **28**, 105–112.

91 B. H. Meier, *Chem. Phys. Lett.*, 1992, **188**, 201–207.

92 G. Metz, X. L. Wu and S. O. Smith, *J. Magn. Reson., Ser. A*, 1994, **110**, 219–227.

93 S. E. Ashbrook and S. Wimperis, *Mol. Phys.*, 2000, **98**, 1–26.

94 J. P. Amoureux and M. Pruski, *Mol. Phys.*, 2002, **100**, 1595–1613.

95 A.J. Vega, *J. Magn. Reson*., 1992, **96**, 50–68.

96 S. E. Ashbrook and S. Wimperis, *J. Chem. Phys.*, 2009, **131**, 194509–194523.

97 D. C. Apperley, R. K. Harris and P. Hodgkinson, in *Solid State NMR Basic Principles & Practice*, Momentum Press, 2012, Chapter 5.

98 B. Hu, J. Trebosc and J. P. Amoureux, *J. Magn. Reson.*, 2008, **192**, 112–122.

99 A. Brinkmann and A. P. M. Kentgens, *J. Am. Chem. Soc.*, 2006, **128**, 14758–14759.

100 J. Keeler, in *Understanding NMR Spectroscopy,* Wiley, 2005, Chapter 8.

101 L. Frydman and J. S. Harwood, *J. Am. Chem. Soc.*, 1995, **117**, 5367–5368.

102 S. P. Brown and S. Wimperis, *J. Magn. Reson.*, 1997, **128**, 42–61.

103 C. Fernandez and J. P. Amoureux, *Solid State Nucl. Magn. Reson.*, 1996, **5**, 315–321.

104 J. Rocha, C. M. Morais and C. Fernandez, in *New Techniques in Solid-State NMR*, Springer Berlin Heidelberg, Berlin, Heidelberg, 2004, vol. 246, pp. 141–194.

105 J.-P. Amoureux, C. Fernandez and S. Steuernagel, *J. Magn. Reson., Ser. A*, 1996, **123**, 116–118.

106 D. Massiot, B. Touzo, D. Trumeau, J. P. Coutures, J. Virlet, P. Florian and P. J. Grandinetti, *Solid State Nucl. Magn. Reson.*, 1996, **6**, 73–83.

107 S. H. Wang, Z. Xu, J. H. Baltisberger, L. M. Bull, J. F. Stebbins and A. Pines, *Solid State Nucl. Magn. Reson.*, 1997, **8**, 1–16.

108 K. J. Pike, R. P. Malde, S. E. Ashbrook, J. McManus and S. Wimperis, *Solid State Nucl. Magn. Reson.*, 2000, **16**, 203–215.

109 Z. Gan and H.-T. Kwak, *J. Magn. Reson.*, 2004, **168**, 346–351.

110 H. Colaux, D. M. Dawson and S. E. Ashbrook, *J. Phys. Chem. A*, 2014, **118**, 6018–6025.

111 A. P. M. Kentgens and R. Verhagen, *Chem. Phys. Lett.*, 1999, **300**, 435–443.

112 D. Iuga, H. Schäfer, R. Verhagen and A. P. M. Kentgens, *J. Magn. Reson.*, 2000, **147**, 192–209.

113 S. E. Ashbrook, A. J. Berry, D. J. Frost, A. Gregorovic, C. J. Pickard, J. E. Readman and S. Wimperis, *J. Am. Chem. Soc.*, 2007, **129**, 13213–13224.

114 S. E. Ashbrook and S. Wimperis, *Prog. Nucl. Magn. Reson. Spectrosc.*, 2004, **45**, 53–108.

Results and discussion

3 Isotopic enrichment of UTL-derived zeolites

The main focus of this chapter is the description of the synthetic procedures and isotopic enrichment pathways used for the zeolites investigated. In order to obtain consistent experimental results, all synthetic and ^{17}O-enrichment studies reported, apart from an initial test sample, have been carried out starting from the same Ge-UTL batch. For the final hydrolysed and calcined zeolites, PXRD, N_2 adsorption and EDX have been employed as characterisation techniques in addition to, and complementary to, solid-state NMR.

3.1 Synthesis of Ge-UTL and ^{29}Si-enriched Ge-UTL

Usually, the first step towards the synthesis of a zeolitic framework is the preparation of the structure-directing agent (SDA), whose role has already been discussed, see Section 1.1.1. For Ge-UTL synthesis, (6*R*, 10*S*)-6,10-dimethyl-5-azoniaspiro[4,5]decane, shown in Figure 3.1, was used as the SDA and synthesised by optimising a literature procedure.[1-2]

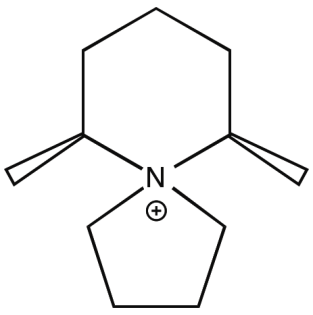

Figure 3.1 *Structure of the (6R, 10S)-6,10-dimethyl-5-azoniaspiro[4,5]decane cation used as the SDA in the Ge-UTL synthesis.*

The synthesis of (6*R*, 10*S*)-6,10-dimethyl-5-azoniaspiro[4,5]decane in its bromide and hydroxide forms is summarised in Table 3.1 and schematically shown in Figure 3.2.

Chemical	Quantity / mmol	Amount
NaOH (pellets)	284	11.36 g
1,4-dibromobutane	284	61.32 g
(2*R*,6*S*)-2,6-dimethylpiperidine	284	32.14 g
Chloroform		4×(100 mL) + 2×(50 mL)
Diethyl ether		Precipitating and washing agent
Ambersep 900-OH		7×(45 g)
HCl		Titration (1 M)
Distilled water		~400 mL + washing

Table 3.1 *Synthesis table for the SDA of Ge-UTL.*

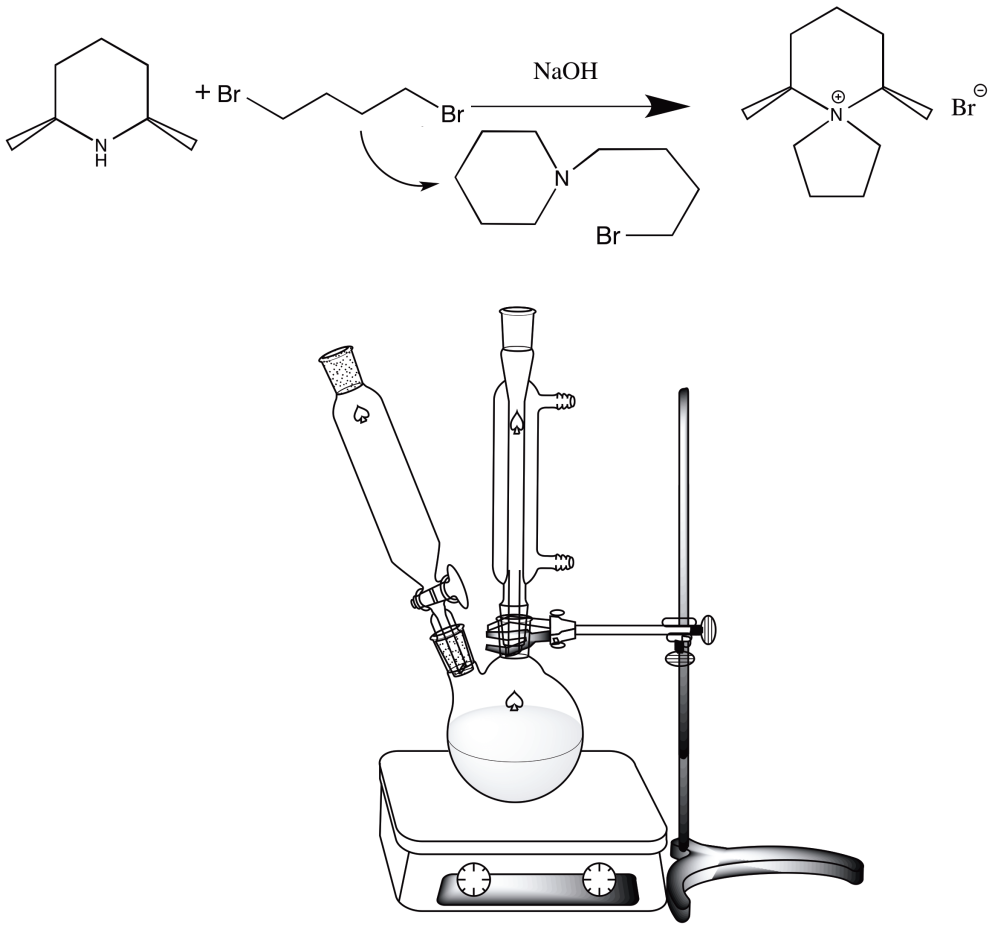

Figure 3.2 *Schematic representation of the synthetic reaction to prepare the SDA in its bromide form and related experimental apparatus.*

The synthetic procedure used can be outlined as follows:

- NaOH pellets were dissolved in 280 mL of deionised water and then 1,4-dibromobutane was added to the solution, which was heated up to reflux temperature (105 °C). At the end of this first stage, the reaction mixture was biphasic with 1,4-dibromobutane forming oily drops in the NaOH solution.
- (2*R*,6*S*)-2,6-dimethylpiperidine was added drop-wise over 20-30 min under reflux and fast stirring. The reaction mixture was left for 24 h in refluxing conditions and subsequently left to cool to room temperature, resulting in a single orange phase.
- A freshly prepared 50% (w/v) iced NaOH solution was added slowly to the reaction mixture at 0 °C and approximately 20 g of NaOH pellets were added to promote the formation of the oily layer containing the reaction product. After this last addition, 30 min of stirring were needed.
- The organic oily phase was extracted with $CHCl_3$, dried with $MgSO_4$, filtered and concentrated by rotoevaporation.
- The precipitating agent, diethylether, was then added and the resulting solid was filtered, washed with diethylether and recovered as a white powder. Yield ≈ 70%.

The identity of the synthesised bromide salt was confirmed by a solution-state ^1H NMR spectrum recorded in $CDCl_3$, shown in Figure 3.3, and assigned as follows: δ 1.4 ppm (d, 6H) corresponds to the two methyl groups; δ 1.6-2 ppm (m, 6H) corresponds to the three $–CH_2$ groups on the six-membered ring; δ 2.15 ppm (m, 4H) corresponds to the $–CH_2$ groups of the five-membered ring not directly bonded to the nitrogen atom; δ 3.35 ppm (t, 2H) and δ 4.1 ppm (t, 2H) correspond to the two $–CH_2$ groups of the five-membered ring directly bonded to the heteroatom; δ 4.4 ppm (m, 2H) corresponds to the –CH groups directly bonded to the heteroatom on the six-membered ring.

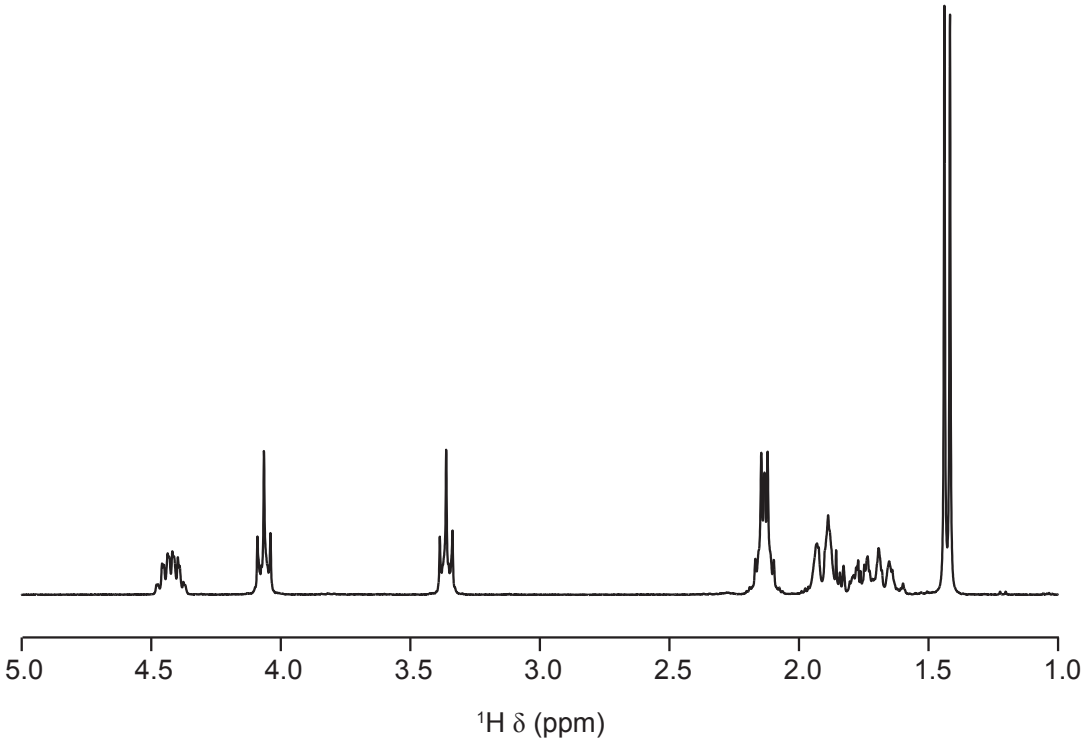

Figure 3.3 *^{1}H solution-state NMR spectrum recorded at 7.05 T in $CDCl_3$ of the as-synthesised SDA bromide salt.*

According to the reported synthesis[2] of Ge-UTL, the synthesised bromide salt was then ion-exchanged with Ambersep 900-OH resin. Typically, 45 g of (6*R*, 10*S*)-6,10-dimethyl-5-azoniaspiro[4,5]decane bromide were dissolved in 100 mL of deionised water to which 45 g of Ambersep 900-OH resin were added. After 24 h of stirring, the resin was filtered and washed. This same procedure was repeated 7 times in total so that a 0.55 M solution of (6*R*, 10*S*)-6,10-dimethyl-5-azoniaspiro[4,5]decane hydroxide was obtained.

A gel with a molar composition of 1 SiO_2: 0.5 GeO_2: 0.5 SDA, as summarised in Table 3.2, was prepared by dissolving germanium dioxide in 150 mL of a 0.55 M (6*R*, 10*S*)-6,10-dimethyl-5-azoniaspiro[4,5]decane hydroxide solution. Silicon dioxide was subsequently added in small portions into the solution and the resulting mixture was stirred at room temperature for 30 min.

	SiO_2 (Cab-o-sil)	GeO_2 (99.999 % Acros)	SDA
Quantity / mmol	178.1	88.6	81.8
Molar ratio	1	0.5	0.5
Amount	10.7 g	9.3 g	150 mL of 0.55 M sol.

Table 3.2 *Synthesis table for Ge-UTL.*

The gel was transferred into a 300 mL Teflon-lined Parr® autoclave, as schematically shown in Figure 3.4, and heated at 175 °C for 7 days in static conditions. The solid was recovered by filtration, washed with copious amounts of distilled water, air dried overnight (15.5 g) and characterised by PXRD, as shown in Figure 3.5.

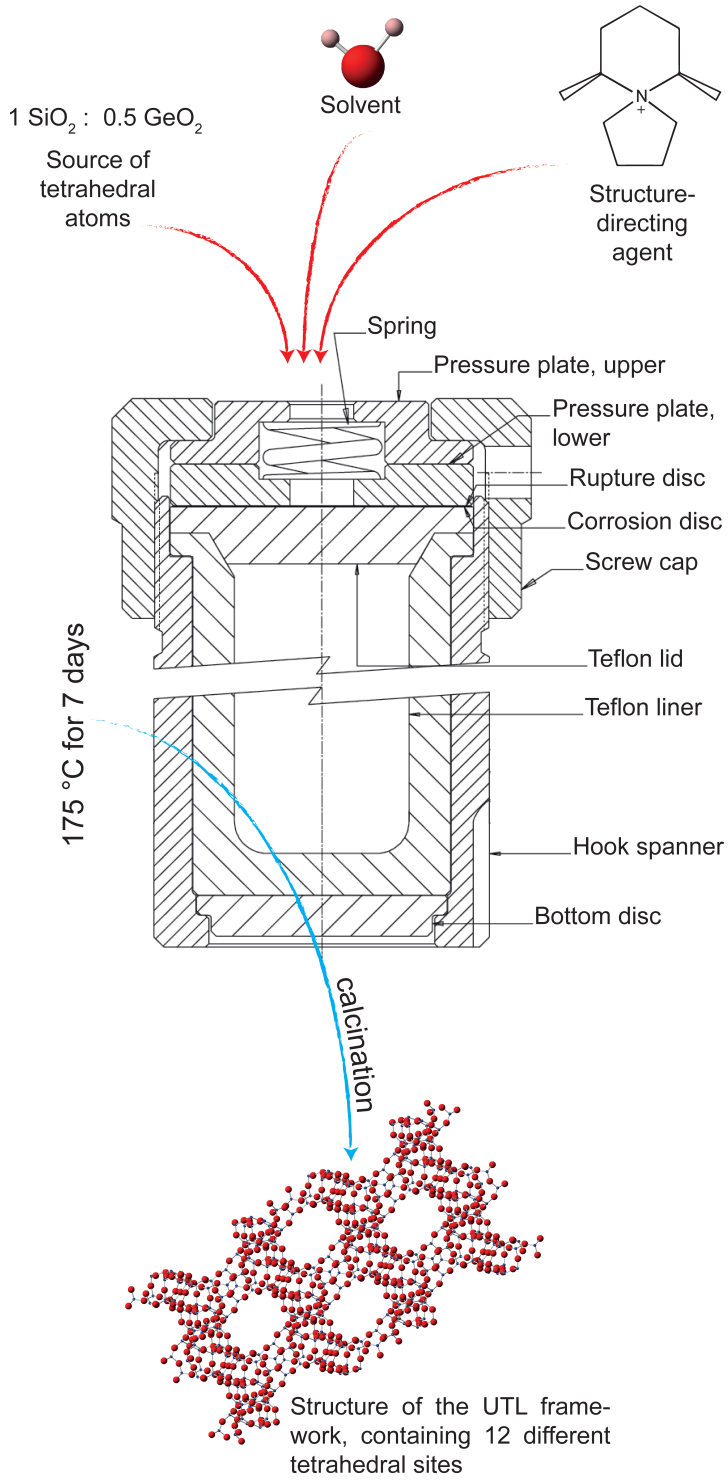

Figure 3.4 *Schematic representation of Ge-UTL synthetic reaction. The autoclave sketch has been adapted from Parr® 4744 and 4749 general purpose acid digestion bomb instruction manual.*

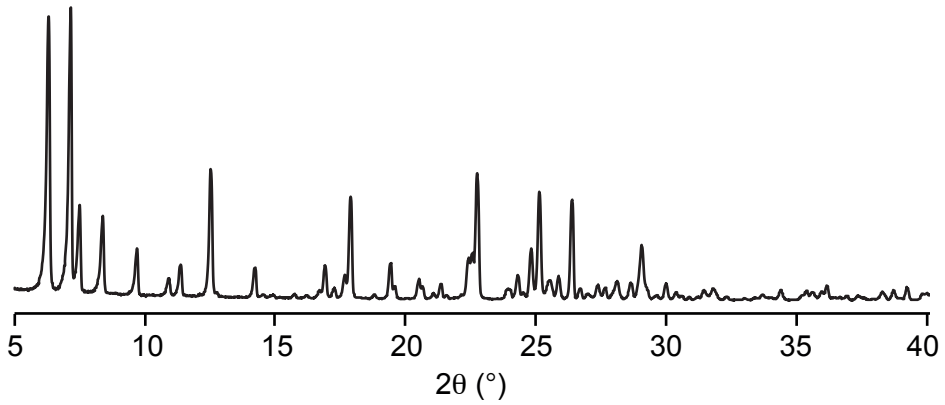

Figure 3.5 *PXRD pattern of as-made Ge-UTL.*

In order to remove the SDA, calcination has to be performed on the as-synthesised zeolite. Therefore, the Ge-UTL zeolite was heated up to 575 °C at a rate of 1 °C/min, held at this constant temperature for 6 h and cooled to 25 °C at a rate of 2 °C/min under an atmosphere of air. The ^{29}Si MAS NMR spectrum of the calcined zeolite in Figure 3.6 clearly shows the presence of an ordered material (with multiple Q^4 sites, as described in Chapter 4), while its PXRD pattern proves its phase purity, as shown in Figure 3.7.[3] The Si/Ge ratio of the material was determined to be 4.4 ± 0.3 by EDX.

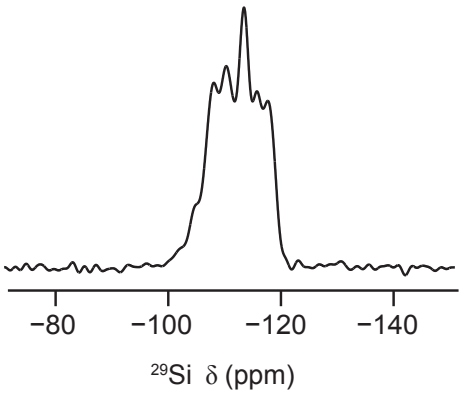

Figure 3.6 *^{29}Si (9.4 T, 10 kHz) MAS NMR spectrum of calcined Ge-UTL. For this spectrum 432 transients were averaged with a recycle interval of 120 s.*

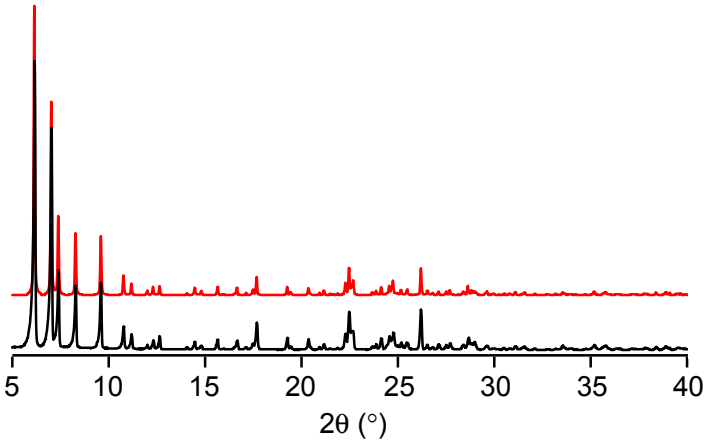

Figure 3.7 *PXRD patterns of calcined Ge-UTL (black) and a pattern simulated for the UTL framework from IZA database (red).*[3]

The ^{29}Si-enriched Ge-UTL was synthesised within the group following a similar procedure, but starting from a different silicon source, tetraethoxysilane (TEOS), $Si(OEt)_4$, a part of which, as summarised in Table 3.3, was 99% ^{29}Si-enriched (CortecNect).

	$Si(OEt)_4$ (TEOS) ~18% ^{29}Si-enriched	GeO_2	SDA
Quantity / mmol	1.6 (99% ^{29}Si-enriched) + 10.1 (nat. ab.)	5.8	5.8
Molar ratio	1	0.5	0.5
Amount	0.333 g + 2.094 g	0.609 g	10 mL of 0.58 M sol.

Table 3.3 *Synthesis table for ^{29}Si-enriched Ge-UTL.*

A gel with a molar composition of 1 SiO_2: 0.5 GeO_2: 0.5 SDA, as summarised in Table 3.3, was prepared by dissolving germanium dioxide in 10 mL of a 0.58 M (6*R*, 10*S*)-6,10-dimethyl-5-azoniaspiro[4,5]decane hydroxide solution. TEOS, with an overall ^{29}Si-enrichment level of approximately 18%, was subsequently added and the resulting reaction mixture was stirred for 2 h to remove EtOH. This gel was transferred into a 23 mL Teflon-lined Parr® autoclave and heated at 175 °C for 14 days. The solid was recovered by filtration, washed with copious amounts of distilled

water and air dried overnight. The PXRD of the as-made zeolite is shown in Figure 3.8 and can be compared to Figure 3.5. In order to remove the SDA, calcination of the as-synthesised zeolite was performed, as previously described. The corresponding NMR spectrum of the ^{29}Si-enriched starting Ge-UTL sample is shown in Chapter 4.

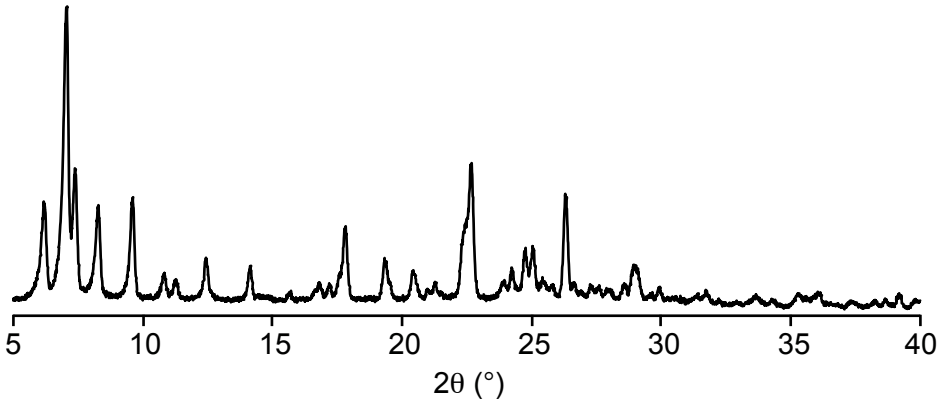

Figure 3.8 *Capillary PXRD pattern of as-made ^{29}Si-enriched Ge-UTL.*

3.2 Incorporation of Al in Ge-UTL

In view of possible catalytic applications of UTL, the synthetic conditions for the incorporation of heteroatoms, such as B, Al, Ga, In and Fe, have been previously reported[4] with the aim of introducing acid sites in the germanosilicate framework. In these syntheses, the nature of the SDA, the pH of the reaction gel and synthesis time are of crucial importance to determine the phase selectivity of the reaction. In particular, when Al is incorporated in the germanosilicate reaction mixture, a narrow pH window (11.3-12.0) for the formation of the UTL phase and longer reaction times are observed. For higher values of pH the formation of the STF phase occurs, whereas with lower pH values an amorphous material is formed.

Attempts to incorporate Al into the Ge-UTL structure by adding aluminium isopropoxide, $Al(OCH(CH_3)_2)_3$, as the Al source, according to the reported[4] molar compositions of the reaction mixture and using the same SDA as shown in Figure 3.1, were unsuccessful owing to the formation of the competing STF (**S**SZ-35 (**t**hirty-**f**ive))[3] phase in the final product. Even when attempting to carefully optimise

reaction conditions (such as the pH and reaction time) it was not possible to achieve a pure product. For this reason, a post-synthesis incorporation procedure (optimised within the group) was used where a solution of 1M $Al(NO_3)_3$ is mixed in an autoclave with calcined Ge-UTL in a proportion of 100 mL of 1M $Al(NO_3)_3$:1 g of calcined Ge-UTL and heated at 175 °C for 26 h. The product is subsequently filtered, washed with water and left to dry overnight. This method resulted in the incorporation of variable amounts of Al in the final zeolites (Si/Al 16-24) and loss of Ge (Si/Ge ≈ 23), on the basis of EDX measurements, with typical PXRD patterns as shown in Figure 3.9.

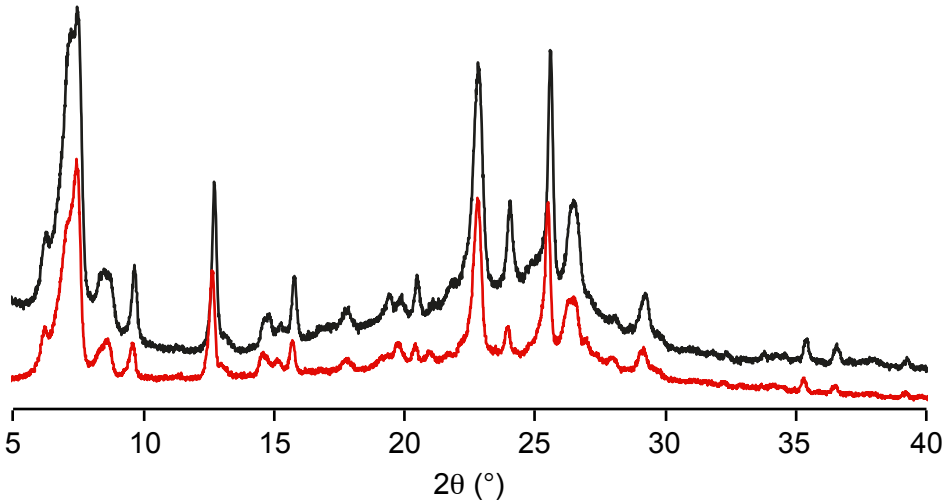

Figure 3.9 *Capillary PXRD patterns of two batches of Al-UTL obtained with the post-synthesis Al incorporation procedure described in the main text.*

The subsequent NMR and catalytic investigation of these materials is described in Section 4.4.

3.3 Optimisation of low-volume hydrolyses

With the aim of ^{17}O enrichment in mind, the implementation of low-volume syntheses in the ADOR method was considered to develop a standard synthetic procedure to be systematically applied and investigated both on enriched and unenriched samples.

The experimental details of such a protocol are summarised in Table 3.4.

Reactant	Quantity
H_2O or $H_2{}^{17}O$ (35-41%, CortecNet)	1.2 mL
12 M HCl	1.2 mL
Ge-UTL or ^{29}Si-enriched Ge-UTL	300 mg
Water used to wash the reaction product	2.4 mL

Table 3.4 *Synthesis protocol for low-volume hydrolyses.*

The hydrolyses were carried out for variable reaction times, ranging from 4 to 48 h, in a round-bottomed 10 mL flask topped with a condenser tube in refluxing conditions at 95 °C in 6 M HCl (freshly prepared from 1.2 mL of H_2O or $H_2{}^{17}O$ and 1.2 mL of 12 M HCl). The resulting hydrolysed products were filtered and washed with a small amount (2.4 mL) of deionised water to avoid any possible ^{17}O back-exchange of ^{17}O-enriched products. The Si/Ge ratio of a typical hydrolysed product was found using EDX to be 17 ± 2, confirming the loss of Ge from the framework upon hydrolysis. The resulting hydrolysed zeolites were left to dry overnight and then calcined, as previously described. For ^{17}O-enriched zeolites, calcination was carried out in an inert atmosphere to avoid any ^{17}O loss.

3.4 ^{17}O enrichment

3.4.1 Ge-UTL

The same experimental procedure has been followed, as described in Section 3.3, for three enriched hydrolysed samples: PSW 163, GPMB 7 and 8. For isotopic enrichment, the 16 h hydrolysis was repeated using 6 M HCl, prepared from 1.2 mL of 12 M HCl and 1.2 mL of $H_2{}^{17}O$.

While the low-volume syntheses and the enrichment of GPMB 7 have been consistently carried out from the same Ge-UTL batch, GPMB 8 has been synthesised from a different batch in order to allow ^{29}Si enrichment, as described in Section 3.1. Nonetheless, for both GPMB 7 and 8, the enrichment procedure has been consistently performed using 41% $H_2{}^{17}O$.

Since PSW 163 was prepared as a first test sample to evaluate the feasibility of the enrichment process, it was synthesised from a different Ge-UTL batch (used by Wheatley *et al.*[2]) and was enriched with 35% $H_2{}^{17}O$.

3.4.2 Amorphous silica

A scaled-down version of the reported synthesis[5] has been followed to obtain the ^{17}O-enriched amorphous silica used to assist with the optimisation of NMR experiments. The reaction, which stoichiometrically proceeds as in Equation 3.1, is summarised in Table 3.5 and the related experimental apparatus is schematically shown in Figure 3.10:

$$SiCl_{4(Liq.)} + 2H_2{}^{17}O_{(Liq.)} \xrightarrow[0\ ^\circ C\ Et_2O]{Ar\ Atm.} Si^{17}O_{2(Sol.)} + 4HCl_{(Gas)} \qquad (3.1)$$

Chemical	Quantity / mmol	Amount / mL
$SiCl_4$	8.7	1
$H_2{}^{17}O$ (35%)	17.4	0.313
Et_2O		12.5

Table 3.5 *Synthesis table for ^{17}O-enriched SiO_2.*

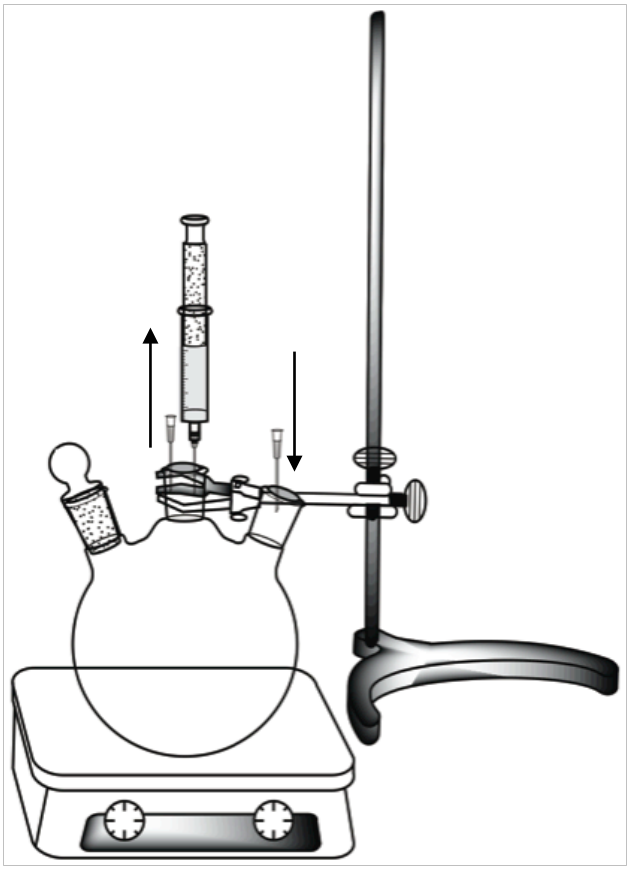

Figure 3.10 *Schematic representation of the experimental apparatus used for the synthesis of ^{17}O-enriched SiO_2.*

The experimental procedure can be briefly described as follows: under a constant argon flow, indicated by the arrows in Figure 3.10, $H_2{}^{17}O$ was slowly added through a syringe to an iced solution of $SiCl_4$ in anhydrous Et_2O under vigorous stirring and the reaction mixture almost immediately turned into a cloudy solution upon $H_2{}^{17}O$ addition. The mixture was then warmed to room temperature and left stirring under argon for 2 h. The resulting powder has been dried under vacuum at 200 °C for 16 h. Unless any isotopic scrambling with the reaction solvent occurs, the final enrichment level of SiO_2 is expected to be consistent with that of the initial ^{17}O-enriched water.

3.5 Powder X-ray diffraction characterisation

For the reported zeolitic materials, the most important aspect of this characterisation, as introduced in Section 2.1.2, is related to the determination of interlayer spacing from PXRD patterns. For such a purpose, the 2θ position of the most intense reflection (200) has been monitored in all the hydrolysed and calcined samples derived from the optimisation process of the low-volume hydrolyses, carried out as described in Section 3.3.

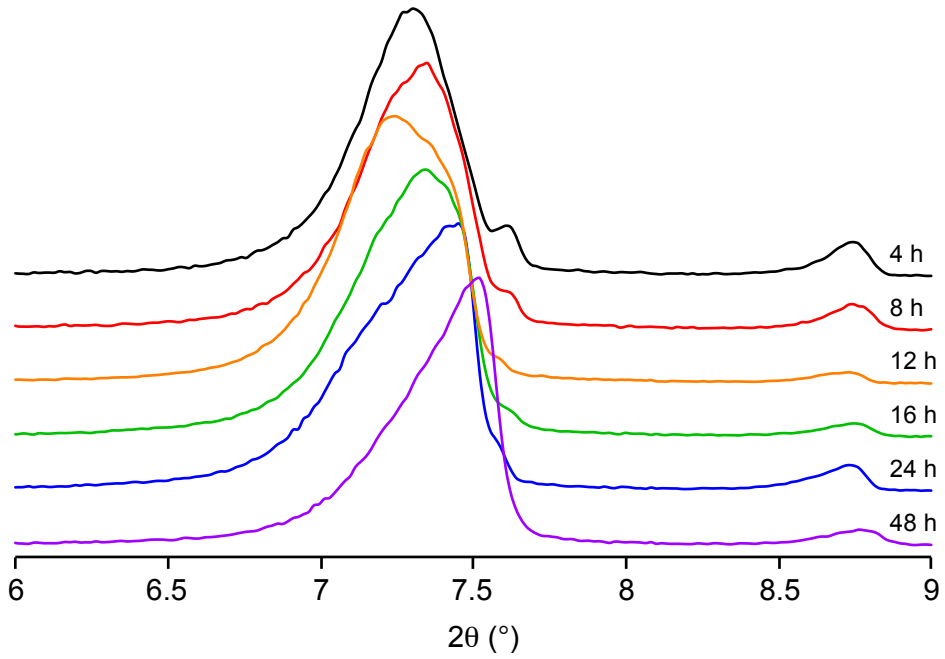

Figure 3.11 *Overlaid PXRD patterns, expanded to show the 200 reflection, of unenriched Ge-UTL hydrolysed for different reaction times.*

For the series of samples prepared using low-volume hydrolysis, the d_{200} spacings derived from the most intense reflection in the PXRD patterns for different reaction times, as shown in Figure 3.11, are listed in Table 3.6 and are characterised by an average value of 12 Å corresponding to an average 2θ of 7.3°.

For the analogous series of calcined samples, the d_{200} spacings derived from the most intense reflection in the PXRD patterns for different reaction times, as shown in Figure 3.12, are listed in Table 3.6 and are characterised by an average value of 11.8 Å corresponding to an average 2θ of 7.5°. These are typical values of the IPC-2 structure, suggesting that a different mechanism controls the ADOR process in low-

volume conditions, compared to the higher-volume conditions described in Section 1.1.2.

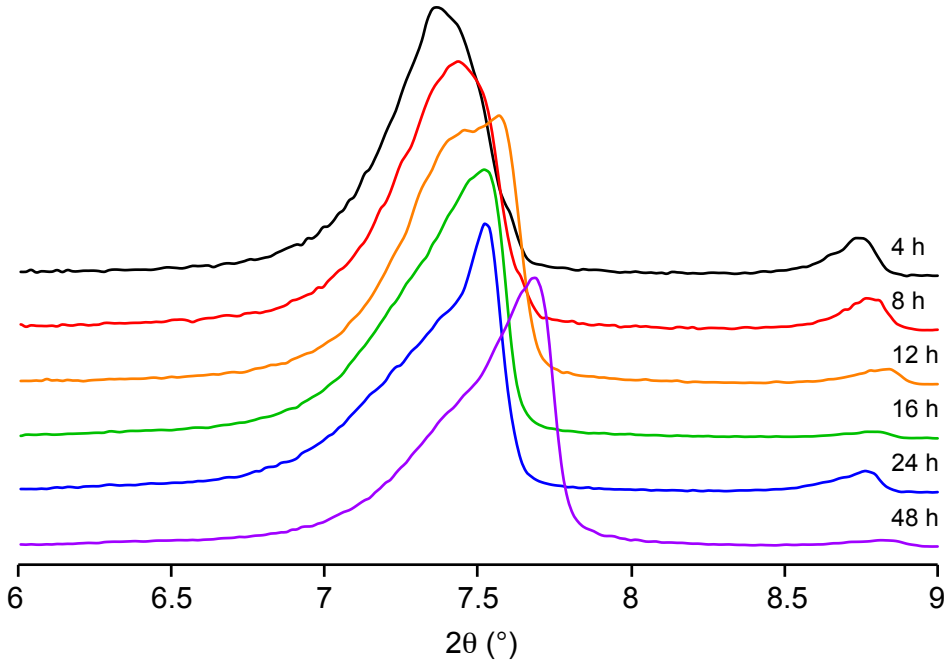

Figure 3.12 *Overlaid PXRD patterns, expanded to show the 200 reflection, of unenriched Ge-UTL hydrolysed for different reaction times and then calcined.*

Reaction time / h	d_{200} spacing / Å	
	Hydrolysed	Calcined
4	12.0	12.0
8	12.0	11.9
12	12.2	11.8
16	12.0	11.7
24	11.9	11.7
48	11.7	11.5

Table 3.6 *Values of d_{200} spacing obtained from PXRD patterns shown in Figures 3.11 and 3.12.*

The representative hydrolysed ^{17}O-enriched (GPMB 7) and ^{29}Si- and ^{17}O-enriched (GPMB 8) samples are characterised by 2θ positions of the 200 peak and corresponding d_{200} spacings of the IPC-2P structure, in agreement with unenriched hydrolysed samples: 7.4° and 11.9 Å for GPMB 7, 7.5° and 11.8 Å for GPMB 8, as shown in Figures 3.13 and 3.14.

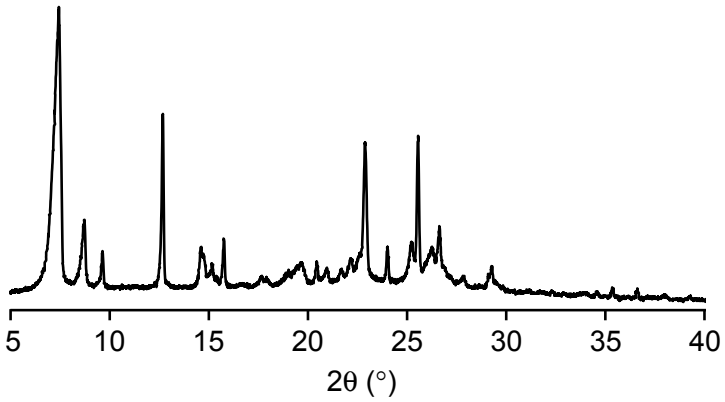

Figure 3.13 *Capillary PXRD pattern of ^{17}O-enriched Ge-UTL hydrolysed for 16 h (GPMB 7).*

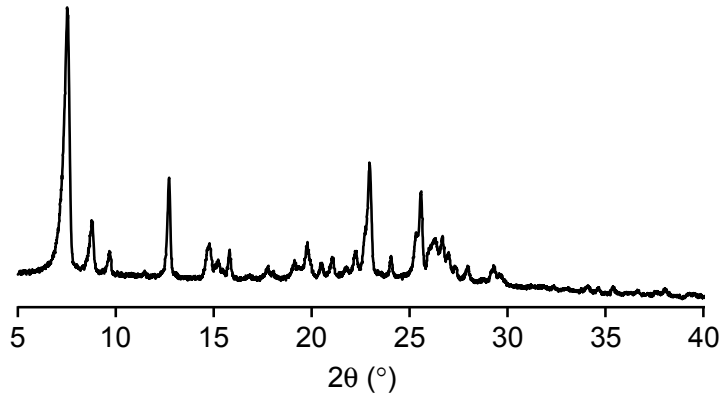

Figure 3.14 *Capillary PXRD pattern of ^{17}O- and ^{29}Si-enriched Ge-UTL hydrolysed for 16 h (GPMB 8).*

3.6 N_2 adsorption characterisation

N_2 adsorption isotherms were collected on the calcined unenriched products obtained for each reaction time tested. Such measurements yielded an average micropore volume of 0.18 ± 0.02 cm^3/g, characteristic of the IPC-2 structure.[2] A

typical adsorption isotherm is shown in Figure 3.15. The relevance of this experimental result not only resides in the confirmation of the type of structure synthesised, but also in the fact that the porosity of the final material does not seem to be affected by the low-volume synthetic conditions implemented with the aim of ^{17}O enrichment. To confirm that the small amounts of washing water used were not affecting the porosity of the sample, the 16 h hydrolysis was repeated using 40 mL of washing water. The d_{200} spacing of the resulting hydrolysed sample was 12.0 Å and the micropore volume of the corresponding calcined form was 0.17 cm^3/g, in agreement with the average obtained from samples washed with 2.4 mL of water.

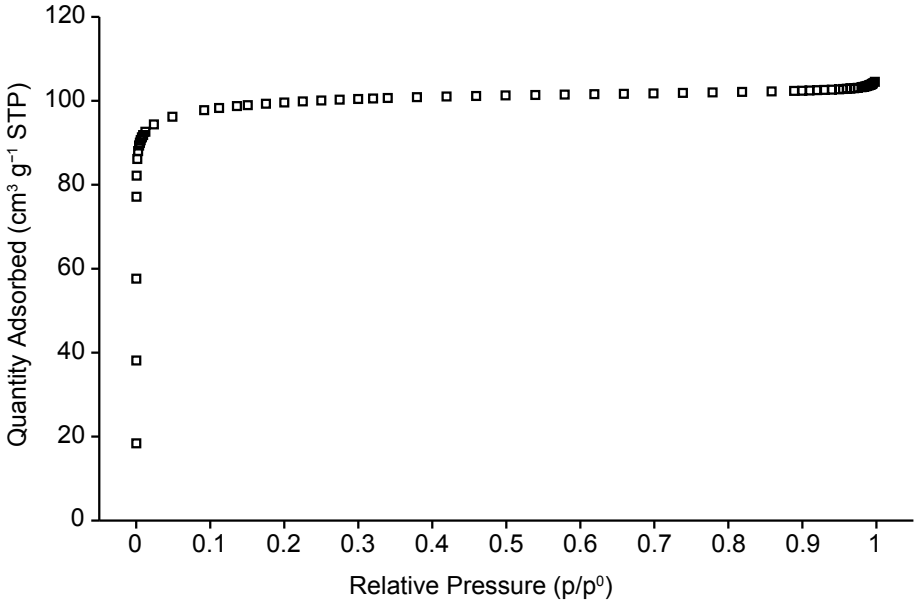

Figure 3.15 *77 K N_2 adsorption isotherm of the Ge-UTL sample hydrolysed for 4 h and subsequently calcined.*

3.7 References

1 J. L. Paillaud, B. Harbuzaru, J. Patarin and N. Bats, *Science*, 2004, **304**, 990–992.

2 P. S. Wheatley, P. Chlubná-Eliášová, H. Greer, W. Zhou, V. R. Seymour, D. M. Dawson, S. E. Ashbrook, A. B. Pinar, L. B. McCusker, M. Opanasenko, J. Čejka and R. E. Morris, *Angew. Chem. Int. Ed.*, 2014, **53**, 13210–13214.

3 Ch. Baerlocher and L. B. McCusker, Database of Zeolite Structures: http://www.iza-structure.org/databases/

4 M. V. Shamzhy, O. V. Shvets, M. V. Opanasenko, P. S. Yaremov, L. G. Sarkisyan, P. Chlubná, A. Zukal, V. R. Marthala, M. Hartmann and J. Čejka, *J. Mater. Chem.*, 2012, **22**, 15793–15803.

5 A. E. Geissberger and P. J. Bray, *J. Non-Cryst. Solids*, 1983, **54**, 121–137.

4 Solid-state NMR results for zeolitic frameworks

The experimental solid-state NMR results presented in this chapter provide insight into the hydrolytic mechanisms of the ADOR process both *ex situ* and *in situ* in different volume conditions. The interaction of $H_2{}^{17}O$ with the zeolitic structure, the resulting ^{17}O incorporation and the dynamics of the interlayer region in hydrolysed materials are also investigated. In the final section of this chapter the incorporation of Al in Ge-UTL and the resulting catalytic activity are characterised with solid-state NMR, catalysis tests and electron microscopy.

4.1 *Ex situ* ^{29}Si NMR investigation

^{29}Si NMR spectroscopy has been employed as a powerful characterisation technique to follow the rearrangement and hydrolytic processes in "ADORable" zeolites as a function of reaction time and volume. ^{29}Si NMR experiments confirmed the known mechanism of the ADOR process when large-volume conditions (i.e., 40 mL) are used, achieving a better understanding of the evolution of the local environment in the interlayer region of hydrolysed zeolites. In view of isotopic enrichment, low-volume conditions have been implemented in the ADOR process leading to the discovery of modified hydrolytic and rearrangement mechanisms in these conditions. Throughout this work, structural changes related to rearrangement and hydrolytic processes are monitored and expressed in terms of the ratio of Q^4 to Q^3 sites, derived from ^{29}Si MAS NMR spectra by processing and integration with Bruker Topspin 2.1 or DMFit 2011 software.[1] Q^4 sites are Si atoms fully coordinated with the rest of the framework, whereas Q^3 sites are characterised by the presence of one hydroxyl moiety, –OH, in the coordination environment of the central Si atom,[2] as shown in Figure 4.1. Therefore, Q^4/Q^3 ratios provide an effective and immediate structural indication of the distribution of silicon sites between the bulk of the layers and the surface of the zeolites.

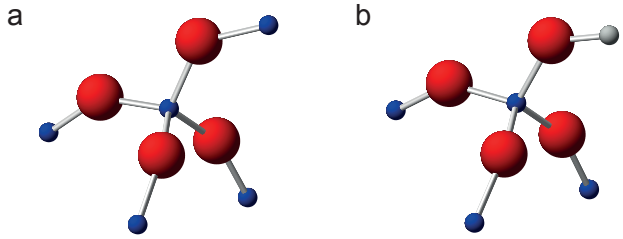

Figure 4.1 *(a) Q^4 Si site and (b) Q^3 Si site. Silicon atoms are shown in blue, oxygen atoms are shown in red and hydrogen atoms are shown in grey.*

Q^3 sites should result entirely from the hydrolytic process, unless the initial framework contains any defects. Indeed, these sites are not present in any significant amount in the ^{29}Si MAS NMR spectrum of the parent Ge-UTL structure which contains only Q^4 (**Si**$(OSi)_n(OGe)_{4-n}$) sites, as shown in Figure 4.2a. The absence of Q^3 sites in the parent material is also confirmed by the lack of ^{1}H-^{29}Si CP signal from this sample. A typical ^{29}Si MAS NMR spectrum of a hydrolysed zeolite is shown in Figure 4.2b, where both Q^4 ($Si(OSi)_4$) and Q^3 (**Si**$(OSi)_3(OH)$) sites are present, highlighting the effects of the hydrolysis on the framework and suggesting the formation of Si-OH groups. A ^{1}H-^{29}Si CP experiment confirmed this spectral assignment[3] with a selective enhancement of the peak at $\delta = -102$ ppm, as shown by the red line in Figure 4.2b. The relative intensities of the Q^4 and Q^3 species change after calcination because of the complete or partial condensation of the Si-OH sites, as shown in Figure 4.2c, depending on the defective nature of the hydrolysed precursor or the completeness of the reaction. ^{29}Si MAS NMR spectra recorded for different reaction times in both large- and small-volume conditions on hydrolysed and calcined samples shed light on the details of the hydrolysis and rearrangement mechanisms, which are otherwise difficult to detect in the average picture provided by diffraction measurements.

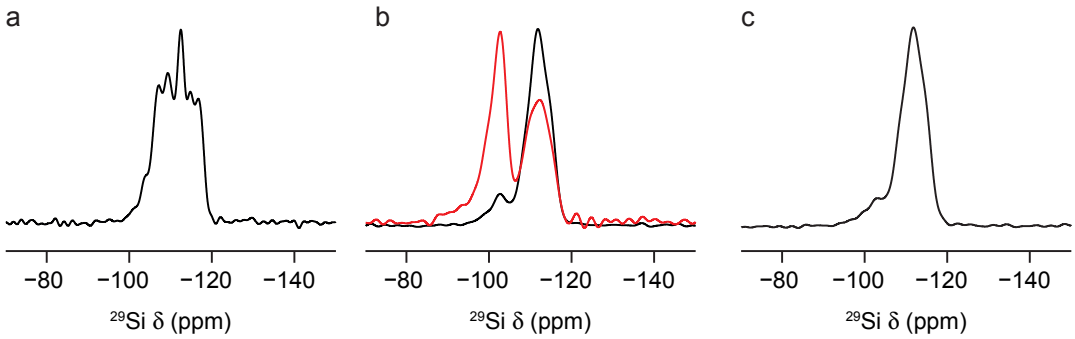

Figure 4.2 *^{29}Si (9.4 T, 10 kHz) MAS NMR spectra of (a) calcined Ge-UTL, (b) after 16 h hydrolysis in the experimental conditions described in Section 3.3 and (c) after calcination, as described in Section 3.1. In (b), the ^{1}H-^{29}Si CP (9.4 T, 10 kHz) MAS NMR spectrum is shown in red.*

4.1.1 ADOR mechanism in large-volume conditions

Samples of Ge-UTL hydrolysed in large-volume conditions and the corresponding calcined samples (with related PXRD data) were provided by Dr Yuyang Tian. Typical experimental conditions involved the hydrolysis of 250 mg of starting Ge-UTL with 40 mL of either 1.5 or 5 M HCl for variable reaction times from 10 min to 48 h at 95 °C. The resulting hydrolysed zeolites were calcined as described in Section 3.1. In these large-volume conditions, typically used in ADOR hydrolyses, the ADOR process follows the mechanism[4] shown in Figure 4.3 and already outlined in Section 1.1.2. The starting parent Ge-UTL zeolite is quickly disassembled to the layered intermediate IPC-1P, characterised by a Q^4/Q^3 ratio of 2.5. Upon calcination, this structure reassembles to IPC-4 with direct oxygen bonds between the layers. With longer reaction times, dependent on the acidity of the hydrolysing solution, this layered material organises to give the IPC-6P structure, characterised by a Q^4/Q^3 ratio of 4. Upon calcination, this structure reassembles to IPC-6, which is an intermediate structure between IPC-2 and IPC-4 with half S4R connections and half direct oxygen bonds between the layers. If the hydrolytic process continues over longer reaction times the IPC-6P structure further organises to the IPC-2P structure, characterised by a Q^4/Q^3 ratio of 7. This hydrolysed precursor yields the IPC-2 structure with S4R connections between the layers upon

reassembly. The structural evolution of these zeolitic frameworks during the ADOR process can be monitored as a function of reaction time both by ^{29}Si NMR and PXRD of the hydrolysed and calcined, reassembled, zeolites.

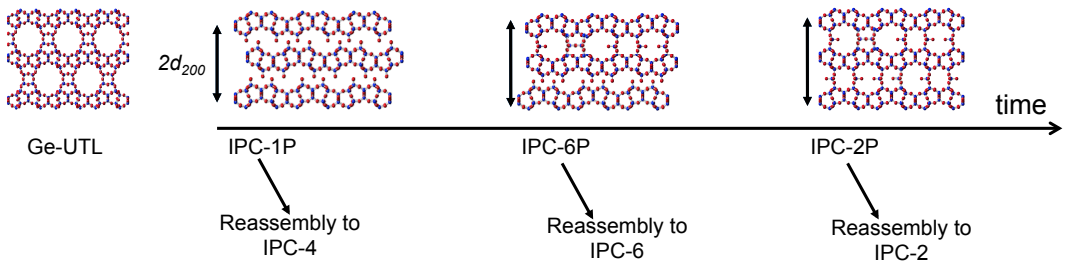

Figure 4.3 *Structural evolution of the zeolite framework during the ADOR process as a function of reaction time. Oxygen and silicon atoms are shown in red and blue, respectively. The increasing interlayer spacing, $2d_{200}$, is also highlighted.*

The changes occurring to the interlayer spacing of the "ADORable" zeolites, shown in detail in Appendix D, can be monitored by PXRD using the d-spacing corresponding to the 200 reflection, as schematically shown in Figure 4.3. In Figure 4.4, it is clearly possible to observe the increase, over reaction time, of the d_{200} spacing of calcined zeolites obtained with two acid concentrations.

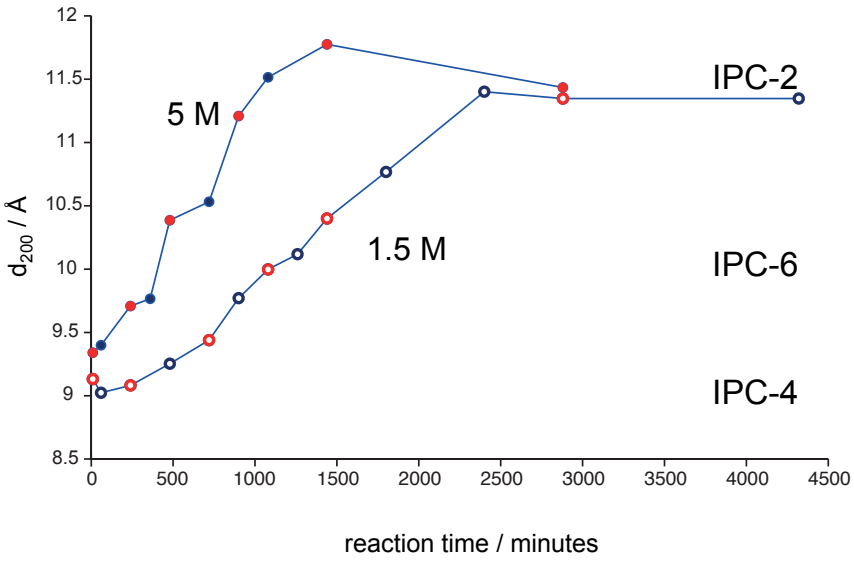

Figure 4.4 *Plot of the d_{200} spacing from PXRD patterns as a function of reaction time for the ADOR process applied to Ge-UTL in large-volume conditions with two acid concentrations (1.5 M, open circles, 5 M HCl, closed circles), showing the evolution of the d_{200} spacing of calcined samples as rearrangement proceeds. Note that red data points indicate samples that, in their hydrolysed form, are analysed by ^{29}Si NMR spectroscopy, as shown in Figure 4.5.*

Under higher acidity conditions, as shown by the closed circles in Figure 4.4, a faster rate of rearrangement is observed with a shorter reaction time needed to reach the IPC-2 structure.

Figure 4.5 shows the evolution of the local environment, as a function of reaction time, in terms of Q^4/Q^3 ratio (from ^{29}Si MAS NMR spectra) of the corresponding hydrolysed products for the red open (1.5 M HCl) and closed (5 M HCl) circles shown in Figure 4.4. The structural evolution of the hydrolysed precursors is consistent with the corresponding calcined samples, confirming a faster rate of rearrangement in higher acidity. Furthermore, it can be observed that changes in the framework local environment also occur when the average d_{200} spacing remains almost constant towards the end of the rearrangement process. A confidence interval of ± 0.4 on the data points was estimated from multiple fits.

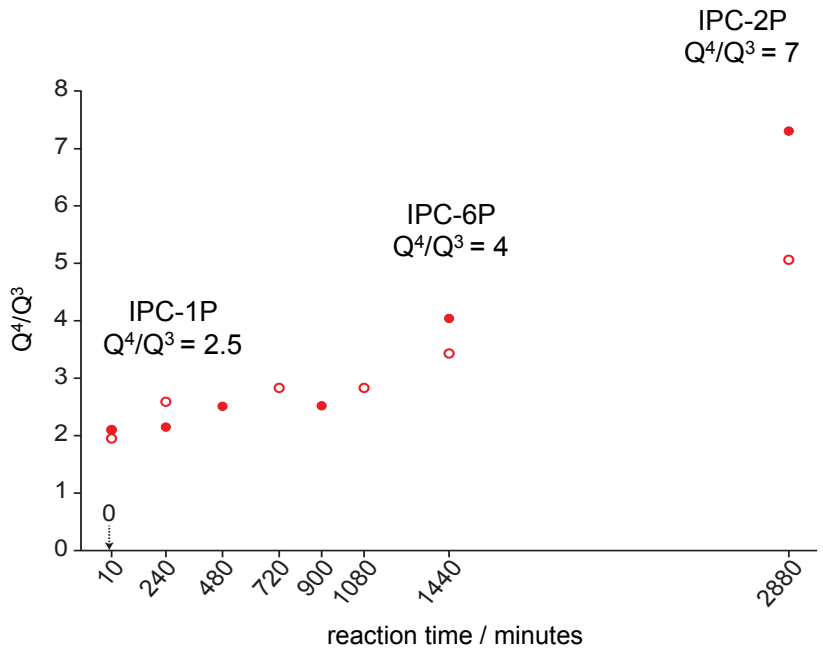

Figure 4.5 *Plot of the Q^4/Q^3 intensity ratio as a function of hydrolysis time from ^{29}Si (9.4 T, 10 kHz) MAS NMR spectra of Ge-UTL hydrolysed precursors of the calcined samples shown as red open (1.5 M HCl) and closed (5 M HCl) circles in Figure 4.4.*

4.1.2 ADOR mechanism in small-volume conditions

Hydrolysed and calcined products obtained from the implementation of the small-volume conditions described in Section 3.3 were analysed by ^{29}Si NMR spectroscopy to understand the effect of a drastic reduction in the reaction volume on the ADOR mechanism. For the different reaction times tested, PXRD patterns of both the hydrolysed and calcined products were presented in Figures 3.11 and 3.12, where it is possible to observe that the hydrolysed IPC-2P or the reassembled IPC-2 structures appear to be obtained for all reaction times. As already suggested, this structural evolution is quite unusual and hints at a different mechanism taking place when reduced amounts of hydrolytic solution are used. While the PXRD investigation proved helpful to understand the long-range order of the hydrolysed and calcined structures obtained at different reaction times, an investigation of the changes in the local environments of the bulk and interlayer region was enabled by ^{29}Si NMR experiments. Hydrolysed and calcined products corresponding to the different reaction times tested have been analysed by ^{29}Si NMR spectroscopy and the resulting spectra were fitted with DMFit to yield the Q^4/Q^3 ratio for each product, as plotted in Figure 4.6. It can be observed that in both cases an initial hydrolytic process occurs up to 12 h, with an increase in the presence of Q^3 sites and an overall decrease of the Q^4/Q^3 ratio. The fully hydrolysed structure does not reach the values of Q^4/Q^3 ratio characteristic of IPC-1P, forming instead a defective IPC-2P*. As the rearrangement process begins after 12 h of reaction time, IPC-2P* further organises in a more ideal hydrolysed precursor that is then reassembled upon calcination to a progressively less defective IPC-2. The presence of defects and some disorder in these structures is also confirmed by the asymmetric shapes of some of the diffraction peaks shown in Figures 3.11 and 3.12. Comparing Figures 4.6a and 4.6b it is possible to notice that the series of hydrolysed and calcined samples show a similar trend up to 12 h, during the disassembly stage. This stage is also much longer compared to large-volume conditions, probably because of the reduced volume and resulting high concentration of zeolite. During the rearrangement stage, calcined samples are characterised by more ideal reassembled structures as rearrangement of the hydrolysed precursor occurs. The repeatability of the results obtained from these

small-volume ADOR hydrolyses was tested by performing a second hydrolysis reaction for 16 h. This second sample was characterised in its as-made and calcined forms by Q^4/Q^3 ratios (5.7 and 5.8, respectively) and d_{200} spacings (11.9 and 11.8 Å, respectively) in good agreement with the sample obtained from the first 16 h hydrolysis reaction, as shown in Figure 4.6 and Table 3.6.

Overall, it is clear that the ADOR process is affected by changes in the volume of the hydrolysing solution with a resulting change in mechanism compared to the standard large-volume conditions. The observed differences can be mostly related to the slower hydrolytic process, given the small volume of solution, and therefore an incomplete hydrolytic reaction before rearrangement starts. A comparison between the two mechanisms is shown in Figure 4.7, highlighting the differences in the structural changes occurring in the framework in small and large hydrolysing volumes and the feasible enrichment pathways in small-volume conditions, as introduced in Sections 3.1 and 3.3-3.4.

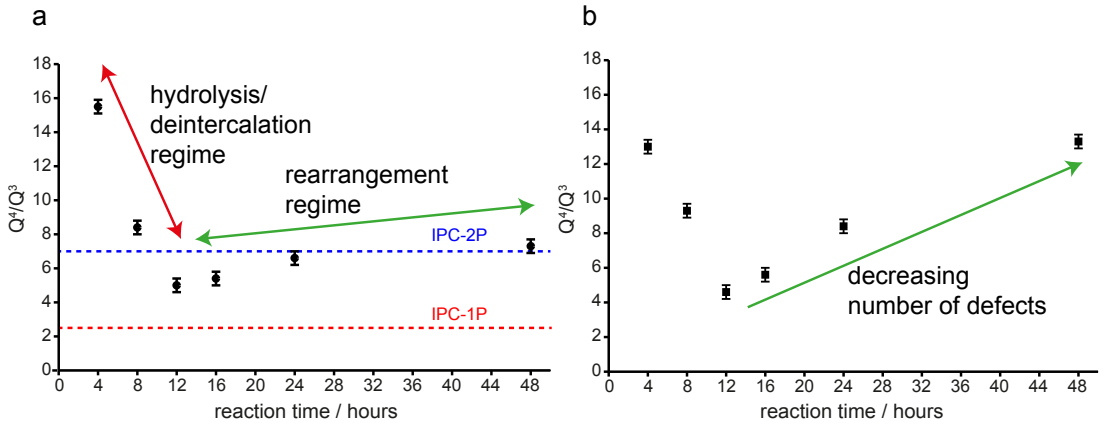

Figure 4.6 *Plot of the Q^4/Q^3 intensity ratio as a function of hydrolysis time from ^{29}Si (9.4 T, 10 kHz) MAS NMR spectra of Ge-UTL (a) hydrolysed under low-volume conditions and (b) subsequently calcined. In (a), the Q^4/Q^3 ratios for idealised IPC-1P (2.5) and IPC-2P (7) are shown by red and blue dashed lines, respectively. Error bars have been estimated from multiple fits.*

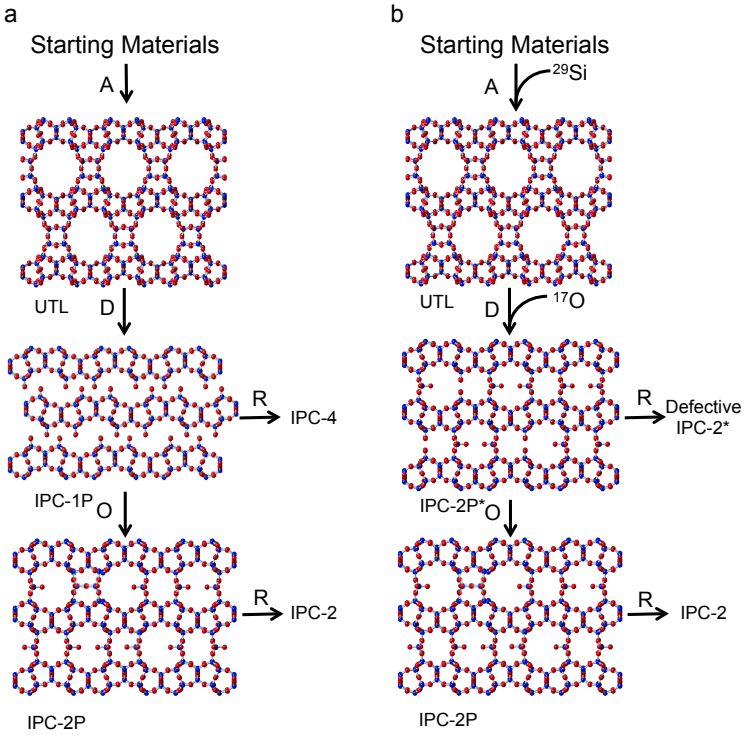

Figure 4.7 *Schematic of the ADOR process when (a) large and (b) small volumes of hydrolysis solutions are used. In (b), full hydrolysis to IPC-1P never reaches completion, forming the defective IPC-2P* instead. The steps where isotopically labeled reactants can be introduced are also shown in (b).*

4.2 *In situ* ^{29}Si, ^{1}H and ^{2}H NMR investigation

All the experiments shown so far to study the mechanism of the ADOR process have been performed *ex situ*. However, to make sure that the hydrolysis and rearrangement of the starting Ge-UTL are actually occurring during the reaction, these processes were monitored *in situ* by carrying out the ADOR process directly in the spectrometer while acquiring spectra. For this purpose, disposable PTFE rotor inserts were used (as described in Section 2.5.1) considering the need to spin the combination of the solid zeolite and the liquid hydrolysing solution. The disassembled zirconia 4 mm rotor and PTFE inserts are shown in Figure 4.8a along with two examples of packed inserts with zeolite/solution mixtures. A quick mixing of the zeolite and solution was carried out before sealing the insert in the attempt to ensure a uniform distribution of the zeolite in the solution. 18% ^{29}Si-enriched Ge-UTL (synthesised as described in Section 3.1) has been used as a parent zeolite to achieve faster signal acquisition and better time resolution of the changes in the ^{29}Si

local environments during the ADOR process. Specifically, when the ^{29}Si-enriched Ge-UTL was mixed with water, an increase in the intensity of Q^3 sites was observed over time, indicating the progress of the hydrolytic process, as shown in Figure 4.8b. After 2 h, no significant change was observed in the ^{29}Si MAS NMR spectra. When freshly prepared 6 M HCl was mixed with the parent ^{29}Si-enriched Ge-UTL, a significant increase in the intensity of the Q^4 sites over a longer period of time (22 h) can be observed in Figure 4.8c, indicating that the Si atoms, washed away in solution with Ge atoms from the interlayer region, are rearranged back into the structure. However, attempts to detect hydrolysed $Si(OH)_x$ aggregates in solution, by using a wide range of recycle intervals and doping the hydrolytic solutions with $CuCl_2$ (30, 50 mM), were unsuccessful. During this rearrangement process in high acidity (6 M HCl), ^{1}H MAS NMR spectra were also acquired, as shown in Figure 4.8d. In the range between 5 and 7 ppm the intensity of a sharp resonance is observed to decrease while a broader resonance simultaneously appears over the monitored reaction time. Since the interpretation of these ^{1}H MAS NMR spectra and their evolution with time proved challenging, further hydrolysis experiments have been carried out mixing D_2O with natural abundance Ge-UTL to obtain more resolution and information on the different ^{1}H species present. ^{2}H MAS NMR spectra appeared to be dominated by the sharp signal from rapidly reorienting D_2O throughout the 21 h of monitoring time. It was only possible to observe the presence of a broad spinning sideband manifold after processing a ^{2}H MAS NMR spectrum acquired (averaging 8192 transients) towards the end of the monitoring period, as shown in Figure 4.9a. These results from the *in situ* ^{2}H investigation are in agreement with ^{2}H MAS NMR spectra recorded on deuterated ADOR zeolites during *ex situ* characterisation, see Section 4.3.3, suggesting the presence of Si-OD species. ^{1}H MAS NMR spectra were recorded at the same time for the residual protons and showed, in the range between 4.3 and 5.7 ppm, the presence of a broad resonance and a sharp resonance with a splitting. The center position of both resonances shifted quite significantly over the period of monitoring, as shown in Figure 4.9b. The split sharp resonance could be assigned to water[5] partially hydrogen bonded and the broad resonance could be assigned to hydrogen-bonded Si-OH species.[6] However, the assignment of these *in situ* ^{1}H MAS NMR spectra is subject of ongoing research, since it was also difficult

to achieve resolution of the different ^{1}H sites in ADOR samples during *ex situ* experiments, considering the possible interference of adsorbed water, as discussed in Section 4.3.2.

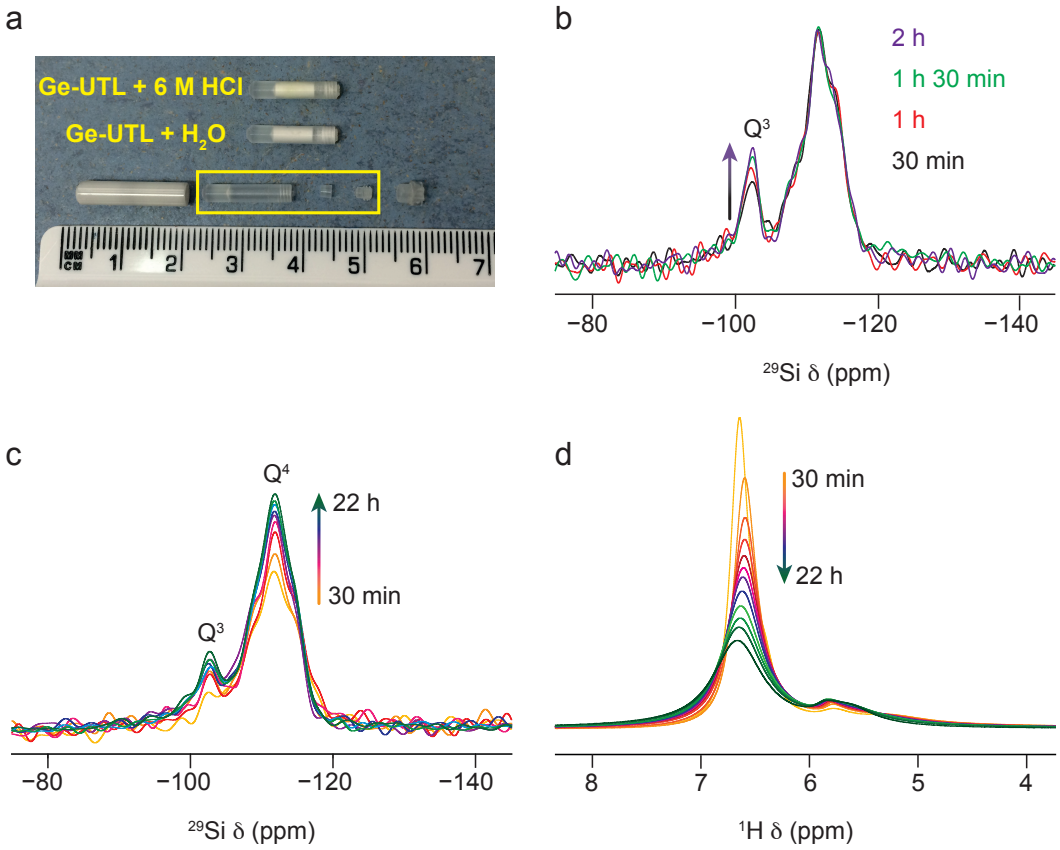

Figure 4.8 *(a) Photograph of the packed inserts (containing ~20 mg of solid zeolite and ~10 µL of liquid hydrolysing solution) and the disassembled rotor for in situ measurements. ^{29}Si (9.4 T, 5 kHz) MAS NMR spectra of 18% ^{29}Si-enriched Ge-UTL mixed with (b) distilled H_2O and (c) 6 M HCl (64-256 transients each, recycle interval = 30 s). (d) ^{1}H (9.4 T, 5 kHz) MAS NMR spectra (2 transients each, recycle interval = 1 s) acquired on the same reaction mixture shown in (c). All spectra have been acquired at room temperature, without temperature control.*

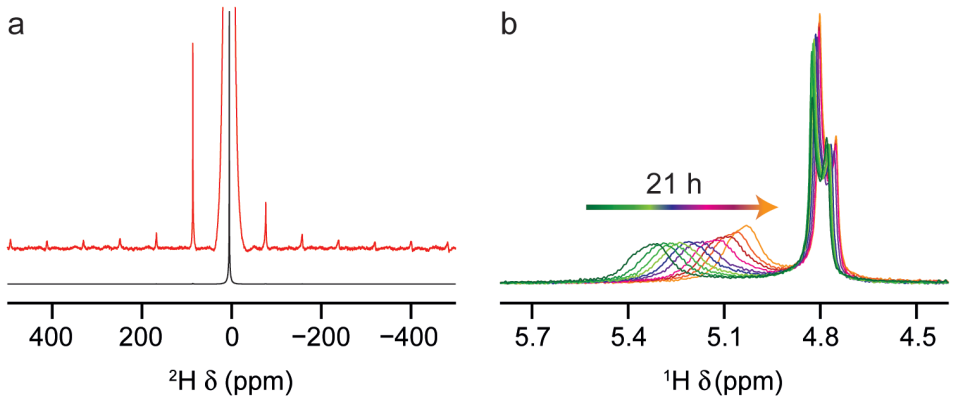

Figure 4.9 *In situ (a) ^{2}H and (b) ^{1}H (9.4 T, 5 kHz) MAS NMR spectra of 13.4 mg of natural abundance Ge-UTL mixed with ~10 μL of D_2O (99.9% D). (a) ^{2}H spectrum (black) acquired after 19 h of hydrolysis and shown after correction of the baseline by spline interpolation (8192 transients, recycle interval = 1 s). The expansion of the baseline is shown in red. (b) ^{1}H spectra recorded over 21 h of monitoring (8 transients each, recycle interval = 1 s). All spectra have been acquired at room temperature, without temperature control.*

4.3 ^{29}Si and ^{17}O NMR investigation of isotopically enriched samples

A wide range of NMR experiments have been used for the characterisation of hydrolysed "ADORable" zeolites isotopically enriched in ^{17}O or in both ^{17}O and ^{29}Si, according to the synthetic procedures described in Sections 3.1 and 3.4.

4.3.1 ^{29}Si and ^{17}O single-pulse experiments

The positive outcome of enrichment in the two isotopes used, ^{29}Si and ^{17}O (as described in Section 3.4), was verified with direct-acquisition experiments. In the case of ^{29}Si NMR experiments, it is possible to observe the increased ^{29}Si signal obtained from calcined ^{29}Si-enriched Ge-UTL compared to the corresponding natural abundance sample, as shown in Figure 4.10a. In the case of ^{17}O NMR experiments, a quadrupolar lineshape was acquired and subsequently observed evolving with increasing relative intensity in the region centered around 0 ppm and decreasing relative intensity of the rest of the ^{17}O signal centered at 35 ppm, as shown in Figure 4.10b. Changes in the lineshape were observed, after hydrolysis, over 30 days, during which the sample remained packed in a rotor at room temperature. After this time, no further changes were observed in the ^{17}O lineshape. Over the same

monitoring period of 30 days, no significant change could be observed in ^{29}Si MAS NMR spectra, probably indicating that this nucleus is a less sensitive probe compared to ^{17}O to monitor small changes in the structure occurring post synthesis. Such post-synthesis structural changes detected by ^{17}O NMR spectroscopy could be related to a low level of ongoing hydrolysis/rearrangement continuing even at room temperature. This is most likely caused by small amounts of acid remaining between the layers of the sample, owing to the reduced volume of natural abundance water used to wash the ^{17}O-enriched hydrolysed products.

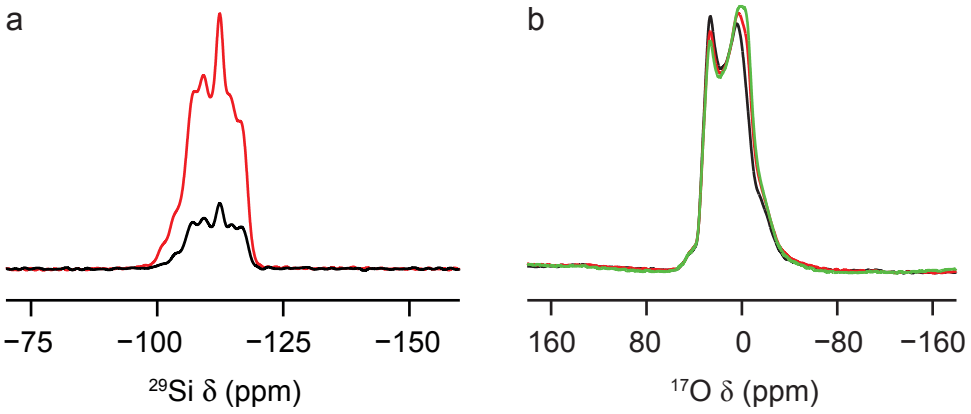

Figure 4.10 *(a) ^{29}Si (9.4 T, 10 kHz) MAS NMR spectra (normalised by number of transients) of natural abundance (black line) and 18% ^{29}Si-enriched (red line) calcined Ge-UTL showing the increased signal (by a factor of ~4) as a result of ^{29}Si enrichment. (b) ^{17}O (14.1 T, 20 kHz) MAS NMR spectra of Ge-UTL hydrolysed with ^{17}O-enriched H_2O for 16 h (GPMB 7), acquired 2 (black line), 16 (red line) and 30 (green line) days after synthesis.*

Two types of oxygen chemical environments are known to be present in hydrolysed layered zeolites leading to two chemically different sets of oxygens in the material: Si-OH interlayer surface hydroxyls and bulk Si-O-Si species. The latter will be further categorised on the basis of their local environment in Section 4.3.6. At high field an extra peak was resolved and assigned to ^{17}O-enriched water, most likely located in the interlayer region, as shown in Figure 4.11a and further discussed in Section 4.3.3. Even though the possible adsorption of water on the surface of the materials cannot be ruled out, washing with natural abundance water and the subsequent drying stage (overnight, in air) should remove any water, at least that ^{17}O enriched, from the surface of the zeolite. Once the hydrolysed materials were calcined, this extra peak was lost, as shown in Figure 4.11a. The assignment of this

peak to water was confirmed by comparative overlay of the spectra at different fields, shown in Figure 4.11b, where no substantial shift in position can be observed for this peak, confirming its negligible quadrupolar coupling. Moreover, as discussed in Section 4.3.4, this peak was not observed in ^{17}O MQMAS experiments. Since Si-OH interlayer sites condense upon calcination, the attention of this investigation was focused on the hydrolysed materials to resolve and quantify the different oxygen sites and to understand the mechanism of enrichment and hydrolysis. From the 1D results shown so far it is clear that spectral editing techniques and 2D NMR experiments are needed to achieve a better resolution and obtain information on the different chemical species contributing to the shape and evolution with time of the ^{17}O resonance. A DNP NMR characterisation of these hydrolysed ^{17}O-enriched samples was also attempted in order to investigate potential enhancements of the ^{17}O signal. However, no significant signal enhancements were observed during indirect DNP experiments, most likely because of inefficient ^{1}H-^{17}O polarisation transfer, as described in Section 4.3.2, and problems with the incorporation of the zeolite sample in the frozen matrix, as introduced in Section 2.1.1.

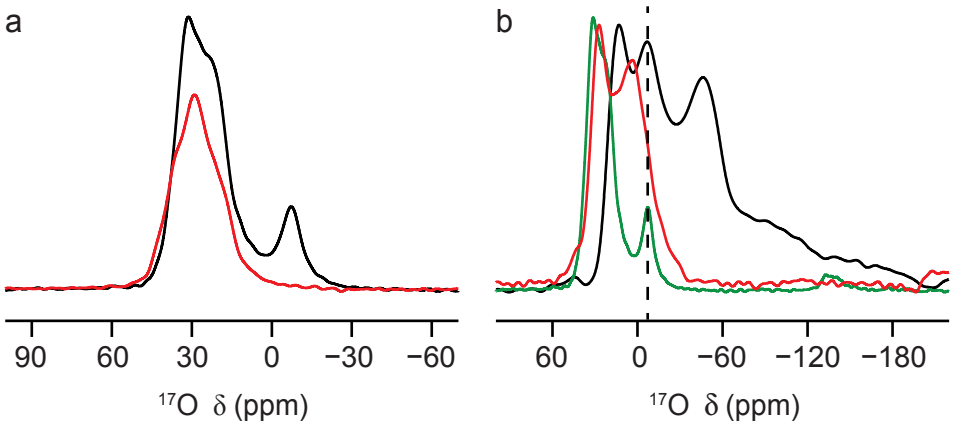

Figure 4.11 *(a) Short flip angle ^{17}O (20.0 T, 20 kHz) MAS NMR spectra of Ge-UTL hydrolysed with ^{17}O-enriched H_2O for 16 h (PSW 163) as made (black line) and calcined (red line). (b) ^{17}O MAS NMR spectra of Ge-UTL hydrolysed with ^{17}O-enriched H_2O for 16 h (PSW 163) acquired at B_0 field strengths of 9.4 T (black line), 14.1 T (red line) and 20.0 T (green line) at MAS rates of 14, 20 and 20 kHz. The negligible change in position of the peak assigned to water (which is only resolved at the highest field) is highlighted by the dashed line.*

4.3.2 ^{1}H-^{17}O cross-polarisation experiments

As introduced in Section 2.5.2.5, CP experiments edit spectra on the basis of spatial proximity to ^{1}H, which would be very useful to preferentially enhance the Si-OH species for the hydrolysed zeolite samples under investigation. However, cross-polarisation to quadrupolar nuclei is a much more challenging experiment compared to its spin I = ½ counterpart, with multiple match conditions and sensitivity also crucially dependent on the spin-lock efficiency (determined by the adiabaticity parameter, α, see Section 2.5.2.5). Therefore, for the ^{17}O-enriched zeolite samples investigated, the conditions for ^{1}H-^{17}O magnetisation transfer have been optimised using a model system: the ^{17}O-enriched SiO_2 synthesised as described in Section 3.4.2. This sample was characterised by ^{29}Si, ^{17}O and ^{1}H NMR spectroscopy, as shown in Figure 4.12. A distribution of Q sites can be observed in the ^{29}Si MAS NMR spectrum in Figure 4.12a (black line) with approximate intensity ratios of 0.1% : 2.9% : 73.5% : 23.5% for Q^1 : Q^2 : Q^3 : Q^4 species. A ^{1}H-^{29}Si CP MAS NMR spectrum, also shown in Figure 4.12a (red line), confirms this distribution, with a greater proportion of Q^3 sites than spectra reported for other amorphous silica samples synthesised following a similar procedure[7-8] to the one described in this work. The ^{1}H MAS NMR spectrum recorded 10 days after synthesis is shown in Figure 4.12b and is characterised by a broad line, indicating the presence not only of isolated and hydrogen-bonded silanols, but also of physisorbed water with varying degrees of hydrogen bond strength (signals in the range 3-8 ppm).[6] The ^{17}O MAS NMR spectrum is shown in Figure 4.12c and the average NMR parameters $\langle C_Q \rangle \approx$ 5.3 MHz, $\langle \eta_Q \rangle \approx 0.2$ and $\langle \delta_{iso} \rangle \approx 42$ ppm were obtained from the ^{17}O MQMAS NMR spectrum shown in Figure 4.12d. These values are in good agreement with data previously reported[8] for bulk Si-O-Si units. As can be observed in Figures 4.12c-d, the resonances from Si-O-Si and Si-OH species are not resolved, but T_1 inversion recovery measurements indicate that the signal centered around 0 ppm relaxes faster (by a factor of ~3) compared to the signal centered around 30 ppm, suggesting the presence of faster-relaxing silanols species, as previously reported.[8]

On the basis of the spin-locking results presented in Section 2.5.2.5, a low-power match condition (corresponding to spin-locking in the sudden regime, $\alpha \ll 1$) with a rf field strength of ν_1 = 10 kHz was used to obtain ^{1}H-^{17}O CP spectra on the amorphous silica sample using different contact times, as shown in Figure 4.13. It can be observed that in the CP spectra shown in Figure 4.13 the signal from Si-O-Si is almost entirely removed.

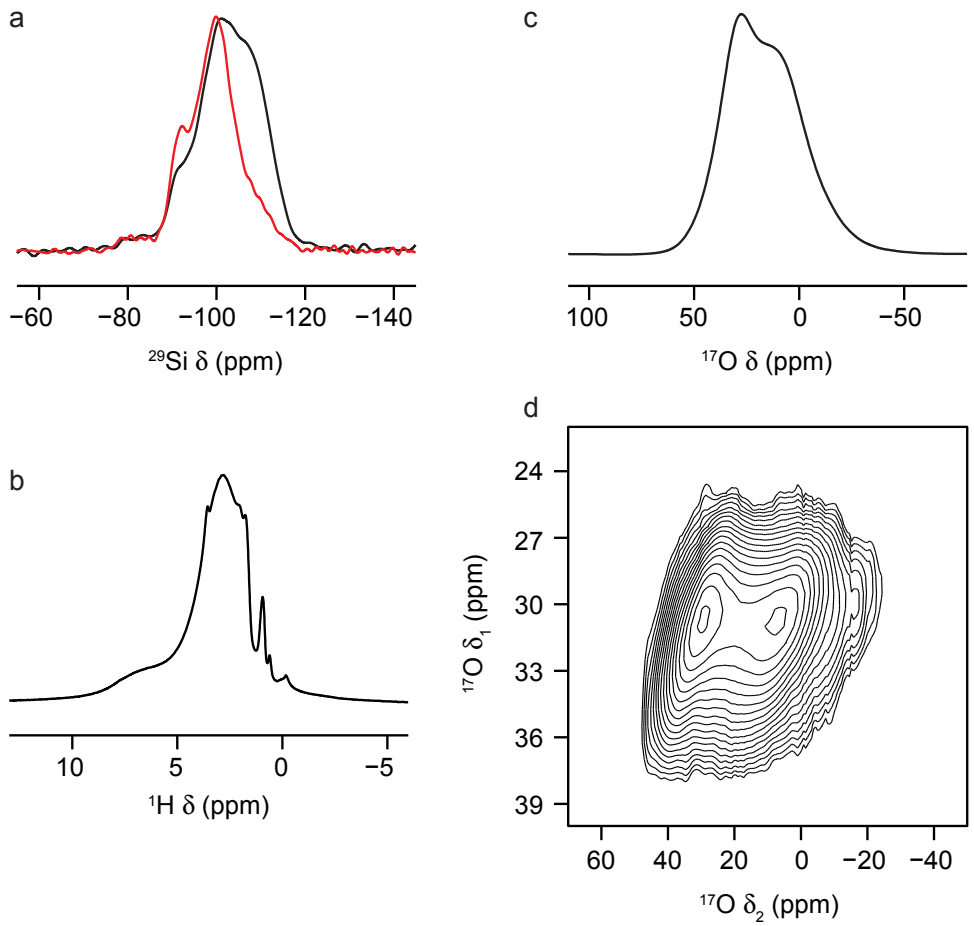

Figure 4.12 *(a) ^{29}Si, (b) ^{1}H and (c) ^{17}O (14.1 T, 20 kHz) MAS NMR spectra of amorphous ^{17}O-enriched SiO_2 synthesised as reported in Section 3.4.2. In (a), the ^{1}H-^{29}Si CP MAS NMR spectrum is shown in red. (d) ^{17}O (14.1 T, 20 kHz) z-filtered 3QMAS NMR spectrum, shown after a shearing transformation, of amorphous ^{17}O-enriched SiO_2.*

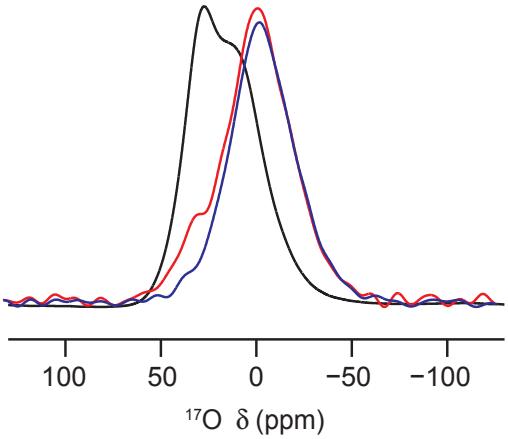

Figure 4.13 *^{1}H-^{17}O CP (14.1 T, 20 kHz) MAS NMR spectra of ^{17}O-enriched SiO_2 with contact times of 100 μs (blue line) and 500 μs (red line). The ^{17}O MAS NMR spectrum is also shown for comparison (black line).*

Using the optimised conditions described, it was possible to record ^{1}H-^{17}O CP spectra on the ^{17}O-enriched hydrolysed zeolite samples, as shown in Figure 4.14. While a selective excitation of the Si-OH can be observed, these experiments showed poor overall sensitivity even after long acquisition times (3 days at 14.1 T, and 13 h at 20.0 T). This possibly suggests a rapid $T_{1\rho}$ relaxation or poor spin-locking behaviour and, for this reason, ^{1}H and ^{17}O spin-lock experiments have been carried out. Figure 4.15a shows the intensity resulting from a ^{1}H spin-lock experiment on an ^{17}O-enriched hydrolysed sample of Ge-UTL (GPMB 22, synthesised and ^{17}O-enriched in the same conditions described for GPMB 7) with the corresponding ^{1}H MAS NMR spectrum shown in Figure 4.15b. It proved difficult to obtain any resolution of the different species present (hydrogen-bonded H_2O and Si-OH) from the ^{1}H spectrum of this material, but, since only a small intensity drop can be observed over a spin-lock duration of 1 ms, fast ^{1}H $T_{1\rho}$ relaxation does not appear to be responsible for the poor ^{1}H-^{17}O cross-polarisation efficiency. An ^{17}O spin-lock experiment has been subsequently carried out on the same sample and the corresponding ^{17}O MAS NMR spectra resulting from different spin-lock durations are shown in Figure 4.16. When a short spin-lock duration is used (up to 50 μs, Figure 4.16a) ^{17}O signals corresponding to Si-O-Si, Si-OH and H_2O can be seen. At progressively longer spin-lock durations (100 and 3000 μs, Figures 4.16b-c) the

signal from H_2O is lost first and then the Si-OH species is primarily observed. This evidence confirms that poor ^{17}O spin-lock efficiency is not responsible for the poor CP signal observed in Figure 4.14.

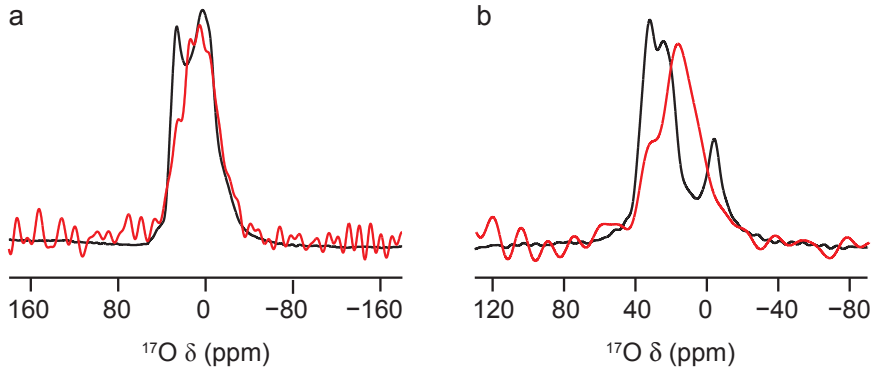

Figure 4.14 *^{1}H-^{17}O (20 kHz MAS) CP NMR spectra (red lines) of Ge-UTL hydrolysed with ^{17}O-enriched H_2O for 16 h (GPMB 7), acquired at (a) 14.1 T and (b) 20.0 T with a contact time of 1000 μs. The corresponding MAS spectra are shown (black lines) for comparison.*

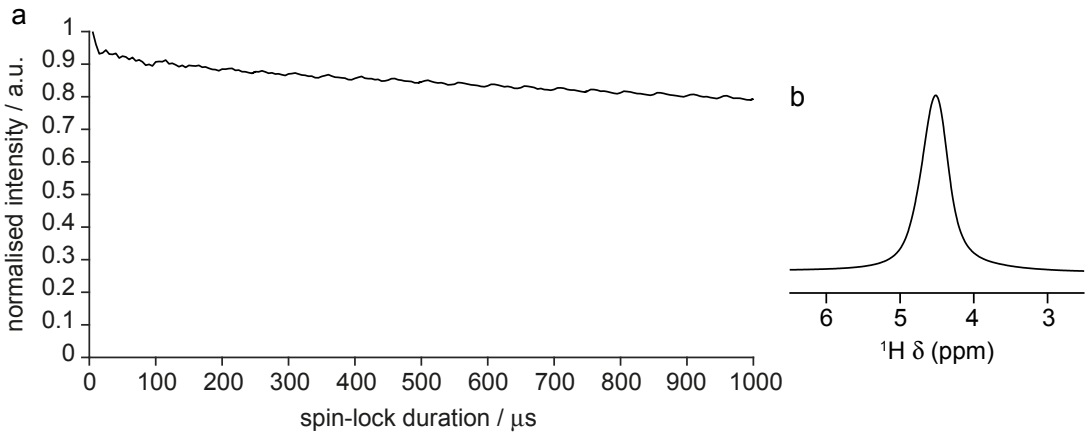

Figure 4.15 *(a) Intensity of the ^{1}H (14.1 T, 20 kHz MAS) spin-lock experiment (i.e., $T_{1\rho}$ measurement) for an ^{17}O-enriched hydrolysed Ge-UTL sample (GPMB 22) with a spin-lock rf field strength, ν_1, of 75 kHz. The corresponding ^{1}H (14.1 T, 20 kHz) MAS NMR spectrum of the same sample is shown in (b) and represents the typical ^{1}H signal obtained from hydrolysed zeolites subsequently dried in air.*

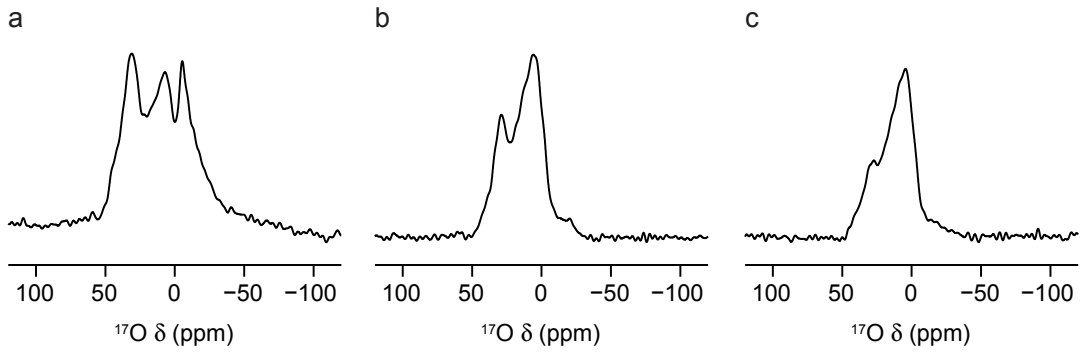

Figure 4.16 *^{17}O (14.1 T, 20 kHz) MAS NMR spectra of an ^{17}O-enriched hydrolysed Ge-UTL sample (GPMB 22) with a spin-lock rf field strength, ν_1, of 8 kHz at spin-lock durations of (a) 50 μs, (b) 100 μs and (c) 3000 μs.*

Given that the ^{1}H $T_{1\rho}$ relaxation has been shown to be sufficient for the contact times used and the Si-OH species exhibit a better ^{17}O spin-locking efficiency than Si-O-Si or H_2O at the rf fields applied, the reduced efficiency in CP experiments is most likely resulting form a reduction of the dipolar interaction mediating the transfer of magnetisation, probably related to motion. Evidence for ^{1}H dynamics in hydrolysed Ge-UTL is provided by ^{2}H NMR spectroscopy, see Section 4.3.3. Further support for the hypothesis that modulation of the dipolar interaction is responsible for the poor efficiency observed in CP experiments is provided by the low-temperature ^{1}H-^{17}O CP MAS NMR spectrum shown in Figure 4.17. At 108 K, a significant increase in cross-polarisation efficiency, and subsequently signal build-up with time, is observed when compared to spectra obtained at room temperature. Moreover, a change in the ^{17}O CP lineshape can be seen resulting from the restriction or removal of any dynamics at low temperature.

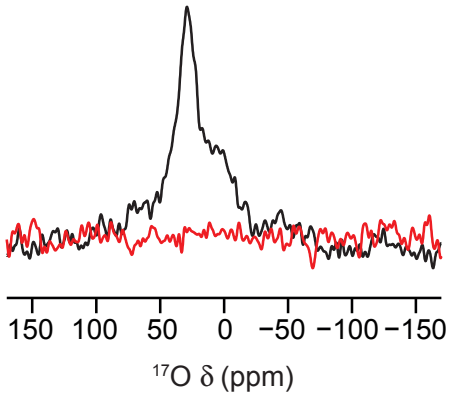

Figure 4.17 *^{1}H-^{17}O (14.1 T, 12.5 kHz) CP MAS NMR spectra of an ^{17}O-enriched Ge-UTL hydrolysed for 16 h (GPMB 7) acquired with a contact time of 1000 μs at 108 K (black line) and at 298 K (red line).*

4.3.3 Deuteration experiments

Different experimental approaches were tested for the deuteration of hydrolysed Ge-UTL samples to study any H dynamics that would affect the efficiency of the magnetisation transfer in ^{1}H-^{17}O CP experiments. In particular, three different deuteration procedures were tested using unenriched material: (i) post-synthetic exchange with D_2O vapour over 42 days, (ii) stirring of the hydrolysed zeolite in D_2O for 24 h at room temperature and (iii) *in situ* hydrolysis using D_2O and DCl. To minimise the possible loss of ^{17}O or ^{29}Si by exchange or significant hydrolysis when large amounts of D_2O were used, only procedure (i) was carried out on ^{17}O- and doubly ^{17}O- and ^{29}Si-enriched zeolites. Deuterated enriched samples were dried under Ar prior to spectral acquisition to remove any excess D_2O.

Figure 4.18a shows the comparison of ^{17}O MAS NMR spectra of an ^{17}O-enriched Ge-UTL zeolite hydrolysed for 16 h (GPMB 7) prior and post deuteration using procedure (i). The signal at −4.2 ppm attributed to water is removed upon deuteration as a result of exchange with both D_2O and atmospheric water (both containing ^{17}O at natural abundance). However, an overall loss of ^{17}O signal (both from Si-O-Si and Si-OH sites) can be observed, indicating that the deuteration process triggers further hydrolytic rearrangement. It was shown in Figure 4.10 that the ^{17}O spectra and subsequently the layered structure of hydrolysed Ge-UTL samples can undergo changes with time when stored at room temperature. However, saturated D_2O vapour creates a more favourable environment for further hydrolysis to occur, resulting in ^{17}O back-exchange with natural abundance $D_2{}^{16}O$. The presence of a further hydrolytic process, triggered by the deuteration conditions, is confirmed by comparison of the ^{29}Si Q^4/Q^3 ratios of the ^{17}O-enriched hydrolysed Ge-UTL sample before and after deuteration. Indeed, the ^{29}Si Q^4/Q^3 ratio of the deuterated sample is lower by a factor of ~1.4 compared to the same sample prior to deuteration. A resulting fast ^{2}H back-exchange was observed which, together with the loss of ^{17}O during the deuteration process, hindered the acquisition of high-resolution ^{17}O MAS NMR spectra for the deuterated samples.

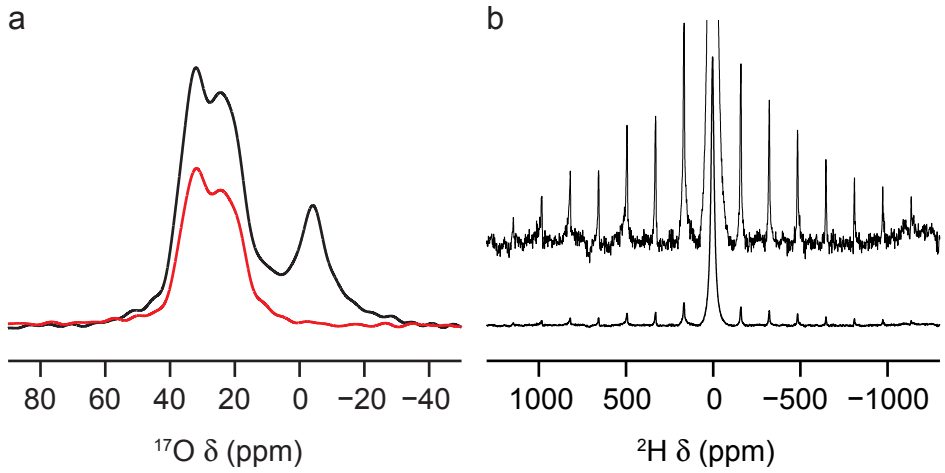

Figure 4.18 *(a) ^{17}O (20.0 T, 20 kHz) MAS NMR spectra of ^{17}O-enriched Ge-UTL hydrolysed for 16 h (GPMB 7) acquired before (black line) and after (red line) exchange with D_2O vapour. (b) ^{2}H (9.4 T, 10 kHz) MAS NMR spectrum of deuterated ^{17}O-enriched Ge-UTL hydrolysed for 16 h (GPMB 7) with an expansion to show the spinning sideband manifold.*

Figure 4.18b shows the ^{2}H MAS NMR spectrum of a deuterated ^{17}O-enriched Ge-UTL zeolite hydrolysed for 16 h (GPMB 7) shortly after its removal from saturated D_2O. It can be noticed that the spectrum appears dominated by a sharp isotropic signal resulting from rapidly reorienting D_2O in the interlayer region. In the expansion, a broad spinning sideband manifold corresponding to Si-OD in the interlayer space can be observed. C_Q has been estimated to be 80-100 kHz for this species, which cannot be simulated with a single quadrupolar lineshape, suggesting that also this signal is motionally averaged possibly by H/D exchange with water. On the basis of the ^{2}H MAS NMR spectrum shown in Figure 4.18b, the intensity ratio of Si-OD:D_2O signal is ≈ 1:4, yielding a 1:2 ratio of silanol to molecular water in the interlayer region. However, the level of water in the hydrolysed zeolites varies depending on storage time and conditions. For the samples analysed in this work the ratio of Si-OH to molecular water in the interlayer region is between 1:2 and 1:4, highlighting that much more water is present in the interlayer spacing than initially expected.[4] As already pointed out in Section 4.3.1, it is reasonable to assume that water molecules should be located in the interlayer region, but the possible presence of adsorbed water on the surface cannot be ruled out.

4.3.4 ^{17}O MQMAS experiments

Resolution of the different ^{17}O species contributing to the ^{17}O 1D spectra presented so far is challenging because of the quadrupolar nature of ^{17}O and the resulting second-order broadening affecting its lineshapes. In this case, as introduced in Section 2.5.2.8, resolution can be improved with MQMAS experiments, where resonances are separated in the indirect (δ_1) dimension (after processing) on the basis of their isotropic chemical shifts and quadrupolar shifts. Higher field will also improve the resolution achieved in the direct dimension since the second-order quadrupolar broadening is inversely dependent on field strength.[9] Figures 4.19b-c show ^{17}O MQMAS NMR spectra of the ^{17}O-enriched Ge-UTL sample hydrolysed for 16 h (GPMB 7) acquired at 20.0 T without and with ^{1}H decoupling, respectively. The corresponding ^{17}O MAS NMR spectrum is shown in Figure 4.19a. In both MQMAS spectra it is possible to observe a resonance at $\delta_1 \approx 25$ ppm showing a distribution of parameters with average $\langle P_Q \rangle \approx 5.3$ MHz and $\langle \delta_{iso} \rangle \approx 39$ ppm. Only upon ^{1}H decoupling was it possible to observe an additional resonance, indicated by lower intensity at $\delta_1 \approx 13$ ppm, assumed to originate from Si-OH species. This assignment is confirmed by the good agreement between the positions of this weak, resolved signal and the peak maximum in CP experiments at 20.0 T shown in Figure 4.14b, where a selective enhancement of the Si-OH signal is obtained. The extraction of accurate NMR parameters for this resonance resulted difficult, owing to the low sensitivity and lack of any characteristic quadrupolar broadening. However, approximate average parameters of $\langle P_Q \rangle \approx 3.4$ MHz and $\langle \delta_{iso} \rangle \approx 23$ ppm can be obtained from the center of gravity of the resonance. The sharp peak at $\delta = -5.1$ ppm in Figure 4.19a is only resolved at 20.0 T and does not appear in the MQMAS spectra in agreement with its assignment as water, as discussed in Section 4.3.1. Figure 4.20 shows ^{17}O MAS and MQMAS NMR spectra of ^{17}O-enriched Ge-UTL hydrolysed for 16 h (GPMB 7) acquired at different fields (14.1 and 20.0 T) to further support the NMR parameters obtained from Figure 4.19 for the Si-O-Si sites. Only the resonance of these bulk sites can be seen, since the Si-OH signal is only observed in MQMAS NMR spectra recorded at high field with ^{1}H decoupling. The resulting ^{17}O NMR parameters are reported in Table 4.1.

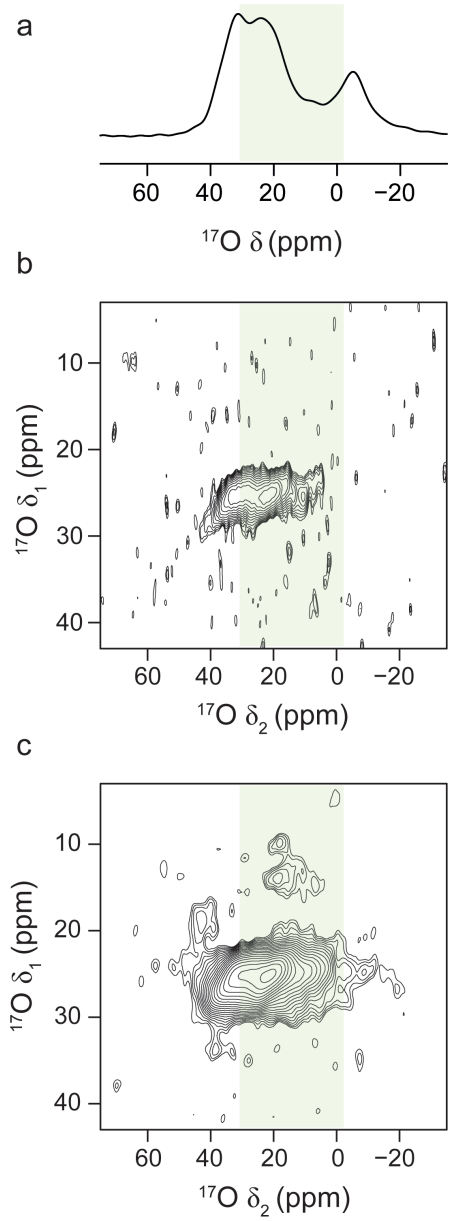

Figure 4.19 *^{17}O (20.0 T, 20 kHz) 3QMAS NMR spectra of ^{17}O-enriched Ge-UTL hydrolysed for 16 h (GPMB 7) acquired using a z-filtered pulse sequence (and shown after a shearing transformation) (b) without and (c) with CW ^{1}H decoupling. The total acquisition times are (b) 7 and (c) 22 h. In (a), the corresponding ^{17}O MAS NMR spectrum is shown. The position of the signal in CP experiments is highlighted by the green box in all three spectra.*

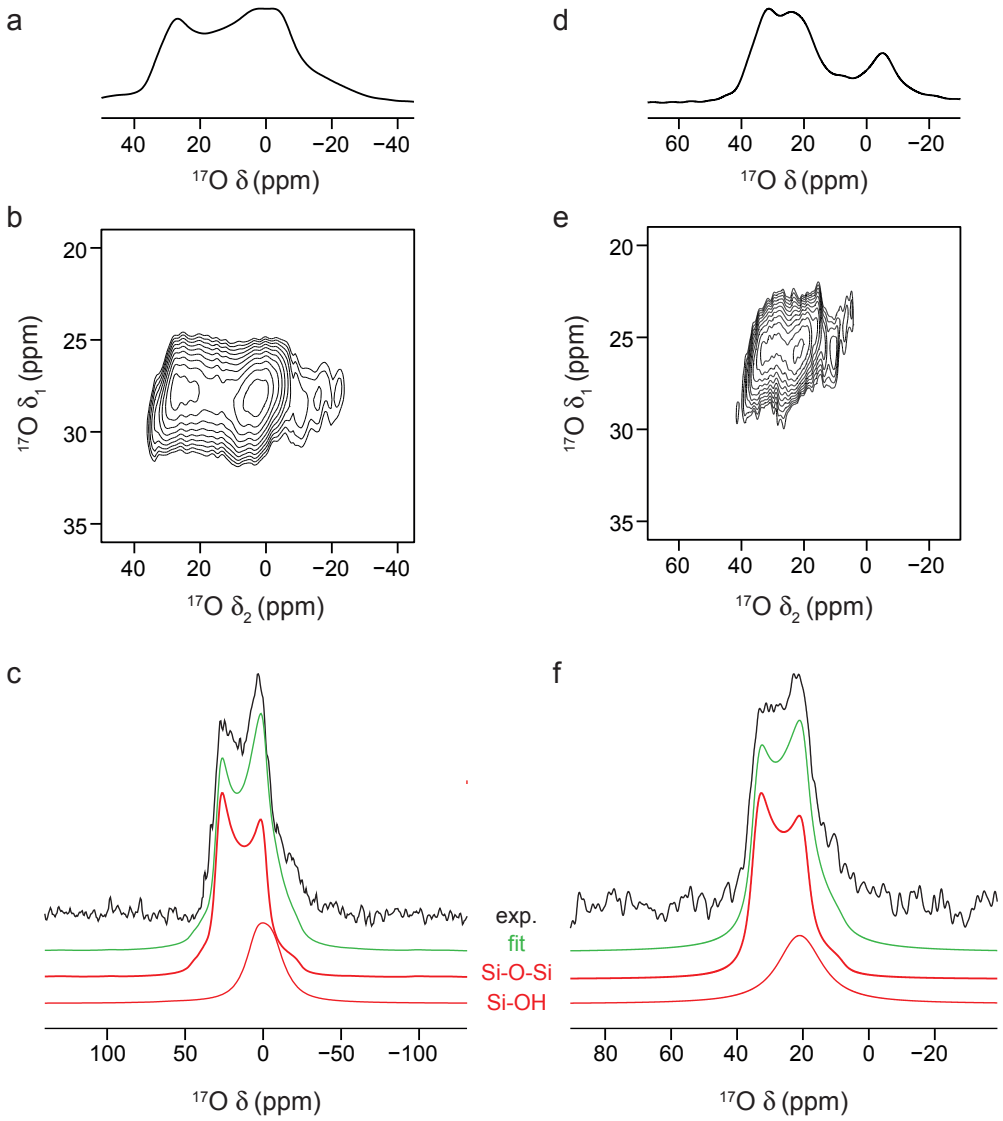

Figure 4.20 *^{17}O MAS and z-filtered 3QMAS NMR spectra of ^{17}O-enriched Ge-UTL hydrolysed for 16 h (GPMB 7), shown after a shearing transformation, at B_0 field strengths of (a,b) 14.1 T and (d,e) 20.0 T with a MAS rate of 20 kHz. Cross sections from the MQMAS spectra in (b) and (e) are shown in (c) and (f), respectively, with (from the top) the overall fit (green), and the individual contributions from Si-O-Si and Si-OH (red).*

B_0 / T	δ_1 (ppm)	$\langle\delta_{iso}\rangle$ (ppm)	$\langle P_Q\rangle$ / MHz	C_Q / MHz
14.1	28(1)	38(1)	5.0(3)	5.2(1)
20.0	26(1)	39(1)	5.3(3)	5.2(1)

Table 4.1 *^{17}O NMR parameters for the Si-O-Si species: average δ_{iso} and P_Q were extracted from the MQMAS NMR spectra in Figures 4.20b and 4.20e; C_Q values were determined from the fitted cross sections shown in Figures 4.20c and 4.20f.*

4.3.5 ^{17}O-^{29}Si correlation experiments

To investigate the location of ^{17}O atoms in the hydrolysed structure with respect to the different ^{29}Si environments, ^{17}O-^{29}Si D-HMQC correlation experiments have been carried out at high field (20.0 T) recoupling the Si-O dipolar interaction with the $SR4^2_1$ sequence, as introduced in Section 2.5.2.7. Preliminary spectra acquired to test the feasibility of this experiment showed that an overall time of 48 h per experiment was needed on samples enriched only in ^{17}O. Therefore, enrichment not only in ^{17}O but also in ^{29}Si appeared necessary for this experiment to obtain a better ^{29}Si spectrum with an overall reduced acquisition time. For this reason, the doubly ^{17}O- and ^{29}Si-enriched IPC-2P sample (GPMB 8), synthesised and enriched as described in Sections 3.1 and 3.4.1, was used in these experiments. Different recoupling times were investigated by changing the number of loops in the recoupling sequence, as shown in Figure 4.21. At short recoupling times, Figure 4.21b, the only signal present in the spectrum comes from the Si-O-Si coordinated to Q^4 Si species, while at longer recoupling times a correlation can be observed between the same ^{17}O species and Q^3 Si sites (Si-OH groups). Since a correlation to the interlayer ^{29}Si Q^3 sites can only be detected when probing greater distances, this experiment suggests that ^{17}O atoms are also located in the bulk of the zeolite layers and not only in the interlayer spacing. This was unexpected and cannot be explained by the incorporation of ^{17}O only in the interlayer region, which was the initially predicted outcome of the ADOR process carried out with ^{17}O-enriched water. Even considering the possibility of a faster back-exchange for Si-^{17}OH sites, the experimental results suggest that a significant proportion of ^{17}O is located in the bulk of the zeolite layers with a much more extensive rearrangement occurring during

hydrolysis than previously thought. In both Figures 4.21b and 4.21c there is no correlation of the ^{17}O signal at $\delta \approx -6.4$ ppm in Figure 4.21a with any ^{29}Si species, confirming its assignment as non-structural water. Moreover, no correlation in the spectra can be observed in the region where the CP signal from interlayer Si-OH sites was observed at 20.0 T as indicated by the green dashed line in Figures 4.21a-c. This can be related to the fast relaxation of these sites during magnetisation transfer because of the presence of dynamic interlayer water, as already discussed in Section 4.3.3.

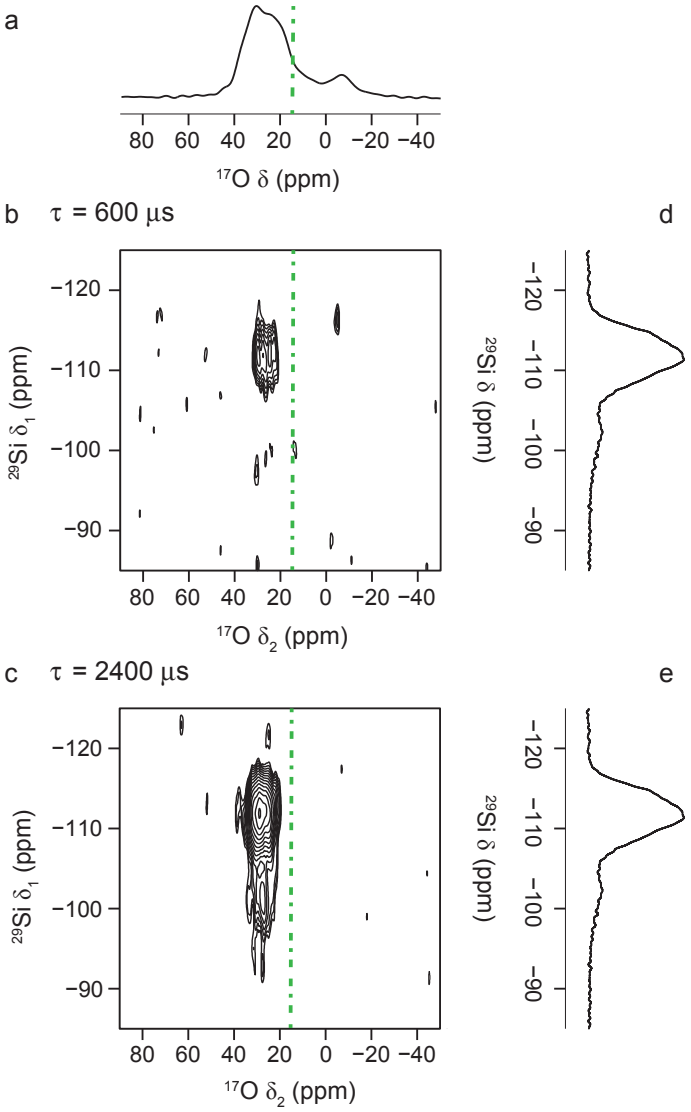

Figure 4.21 *^{17}O-^{29}Si (20.0 T, 20 kHz MAS) D-HMQC correlation spectra of ^{17}O- and ^{29}Si-enriched Ge-UTL hydrolysed with $H_2{}^{17}O$ for 16 h (GPMB 8) acquired with (b) τ = 600 μs and (c) τ = 2400 μs of $SR4^2_1$ recoupling. Also shown are the corresponding ^{17}O (a) and ^{29}Si (d,e) MAS NMR spectra. The dashed green line denotes the position of maximum signal intensity for the Si-OH species identified in CP experiments at 20.0 T.*

4.3.6 ^{17}O incorporation in the zeolite structure

To confirm and quantitatively evaluate the degree of incorporation of ^{17}O in the ADOR hydrolysed product, different structural models were produced. Oxygen atoms in IPC-2P can be broadly categorised into Si-OH oxygen atoms and three types of Si-O-Si units: (i) those in the interlayer region; (ii) those in the layers accessible to pore spaces; (iii) those in the layers not accessible to the pores. It should be noted that only a low intensity of signal is seen in the D-HMQC experiments shown in Figure 4.21 from Si-O-Si units coordinated to Q^3 species in the interlayer region. This is most likely related to the proportionately smaller number of these species in IPC-2P, especially if defective (IPC-2P*), and to the possible faster relaxation of these units because of their proximity to dynamic interlayer water. As shown in Figure 4.22, four idealised models of ^{17}O incorporation can be considered: (a) ^{17}O atoms are incorporated only into the interlayer region resulting in the presence of Si-^{17}OH sites and no Si-^{17}O-Si sites; (b) ^{17}O atoms are incorporated into Si-OH units and in the Si-O-Si units within the interlayer region resulting in a Si-^{17}O-Si:Si-^{17}OH of 2.5:1; (c) ^{17}O atoms are incorporated into Si-OH units, Si-O-Si units within the interlayer region and in the first layer of tetrahedra in the bulk of the layers resulting in a Si-^{17}O-Si:Si-^{17}OH of 11.5:1; (d) ^{17}O atoms are located everywhere in the structure resulting in a Si-^{17}O-Si:Si-^{17}OH of 16.5:1. Even if these calculated Si-^{17}O-Si:Si-^{17}OH ratios don't take into account any difference in the probability of any particular site being preferentially occupied by ^{17}O over another, these models are good structural references to quantify the level of ^{17}O incorporation and shed light on the mechanism of ADOR hydrolysis. To determine which of the hypothesised models more accurately represents the actual pattern of ^{17}O incorporation in the investigated ^{17}O-enriched hydrolysed Ge-UTL samples, it is necessary to estimate the relative proportions of the different O species. This can be achieved by fitting a quantitative (i.e., short flip angle) ^{17}O MAS NMR spectrum on the basis of the information obtained on the Si-O-Si and Si-OH lineshapes from previous experiments. Indeed, cross sections extracted from ^{17}O MQMAS experiments provided the NMR parameters for the Si-O-Si lineshape and the Si-OH lineshape was primarily observed in ^{1}H-^{17}O CP and spin-lock experiments.

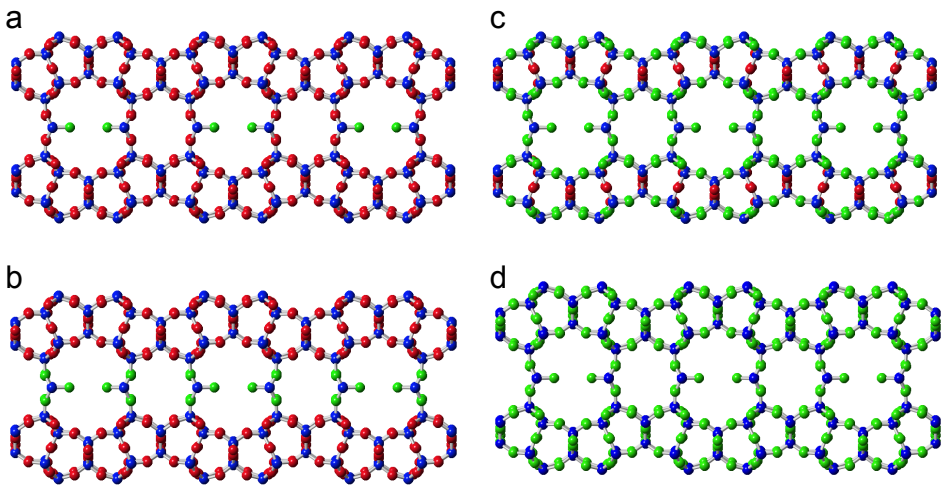

Figure 4.22 *Hypothetical models of the most likely ^{17}O incorporation patterns into idealised IPC-2P after hydrolysis with ^{17}O-enriched water. The models are where (a) only the Si-OH units contain ^{17}O; (b) Si-OH and Si-O-Si units in the interlayer spacing contain ^{17}O, with expected Si-^{17}O-Si:Si-^{17}OH ratio of 2.5:1; (c) Si-OH units, Si-O-Si units in the interlayer spacing and in the first layer of tetrahedra in the layers contain ^{17}O, with expected Si-^{17}O-Si:Si-^{17}OH ratio of 11.5:1; (d) all possible oxygen sites in the structure are equally likely to contain ^{17}O, with expected Si-^{17}O-Si:Si-^{17}OH ratio of 16.5:1. Oxygen atoms with a high probability of ^{17}O incorporation are shown in green and oxygen atoms with a low probability of ^{17}O incorporation are shown in red. Silicon atoms are shown in blue. Water molecules in the interlayer region are omitted for clarity.*

Figure 4.23 shows the short flip angle ^{17}O MAS NMR spectrum along with the best fit and lineshapes for the individual components using the estimated NMR parameters determined from MQMAS, CP and spin-lock experiments. It should be noted that the amount of water in the samples varies depending on the hydrolysis and storage conditions. Furthermore, owing to the more distorted lineshape of the Si-OH species observed in CP and spin-lock experiments, it is not possible to determine accurate NMR parameters for this species, resulting in some uncertainty in the quantitative determination. From the fit shown in Figure 4.23b, the ratio of Si-O-Si:Si-OH:H_2O species is 8:1:1. This Si-^{17}O-Si:Si-^{17}OH ratio of ~8:1 confirms that the incorporation of ^{17}O is not restricted only to the interlayer region, supporting previous experimental evidence of a more extensive rearrangement during ADOR hydrolyses. In particular, the obtained Si-^{17}O-Si:Si-^{17}OH ratio suggests a pattern of ^{17}O incorporation closer to the one shown in Figure 4.22c, where ^{17}O is also present in the first layer of tetrahedral units in the bulk of the layers.

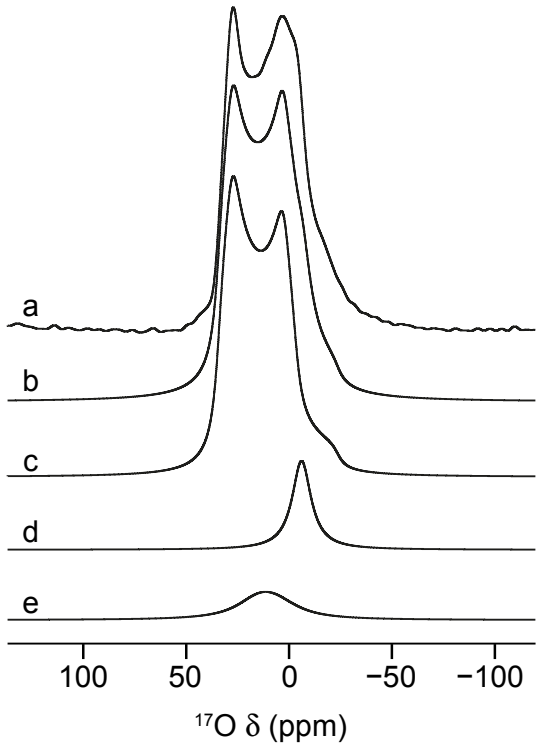

Figure 4.23 *(a) Short flip angle ^{17}O (14.1 T, 20 kHz) MAS NMR spectrum of ^{17}O-enriched Ge-UTL hydrolysed for 16 h (GPMB 22). Also shown are (b) the overall fit and individual lineshapes for (c) Si-O-Si species, (d) water and (e) Si-OH species.*

A possible explanation of the rearrangement phenomenon could be related to the high temperature at which the hydrolysis reaction is carried out, i.e., 95 °C. In these conditions, cleavage and formation of Si-O bonds could be promoted throughout the solid from the interlayer region, where hydrolysis takes place, to the bulk of the layers. Furthermore, similar fits were also carried out on the ^{17}O MAS NMR spectra shown in Figure 4.10b. These spectra were not acquired using a short flip angle and, therefore, cannot be considered quantitative, but fits shown in Figure 4.24 and the resulting integrated intensities in Table 4.2 provide insight into the changes in the lineshapes over a period of 30 days. Notwithstanding the low intensity and broad nature of the Si-OH signal, it is still possible to estimate the evolution of the relative intensities of the three components, Si-O-Si, Si-OH and water, in the ^{17}O MAS NMR spectra in Figure 4.24. This confirms the presence of a low level of ongoing hydrolysis, as hypothesised in Section 4.3.1, with an increase in the proportion of Si-OH species and a relative decrease of the Si-O-Si signal. The phenomenon is most

likely due, as introduced in Section 4.3.1, to the reduced volume of natural abundance washing water used, leading to some residual acidity in the layers of the zeolite. Going from 2 to 30 days after synthesis a slight change is observed in the position of the Si-OH lineshape in Figure 4.24. A possible explanation for this could be related to the evolution of the hydrogen-bonding patterns during the hydrolytic process.[10]

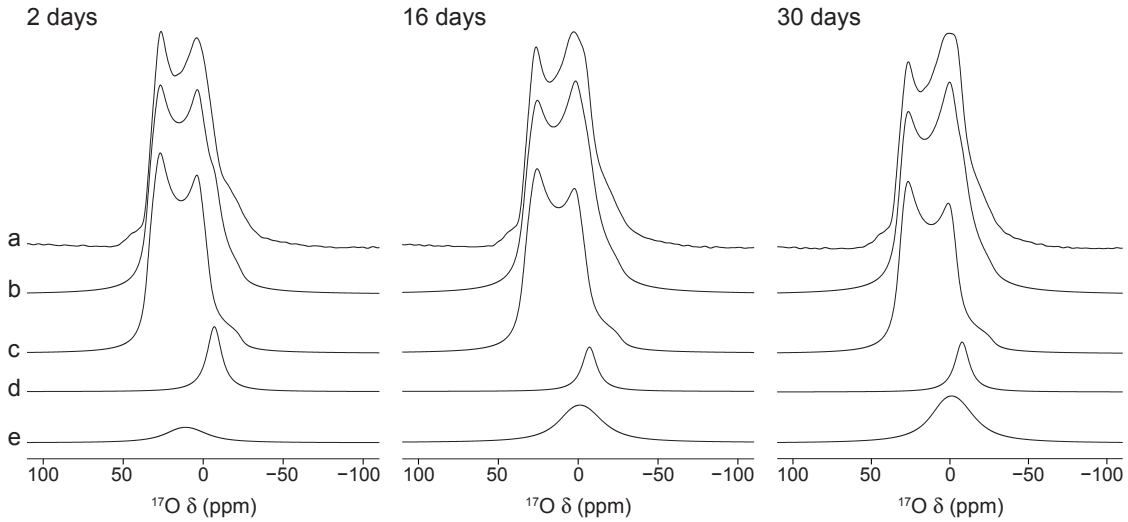

Figure 4.24 *^{17}O (14.1 T, 20 kHz) MAS NMR spectra of ^{17}O-enriched Ge-UTL hydrolysed for 16 h (GPMB 7) 2, 16 and 30 days after hydrolysis as shown in Figure 4.10b. Also shown are (b) overall lineshape fitting and individual lineshapes for (c) Si-O-Si species, (d) H_2O and (e) Si-OH species.*

	2 days	16 days	30 days
Si-**O**-Si	83.4	76.9	71.4
Si-**O**H	8.3	15.4	21.5
H_2**O**	8.3	7.7	7.1

Table 4.2 *Integrated intensities (%) of the three different types of ^{17}O species from the fits of the MAS NMR spectra shown in Figure 4.24. Errors are estimated as 0.5%.*

4.4 NMR and catalytic study of post-synthesis aluminated Ge-UTL

Ge-UTL samples where Al was introduced post-synthesis, as described in Section 3.2, were studied by ^{27}Al NMR spectroscopy to investigate the structural incorporation of Al. Initial attempts to study the influence of the presence of Al in the framework on the mechanism of the ADOR process were not successful because of the rapid loss of Al in the typical experimental hydrolysis conditions. Catalytic tests for NO production were then carried out, as introduced in Section 2.1.5, on the post-synthesis aluminated Ge-UTL, after ion-exchange, to investigate its catalytic activity upon injection of 250 μL of 0.05 M $NaNO_2$ solution 5 min into the run (testing a fixed sample amount of 5 mg suspended in 2.6 mL of water). The influence of different conditions of ion-exchange on the distribution of Al in the structure, probed by ^{27}Al NMR experiments, and on the resulting catalytic activity was studied. In particular, 5 different types of ion-exchange procedures have been tested on 100-200 mg of sample from the same starting batch of post-synthesis aluminated material: (i) overnight stirring of the zeolite sample at room temperature in 0.3 M NH_4Cl solution; (ii) overnight stirring of the zeolite sample at room temperature in 0.6 M NH_4Cl solution; (iii) overnight stirring of the zeolite sample at room temperature in 0.06 M NH_4Cl solution; (iv) 2 h stirring of the zeolite sample at 80 °C in 0.6 M NH_4Cl solution; (v) 2 h stirring of the zeolite sample at 80 °C in 0.06 M NH_4Cl solution. It should be noted that all ion-exchange procedures have been repeated three times on each sample to ensure a complete exchange. After ion-exchange, NH_4^+ charge-balances the negative charge of the Al-containing framework and, upon calcination of the sample, NH_3 is released leading to the formation of Brønsted acid sites.[11] The diffraction pattern of the starting post-synthesis aluminated Ge-UTL is shown in Figure 4.25a and the corresponding ^{27}Al, ^{29}Si and ^{1}H MAS NMR spectra are shown in 4.26a. The presence of both tetrahedrally and octahedrally coordinated Al sites, ^{29}Si Q^3 and Q^4 sites and a ^{1}H composite resonance between 0 and 10 ppm can be observed. Calcination of this sample resulted in the appearance of a sharp component in the octahedral region of the ^{27}Al MAS NMR spectrum, the condensation of ^{29}Si Q^3 sites and the narrowing of the signal in the ^{1}H MAS NMR spectrum, where a sharp resonance, probably deriving from adsorbed

water, can be observed at 1.9 ppm, as shown in Figure 4.26b. No significant changes were observed in the crystallinity of the sample upon calcination, as shown by the PXRD patterns in Figure 4.25b. Particles reaching Al content of up to five times the average composition of a crystallite were observed on the surface of crystallites upon calcination, as shown in Figure 4.27a, providing evidence of dealumination.[12] Moreover, mapping of SEM images suggests a migration of part of the Al to the surface of the structure, as shown in Figure 4.27b. This phenomenon can be identified as Al "zoning", which describes the long-range heterogeneous distribution of Al, resulting, in this particular case, from the migration of Al upon heat treatment.[13-14] Subsequently, the sample was prepared for catalytic tests by ion-exchange according to procedure (i) and recalcination. During this exchange process, EDX showed Ge was lost (Si/Ge ≈ 50), but variations in Al content were challenging to evaluate because of its non-uniform distribution throughout the sample. The PXRD pattern, shown in Figure 4.25c, appears unchanged, while the ^{27}Al MAS NMR spectrum in Figure 4.26c shows a significant broadening of the resonances and a loss of signal from octahedral Al relative to the tetrahedral sites. No change is observed in ^{29}Si and ^{1}H MAS NMR spectra between Figure 4.26b and c, apart from the loss of the sharp ^{1}H resonance at 1.9 ppm. Representative results of the catalytic tests, carried out in triplicate, are shown in Figure 4.28 with a NO production for this first sample of 48 ± 5 nmol.

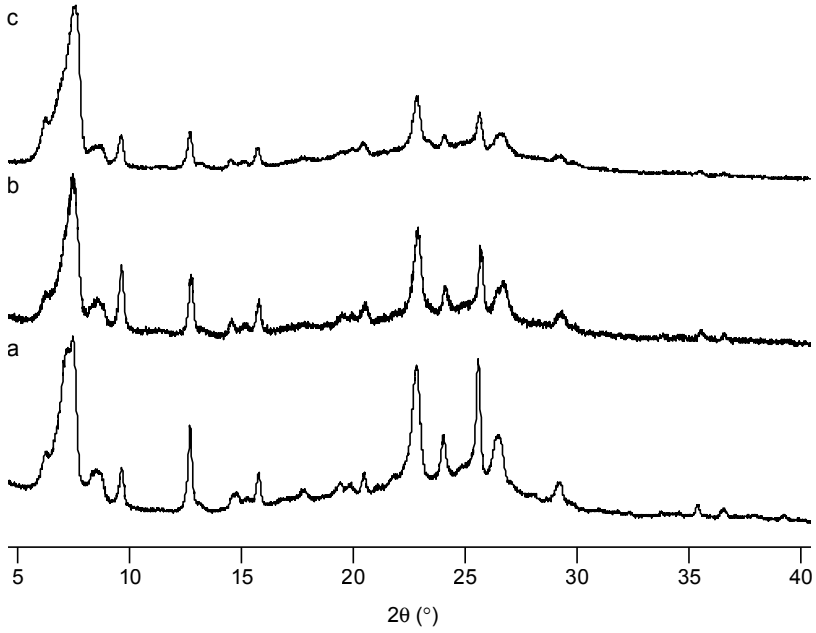

Figure 4.25 *Capillary PXRD patterns of (a) post-synthesis aluminated Ge-UTL, (b) calcined version of the sample in (a) and (c) exchanged and recalcined version of the sample in (b).*

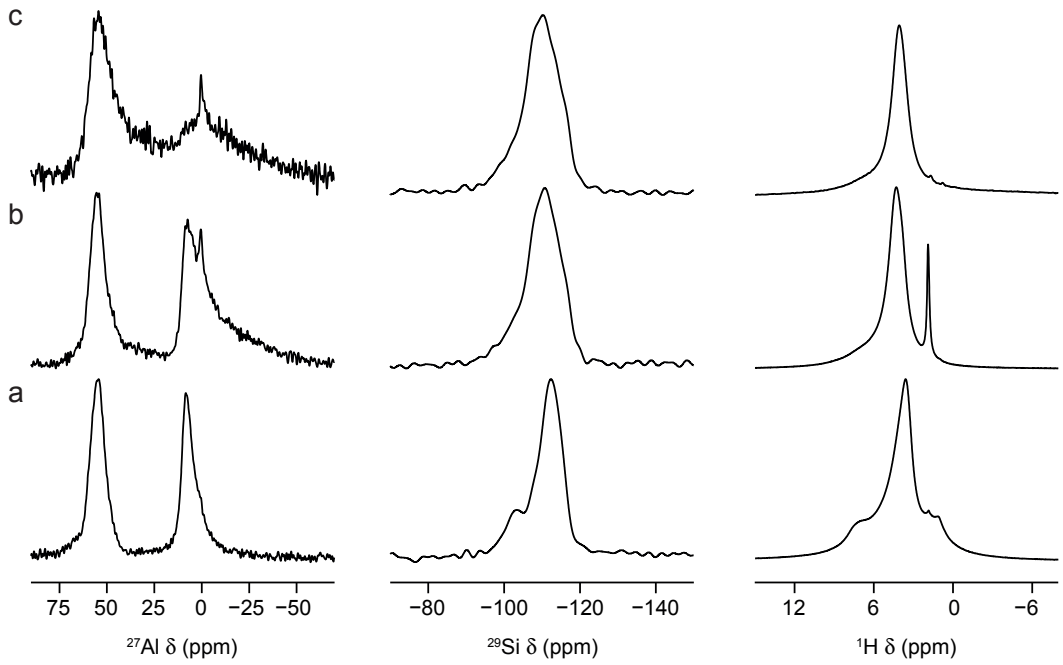

Figure 4.26 *^{27}Al (short flip angle), ^{29}Si and ^{1}H (9.4 T, 10 kHz) MAS NMR spectra of (a) post-synthesis aluminated Ge-UTL, (b) calcined version of sample in (a) and (c) exchanged and recalcined version of the sample in (b).*

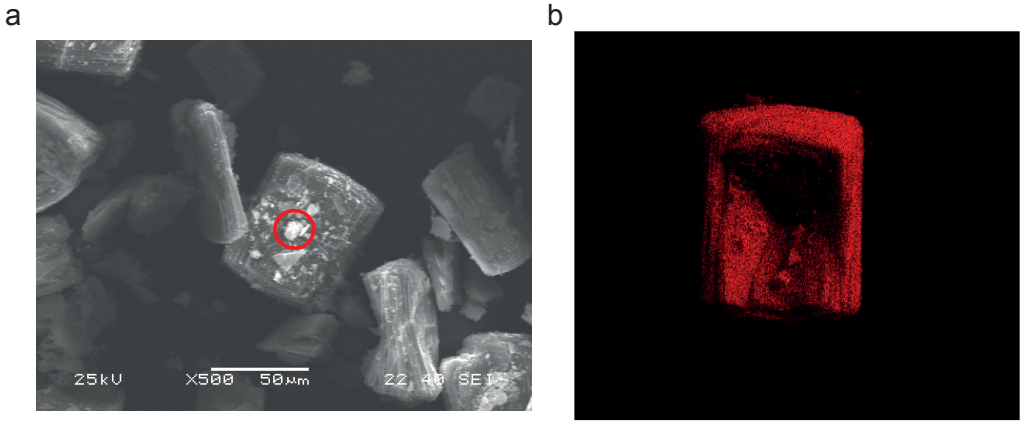

Figure 4.27 *(a) SEM image of calcined post-synthesis aluminated Ge-UTL with evidence of dealumination as shown by the particle highlighted by the red circle on the surface of the platelet. (b) Mapping of a different platelet of the same sample analysed in (a) showing evidence of Al zoning on the surface.*

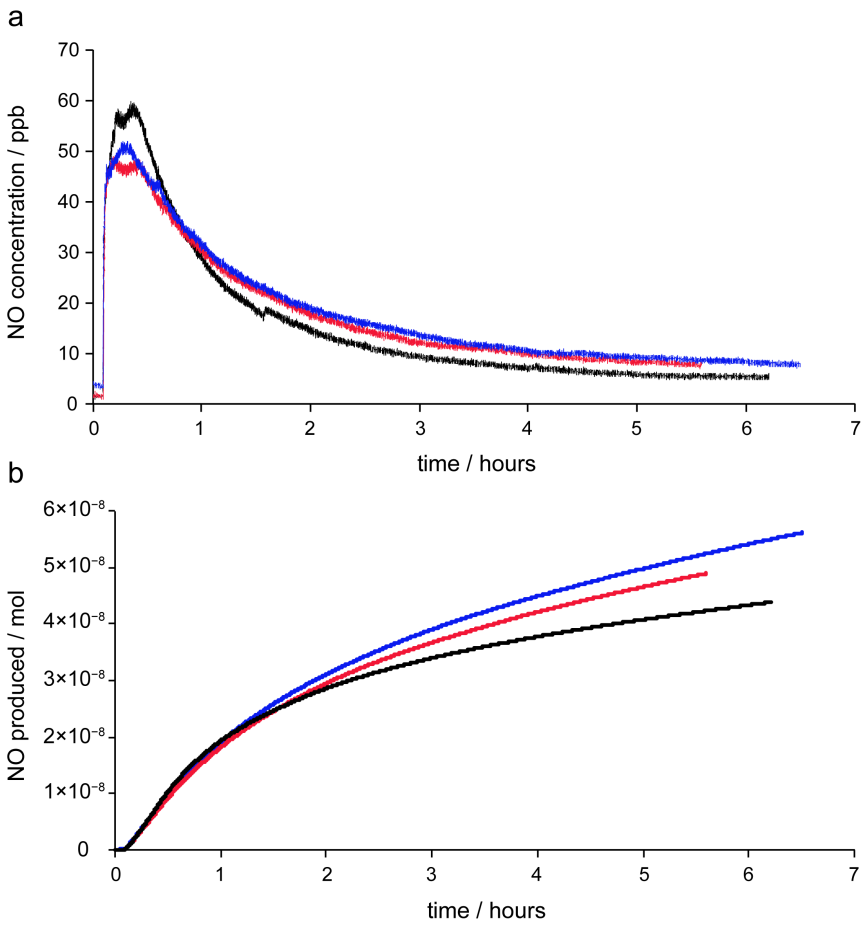

Figure 4.28 *Representative plots of (a) NO concentration and (b) NO produced, obtained from the integration of (a), as a function of time for the post-synthesis aluminated Ge-UTL calcined, exchanged according to procedure (i) and finally recalcined. Catalytic tests have been carried out in triplicate as shown by the different coloured lines in (a) and (b).*

Since the phenomenon of dealumination/Al migration was observed upon calcination, all successive samples have been exchanged directly from the post-synthesis procedure without any prior heat treatment. Figure 4.29 compares SEM images of the samples exchanged at high and room temperature and then recalcined, showing that the typical morphology of UTL is preserved even when performing the exchange procedure at high temperature. The diffraction patterns shown for all the exchanged and recalcined samples in Figure 4.30 are characterised by little or no variation, even when compared to the starting material.

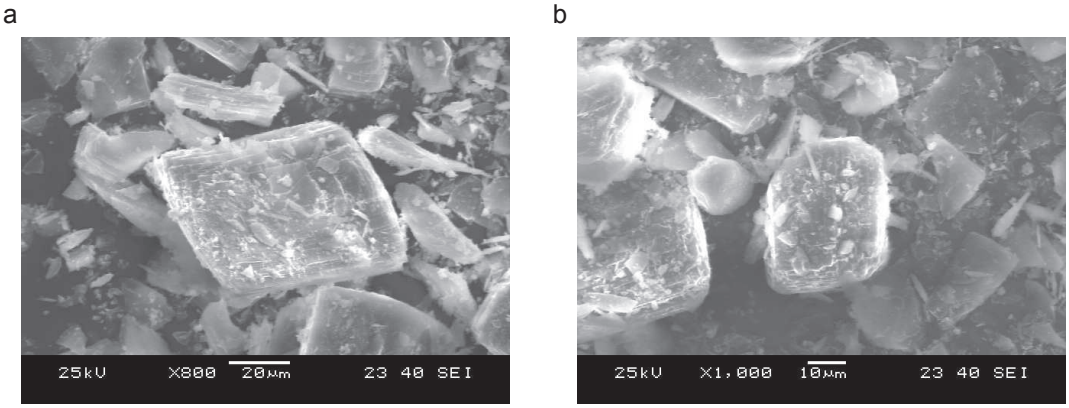

Figure 4.29 *SEM images of post-synthesis aluminated Ge-UTL samples exchanged (a) for 2 h at 80 °C in 0.6 M NH_4Cl and (b) overnight at room temperature in 0.06 M NH_4Cl and then recalcined.*

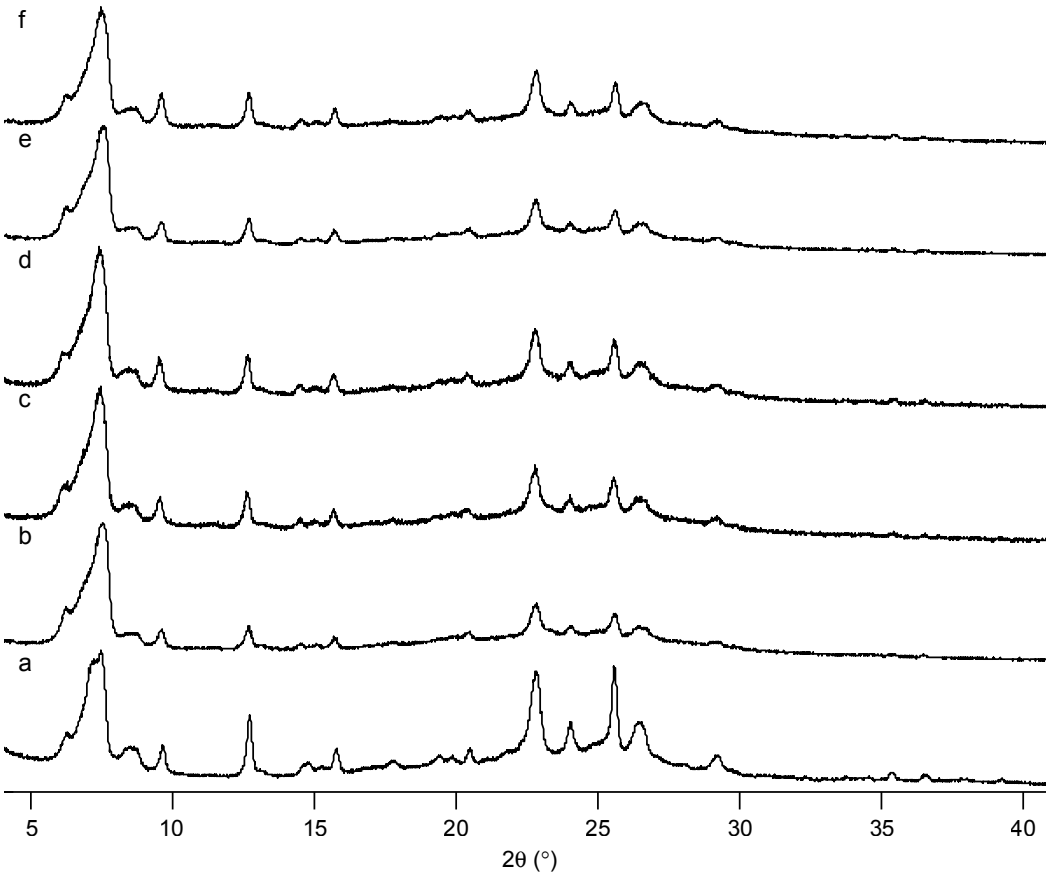

Figure 4.30 *Capillary PXRD patterns of (a) post-synthesis aluminated Ge-UTL and exchanged and recalcined versions of the sample in (a) according to procedure (i) for (b), (ii) for (c), (iii) for (d), (iv) for (e) and (v) for (f).*

^{27}Al MAS NMR spectra in Figure 4.31 show that the relative distribution of Al between the octahedral and tetrahedral sites is not changing significantly among the samples exchanged in different conditions and then recalcined. Moreover, a sharp resonance in the octahedral region can still be observed, probably resulting from the final recalcination after exchange.[12] In an analogous way, no changes could be observed in the ^{29}Si or ^{1}H MAS NMR spectra that proved in all cases to be comparable to the ones shown in Figure 4.26c. The results from catalytic tests listed in Table 4.3 show that samples exchanged and recalcined without calcination of the starting material had a better catalytic performance compared to the first sample that was exchanged after calcination of the starting aluminated Ge-UTL. No significant variation can be observed in the final values of NO produced from the samples exchanged at high temperature. For exchange procedures carried out at room temperature the lowest and highest concentrations of NH_4Cl result in higher NO production values, which, however, are lower than typical values of NO production from zeolite frameworks with acid sites tested in the same conditions (~250 nmol).[11]

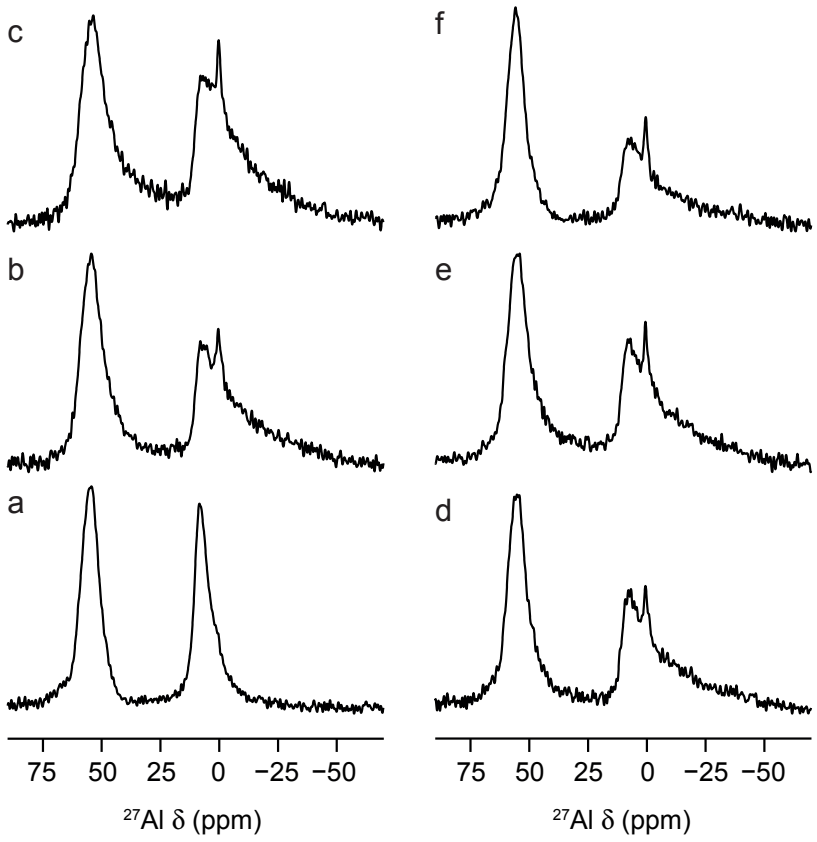

Figure 4.31 *Short flip angle ^{27}Al (9.4 T, 10 kHz) MAS NMR spectra of post-synthesis aluminated Ge-UTL (a) as-made and (b)-(d) exchanged and recalcined following procedures (i)-(v), respectively.*

Calcination of aluminated Ge-UTL prior to exchange	Exchange procedure	NO production / nmol
Yes	0.3 M overnight at RT	48 ± 5
No	0.3 M overnight at RT	66 ± 5
No	0.6 M overnight at RT	88 ± 7
No	0.06 M overnight at RT	98 ± 9
No	0.6 M 2 h at 80 °C	84 ± 5
No	0.06 M 2 h at 80 °C	92 ± 6

Table 4.3 *Table summarising sample preparation prior to exchange, different exchange procedures used and resulting NO production reported as average with associated standard deviation deriving from triplicate measurements on each sample. It should be noted that all exchange procedures are repeated three times and that all samples, once exchanged, are recalcined to obtain protonated sites for catalysis. In the absence of zeolite catalyst the NO production detected was 2 nmol. Exchange procedures and catalytic tests were performed in collaboration with Samantha Russell.*

While the exact structural nature of the octahedrally coordinated Al sites is not known, it is hypothesised these sites could be located on the surface of the zeolite.[15] ^{1}H-^{27}Al CP experiments, as the one shown in Figure 4.32, were carried out and showed selective enhancement mostly of the octahedral sites, suggesting these could be located in a more proton-rich environment than tetrahedral sites. No additional information was obtained from the corresponding ^{1}H-^{27}Al 2D (CP HETCOR) correlation experiments. However, more investigation is required on the processes of heteroatom introduction, especially post-synthesis, to study the influence of Al incorporation in the framework on the resulting catalytic activity. The identification of the location of the Al active sites and the characterisation of their inhomogeneous distribution in the framework of zeolites remains a challenging subject of ongoing research,[16] considering recent experimental and theoretical evidence of Loewenstein's rule violation.[17-18]

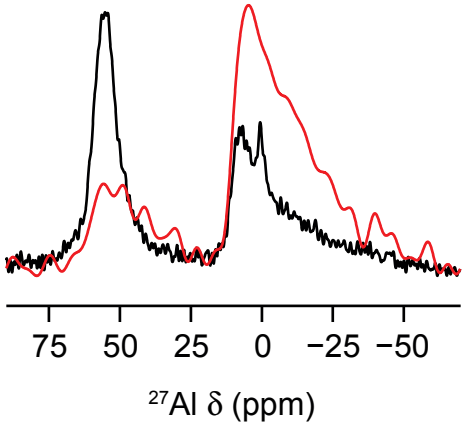

Figure 4.32 *^{1}H-^{27}Al CP and ^{27}Al short flip angle (9.4 T, 10 kHz) MAS NMR spectra, shown by red and black lines respectively, of the post-synthesis aluminated Ge-UTL exchanged following procedure (iii) and then recalcined.*

4.5 References

1 D. Massiot, F. Fayon, M. Capron, I. King, S. Le Calvé, B. Alonso, J.-O. Durand, B. Bujoli, Z. Gan and G. Hoatson, *Magn. Reson. Chem.*, 2001, **40**, 70–76.

2 P. A. Wright, in *Microporous Framework Solids*, Royal Society of Chemistry, Cambridge, 2007, Chapter 2.

3 X. S. Zhao, G. Q. Lu, A. K. Whittaker, G. J. Millar and H. Y. Zhu, *J. Phys. Chem. B*, 1997, **101**, 6525–6531.

4 P. S. Wheatley, P. Chlubná-Eliášová, H. Greer, W. Zhou, V. R. Seymour, D. M. Dawson, S. E. Ashbrook, A. B. Pinar, L. B. McCusker, M. Opanasenko, J. Čejka and R. E. Morris, *Angew. Chem. Int. Ed.*, 2014, **53**, 13210–13214.

5 H. E. Gottlieb, V. Kotlyar and A. Nudelman, *J. Org. Chem.*, 1997, **62**, 7512–7515.

6 H. N. Kim and S. K. Lee, *Geoch. Cosmochim. Acta*, 2013, **120**, 39–64.

7 A. E. Geissberger and P. J. Bray, *J. Non-Cryst. Solids*, 1983, **54**, 121–137.

8 E. R. H. van Eck, M. E. Smith and S. C. Kohn, *Solid State Nucl. Magn. Reson.*, 1999, **15**, 181–188.

9 S. E. Ashbrook and S. Sneddon, *J. Am. Chem. Soc.*, 2014, **136**, 15440–15456.

10 X. Xue and M. Kanzaki, *J. Phys. Chem. B*, 2001, **105**, 3422–3434.

11 S. E. Russell, J. M. González Carballo, C. Orellana-Tavra, D. Fairen-Jimenez and R. E. Morris, *Dalton Trans.*, 2017, **46**, 3915–3920.

12 S. M. Campbell, D. M. Bibby, J. M. Coddington, R. F. Howe and R. H. Meinhold, *J.Catal.*, 1996, **161**, 338–349.

13 D. E. Perea, I. Arslan, J. Liu, Z. Ristanović, L. Kovarik, B. W. Arey, J. A. Lercher, S. R. Bare and B. M. Weckhuysen, *Nature Commun.*, 2015, **6**, 7589–7596.

14 Z. Ristanović, J. P. Hofmann, G. De Cremer, A. V. Kubarev, M. Rohnke, F. Meirer, J. Hofkens, M. B. J. Roeffaers and B. M. Weckhuysen, *J. Am. Chem. Soc.*, 2015, **137**, 6559–6568.

15 J. A. van Bokhoven, D. C. Koningsberger, P. Kunkeler, H. van Bekkum and A. P. M. Kentgens, *J. Am. Chem. Soc.*, 2000, **122**, 12842–12847.

16 N. Danilina, F. Krumeich, S. A. Castelanelli and J. A. van Bokhoven, *J. Phys. Chem. C*, 2010, **114**, 6640–6645.

17 E. Pavón, F. J. Osuna, M. D. Alba and L. Delevoye, *Chem. Commun.*, 2014, **50**, 6984–6986.

18 R. E. Fletcher, S. Ling and B. Slater, *Chem. Sci.*, 2017, **8**, 7483–7491.

5 Isotopic enrichment of MOFs

The main focus of this chapter is the description of the synthetic procedures used for the isotopic enrichment of the terephthalate MOFs investigated in this work along with the results obtained from powder X-ray diffraction, electron microscopy and mass spectrometry. The different phases present at the various stages of the breathing process of the MOF structures, their morphology and cation distribution, as well as the final level of ^{17}O enrichment obtained are discussed.

5.1 Synthetic procedures for ^{17}O enrichment of terephthalate MOFs

Dry gel conversion (DGC) syntheses, introduced in Section 1.2.2, were carried out using the reagents as described in Table 5.1, following the method reported in He *et al.*,[1] but using different and mixed metals. The hydrated metal nitrates were used as the cation sources and 1,4-benzenedicarboxylic acid (H_2BDC) as the linker. The metal nitrates and H_2BDC were weighed and placed in a Teflon cup, which was then placed inside a Teflon-lined autoclave containing ^{17}O-enriched water (130 µL, 90% ^{17}O-enriched, CortecNet, 1800 €/g). Attempts to incorporate ^{17}O were also carried out with water with lower levels of enrichment (130 µL, 40% ^{17}O-enriched, CortecNet, 475 €/g) to reduce the cost per reaction. However, the resulting ^{17}O signal proved to be not sufficient to acquire high-resolution spectra on a reasonable timescale. Once sealed, the autoclaves were placed in an oven and heated to 200 °C at autogenous pressure for 72 h. The product was then recovered from the Teflon cup, washed with minimum amounts of water (~2 mL) to minimise any possible ^{17}O loss, and left overnight to dry in air. In the cases where $Al(NO_3)_3.9H_2O$ or $Ga(NO_3)_3.xH_2O$ were used as starting reactants, MIL-53 MOFs were obtained and the resulting products were white. When mixing different metals their proportion in the final MOFs was different to the stoichiometric ratio. In the following sections, XRD, EDX and NMR results for the determination of the actual metal ratio present in the final MOFs will be discussed. For DGC syntheses starting from $Sc(NO_3)_3.xH_2O$, the product formed was shown to be the smaller pore MOF Sc_2BDC_3, with a yellow colour, rather than the intended MIL-53 material. In the case

where $Al(NO_3)_3.9H_2O$ and $Sc(NO_3)_3.xH_2O$ were mixed in the DGC synthesis, two separate phases were obtained containing the two separate MOFs: Al MIL-53 and $Sc_2(BDC)_3$.

$Al(NO_3)_3.9H_2O$ / mmol	$Ga(NO_3)_3.xH_2O$ / mmol	$Sc(NO_3)_3.xH_2O$ / mmol	H_2BDC / mmol	Product[a]
1.38	-	-	1.81	Al MIL-53
-	1.38	-	1.81	Ga MIL-53
0.69	0.69	-	1.81	(Al,Ga) MIL-53 (50:50)
1.10	0.28	-	1.81	(Al,Ga) MIL-53 (80:20)
0.69	-	0.69	1.81	Al MIL-53 + $Sc_2(BDC)_3$
-	-	1.38	1.81	$Sc_2(BDC)_3$

[a] Stoichiometric ratios are reported in brackets for MIL-53 mixed-metal compounds.

Table 5.1 *Molar quantities of reagents used for DGC syntheses. In the cases where the water content of the nitrate salt was not known exactly the weight was determined on the basis of the anhydrous molar mass. After DGC syntheses, ~310 mg of product were recovered.*

Attempts to prepare Sc MIL-53 in a DGC synthesis failed even when changing reaction conditions. In particular, the amount of H_2BDC used in the reaction was decreased, considering the lower metal:linker ratio of $Sc_2(BDC)_3$, and the reaction temperature was lowered, as the $Sc_2(BDC)_3$ phase is more stable at higher temperatures due to the lack of any easily removable coordinated species.[2] Sc MIL-53 was then synthesised solvothermally as described in Mowat *et al*.[3] A solution of $Sc(NO_3)_3.xH_2O$ (0.117 g), H_2BDC (0.068 g), pyridine (0.487 g) and *N,N*-dimethylformamide (6 g) was stirred, subsequently transferred to a Teflon-lined autoclave and then heated to 190 °C at autogenous pressure for 40 h. The resulting compound was filtered and washed with ethanol to remove DMF and pyridine before drying overnight at 60 °C in air. Once the product was obtained using the solvothermal route, ^{17}O enrichment through post-synthetic steaming was performed, by placing the material into a Teflon cup, which was then placed inside a Teflon-lined autoclave containing ^{17}O-enriched water (130 μL, 90% ^{17}O-enriched,

CortecNet, 1800 €/g). The autoclave was then heated to 200 °C at autogenous pressure for 72 h, after which the product was recovered from the Teflon cup. Calcination of this enriched sample was carried out by heating the sample in a tube furnace at 350 °C for 12 h under N_2 gas flow to avoid any ^{17}O back-exchange. For all other samples, calcination of Al, Ga, Sc and mixed-metal as-made terephthalate MOFs was performed by heating the compounds, placed in ampules or capillaries, in a Buchi furnace at 300 °C under a dynamic vacuum of 10^{-3}-10^{-4} Torr, generated initially by a rotary pump and, subsequently, by a diffusion pump, for a total of 72 h, enabling the removal of unreacted linker from within the MOF pores. In an analogous way, dehydration was carried out using the same equipment, but at a reduced temperature of 100 °C for 20 h. The calcined and dehydrated samples were then flame-sealed under an argon atmosphere. To avoid rehydration, for the NMR investigation, calcined and dehydrated samples were quickly packed in rotors after breaking open the ampules in air. For PXRD characterisation, capillaries were either quickly packed in air or, for dehydrated samples only, packed prior to the dehydration process, which was then carried out *in situ* and completed with the sealing of the capillaries under argon. A systematic protocol of hydration and dehydration was used for the study of the mixed-metal compounds that were left exposed to air to hydrate in vials covered by pierced plastic paraffin film for a minimum of five days and then dehydrated in the conditions outlined above.

5.2 Powder X-ray diffraction characterisation

Figures 5.1 and 5.2 show PXRD patterns of as-made, calcined, hydrated and dehydrated Al MIL-53 and Ga MIL-53, respectively. In the case of Al MIL-53, the as-made form with disordered excess terephthalic acid in the pores converts to the large-pore (lp) form after calcination. This large-pore form, upon exposure to atmospheric water, can be reversibly converted to the narrow-pore (np) hydrated form. However, for Ga MIL-53 this final stage is not as reversible, with the narrow-pore form observed to be stable also in dehydration conditions.[4] Figure 5.2 also reveals the partial decomposition[5] of Ga MIL-53 in the calcination conditions used.

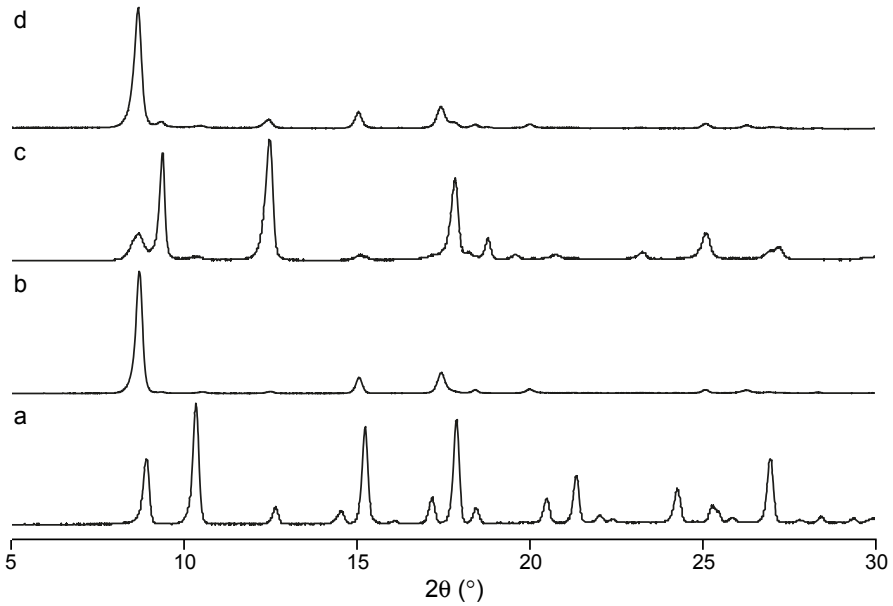

Figure 5.1 *Stacked PXRD patterns of Al MIL-53 in its (a) as-made, (b) calcined large-pore, (c) hydrated narrow-pore and (d) dehydrated large-pore forms.*

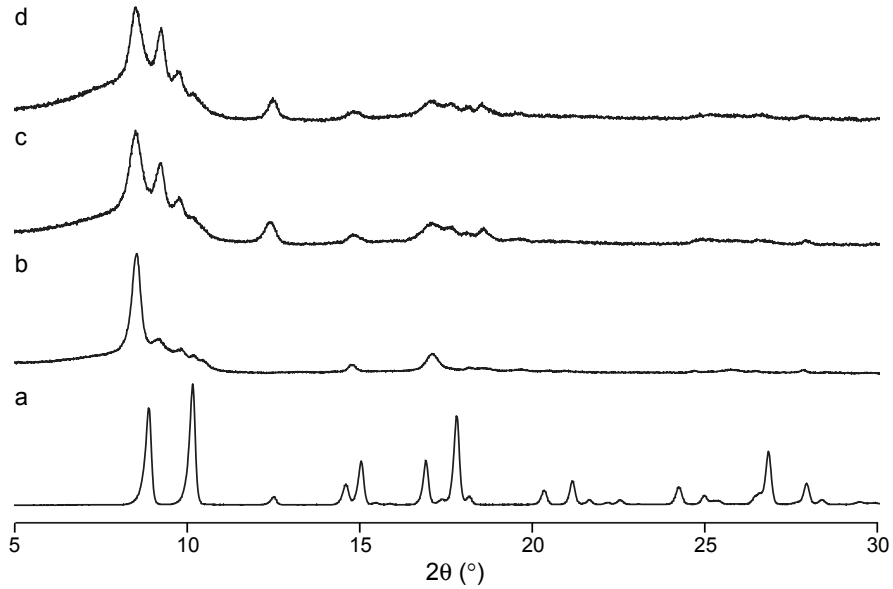

Figure 5.2 *Stacked PXRD patterns of Ga MIL-53 in its (a) as-made, (b) calcined large-pore, (c) hydrated narrow-pore and (d) dehydrated narrow-pore forms.*

For the mixed-metal materials, with Al:Ga 50:50 and 80:20 nominal compositions, refinements of the PXRD data were carried out by Dr Samuel Morris using TOPAS v5.2 between 3-50° 2θ. Pawley refinements were carried out step-wise, refining the background first, followed by experimental and peak shape functions and lattice parameters. If a Rietveld refinement was to be carried out, atoms were added in and

bond length and angle restraints used to ensure a smooth convergence prior to refining atomic positions. The Al/Ga ratio was determined by modelling both over a disordered site with a total occupancy of 1 and refining their relative occupancies with fixed isotropic displacement parameters. Each element was refined with a single isotropic displacement parameter to reduce over-parameterisation. The disordered organic molecule found in the as-synthesised form was treated in the same fashion as in Loiseau *et al*.[6] Each carbon was treated with the same isotropic displacement parameter and occupancy factor that refined to an occupancy of 83.5(5)%.

Rietveld refinements of the PXRD patterns were carried out, as described, for the as-made forms of the two nominal compositions and are shown in Figures 5.3 and 5.4. The unit cell parameters derived from these fits are given in Tables 5.2 and 5.3. The refinements confirmed the presence of the two types of metal cations and are consistent with Al:Ga ratios of 70(2):30(2) (from a starting model with a composition of 50:50) and 78(2):22(2) (from a starting model with a composition of 80:20). Even if the refinement of PXRD data is not the ideal way to determine composition, these values are in agreement, as discussed in Section 5.3, with EDX results. A smaller cell volume for the sample with a nominal composition of 80:20, compared to the sample with a nominal composition of 50:50, confirms the lower degree of incorporation of Ga in the structure.

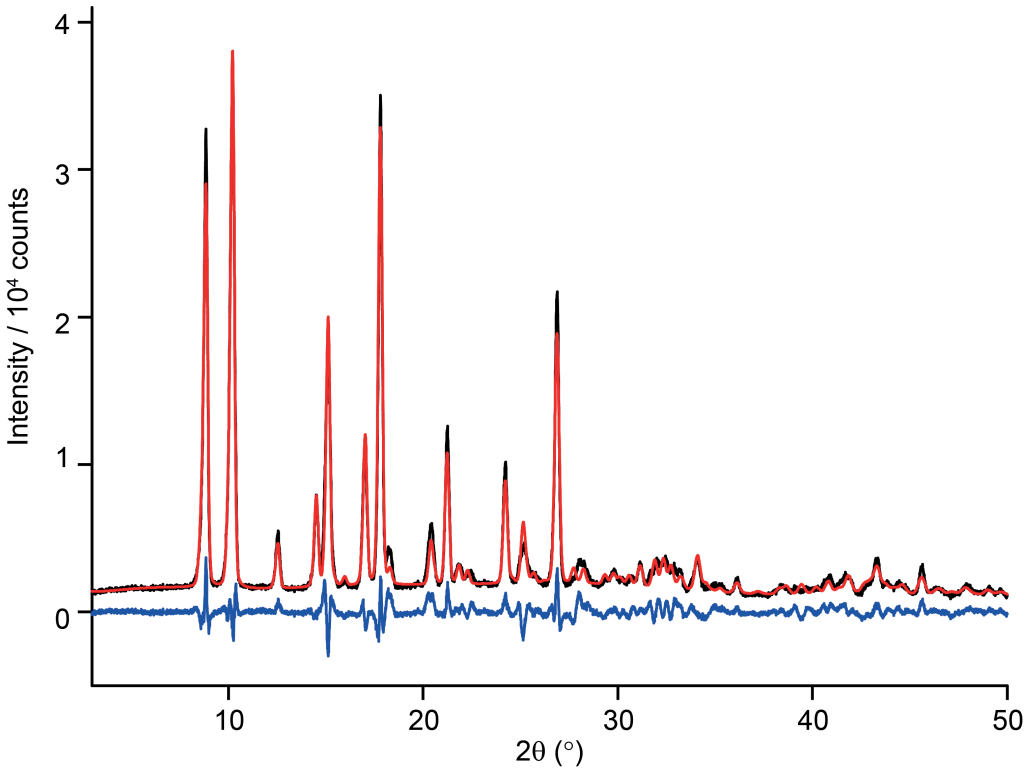

Figure 5.3 *Rietveld fit of the PXRD pattern for as-made Al,Ga MIL-53 with a nominal composition of 50:50 (shown in the extended 2θ range 3-50°).*

Parameter	
R_{wp} (%)	11.03
R_{exp} (%)	1.84
space group	*Pnma*
a / Å	17.220 (1)
b / Å	6.6553 (7)
c / Å	12.1545 (7)
volume / Å^3	1393.5 (2)

Table 5.2 *Unit cell parameters derived from the PXRD pattern in Figure 5.3 for Al,Ga MIL-53 with a nominal composition of 50:50.*

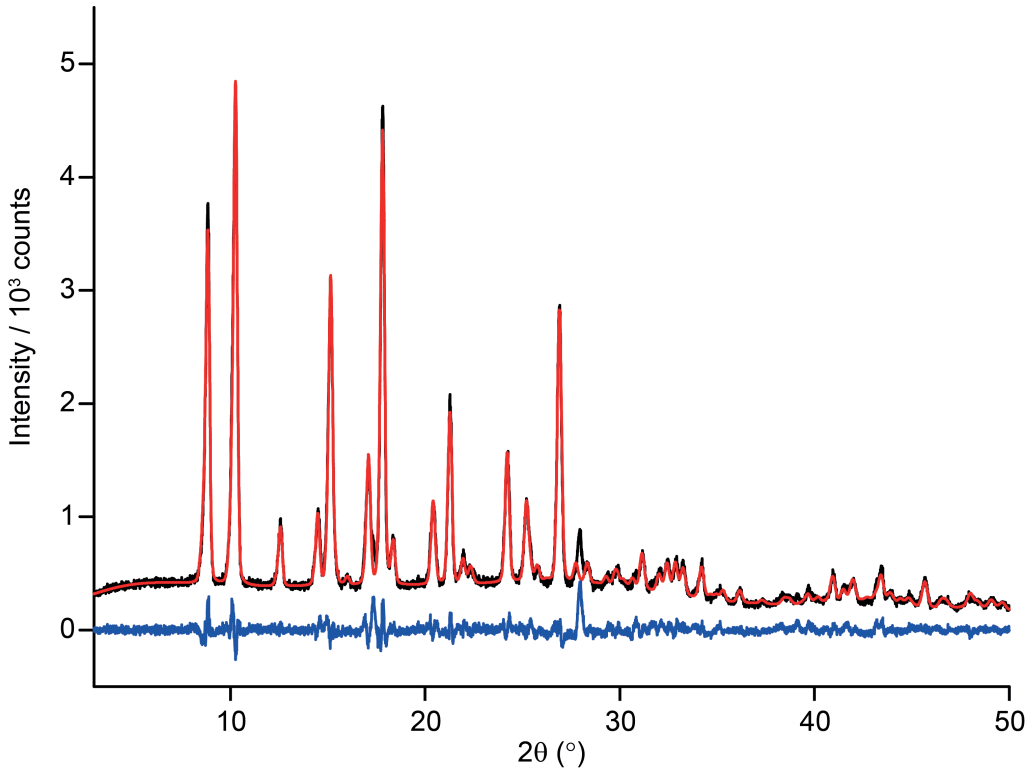

Figure 5.4 *Rietveld fit of the PXRD pattern for as-made Al,Ga MIL-53 with a nominal composition of 80:20 (shown in the extended 2θ range 3-50°).*

Parameter	
R_{wp} (%)	7.68
R_{exp} (%)	4.33
space group	*Pnma*
a / Å	17.118 (1)
b / Å	6.6284 (6)
c / Å	12.1666 (6)
volume / Å^3	1380.5 (2)

Table 5.3 *Unit cell parameters derived from the PXRD pattern in Figure 5.4 for Al,Ga MIL-53 with a nominal composition of 80:20.*

The mixed-metal Al,Ga MIL-53 sample with a nominal composition of 50:50 has been investigated throughout its breathing cycle, as shown in Figure 5.5. For all stages Pawley fits have been carried out, with results reported in Table 5.4.

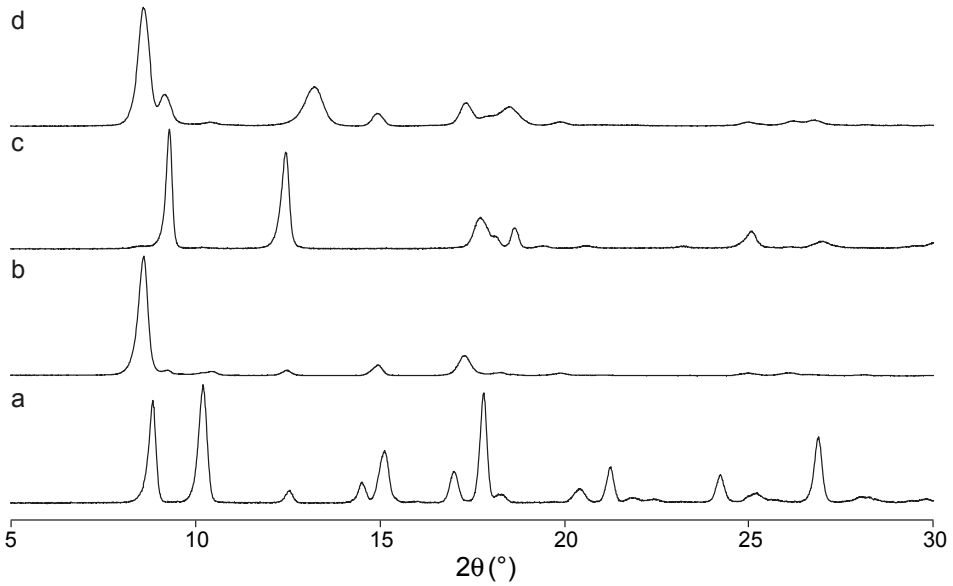

Figure 5.5 *PXRD patterns of (a) as-made, (b) calcined (large pore), (c) hydrated (narrow pore) and (d) dehydrated Al,Ga MIL-53 with a nominal composition of 50:50.*

	as-made	calcined		hydrated	dehydrated	
R_{wp} (%)	5.96	5.45		8.76	5.56	
R_{exp} (%)	1.82	3.16		2.61	1.79	
phase	as-made	lp	np	np	lp	np
space group	*Pnma*	*Imma*	*Cc*	*Cc*	*Imma*	*Cc*
a / Å	17.220 (1)	6.641 (1)	19.592 (9)	19.608 (3)	6.648 (1)	19.53 (3)
b / Å	6.6570 (5)	16.774 (5)	7.576 (2)	7.6637 (8)	16.803 (6)	7.1136 (9)
c / Å	12.1546 (6)	12.751 (5)	6.583 (3)	6.6203 (9)	12.799 (2)	6.98 (1)
β (°)	-	-	105.09 (8)	104.17 (2)	-	101.5 (5)
volume / $Å^3$	1393.3 (2)	1420.4 (7)	943.4 (9)	964.6 (2)	1429.8 (7)	951 (3)

Table 5.4 *Results from Pawley fits of PXRD patterns, shown in Figure 5.5, of as-made, calcined, hydrated and dehydrated Al,Ga MIL-53 with a nominal composition of 50:50.*

The unit cell size, as reported in Table 5.4, is larger than that observed for the same breathing stages of the original Al MIL-53 structure,[6] confirming substitution of the larger Ga cation in the structure. Upon calcination, this mixed-metal form showed no evidence of decomposition, unlike pure Ga MIL-53, suggesting that the mixture of Al with Ga stabilised the structure throughout the calcination process. The presence of a minor np phase in the calcined material could be the result of traces of hydration or a small amount of Ga MIL-53 in the material keeping a narrow-pore (empty) form after calcination.[5] Upon dehydration, however, an interesting deviation from the known reversible breathing behaviour for Al MIL-53 was observed, as shown in Figure 5.5d. The dehydrated form is characterised by the presence of a mix of narrow-pore and large-pore forms. The results from Pawley fits shown in Table 5.4 suggest that the dehydrated narrow-pore form is slightly distorted compared to the hydrated form of the same compound. To exclude any possible interference from adsorption of small amounts of atmospheric water, the dehydration process was carried out *in situ* to avoid any air exposure of the solid packed in the capillary. Therefore, this behaviour can be explained by the greater thermodynamic stability of Ga MIL-53 in its narrow-pore form after dehydration (at 100 °C).[4] This hypothesis is also supported by EDX results, which will be shown in the following section, in relation to the non-uniform distribution of the two cations in different crystallites. Further insight into this unusual breathing behaviour will also be given on the basis of ^{13}C, ^{1}H and ^{17}O NMR results in Chapter 6. An analogous behaviour was observed for the mixed-metal Al,Ga MIL-53 sample with a nominal composition of 80:20, as shown for the various breathing stages in Figure 5.6. In the dehydrated state, as expected, the amount of narrow-pore form in the mixed-pore structure decreased, as shown in Figure 5.7 with a normalised comparison of the dehydrated patterns of the two nominal compositions.

When the DGC method was extended to Sc in order to obtain Sc MIL-53, the product repeatedly was a yellow powder, identified as $Sc_2(BDC)_3$,[2] as shown in Figure 5.8. This is a smaller pore MOF without any bridging hydroxyls in the structure, unlike MIL-53.

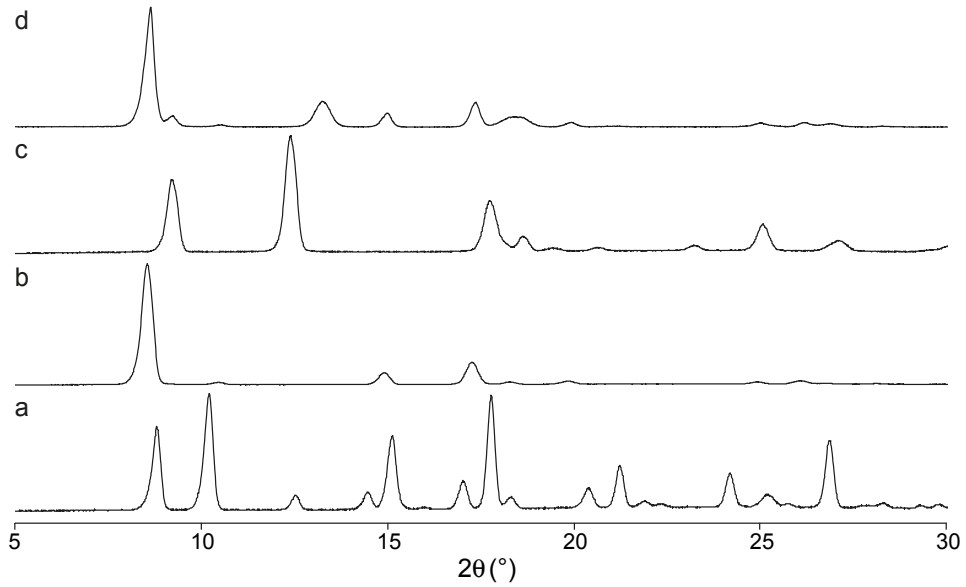

Figure 5.6 *PXRD patterns of (a) as-made, (b) calcined (large pore), (c) hydrated (narrow pore) and (d) dehydrated Al,Ga MIL-53 with a nominal composition of 80:20.*

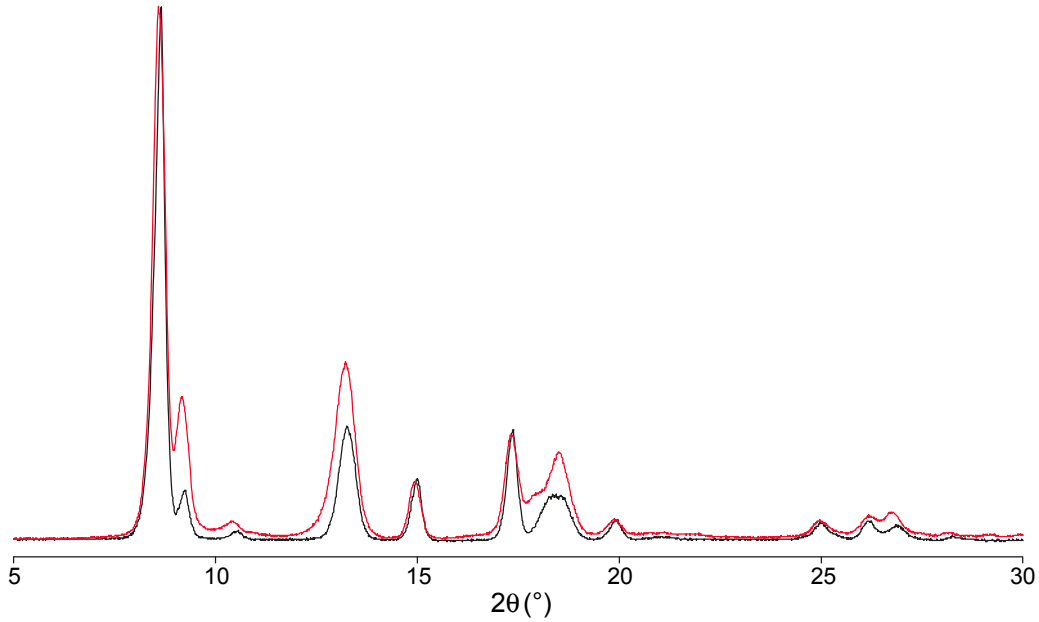

Figure 5.7 *Comparison of normalised PXRD patterns of dehydrated mixed-pore Al,Ga MIL-53 with nominal compositions of 80:20 (black line) and 50:50 (red line) showing the decreased intensity of the peaks related to the narrow-pore form in the sample with lower Ga content.*

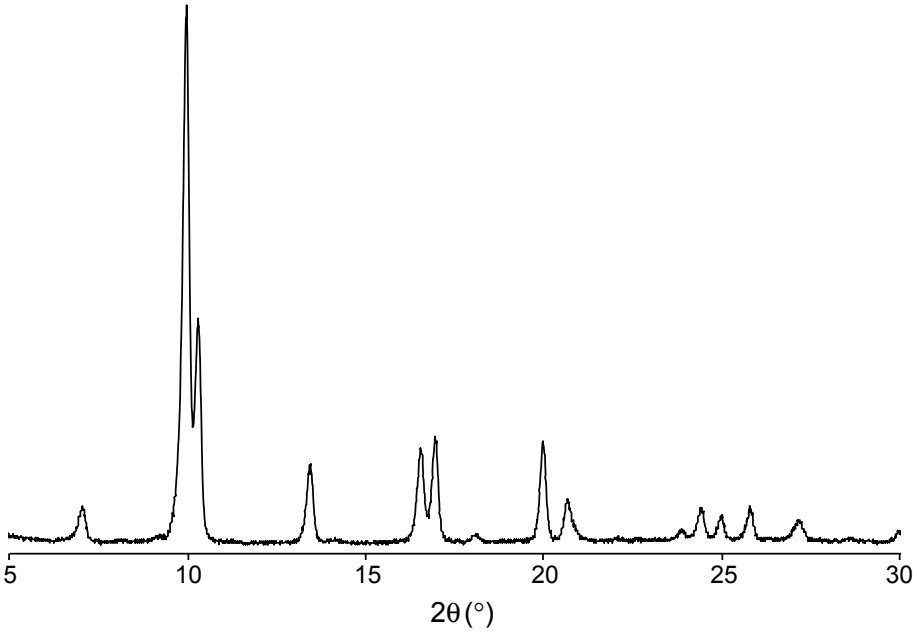

Figure 5.8 *PXRD pattern of $Sc_2(BDC)_3$.*[2]

When a mixture of $Al(NO_3)_3$ and $Sc(NO_3)_3$ was used in the DGC synthesis, a phase mixture of Al MIL-53 and $Sc_2(BDC)_3$ was obtained with little or no cation mixing, as shown in Figure 5.9, where the clear presence of the two separate phases can be observed. As already discussed, changes in the synthetic conditions did not help to obtain Sc MIL-53. Therefore, the desired MOF was first synthesised solvothermally, as described in Section 5.1, and subsequently steamed using DGC conditions in its as-made form, after washing with ethanol. The steaming process was initially monitored in unenriched conditions on a daily basis for three days to confirm the stability of the MOF and to find the best conditions for ^{17}O enrichment. The resulting patterns indicate that the starting as-made, ethanol-washed MOF (Figure 5.10a) survives the thermal treatment in a crystalline form, as shown in Figure 5.10. Peaks in the patterns of the steamed material (Figures 5.10b-d) show varying relative intensities as a function of steaming time and can be compared to the pattern obtained for a hydrated "intermediate"[3] Sc MIL-53, indicating the presence of exchanged water molecules in the pores. Subsequent batches of solvothermally synthesised Sc MIL-53 were characterised by the presence of the competing phase $Sc_2(BDC)_3$ in the synthesis, leading to an impure Sc MIL-53 product, as highlighted by the red box on the PXRD patterns of one of the batches in Figures 5.11a-c. This

batch was steamed in ^{17}O-enriched water and it was possible to record ^{17}O MAS spectra of the resulting steam-enriched product (as shown in Figure 6.25). (Possible variations in the level of the competing $Sc_2(BDC)_3$ phase after steaming or calcination in Figure 5.11 are challenging to evaluate due to changes in peaks positions and intensities.) Calcination was subsequently carried out to remove all guest species, i.e., solvent or any terephthalic acid, from the pores. Unexpectedly, upon calcination in inert conditions, this product, while retaining its crystallinity (see Figure 5.11c), lost considerable ^{17}O NMR signal compared to the original spectrum of the steamed material. This is not completely understood and will require more investigation to optimise the conditions for calcination. Moreover, it can be noted that patterns before and after calcination, Figures 5.11b and 5.11c, respectively, are very similar, probably because both products contain water molecules in their pores. Indeed, the steamed product has water molecules exchanged in the pores and the calcined product, once exposed to air, adsorbs atmospheric water. Further attempts to steam different batches of solvothermally synthesised Sc MIL-53 resulted in the partial or total transition of Sc MIL-53 to the $Sc_2(BDC)_3$ phase. This phenomenon, however, didn't occur when testing the steaming of Al MIL-53 in unenriched water, highlighting the need for further investigation in the optimisation of the steaming conditions more generally.

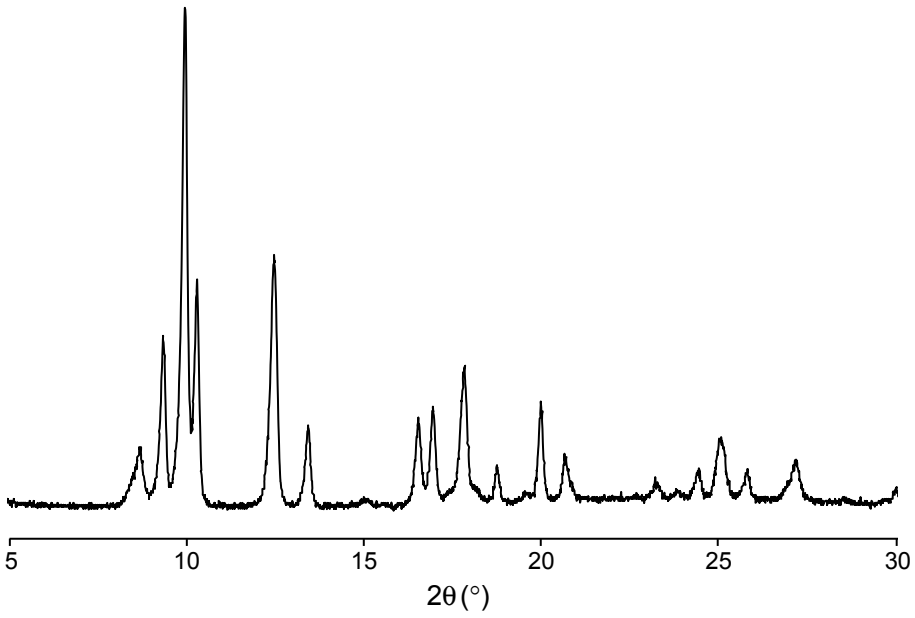

Figure 5.9 *PXRD pattern of mixed-phase Al MIL-53 and $Sc_2(BDC)_3$.*

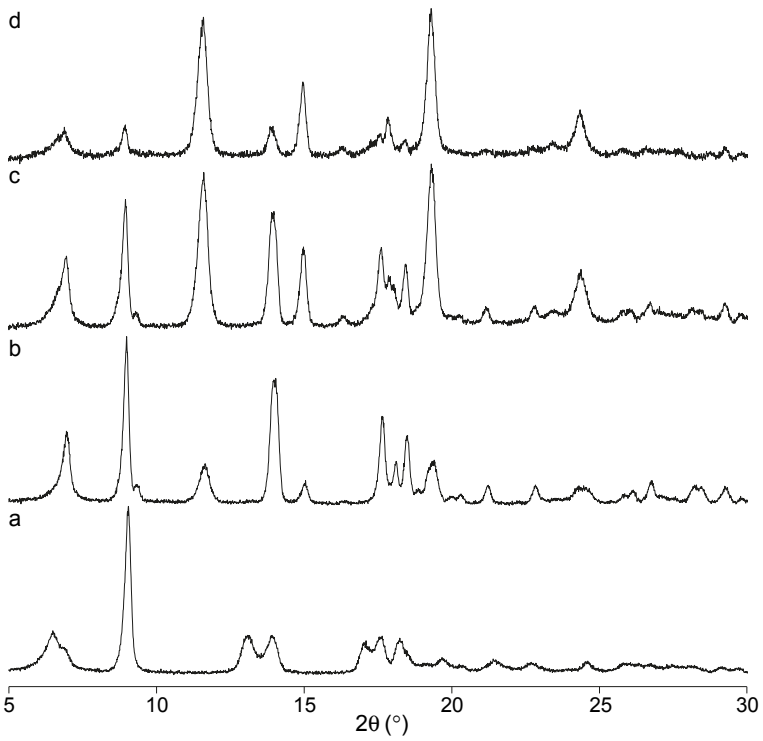

Figure 5.10 *PXRD patterns of (a) as-made ethanol-washed and dried (in air), (b) 1-day steamed, (c) 2-day steamed and (d) 3-day steamed Sc MIL-53.*

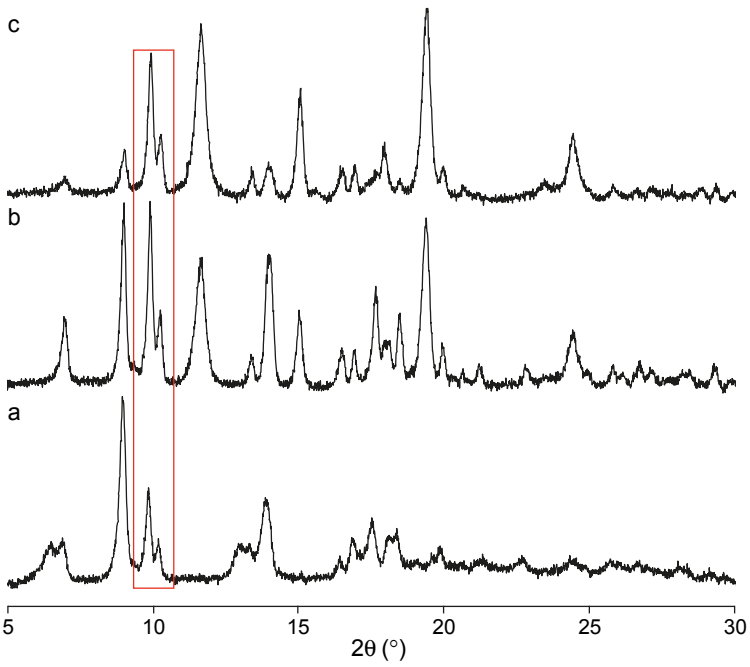

Figure 5.11 *PXRD patterns of the batch of Sc MIL-53 that was ^{17}O steam-enriched in its (a) as-made ethanol-washed and dried (in air), (b) 3-day steamed and (c) calcined and subsequently exposed to air forms. The peaks belonging to $Sc_2(BDC)_3$ are highlighted in the red box.*

5.3 SEM-EDX characterisation

A SEM-EDX study has been carried out on the synthesised MIL-53 MOFs to investigate the morphology of the final products, actual cation ratios and the cation distribution across crystallites. SEM images of as-made MIL-53 products, prepared by DGC, are shown in Figure 5.12.

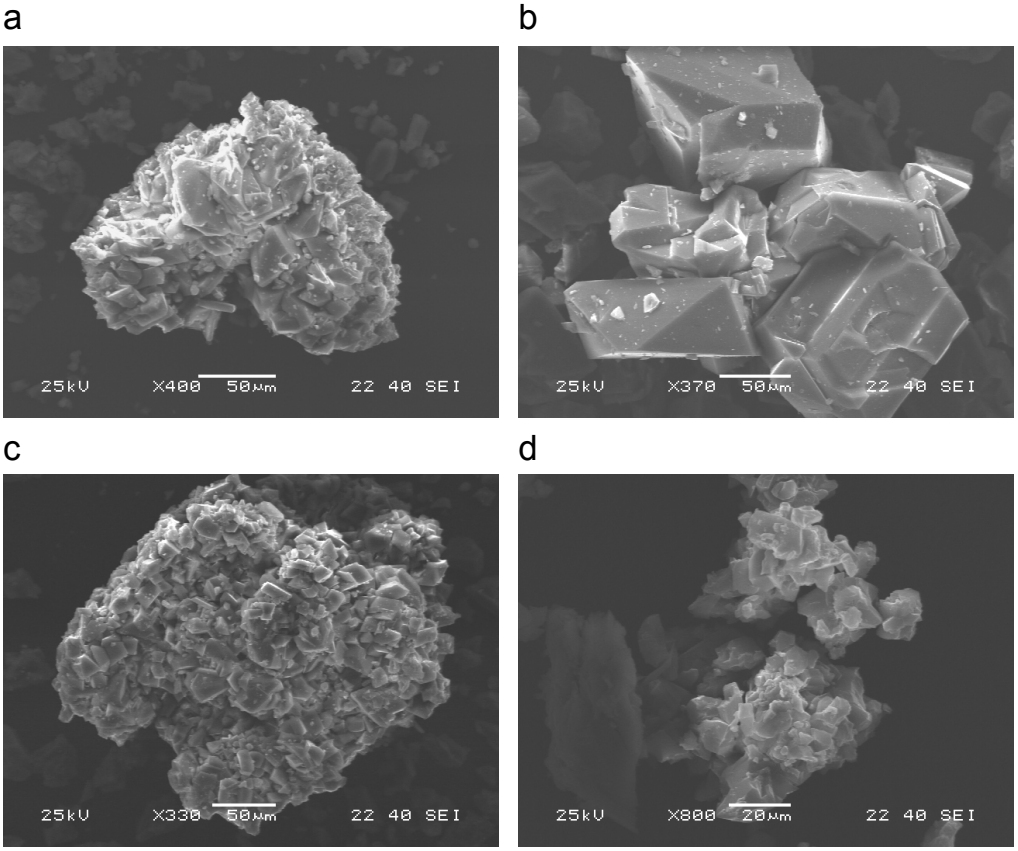

Figure 5.12 *SEM images of as-made (a) Al, (b) Ga, (c) Al,Ga (50:50, nominal composition) and (d) Al,Ga (80:20, nominal composition) MIL-53.*

It is possible to observe in Figure 5.12 the presence of aggregates formed by crystallites with approximate sizes of 20 to 50 µm for Al and mixed-metal MIL-53 samples and 100-150 µm for Ga MIL-53 samples. This confirms that the crystallinity of these materials is preserved even in DGC conditions, where very small amounts of solvent are used compared to the standard solvothermal conditions. To gain a better insight into the uniformity of the distribution of the Al and Ga cations between crystallites and the actual ratios of two metal centers in the mixed-metal compounds, EDX analyses were carried out on the sieved powders. These measurements were

performed on calcined samples to avoid any interference from unreacted material. A 250 mesh sieve (63 μm opening) was used to achieve a good dispersion of the crystallites and resolution of EDX measurements. A SEM image, representative of a typical sieved sample, is shown in Figure 5.13 for a calcined hydrated Al,Ga (50:50, stoichiometric ratio) MIL-53 sample.

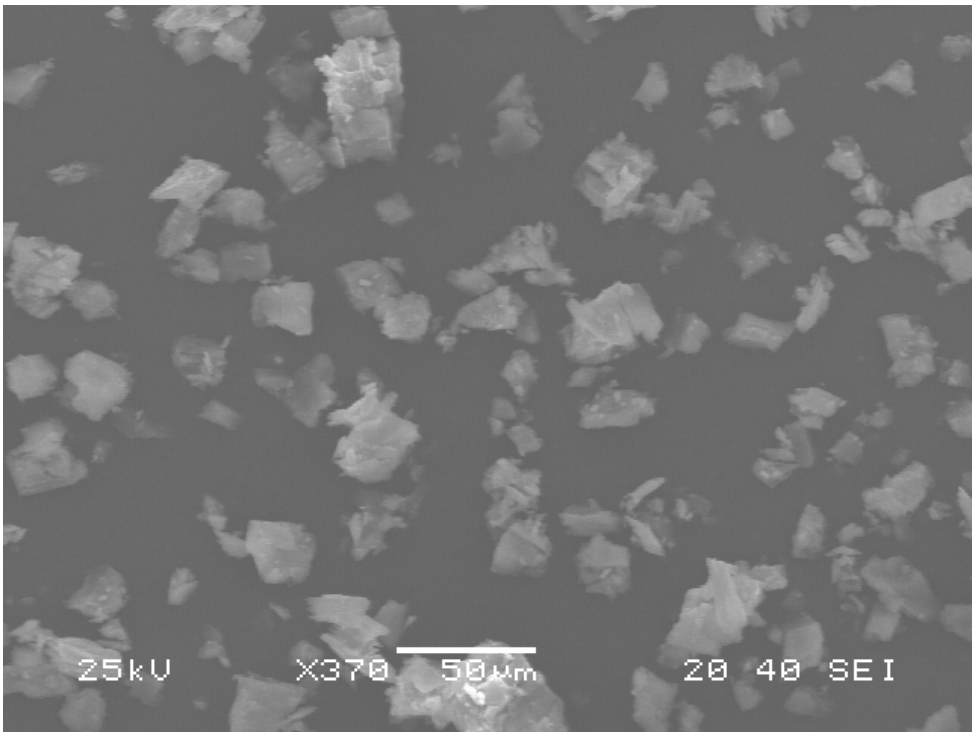

Figure 5.13 *SEM images of calcined hydrated Al,Ga (50:50, nominal composition) prepared for EDX measurements.*

Different batches of both 50:50 and 80:20 stoichiometric compositions have been analysed, see Table 5.5 and corresponding Figures 5.14-5.15, to obtain the average values of the Al:Ga ratio for each sample. For the 50:50 starting composition, the average values of Al:Ga ratio for the two batches analysed are 72:28 and 74:26. For the 80:20 composition, the average values of Al:Ga ratio for the two batches analysed are 84:16 and 83:17. The experimental variation for each measurement of Al(%) and Ga(%) has been determined by repeating the EDX measurement several times on the same area of some of the crystallites and has been quantified as ± 2 on the final percentage value. The average of all values has then been calculated for each sample batch and is reported with the standard deviation. It can be noted that a large standard deviation is associated with the average values and this can be related

to the significant distribution observed in the composition of each crystallite. This non-uniformity in the distribution of the two metal centers can probably be ascribed to the DGC method. Indeed, in this synthetic procedure the solid reactants are isolated from the small amounts of solvent used (130 μL) with a potentially reduced degree of mixing compared to a synthetic solution or gel. More generally, it is likely that the overall distribution and disorder of the metal centers will be affected by the synthetic, i.e., solvothermal or DGC, or post-synthetic, i.e., transmetallation,[7-8] route used to introduce different metals in the structure. Moreover, the difference in the Al/Ga composition in each crystallite suggests that different crystallites could adopt different forms depending on their Al and Ga content, supporting the XRD evidence discussed previously of a mixed-pore form upon dehydration. The average values obtained from EDX are in agreement with the Al:Ga ratios from Rietveld refinements, see Section 5.2, even if, as already pointed out, the numbers obtained from the refinement of PXRD data are affected by a significant uncertainty. Overall, it can be seen that, at least for the 50:50 stoichiometric composition, not all the Ga is incorporated in the final product. It should also be noted, however, that the hydration level of the starting hydrated nitrate salt is not known exactly.

Nominal sample composition of 50:50				Nominal sample composition of 80:20			
Sample batch 1		Sample batch 2		Sample batch 1		Sample batch 2	
Al (%)	Ga (%)	Al (%)	Ga (%)	Al (%)	Ga (%)	Al (%)	Ga (%)
59	42	71	29	74	26	86	14
61	39	68	32	72	28	89	11
73	27	62	39	76	24	85	15
86	14	75	25	61	39	77	23
69	31	65	35	91	10	91	9
69	31	85	15	91	9	87	13
72	28	71	29	66	34	90	11
63	37	84	16	89	11	89	11
69	31	72	28	92	8	81	19
69	31	80	20	91	9	79	21
73	27	84	16	93	7	92	8
68	32	84	16	90	10	81	19
75	26	72	29	94	6	88	12
88	13	75	25	91	9	86	14
81	19	65	35	91	9	77	23
71	29	42	58	67	33	72	28
68	32	83	17	90	10	95	5
90	10	74	26	92	8	82	18
		81	19	92	8	88	13
		85	15	88	13	78	22
		79	21	86	14	95	5
		74	26	70	31	96	4
				89	11	65	35
						60	40
						85	15
						71	29
						90	10
						94	6
						95	5
						87	13
						91	9
						71	29
						71	29
						88	12
						85	15
						94	6
						70	30
						74	26
						63	38
						84	16
						69	31
						88	12
						68	33
						84	17
						89	11
72 ± 9	28 ± 9	74 ± 10	26 ± 10	84 ± 11	16 ± 11	83 ± 10	17 ± 10

Table 5.5 *EDX measurements of Al and Ga content (%) for samples of calcined hydrated Al,Ga MIL-53 with nominal compositions of 50:50 and 80:20.*

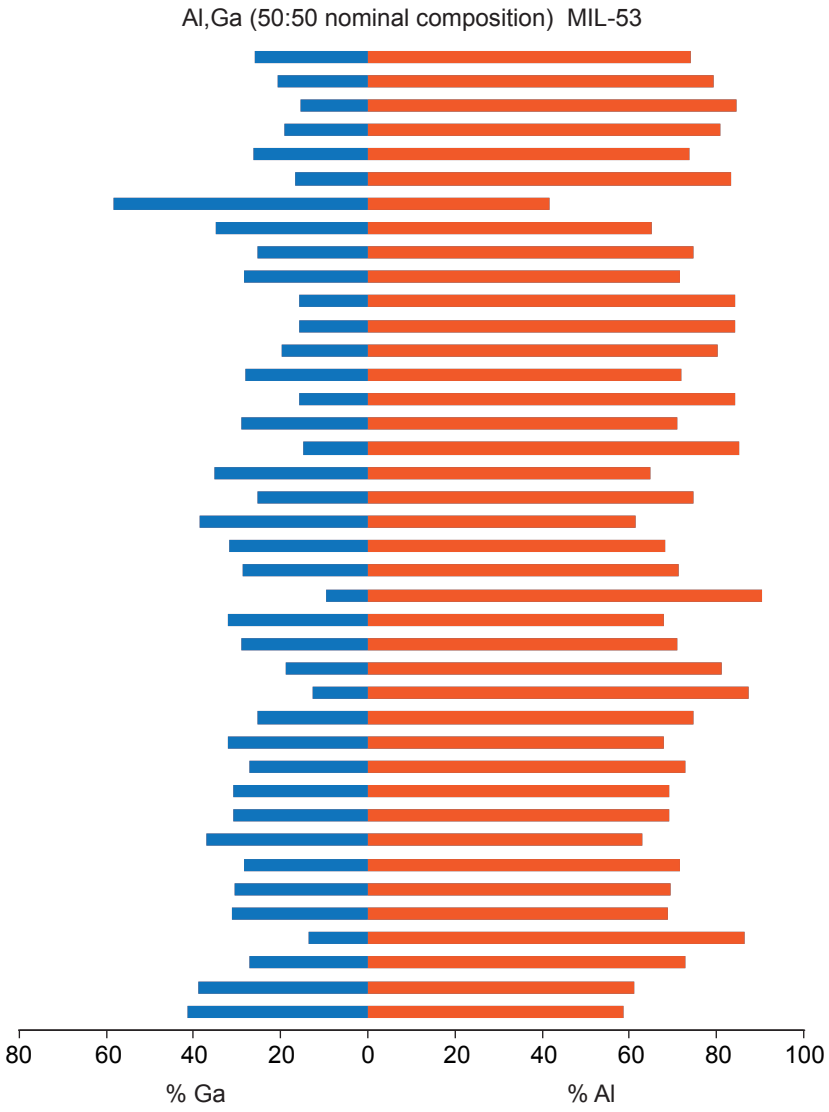

Figure 5.14 *Overall plot of the Al and Ga content (%) from EDX measurements for calcined hydrated Al,Ga MIL-53 samples (both sample batch 1 and 2 from Table 5.5) with a nominal composition of 50:50.*

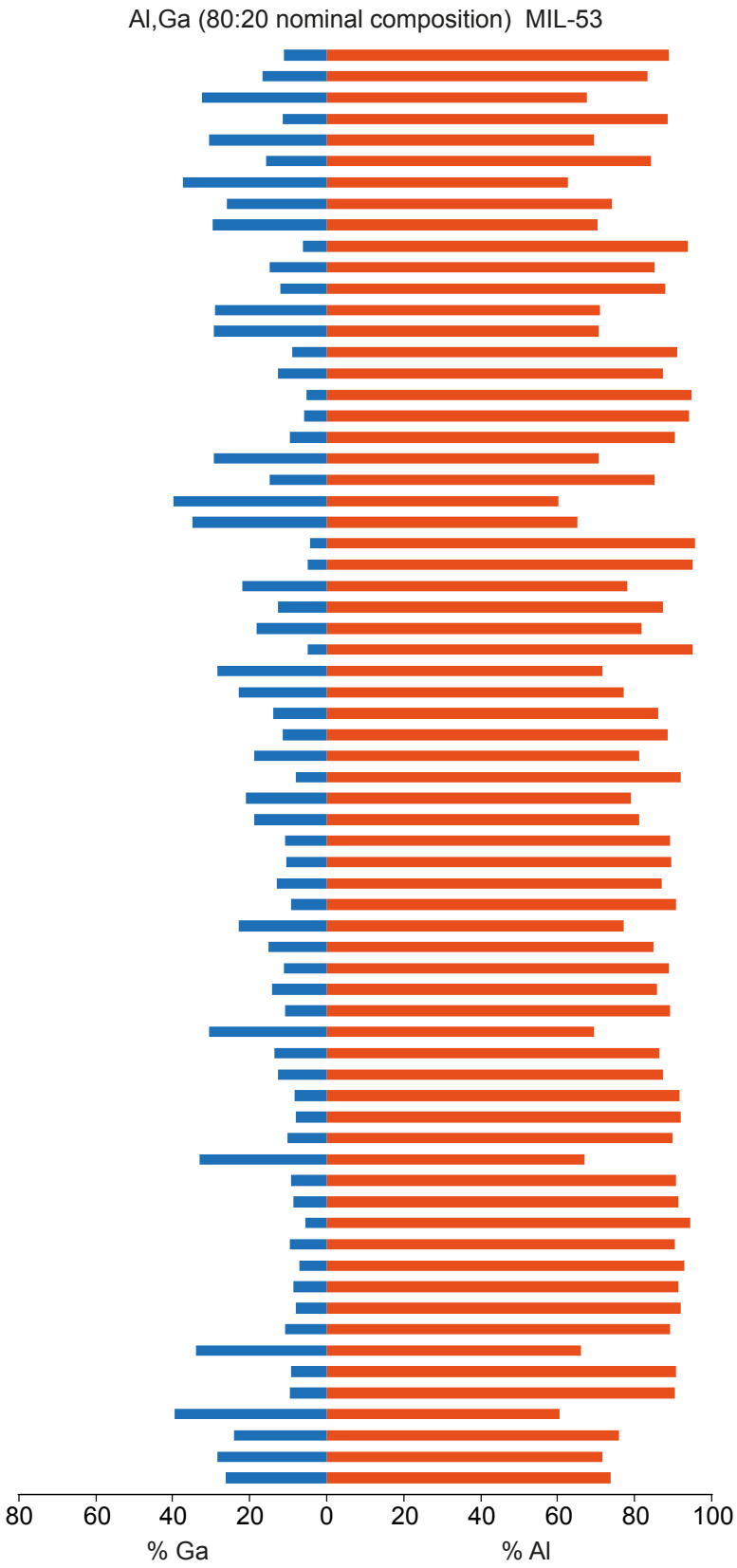

Figure 5.15 *Overall plot of the Al and Ga content (%) from EDX measurements for calcined hydrated Al,Ga MIL-53 samples (both sample batch 1 and 2 from Table 5.5) with a nominal composition of 80:20.*

5.4 Mass spectrometry characterisation

The isotopic composition of the synthesised MOFs was studied using mass spectrometry, introduced in Section 2.2.4, and samples were prepared for these measurements by embedding the MOF powders in indium mounts, as shown in Figure 5.16.

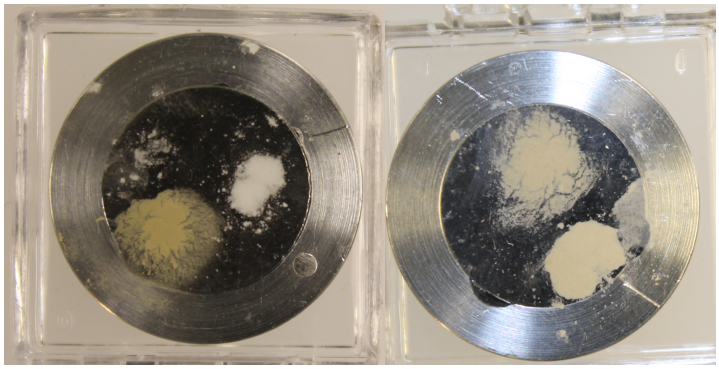

Figure 5.16 *Photograph of the Al disks containing the samples embedded in indium.*

SEM images in Figure 5.17 show the surface of the embedded MOFs and the traces left on the sample by the ion beam, after analysis.

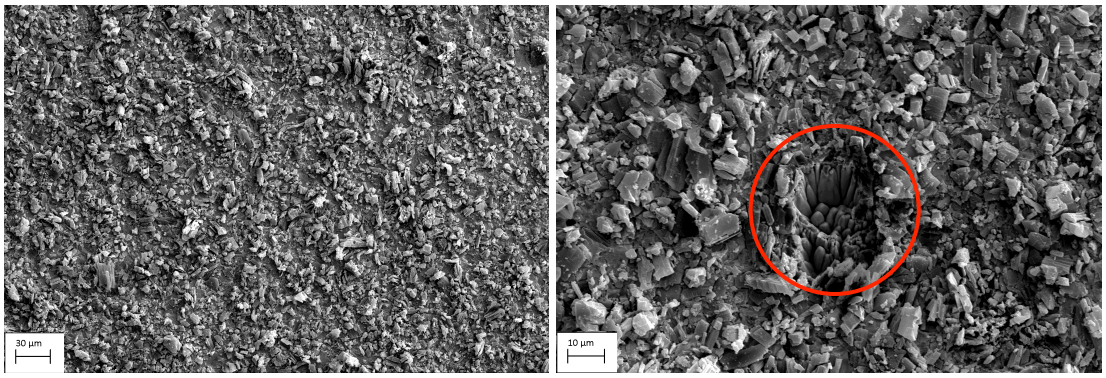

Figure 5.17 *SEM images of the surface of one of the MOF samples. On the right, it is possible to notice the traces (highlighted by the red circle) left on the surface by the ion beam after analysis.*

A mass scan was also carried out on a batch of natural abundance Al MIL-53 to identify the isotope peaks to be taken in consideration and confirm the resolution achieved by the instrumentation used, as shown in Figures 5.18-5.20.

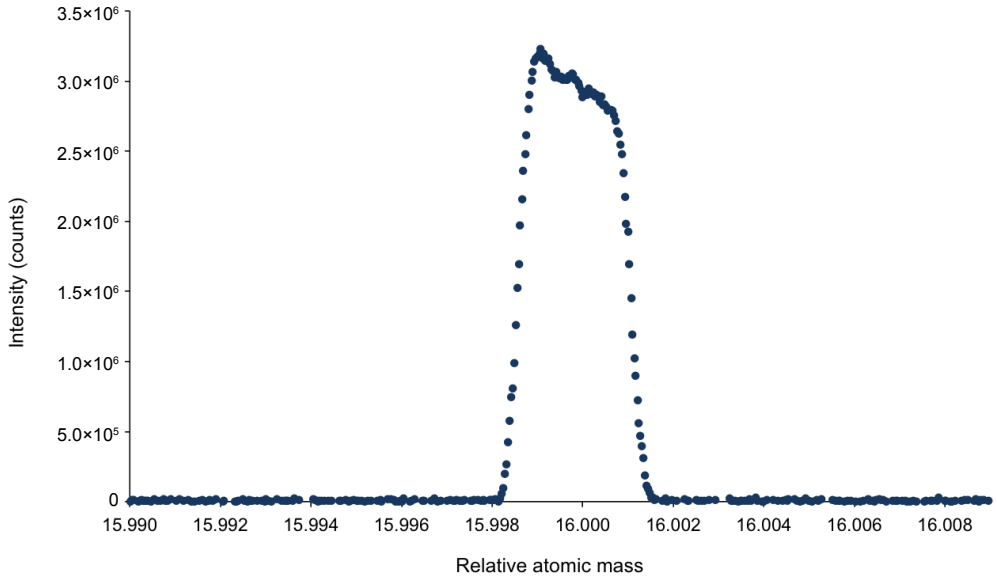

Figure 5.18 *^{16}O mass scan, showing the ^{16}O isotopic peak.*

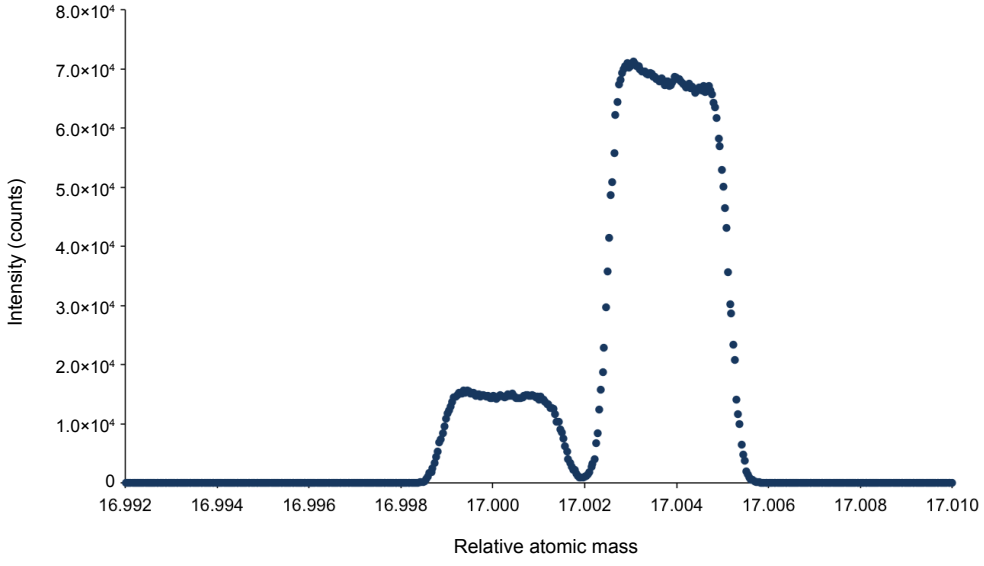

Figure 5.19 *^{17}O mass scan, showing the ^{17}O isotopic peak along with the ^{16}OH peak at a slightly higher mass.*

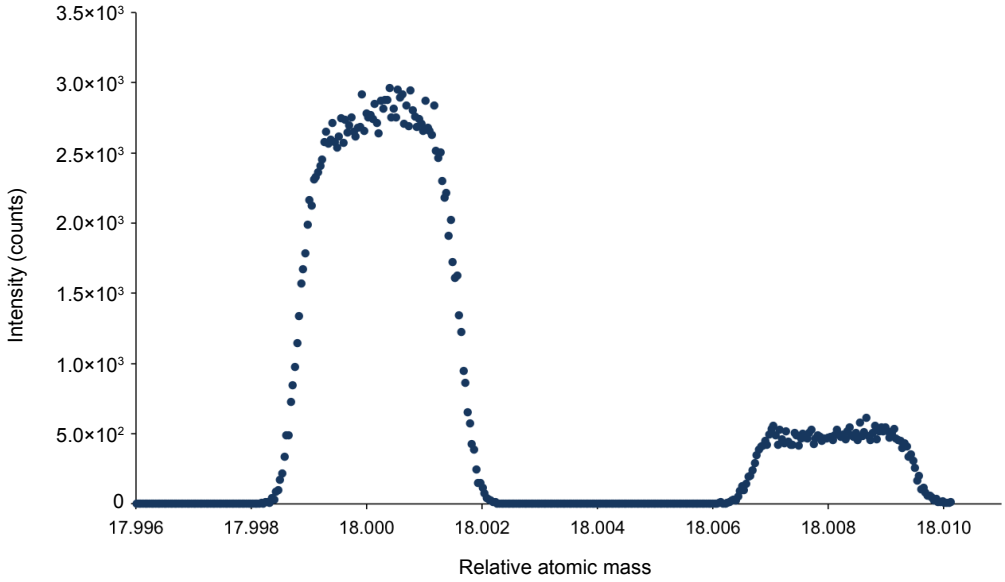

Figure 5.20 *^{18}O mass scan, showing the ^{18}O isotopic peak along with the ^{17}OH peak at a slightly higher mass.*

The results of the isotope ratio measurements carried out on this sample surprisingly showed a small level of ^{17}O enrichment of 0.95%. This could be due to some ^{17}O-enriched H_2O left absorbed in the Teflon liner of the autoclave from previous syntheses using enriched water.

For ^{17}O-enriched MIL-53 MOFs the results of the mass spectrometry characterisation are reported below as counts per isotope, with the instrumental standard error of the mean per measurement. As-made, calcined and hydrated samples of Al or mixed-metal Al,Ga MIL-53 from different synthetic batches have been analysed and results are shown in Tables 5.8 to 5.10. The final percentage of ^{17}O is obtained by comparison to the natural abundance $^{16}O/^{17}O$ ratio and is reported as the interval determined by the standard deviation calculated on the average of all measurements. As a reference, a natural abundance ilmenite sample was also analysed, Table 5.6, along with a batch of a natural abundance Al MIL-53 sample (different to the one used for mass scan experiments, see Figures 5.18-5.20), Table 5.7.

^{16}O (counts)	% standard error	^{17}O (counts)	% standard error	^{18}O (counts)	% standard error
4.20×10^8	3.1	1.49×10^5	3.0	7.50×10^5	3.1
5.14×10^8	0.3	1.83×10^5	0.2	9.38×10^5	0.2
5.15×10^8	0.1	1.82×10^5	0.1	9.32×10^5	0.1

Table 5.6 *O isotopes in the standard $FeTiO_3$ (ilmenite) sample, used as a reference with a flat and polished surface. The amount of ^{17}O detected is 0.035-0.036%.*

^{16}O (counts)	% standard error	^{17}O (counts)	% standard error	^{18}O (counts)	% standard error
6.18×10^7	4.9	2.17×10^4	4.9	1.07×10^5	5.0
2.30×10^7	13.0	7.93×10^3	13.0	3.80×10^4	13.0
1.44×10^7	13.0	4.93×10^3	13.0	2.39×10^4	13.0

Table 5.7 *O isotopes in a natural abundance calcined hydrated Al MIL-53 sample, prepared by DGC. The amount of ^{17}O detected is 0.034-0.035%.*

^{16}O (counts)	% standard error	^{17}O (counts)	% standard error	^{18}O (counts)	% standard error
8.34×10^7	1.8	1.59×10^7	1.9	2.59×10^5	1.7
1.21×10^7	5.4	2.15×10^6	5.4	3.51×10^4	6.7
3.49×10^7	1.3	8.57×10^6	1.7	1.26×10^5	1.5
1.02×10^8	0.3	1.86×10^7	0.4	3.12×10^5	0.3
1.27×10^8	0.7	2.31×10^7	1.3	3.98×10^5	1.0

Table 5.8 *O isotopes in an as-made ^{17}O-enriched Al MIL-53 sample, prepared by DGC. The amount of ^{17}O detected is 15-20%.*

^{16}O (counts)	% standard error	^{17}O (counts)	% standard error	^{18}O (counts)	% standard error
3.83×10^7	2.0	8.55×10^6	3.4	2.94×10^5	3.0
2.99×10^7	0.6	6.20×10^6	1.1	2.21×10^5	0.9
3.67×10^7	1.3	9.24×10^6	1.2	3.12×10^5	1.2
3.38×10^7	0.8	8.83×10^6	1.1	3.01×10^5	1.0
3.78×10^7	2.5	7.38×10^6	4.5	2.62×10^5	4.0

Table 5.9 *O isotopes in a calcined hydrated ^{17}O-enriched Al,Ga (50:50, stoichiometric ratio) MIL-53 sample, prepared by DGC. The amount of ^{17}O detected is 16-21%.*

^{16}O (counts)	% standard error	^{17}O (counts)	% standard error	^{18}O (counts)	% standard error
5.87×10^5	4.1	7.36×10^4	4.8	3.17×10^3	4.6
3.98×10^7	1.5	6.49×10^6	2.0	2.44×10^5	1.7
1.64×10^7	7.3	3.24×10^6	7.4	1.13×10^5	7.6
3.15×10^7	4.4	5.02×10^6	4.6	1.87×10^5	4.5
3.63×10^7	2.7	6.63×10^6	1.8	2.39×10^5	2.0
3.44×10^7	6.2	5.48×10^6	5.9	2.02×10^5	6.1

Table 5.10 *O isotopes in a calcined ^{17}O-enriched Al MIL-53 sample, prepared by DGC. The amount of ^{17}O detected is 11-16%.*

Final values of ^{17}O enrichment range between 11-21%, showing significant variability between batches. This suggests a different level of overall ^{17}O incorporation for every batch of reaction rather than variations in enrichment levels related to the as-made, calcined or hydrated state of the material.

In the ^{17}O-enriched samples the $^{16}O/^{18}O$ ratio was lower compared to natural abundance samples and this can be related to the isotopic composition of the 90% ^{17}O-enriched water used (^{18}O 8.6%, ^{17}O 90.4% and ^{16}O 1.0%), that is richer in ^{18}O than natural abundance water. A graphical comparison of the isotope counts on a

natural abundance and ^{17}O-enriched sample is shown in Figure 5.21. It can be noticed, from Tables 5.6-5.10 and Figure 5.21, that, depending on the sample and the uniformity of the embedding procedure, a different degree of variability in the obtained isotope counts is observed as a function of the surface region analysed.

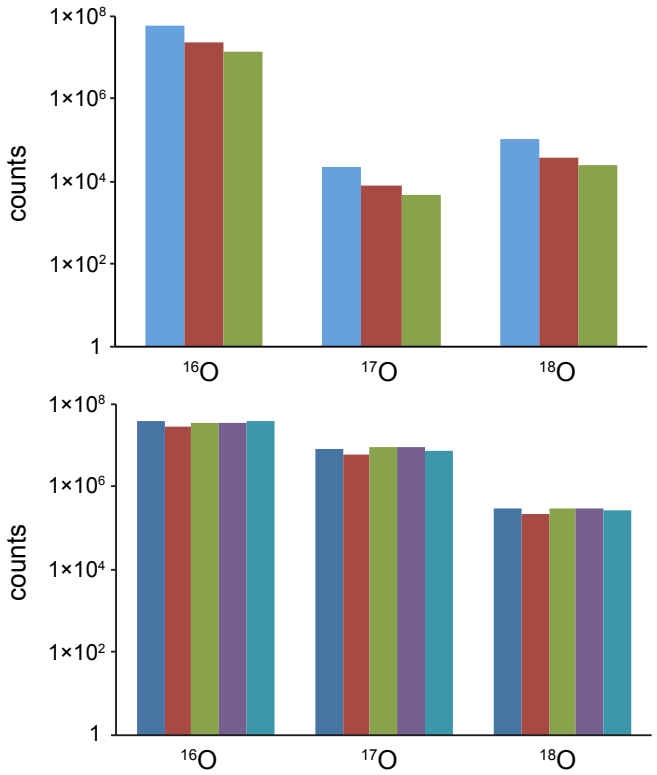

Figure 5.21 *Graphical comparison of isotope counts for (top) a natural abundance calcined hydrated Al MIL-53 sample and (bottom) an ^{17}O-enriched Al,Ga (50:50, stoichiometric ratio) calcined hydrated MIL-53 sample with an average enrichment level of 19%, as reported in Table 5.9. Bars of different colours represent measurements of the three isotopes carried out on different regions of the sample surface.*

These final levels of enrichment, obtained at a cost of approximately €750 per g of as-made MOF, can be compared to a recent study involving an economic mechanochemical ^{17}O enrichment of strategic precursors, such as carboxylic acids.[9] Following a mechanochemical procedure, linkers, such as terephthalic acid, are shown to be enriched at levels of 3.5% in 2 h with a lower cost of €220 per g of linker. However, for MOFs and more complex materials in general, enrichment of the starting linker might turn out to be a less favourable enrichment pathway since back-exchange of the enriched linker is likely to occur, lowering the level of

enrichment of the final product, in the typical conditions used in DGC or hydrothermal syntheses.

5.5 References

1 P. He, J. Xu, V. V. Terskikh, A. Sutrisno, H.-Y. Nie and Y. Huang, *J. Phys. Chem. C*, 2013, **117**, 16953–16960.

2 S. R. Miller, P. A. Wright, C. Serre, T. Loiseau, J. Marrot and G. Férey, *Chem. Commun.*, 2005, 3850–3852.

3 J. P. S. Mowat, S. R. Miller, A. M. Z. Slawin, V. R. Seymour, S. E. Ashbrook and P. A. Wright, *Micropor. Mesopor. Mater.*, 2011, **142**, 322–333.

4 F.-X. Coudert, A. U. Ortiz, V. Haigis, D. Bousquet, A. H. Fuchs, A. Ballandras, G. Weber, I. Bezverkhyy, N. Geoffroy, J.-P. Bellat, G. Ortiz, G. Chaplais, J. Patarin and A. Boutin, *J. Phys. Chem. C*, 2014, **118**, 5397–5405.

5 C. Volkringer, T. Loiseau, N. Guillou, G. Férey, E. Elkaïm and A. Vimont, *Dalton Trans.*, 2009, 2241–2249.

6 T. Loiseau, C. Serre, C. Huguenard, G. Fink, F. Taulelle, M. Henry, T. Bataille and G. Férey, *Chem. Eur. J.*, 2004, **10**, 1373–1382.

7 M. Dincă and J. R. Long, *J. Am. Chem. Soc.*, 2007, **129**, 11172–11176.

8 K. S. Asha, R. Bhattacharjee and S. Mandal, *Angew. Chem.*, 2016, **128**, 11700–11704.

9 T.-X. Métro, C. Gervais, A. Martinez, C. Bonhomme and D. Laurencin, *Angew. Chem.*, 2017, **129**, 6907–6911.

6 Solid-state NMR and DNP NMR results for ^{17}O-enriched MOFs

This chapter presents the NMR and DNP NMR results obtained on the terephthalate MOFs investigated. For MIL-53 samples, ^{17}O-enriched Al, Ga and mixed-metal samples synthesised using DGC have been characterised by ^{1}H, ^{13}C, ^{27}Al and ^{17}O NMR spectroscopy throughout the different stages of their breathing behaviour. As described in Section 5.1, when using Sc as a metal center in DGC syntheses, the ^{17}O-enriched smaller-pore MOF $Sc_2(BDC)_3$ was obtained instead of Sc MIL-53 and, upon mixing metal centers (i.e., Sc and Al), an ^{17}O-enriched mixed-phase MOF was formed. In order to obtain ^{17}O-enriched Sc MIL-53, the solvothermal synthetic procedure for this compound[1] was followed and the obtained Sc MIL-53 was enriched via steaming in ^{17}O-enriched water. These products have been identified and characterised by ^{1}H, ^{13}C, ^{27}Al, ^{45}Sc and ^{17}O NMR spectroscopy. In relation to metal centers, only ^{27}Al and ^{45}Sc have been investigated by NMR spectroscopy in this work due to the more challenging nature of $^{69/71}$Ga. While study of other nuclei, such as ^{91}Zr, $^{47/49}$Ti, ^{115}In and ^{139}La, requires wideline[2] experiments and high field.[3-4] Samples of ^{17}O-enriched Al MIL-53 have also been studied by DNP NMR spectroscopy and a set of preliminary results is presented in the final section of this chapter, showing the importance of the choice of the impregnating solution when performing experiments on breathing MOFs.

6.1 NMR investigation of ^{17}O-enriched Al MIL-53 and Ga MIL-53

^{17}O spin echo MAS and MQMAS NMR spectra of as-made and calcined Al MIL-53 and Ga MIL-53 samples ^{17}O-enriched during DGC are shown in Figure 6.1. Two broadened ^{17}O resonances are observed in the as-made forms (Figures 6.1a and 6.1d), but these lineshapes sharpen upon calcination displaying characteristic quadrupolar features (Figures 6.1b and 6.1e). The signal located at higher shift is assigned to carboxylate oxygens in the terephthalate linker and the signal at lower shift results from hydroxyl groups bridging between metal centers.[5] This assignment was confirmed by ^{1}H-^{17}O CP experiments, where only the hydroxyl signal is selectively enhanced, as shown by the red lines in Figures 6.1b and 6.1e. Upon

calcination, a relative loss of ~40% of ^{17}O signal from the carboxylate sites is observed as a result of the loss of excess linker, also ^{17}O-enriched in the synthetic process and located in the pores. The accurate quantitative evaluation of the relative level of enrichment of the two sites in these materials has been hampered by the long relaxation times characteristic of the carboxylate and the distorted baselines observed in direct polarisation experiments. However, preliminary quantitative ^{17}O MAS NMR spectra indicate a hydroxyl:carboxylate ratio of ~1:3, suggesting a preferential enrichment of the OH groups, given the expected 1:4 ratio. A broader component is observed in the spectral lineshapes of calcined Ga MIL-53, highlighting the presence of some decomposition[6] in this material in agreement with PXRD results shown in Figure 5.2. As shown in Figures 6.1b and 6.1e, there is a clear difference in the position of the hydroxyl resonances, which are centered at −6.6 ppm and 14.2 ppm for Al and Ga MIL-53, respectively. This represents the first important evidence of the sensitivity of ^{17}O NMR spectroscopy to the metal nodes present in the framework. The corresponding ^{17}O MQMAS NMR spectra of the calcined samples are shown in Figures 6.1c and 6.1f. NMR parameters (δ_{iso} and P_Q) extracted from the position the center of gravity of the resonances belonging to the two types of chemical species are given in Table 6.1. It should be noted that for Al MIL-53 the ^{17}O lineshape in the spin echo MAS experiment of the calcined sample was fitted to obtain estimates of C_Q and η_Q. While there is no significant change in the NMR parameters of the carboxylate sites between the two materials, a large difference can be observed in the case of the hydroxyl sites. Indeed, for these latter sites the largest change upon substitution of the metal center is not in δ_{iso}, but in the magnitude of the quadrupolar coupling with P_Q values for the hydroxyl sites of 6.0 and 4.6 MHz for Al and Ga MIL-53, respectively.

Changes occurring to the MOF framework upon calcination have also been investigated by ^{1}H, ^{13}C and ^{27}Al NMR spectroscopy. Figure 6.2 shows ^{1}H MAS NMR spectra before and after calcination for Al and Ga MIL-53. For the ^{1}H MAS NMR spectrum of as-made Al MIL-53, shown in Figure 6.2a, resonances at 2.6, 7.2 and 12.1 ppm can be assigned to bridging hydroxyls, aromatic –CH and –COOH groups, respectively. Upon calcination, the signal from the excess linker is lost, leaving resonances resulting from the ^{1}H atoms on the linker at 7.8 ppm and from the

hydroxyls at 2.2 ppm, as shown in Figure 6.2b.[7] The ^{1}H spin echo MAS NMR spectrum of as-made Ga MIL-53, shown in Figure 6.2c, is characterised by the same set of resonances (at 3.2, 7.2 and 12.1 ppm) observed for as-made Al MIL-53. However, after removal of excess linker during calcination, the resulting resonances are affected by the partial decomposition of the framework, as shown by the ^{1}H MAS NMR spectrum in Figure 6.2d.

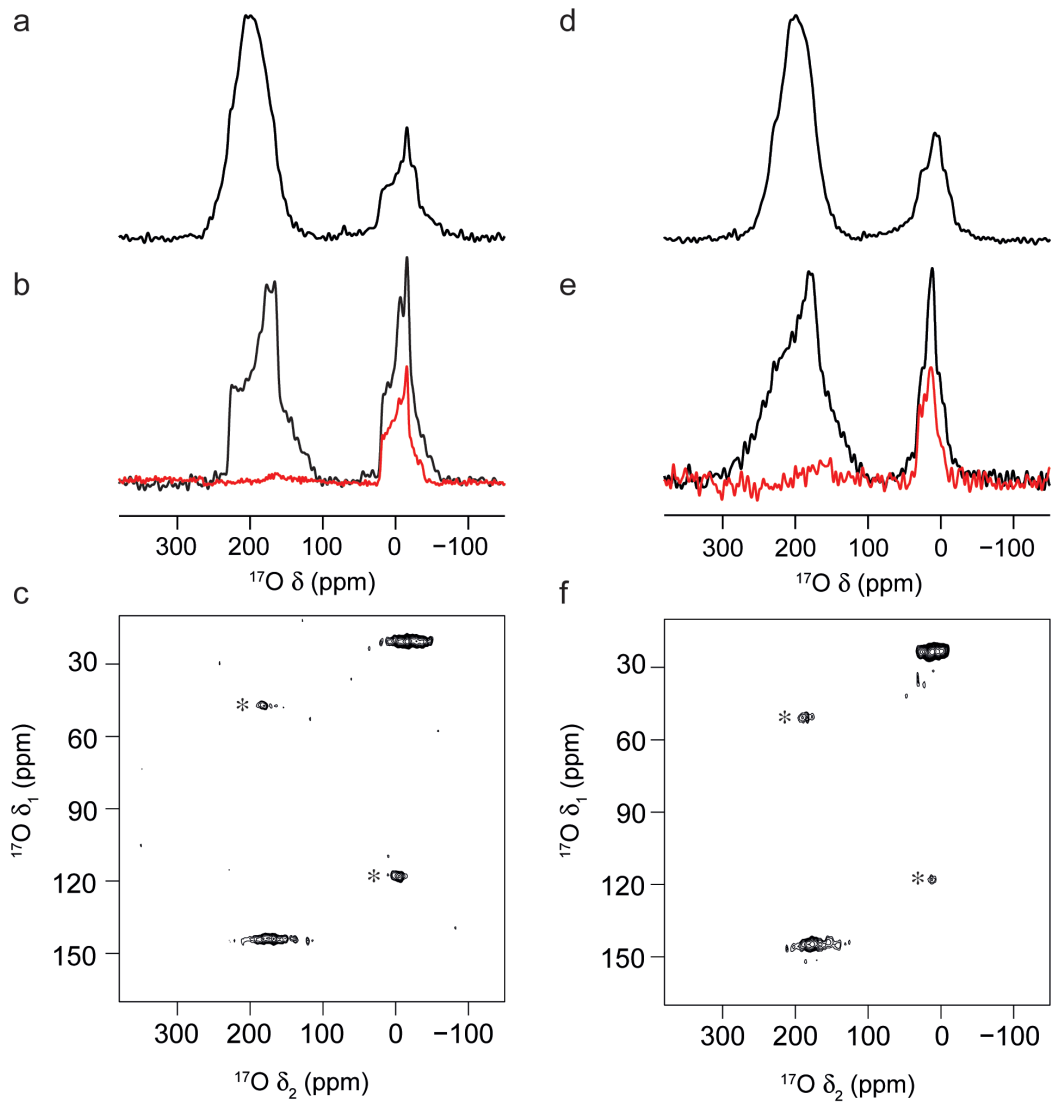

Figure 6.1 *^{17}O (14.1 T, 20 kHz) spin echo MAS NMR spectra of (a,d) as-made and (b,e) calcined samples of (a,b) Al MIL-53 and (d,e) Ga MIL-53. ^{1}H-^{17}O (14.1 T, 20 kHz) CP MAS NMR spectra (with a contact time of 1000 μs) are overlaid in red for calcined (b) Al MIL-53 and (e) Ga MIL-53. ^{17}O (14.1 T, 20 kHz) z-filtered 3QMAS NMR spectra, shown after a shearing transformation, of calcined (c) Al MIL-53 and (f) Ga MIL-53. Asterisks denote spinning sidebands.*

O species	δ_{iso} (ppm)	P_Q / MHz	C_Q / MHz	η_Q
Calcined Al MIL-53				
carboxylate	230(3)	7.8(3)	7.1(2)	0.8(2)
hydroxyl	20(3)	6.0(3)	5.5(2)	0.7(2)
Calcined Ga MIL-53				
carboxylate	230(3)	7.7(3)		
hydroxyl	31(3)	4.6(4)		

Table 6.1 *NMR parameters obtained from the ^{17}O MQMAS NMR spectra in Figure 6.1.*

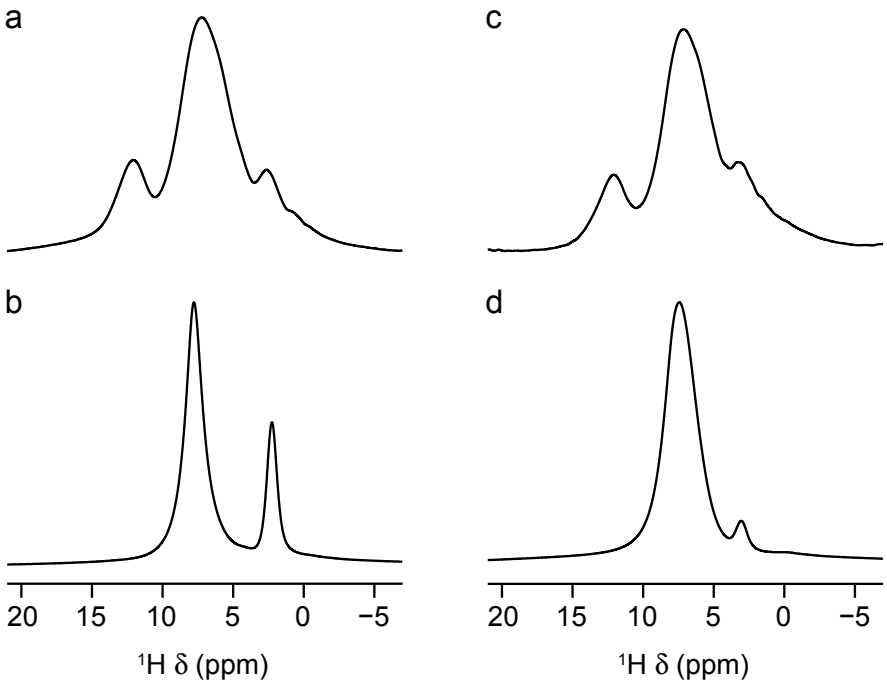

Figure 6.2 *^1H (14.1 T, 12.5 kHz) MAS NMR spectra of (a,c) as-made and (b,d) calcined samples of (a,b) Al MIL-53 and (c,d) Ga MIL-53. The spectrum in (c) was acquired using a spin echo.*

^{1}H-^{13}C CP MAS NMR spectra are shown in Figure 6.3 for as-made and calcined Al and Ga MIL-53. In Figures 6.3a and 6.3c, resonances in the range 126-139 ppm are assigned to aromatic carbons and quaternary carbons with some splitting resulting from the co-existence of the anionic and acidic forms of the linker in the framework and in the pores, respectively. Resonances centered at δ = 171 ppm also show some splitting and can be assigned to the carboxylic carbons of the linker molecules in their protonated and deprotonated forms. As Figure 6.3b shows, upon removal of excess linker during calcination, three ^{13}C resonances can be identified for Al MIL-53 at 129, 137, 171 ppm and assigned to aromatic carbons, quaternary carbons and carbons on the carboxylate group, respectively. The presence of an extra resonance with very low intensity at 175 ppm can be ascribed to traces of hydration in the solid.[7] As shown in Figure 6.3d, calcination of as-made Ga MIL-53 resulted in a less resolved ^{1}H-^{13}C CP MAS NMR spectrum compared to Figure 6.3b. Indeed, broader lineshapes, attributed to the partial decomposition of Ga MIL-53 after heat treatment, are present along with the same set of three ^{13}C resonances (at 129, 137, 172 ppm) observed for calcined Al MIL-53.

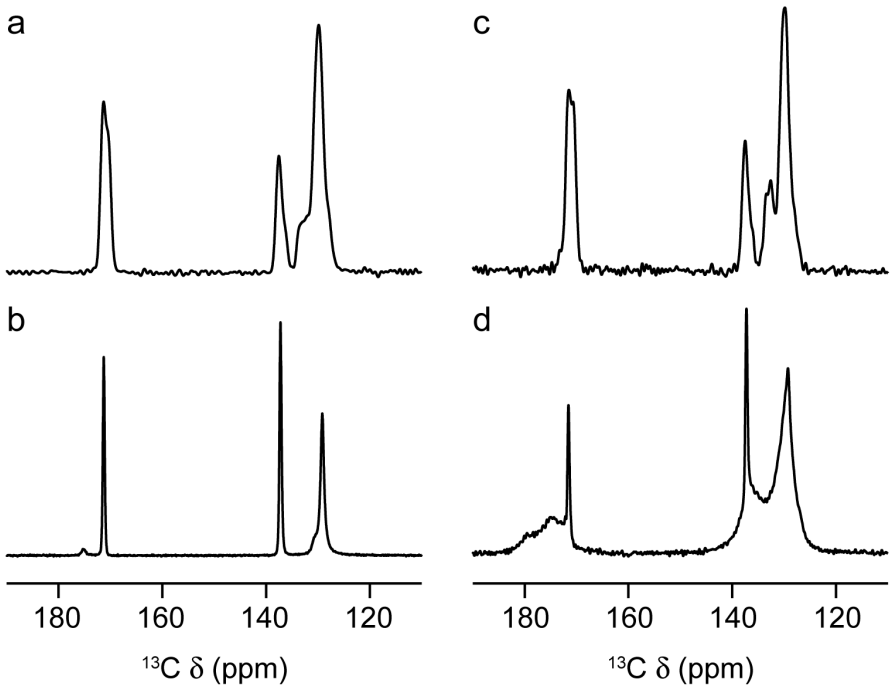

Figure 6.3 *^{1}H-^{13}C (14.1 T, 12.5 kHz) CP MAS NMR spectra of (a,c) as-made and (b,d) calcined samples of (a,b) Al MIL-53 and (c,d) Ga MIL-53.*

Figure 6.4 shows ^{27}Al MAS NMR spectra acquired for Al MIL-53 before and after calcination. A single quadrupolar lineshape is observed in the as-made form of Al MIL-53, as shown in Figure 6.4a, and can be reasonably fitted to δ_{iso} = 2.2(2) ppm, C_Q = 7.6(1) MHz and η_Q = 0.1(1). A broader shoulder on the right side of the main resonance cannot be fitted to the quadrupolar lineshape and is most likely resulting from disorder in the as-made sample, as confirmed by the ^{27}Al MQMAS NMR spectrum in Figure 6.5a. Upon calcination, the ^{27}Al MAS NMR spectrum is characterised by a well-defined quadrupolar lineshape with δ_{iso} = 3.1(1) ppm, C_Q = 8.4(1) MHz and η_Q = 0, as shown in Figure 6.4b. The corresponding ^{27}Al MQMAS NMR spectra for as-made and calcined Al MIL-53 are shown in Figure 6.5. A distribution of NMR parameters can be observed in the as-made form in Figure 6.5a indicating the presence of disorder in the local structure, probably arising from excess linker molecules in the pores. Fitting of cross sections parallel to δ_2 shows that there is a variation in C_Q from ~7.8 to ~9.1 MHz, but only a small variation in δ_{iso} (of ~0.6 ppm).

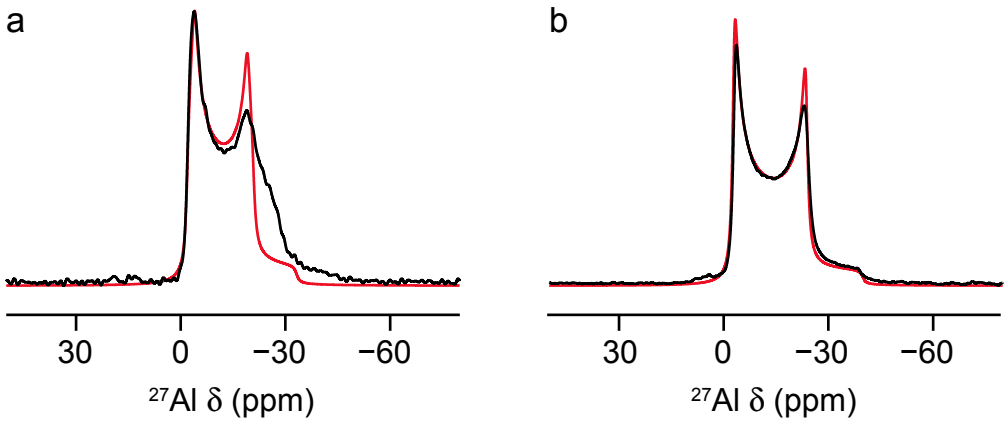

Figure 6.4 *^{27}Al (14.1 T) MAS NMR spectra of (a) as-made (MAS rate of 16 kHz) and (b) calcined (MAS rate of 14 kHz) Al MIL-53, acquired using a short flip angle (black line), and corresponding fits (red line).*

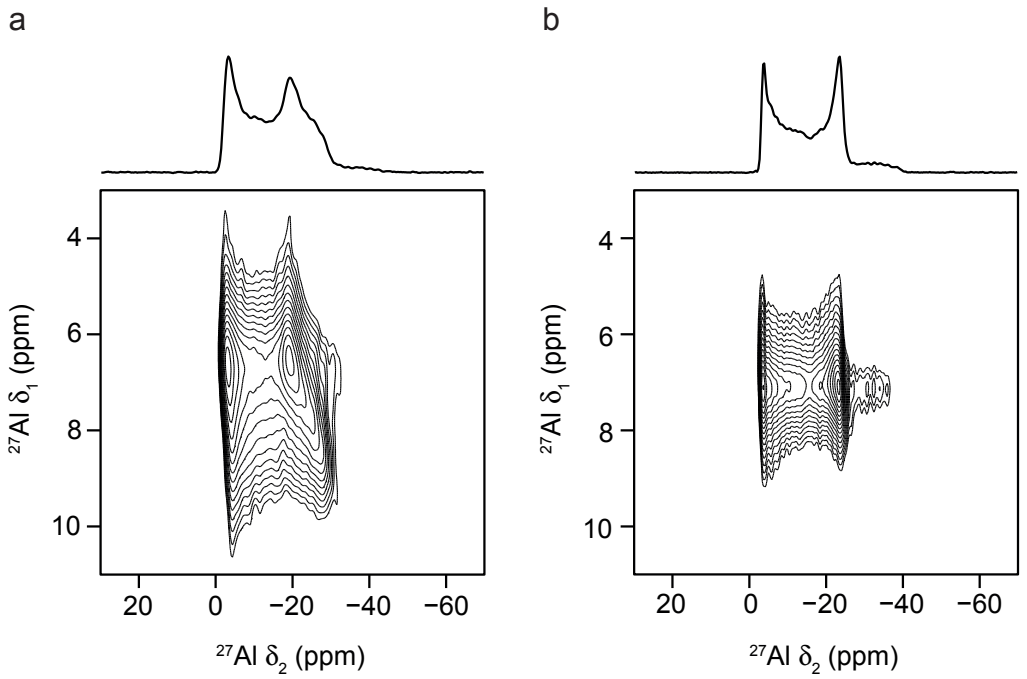

Figure 6.5 *^{27}Al (14.1 T) 3QMAS NMR spectra (and projections), acquired with a split-t_1 shifted-echo pulse sequence, of (a) as-made (MAS rate of 16 kHz) and (b) calcined (MAS rate of 14 kHz) Al MIL-53.*

Upon hydration, a significant change is observed in the ^{17}O MAS NMR spectra of Al and Ga MIL-53, as shown in Figures 6.6a and 6.6c, respectively. In particular, the ^{17}O MQMAS NMR spectra, shown in Figures 6.6b and 6.6d, resolve two distinct species in the carboxylate region of the spectrum. The corresponding average NMR parameters, extracted from the center of gravity of the spectral lineshapes, are given in Table 6.2. This demonstrates the sensitivity of ^{17}O NMR spectroscopy to changes in the local geometry of the framework upon interaction with guest molecules of water. The observation of two resolved ^{17}O species in the MQMAS NMR spectrum supports previous computational[7] and structural[6,8-9] investigations of different hydrogen-bonding patterns originating from inequivalent water molecules adsorbed in the pores of the framework. Specifically, Ortiz *et al.*[9] provided structures of Al and Ga MIL-53 with two channels per unit cell where refinement of PXRD data was based on information from ^{1}H solid-state NMR spectroscopy,[7-9] suggesting that two inequivalent water molecules are present in the material. The two different water molecules were proposed[7-8] to preferentially hydrogen bond to the carboxylate

oxygens of the framework and possible hydrogen-bonding interactions between water molecules were also suggested on the basis of the position of ^{1}H resonances.[9]

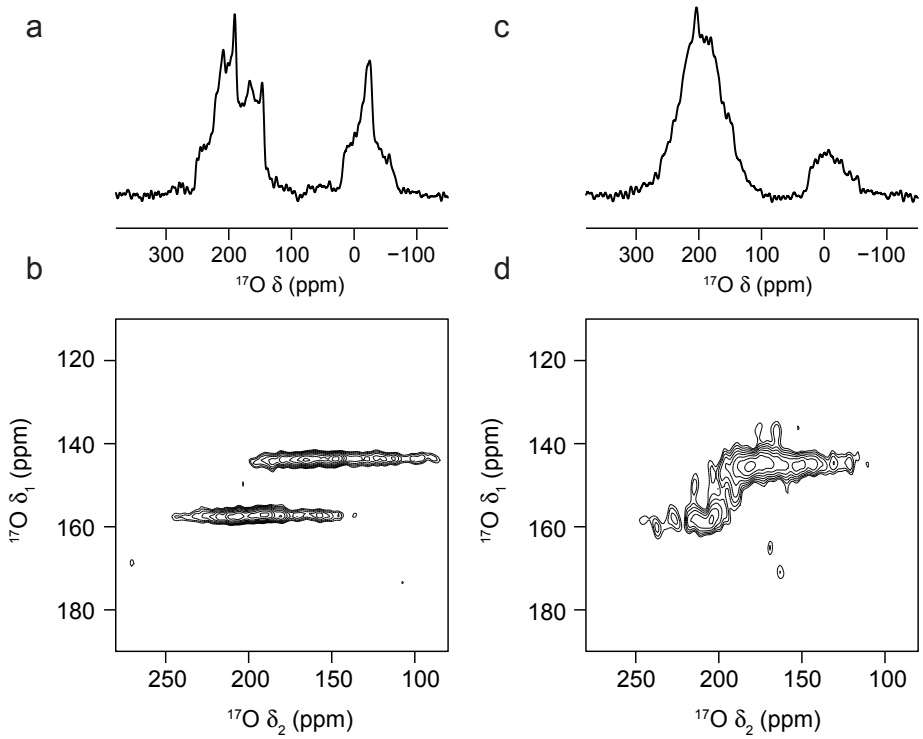

Figure 6.6 *^{17}O (14.1 T, 20 kHz) (a,c) spin echo MAS and (b,d) z-filtered 3QMAS NMR spectra, shown after a shearing transformation, of calcined hydrated (a,b) Al MIL-53 and (c,d) Ga MIL-53. In (b,d), only the carboxylate region of the spectrum is shown.*

O species	δ_{iso} (ppm)	P_Q / MHz	C_Q / MHz	η_Q
Calcined hydrated Al MIL-53				
carboxylate 1	255(3)	7.8(3)	7.1(3)	0.7(1)
carboxylate 2	225(5)	8.5(3)	7.9(3)	0.7(1)
hydroxyl	15(5)	7.2(5)	5.8(5)	0.9(1)
Calcined hydrated Ga MIL-53				
carboxylate 1	259(2)	7.5(2)		
carboxylate 2	230(5)	8.1(5)		
hydroxyl	24(6)	5.9(8)		

Table 6.2 *Average NMR parameters obtained from the ^{17}O MQMAS NMR spectra in Figure 6.6. Parameters are average values as a result of disorder in the hydrated samples.*

A computational investigation was carried out (in collaboration with Dr David McKay) to determine the relation between carboxylate O inequivalence and the hydrogen-bonding network in the narrow-pore forms of the MOFs when water molecules are encapsulated. The structural models provided by Ortiz *et al.*[9] of hydrated Al MIL-53 (Al-MIL-53_np_H_2O_dc) and Ga MIL-53 (Ga-MIL-53_np_H_2O_dc) were used as a starting point and are termed $\mathbf{A}_{Al}$ and $\mathbf{B}_{Ga}$, respectively herein. The two starting models were subjected to geometry optimsation via periodic density functional theory (DFT) calculations performed using the CASTEP code (version 16.11).[10-11] The PBE exchange correlation functional[12] was adopted with dispersion corrections provided by the scheme of Tkatchenko and Scheffler.[13] Calculations used a plane-wave cut-off of 50 Ry and the Brillouin zone was sampled on a Monkhorst-Pack grid[14] with a k-point spacing of 0.04 2π $Å^{-1}$. Ultrasoft pseudopotentials were used with the inclusion of ZORA scalar relativistic effects.

As a result of the geometry optimisation, during which all atomic positions and the unit cell parameters were allowed to vary, the structures $\mathbf{A}_{Al}'$ and $\mathbf{B}_{Ga}'$ were obtained. To test the influence of different metal centers in these hydrated structures, metal ions were swapped between the two structures and re-optimisation provided new models, termed $\mathbf{A}_{Ga}'$ and $\mathbf{B}_{Al}'$, with the hydrogen-bonding arrangement of model **A** with Ga-centered metal nodes and **B** with Al-centered metal nodes. However, upon re-optimisation, no significant variation was observed in the position of the water molecules. NMR parameters were predicted for all models using calculations performed on the all-electron wavefunction reconstructed through the GIPAW method.[11,15-16] Isotropic shieldings, σ_{iso}, were obtained from the trace of the absolute shielding tensor, $\boldsymbol{\sigma}$, and isotropic chemical shifts, δ_{iso}, given by $\delta_{iso} = -(\sigma_{iso} - \sigma_{ref})/m$,[17] where σ_{ref} = 271.31 ppm and m = −1.117 were provided by comparison, via linear regression, of computed isotropic shieldings and experimental isotropic shifts of the hydroxyl and carboxylate ^{17}O species in calcined Al MIL-53. The quadrupolar coupling constant, C_Q (see Equation 2.37), and the asymmetry parameter, η_Q (see Equation 2.38), are obtained directly from the principal components of the electric field gradient tensor, **V**.[17] Computed NMR data were

extracted from CASTEP magres files using Python scripts based on the magres-format Python library.[18]

Figure 6.7 shows the hydrogen-bonding arrangements for the original, $\mathbf{A}_{Al}$ and $\mathbf{B}_{Ga}$, and DFT-optimised, $\mathbf{A}_{Al}'$ and $\mathbf{B}_{Ga}'$, with the two crystallographically distinct pores labelled I and II. Pores narrow upon optimisation as a result of decreasing cell volumes from 1888 Å^3 in $\mathbf{A}_{Al}$ to 1830 Å^3 in $\mathbf{A}_{Al}'$ and from 1928 Å^3 in $\mathbf{B}_{Ga}$ to 1905 Å^3 in $\mathbf{B}_{Ga}'$. The most significant movement is observed in the water molecules, which have shorter hydrogen-bonding interactions in the optimised structures (compared to those obtained from XRD) owing to the reduced cell volume. Upon geometry optimisation of A-type structures, both pores retain their different hydrogen-bonding arrangement. In type I pores, water molecules donate two inequivalent hydrogen bonds to carboxylate oxygen centers and the water accepts a hydrogen bond from the hydroxyl. In type II pores, the hydrogen bonds donated from water to the carboxylate oxygen atoms are more similar, but with significantly different OH···O angles.

In the case of the B-type structures, significant changes are observed in the position of water molecules upon geometry optimisation. Indeed, in the original structure proposed for hydrated Ga MIL-53 pores I and II exhibit water molecules that are oriented differently. In pore I, the O-H bonds of water molecules lie in near planarity with the crystallographic *ac* plane and do not interact with carboxylate oxygens, whereas in pore II the water molecules lie perpendicular to the *ac* plane with shorter OH···O contacts. On optimisation, the two pores become equivalent in terms of their sets of hydrogen-bonding arrangements, which are the same as those found in pore II of $\mathbf{A}_{Al}'$. The optimised structures, $\mathbf{A}_{Al}'$ and $\mathbf{B}_{Ga}'$, are significantly lower in energy (by 14.8 eV and 17.2 eV, respectively) compared to the starting crystal structures, highlighting the stabilising effect of hydrogen bond formation between the carboxylate linker and water molecules in the pores. It should be noted that for either of the two types of hydrogen-bonding arrangement found, the same set of carboxylate oxygen atoms accepts hydrogen bonds from water. Omission of the water molecules, as shown in Figure 6.8, reveals that the geometry of the narrow-pore framework is inherently characterised by a set of relatively short carboxylate to hydroxyl internuclear distances and a set of relatively large carboxylate to hydroxyl distances. It follows therefore that water molecules, if present in the pores, will be

preferentially involved in hydrogen bonding with the former set of carboxylates and hydroxyls.

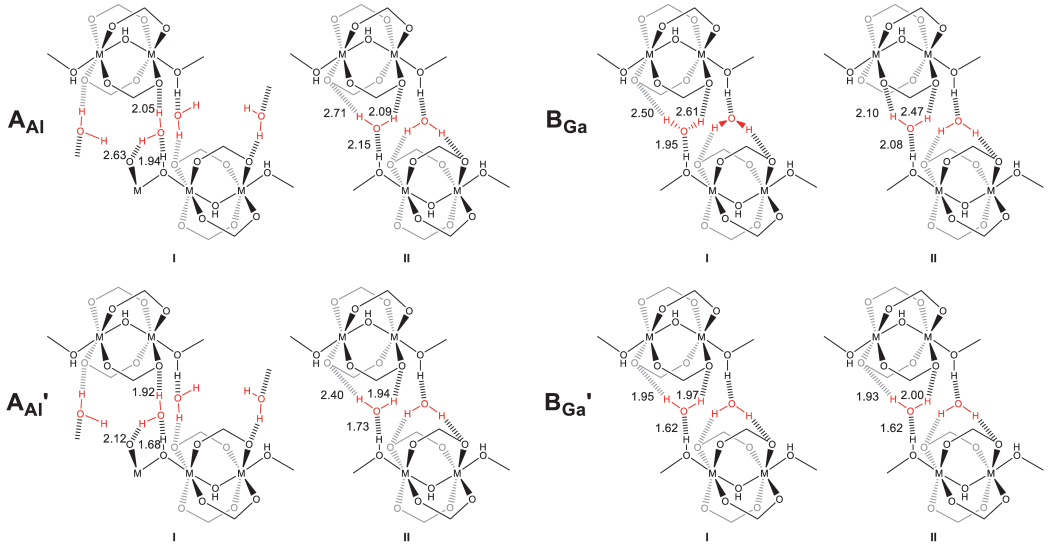

Figure 6.7 *Schematic representation of the two chemically inequivalent pores (I and II) in the crystallographically determined[9] structures,* $\boldsymbol{A}_{Al}$ *and* $\boldsymbol{B}_{Ga}$*, and DFT-optimised structures,* $\boldsymbol{A}_{Al}'$ *and* $\boldsymbol{B}_{Ga}'$*, with hydrogen bonds around adsorbed water molecules highlighted. The BDC aromatic rings are omitted for clarity.*

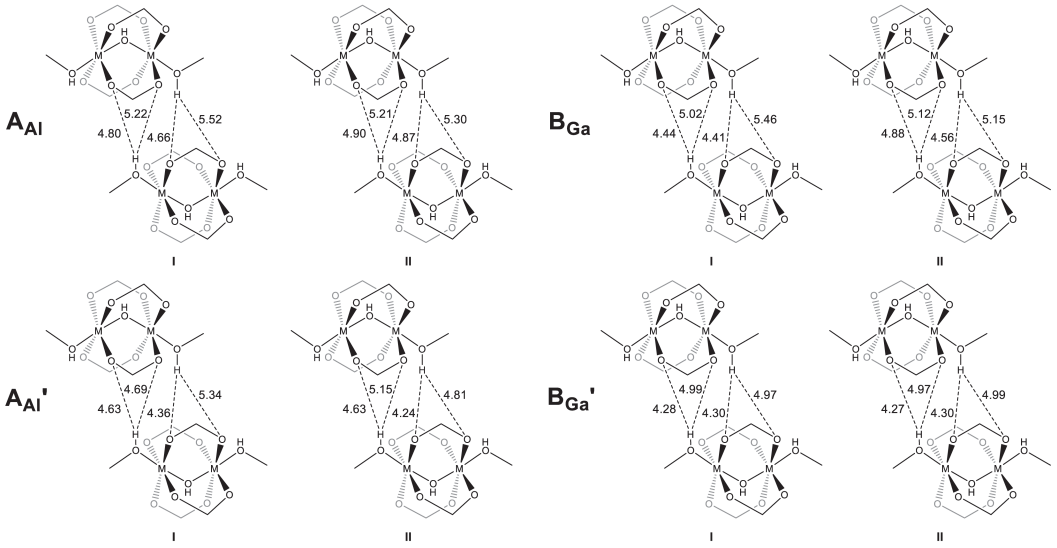

Figure 6.8 *Schematic representation of the structures shown in Figure 6.7 with water molecules omitted, showing the distances between hydroxyl and carboxylate oxygens across the structure of the narrow pore.*

Computed ^{17}O NMR data are given in Table 6.3, with calcined Al MIL-53 used to provide the reference shielding, as described above. (It should be noted that calculations can determine both the magnitude and sign of C_Q, while only the absolute magnitude is typically available experimentally.) The NMR parameters of the carboxylate ^{17}O fall into to two groups, which become better defined upon geometry optimisation owing to the strengthening of the hydrogen-bonding interactions. The resulting predicted chemical shifts of hydrogen-bonded and non-hydrogen-bonded ^{17}O species are ~225 ppm and ~255 ppm, respectively. Notably, since each different model exhibits the same set of hydrogen-bonded O centers, any motion of encapsulated water molecules would not exchange the carboxylate oxygens, in agreement with their experimental observation as inequivalent. Exchange between structures with different hydrogen-bonding arrangements cannot be ruled out by calculations because models **A** and **B** are very similar in terms of their DFT energies. The DFT-predicted NMR parameters based on optimised geometries are within experimental error, with the exception of the hydroxyl oxygen in calcined Al MIL-53, where, as found by He *at al.*,[5] the magnitude of the C_Q is overestimated with respect to the experimental value.

^{17}O species	δ_{iso} (ppm)	C_Q / MHz	η_Q	ΔE / eV
Calcined Al MIL-53				
carboxylate	230[a]	7.3	0.8	
hydroxyl	20[a]	–8.3	0.8	
$\mathbf{A_{Al}}$				14.8[b]
carboxylate 1	261	7.3	0.8	
carboxylate 2	269	7.8	0.5	
carboxylate 3	262	7.5	0.7	
carboxylate 4	280	7.6	0.5	
carboxylate 5	249	8.3	0.6	
carboxylate 6	214	8.3	0.7	
carboxylate 7	239	8.6	0.5	
carboxylate 8	203	8.0	0.8	
hydroxyl 1	8	6.1	1.0	
hydroxyl 2	1	–6.5	1.0	

water 1	1	10.5	0.7	
water 2	0	9.9	0.8	
A_{Al}'				0.0[b]
carboxylate 1	250	7.1	0.8	
carboxylate 2	255	7.4	0.7	
carboxylate 3	271	7.5	0.7	
carboxylate 4	274	7.7	0.5	
carboxylate 5	225	7.4	0.7	
carboxylate 6	230	7.9	0.8	
carboxylate 7	224	8.6	0.6	
carboxylate 8	226	8.8	0.6	
hydroxyl 1	24	6.4	0.9	
hydroxyl 2	23	6.4	1.0	
water 1	−5	9.1	0.8	
water 2	−9	9.0	0.8	
B_{Al}'				0.0[b]
carboxylate 1	267	7.4	0.6	
carboxylate 2	264	7.4	0.6	
carboxylate 3	264	7.4	0.6	
carboxylate 4	262	7.3	0.7	
carboxylate 5	225	8.4	0.7	
carboxylate 6	226	8.4	0.7	
carboxylate 7	226	8.4	0.7	
carboxylate 8	228	8.3	0.7	
hydroxyl 1	22	6.4	1.0	
hydroxyl 2	22	6.4	1.0	
water 1	−8	9.4	0.7	
water 2	−8	9.3	0.7	
B_{Ga}				17.2[c]
carboxylate 1	250	7.5	0.6	
carboxylate 2	267	6.5	0.8	
carboxylate 3	263	−6.7	1.0	
carboxylate 4	289	7.0	0.7	
carboxylate 5	253	8.3	0.7	

carboxylate 6	250	8.9	0.5	
carboxylate 7	250	8.3	0.6	
carboxylate 8	228	8.7	0.6	
hydroxyl 1	34	8.0	0.7	
hydroxyl 2	19	8.0	0.6	
water 1	33	11.6	0.6	
water 2	3	10.5	0.8	
$\mathbf{B_{Ga}'}$				0.0[c]
carboxylate 1	278	6.9	0.7	
carboxylate 2	277	6.8	0.7	
carboxylate 3	277	6.8	0.7	
carboxylate 4	275	6.8	0.8	
carboxylate 5	230	8.6	0.6	
carboxylate 6	231	8.6	0.6	
carboxylate 7	231	8.6	0.6	
carboxylate 8	232	8.5	0.6	
hydroxyl 1	46	8.1	0.3	
hydroxyl 2	46	8.1	0.3	
water 1	−5	9.4	0.7	
water 2	−4	9.3	0.7	
$\mathbf{A_{Ga}'}$				0.3[c]
carboxylate 1	261	6.5	0.9	
carboxylate 2	264	6.9	0.8	
carboxylate 3	285	7.0	0.7	
carboxylate 4	286	7.4	0.6	
carboxylate 5	239	7.8	0.8	
carboxylate 6	232	7.9	0.8	
carboxylate 7	226	8.9	0.6	
carboxylate 8	230	9.1	0.5	
hydroxyl 1	48	7.9	0.3	
hydroxyl 2	48	8.1	0.4	
water 1	0	8.9	0.8	
water 2	−5	8.9	0.8	

[a] used for reference shielding [b] relative energy *vs* $\mathbf{A_{Al}'}$ [c] relative energy *vs* $\mathbf{B_{Ga}'}$

Table 6.3 *Computed ^{17}O NMR parameters for calcined Al MIL-53, $\boldsymbol{A_{Al}}$, $\boldsymbol{A_{Al}'}$, $\boldsymbol{B_{Al}'}$, $\boldsymbol{B_{Ga}}$, $\boldsymbol{B_{Ga}'}$ and $\boldsymbol{A_{Ga}'}$.*

The hydrated state was also characterised by ^{1}H, ^{13}C and ^{27}Al MAS NMR spectra for both compounds. Figure 6.9 shows the ^{1}H and ^{13}C MAS NMR spectra of hydrated Al and Ga MIL-53. The ^{1}H MAS NMR spectrum of hydrated Al MIL-53 in Figure 6.9a features three resonances at δ = 2.5, 5.1 and 7.4 ppm, characteristic of the hydrated state with signals from water molecules overlapping with the hydroxyls at 2.5 ppm and with signal from the linker molecules.[9] The corresponding ^{1}H-^{13}C CP MAS NMR spectrum in Figure 6.9c shows three resonances at δ = 131, 137 and 175 ppm and a minor signal at 171 ppm. While a small shift is observed, upon hydration, for the first two resonances, assigned to aromatic CH and quaternary carbons, respectively, a more significant shift is observed for the carboxylate group, clearly more affected by the presence of the water molecules.[7] The minor signal at 171 ppm could be related to the survival of traces of the large-pore structure, as indicated by the XRD in Figure 5.1. In the case of hydrated Ga MIL-53, the ^{1}H and ^{1}H-^{13}C CP MAS NMR spectra are affected by the decomposition process occurring upon calcination leading to more challenges in the assignment of the resonances, as shown in Figures 6.9b and 6.9d. Figure 6.10 shows the ^{27}Al MAS NMR spectrum of hydrated Al MIL-53 and the corresponding fit with resulting parameters δ_{iso} = 3.6(2) ppm, C_Q = 10.5(2) MHz and η_Q = 0.15(5), in agreement with the known increase in C_Q upon hydration.[7]

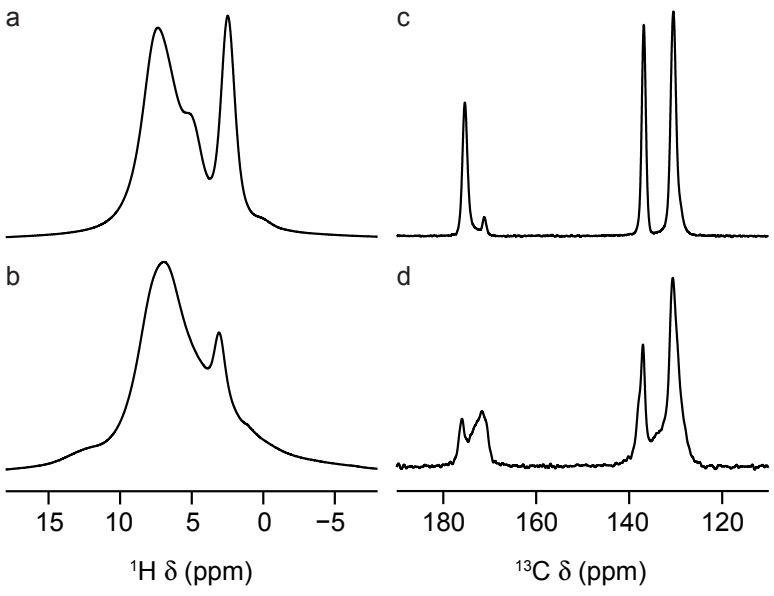

Figure 6.9 *^{1}H and ^{1}H-^{13}C CP (14.1 T, 12.5 kHz) MAS NMR spectra of calcined hydrated (a,c) Al and (b,d) Ga MIL-53.*

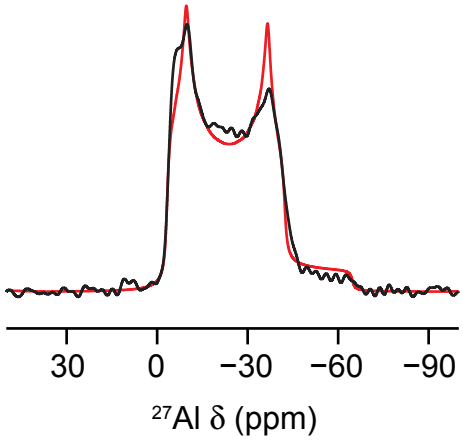

Figure 6.10 *^{27}Al (14.1 T, 16 kHz) MAS NMR short flip angle spectrum (black line) and corresponding fit (red line) for calcined hydrated Al MIL-53.*

6.2 NMR investigation of ^{17}O-enriched Al,Ga mixed-metal MIL-53

Mixed-metal samples were synthesised (and ^{17}O enriched) in DGC conditions by using different stoichiometric ratios (Al:Ga 50:50 and 80:20) of the starting metal nitrates, as described in Section 5.1. Upon calcination of these samples, no decomposition was observed, as shown by the PXRD patterns in Figures 5.5 and 5.6, and confirmed by the ^{1}H and ^{1}H-^{13}C CP MAS NMR spectra shown in Figure 6.11. This confirms that the incorporation of Al into Ga MIL-53 increases the thermal stability of the final compound, as already introduced in Section 5.2. Detailed analysis of these spectra will be carried out in the context of the breathing behaviour discussed later in this section. ^{27}Al MQMAS NMR spectra of calcined Al,Ga (80:20) and (50:50) MIL-53 are shown in Figure 6.12. Unlike calcined Al MIL-53, where a single ^{27}Al resonance is observed (Figure 6.5b), the ^{27}Al MQMAS NMR spectra of the mixed-metal materials exhibit a distribution of NMR parameters. This suggests the presence of a distribution of local environments and, therefore, disorder resulting from cation substitution, as opposed to the more ordered Al MIL-53 structure. A better insight into the magnitude of the distributions observed can be obtained by fitting cross sections parallel to δ_2 extracted from the MQMAS NMR spectra in Figure 6.12. Very little variation is confirmed in δ_{iso}, between ~2.3 and ~3 ppm, but a more significant distribution of C_Q from ~8.1 to ~8.6 MHz for calcined Al,Ga

(80:20) MIL-53 and ~7.8 to ~8.7 MHz for calcined Al,Ga (50:50) MIL-53 is observed.

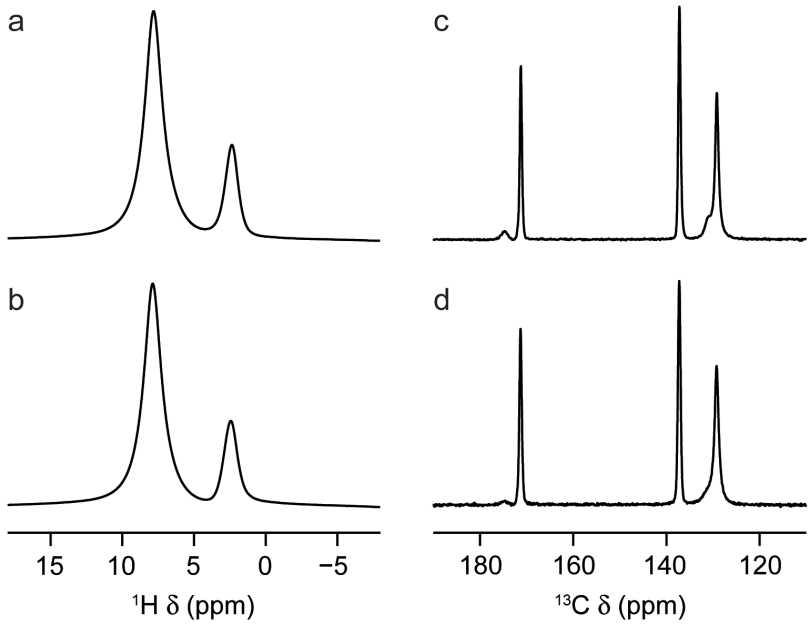

Figure 6.11 *^{1}H and ^{1}H-^{13}C CP (14.1 T, 12.5 kHz) MAS NMR spectra of calcined Al,Ga (a,c) (80:20) and (b,d) (50:50) MIL-53.*

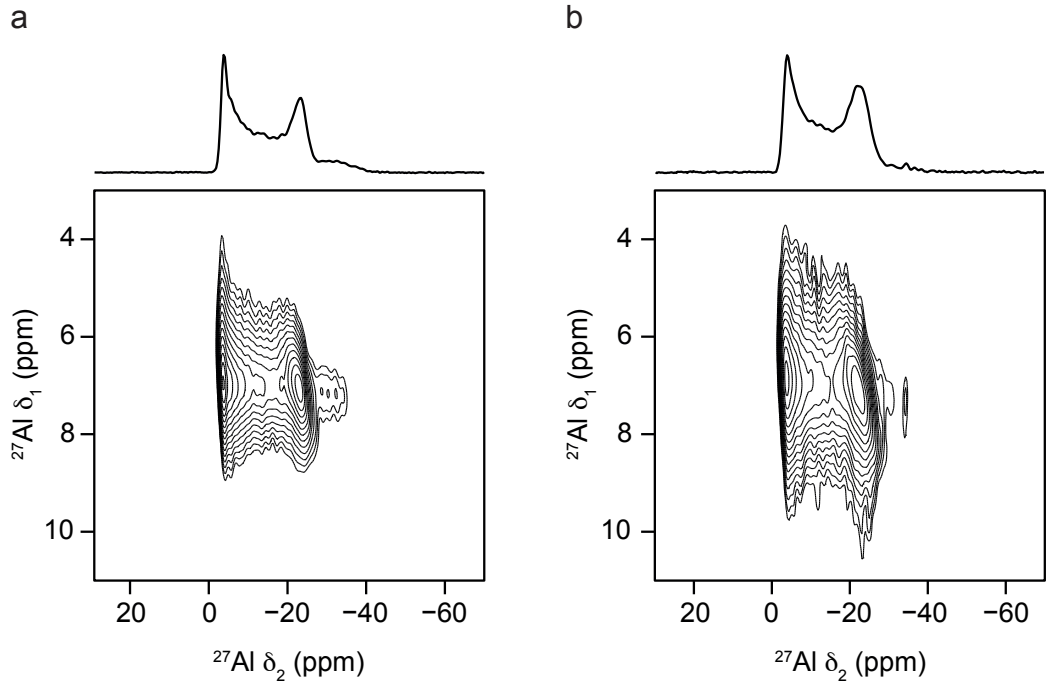

Figure 6.12 *^{27}Al (14.1 T, 16 kHz) 3QMAS NMR spectra (and projections), acquired with a split-t_1 shifted-echo pulse sequence, of calcined Al,Ga (a) (80:20) and (b) (50:50) MIL-53.*

^{17}O MAS NMR spectra (acquired at 20.0 T) of calcined mixed-metal MIL-53 are compared with those for Al and Ga MIL-53 in Figure 6.13. While similar lineshapes are seen for the carboxylate sites, differences in the hydroxyl region are observed depending on the metal centers present, as shown in the expansion on the right in Figure 6.13. To further investigate variations in the ^{17}O lineshapes related to the distribution and mixing of cations in the MIL-53 framework, ^{17}O MQMAS NMR spectra have been acquired both at 14.1 and 20.0 T. Figure 6.14 shows ^{17}O MAS and MQMAS NMR spectra of calcined Al,Ga (50:50) and (80:20) MIL-53 acquired at 14.1 T and the corresponding NMR parameters are reported in Table 6.4. No significant difference can be observed in the carboxylate lineshape and lack of resolution in the hydroxyl region prevents the identification of different contributions to this lineshape (Figures 6.14b and 6.14d).

To achieve a better resolution, ^{17}O MQMAS NMR spectra were recorded at 20.0 T for the two end members and the two mixed-metal MIL-53 compounds, focusing on the hydroxyl region, where lineshape changes are more evident, as shown in Figure 6.15. The corresponding NMR parameters are given in Table 6.5. In the case of the 50:50 material, Figure 6.15c clearly shows that the spectrum is not the sum of the lineshapes of the two end members, but contains an additional, distinct resonance. This suggests an atomic-level mixing of the metal cations with the presence of hydroxyls bridging between Al and Ga, along with hydroxyls bridging between two Al (as in Al MIL-53) and two Ga (as in Ga MIL-53). For the 80:20 material, the ^{17}O MQMAS NMR spectrum in Figure 6.15d is dominated by the signal from Al, but it is clear from the MAS NMR spectrum in Figure 6.13d that two other resonances are also present.

While the MQMAS NMR spectra shown so far provide high resolution, they are inherently non quantitative, owing to the dependence of the efficiency of multiple-quantum filtration on the quadrupolar coupling. An alternative approach is provided by single-quantum DOR experiments, in which the sample is rotated simultaneously about two angles to remove the quadrupolar broadening. As introduced in Section 2.5.2.2, this experiment is technically challenging and only slow rotation rates can be achieved. Experiments were, therefore, performed at two or three different spinning speeds to identify the isotropic peaks from the many spinning sidebands. Figure 6.16

shows ^{17}O DOR NMR spectra acquired at 20.0 T of the two end members, with isotropic resonances highlighted, and the two mixed-metal MIL-53 samples.

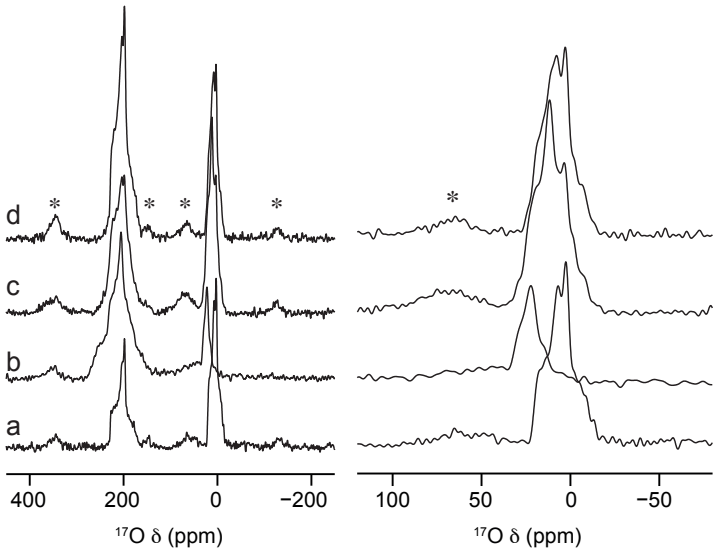

Figure 6.13 *^{17}O (20.0 T, 16 kHz) spin echo MAS NMR spectra of calcined (a) Al, (b) Ga, (c) Al,Ga (50:50) and (d) Al,Ga (80:20) MIL-53. An expansion of the hydroxyl region is shown on the right. Asterisks denote spinning sidebands.*

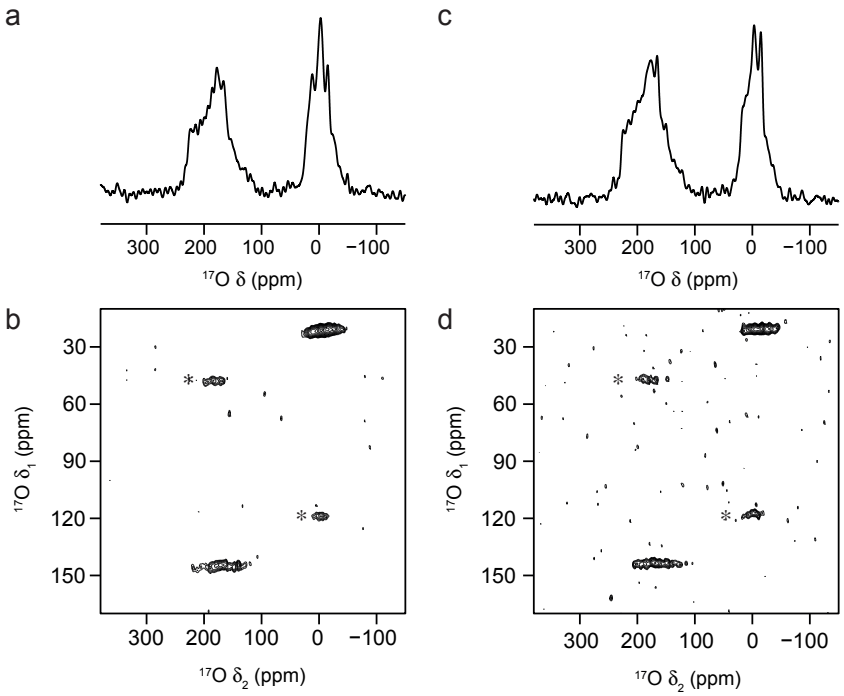

Figure 6.14 *^{17}O (14.1 T, 20 kHz) spin echo MAS NMR spectra of calcined Al,Ga (a) (50:50) and (c) (80:20) MIL-53. ^{17}O (14.1 T, 20 kHz) z-filtered 3QMAS NMR spectra, shown after a shearing transformation, of calcined Al,Ga (b) (50:50) and (d) (80:20) MIL-53. Asterisks denote spinning sidebands.*

O species	δ_{iso} (ppm)	P_Q / MHz
Calcined Al,Ga (50:50)		
carboxylate	229(3)	8.0(3)
hydroxyl	23(3)	5.4(4)
Calcined Al,Ga (80:20)		
carboxylate	228(3)	8.1(3)
hydroxyl	20(3)	5.8(4)

Table 6.4 *NMR parameters obtained from the ^{17}O MQMAS NMR spectra in Figure 6.14.*

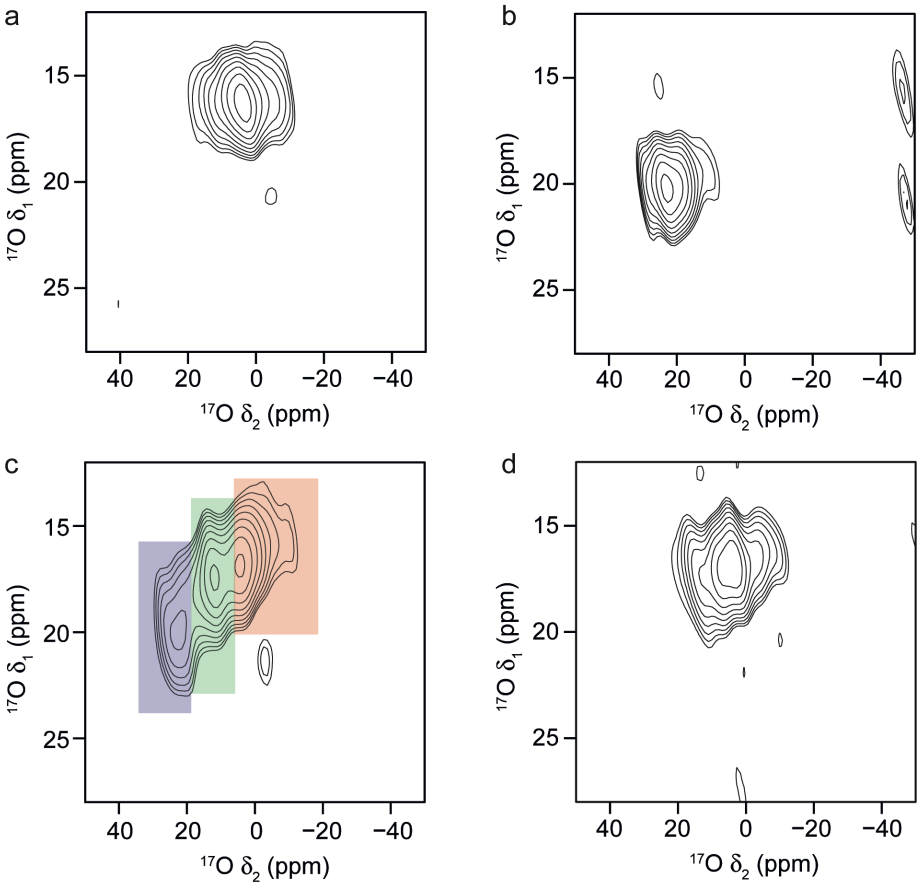

Figure 6.15 *^{17}O (20.0 T, 20 kHz) z-filtered 3QMAS NMR spectra, acquired following the coherence pathway 0→±3→±1→0→−1 (with DFS employed for the ±3→±1 step) and shown after a shearing transformation, of calcined (a) Al, (b) Ga, (c) Al,Ga (50:50) and (d) Al,Ga (80:20) MIL-53. Signals corresponding to hydroxyls bridging Al/Al, Ga/Ga and Al/Ga metal centers are highlighted in red, blue and green, respectively.*

	δ_{iso} (ppm)	P_Q / MHz
Calcined Al MIL-53		
hydroxyl	20(3)	6.0(3)
Calcined Ga MIL-53		
hydroxyl	32(3)	4.4(3)
Calcined Al,Ga (50:50) MIL-53		
hydroxyl 1	21(3)	6.1(3)
hydroxyl 2	24(3)	5.2(3)
hydroxyl 3	31(3)	4.3(3)
Calcined Al,Ga (80:20) MIL-53		
hydroxyl	21(3)	6.1(3)

Table 6.5 *NMR parameters for the hydroxyl ^{17}O species obtained from the MQMAS NMR spectra in Figure 6.15.*

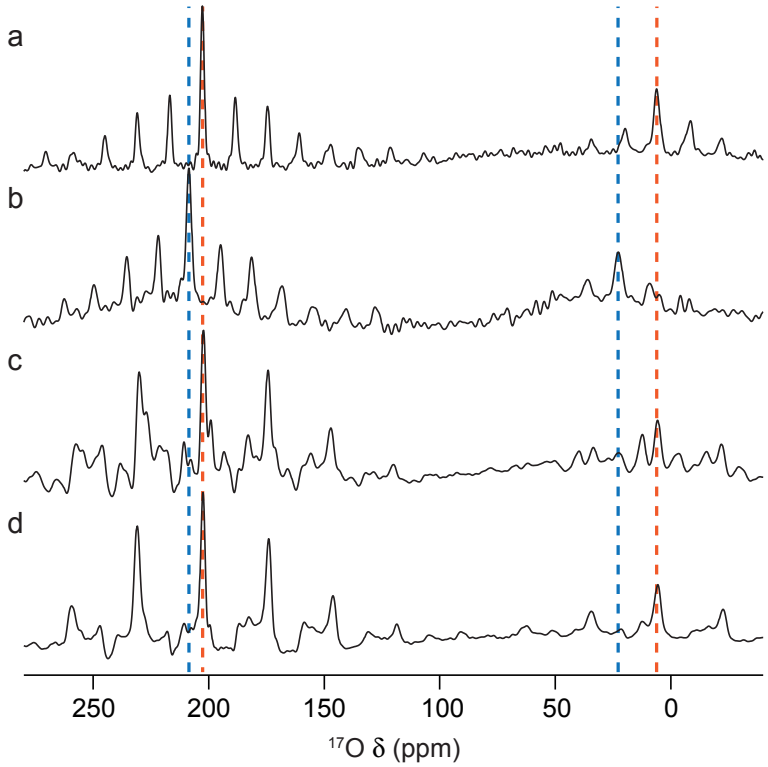

Figure 6.16 *^{17}O (20.0 T) DOR NMR spectra of calcined (a) Al, (b) Ga, (c) Al,Ga (50:50) and (d) Al,Ga (80:20) MIL-53. MAS rates were (a) 1.6/7.7, (b) 1.55/7.9, (c) 1.63/7.9 and (d) 1.65/8.0 kHz. Dashed lines indicate the position of the isotropic resonances for Al (red) and Ga (blue) MIL-53. Spectra shown in (c-d) were recorded with spinning sideband suppression.*

The identification of the isotropic resonances in the ^{17}O DOR NMR spectra shown in Figure 6.16 was achieved by comparison of ^{17}O DOR NMR spectra acquired with variable spinning rates for each MIL-53 sample analysed, as shown in Figure 6.17.

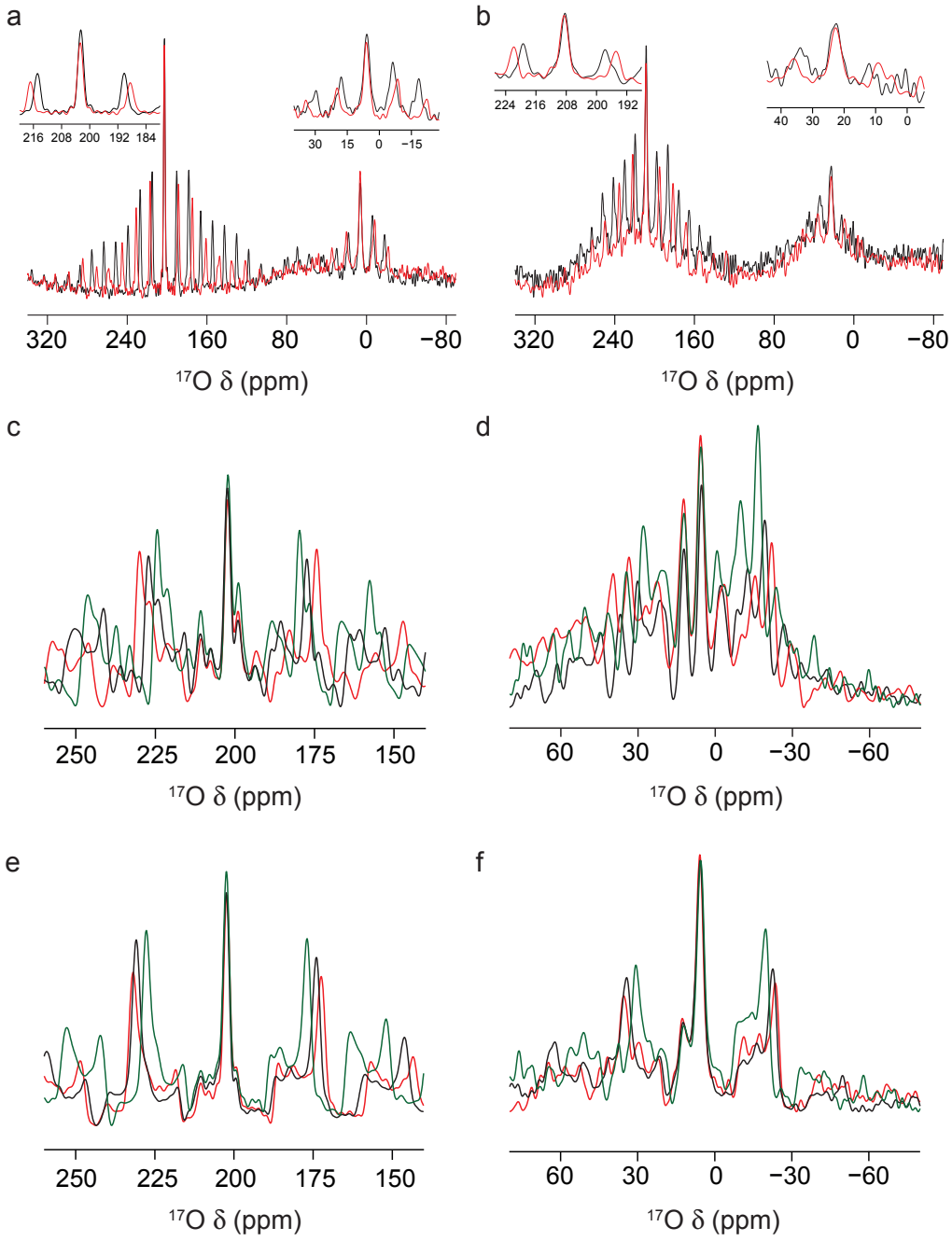

Figure 6.17 *^{17}O (20.0 T) DOR NMR spectra of calcined (a) Al and (b) Ga MIL-53 (and expansions of carboxylate and hydroxyl regions), (c,d) Al,Ga (50:50) and (e,f) Al,Ga (80:20) MIL-53. Rotation rates were (a) 1.4/6.9 kHz (black) or 1.6/7.7 kHz (red), (b) 1.25/6.3 kHz (black) or 1.55/7.9 kHz (red), (c,d) 1.48/7.4 kHz (black), 1.63/7.9 kHz (red) or 1.3/6.8 kHz (green) and (e,f) 1.65/8.0 kHz (black), 1.76/8.3 kHz (red) or 1.5/7.5 kHz (green). Isotropic centerbands and spinning sidebands are identified on the basis of their different behaviour upon change in spinning speed rate. Spectra shown in (c-f) were recorded with spinning sideband suppression.*

For calcined Al and Ga MIL-53, a single isotropic resonance is seen in both the carboxylate and hydroxyl regions of the DOR NMR spectra, at ~202 and ~6 ppm for Al MIL-53 and at ~208 and ~22 ppm for Ga MIL-53, as shown in Figures 6.16a and 6.16b and 6.17a and 6.17b. For Al,Ga (50:50) MIL-53, as shown in Figure 6.16c and Figures 6.17c and 6.17d, peaks are observed in the hydroxyl region at 6 and 22 ppm, in agreement with the position of the corresponding peaks for the end members. It should be noted that the latter peak is overlapped with a spinning sideband and therefore appears distorted. However, a third resonance can also be clearly observed at 12 ppm arising from hydroxyls bridging between Al and Ga centers. Similarly, in the carboxylate region, signals at 208 and 202 ppm are observed, reflecting the positions of the carboxylate isotropic resonances seen for the two end members, and at 199 ppm for this mixed-metal material. Analogous results are obtained for Al,Ga (80:20) MIL-53, as shown in Figure 6.16d and Figures 6.17e and 6.17f, although peaks resulting from carboxylate and hydroxyl species bridging two Al atoms are considerably more intense.

^{17}O and ^{27}Al NMR spectroscopy clearly shows that Al and Ga are intimately mixed in Al,Ga MIL-53 materials, ruling out the hypothesis of a two-phase mixture of Al MIL-53 and Ga MIL-53. However, isotropic resonances obtained from ^{17}O DOR NMR spectra are affected by the presence of many spinning sidebands, in some cases partially overlapping with some of the centerbands, making a quantitative determination very difficult on the basis of these spectra. Using the NMR parameters reported in Table 6.5, it was possible to fit ^{17}O MAS NMR spectra recorded with a short flip angle to ensure quantitative relative intensities were obtained. Only the hydroxyl region of the spectrum was considered owing to the higher resolution exhibited. Figure 6.18 shows the fits for calcined Al,Ga (50:50) and (80:20) MIL-53 and the proportions of each component for the two mixed-metal MOFs are given in Table 6.6. These results are also consistent with the spectra shown in Figure 6.16. The relative proportions in Table 6.6 indicate actual Al:Ga ratios of 70:30 and 92:8 for the samples with stoichiometric compositions of 50:50 and 80:20, respectively. For the nominal 50:50 composition, the value of the Al:Ga actual proportion determined by ^{17}O NMR spectroscopy is in good agreement with values obtained from EDX and Rietveld refinement. However, for the 80:20 nominal composition the

actual ratio determined by ^{17}O NMR spectroscopy is slightly lower in Ga compared to values obtained from EDX and Rietveld refinement. This might be related to some variability affecting the uniformity of the enrichment of the MOFs, which could potentially have a greater impact when smaller quantities of Ga are used. Overall, these results suggest that, for both nominal compositions, not all the Ga introduced in the reaction mixture is incorporated into the final product, even though the level of hydration of the starting nitrate salt is not known exactly. Moreover, incorporated Ga atoms do not appear to have a random distribution in the material. On the basis of Table 6.6, a preferential clustering of like atoms is observed, with only 26% and 9% of hydroxyls bridging two different metal centers in MIL-53 with Al:Ga ratios of 70:30 and 92:8, respectively, compared to the expected 42% and 15% for random distributions of the respective compositions. A comparison of the actual and random cation distributions is plotted in Figure 6.19. This is of crucial importance for the potential catalytic and gas adsorption/storage applications of these materials, since the determination of the actual distribution and arrangement of different metal centers in mixed-metal MOFs is often very challenging.[19]

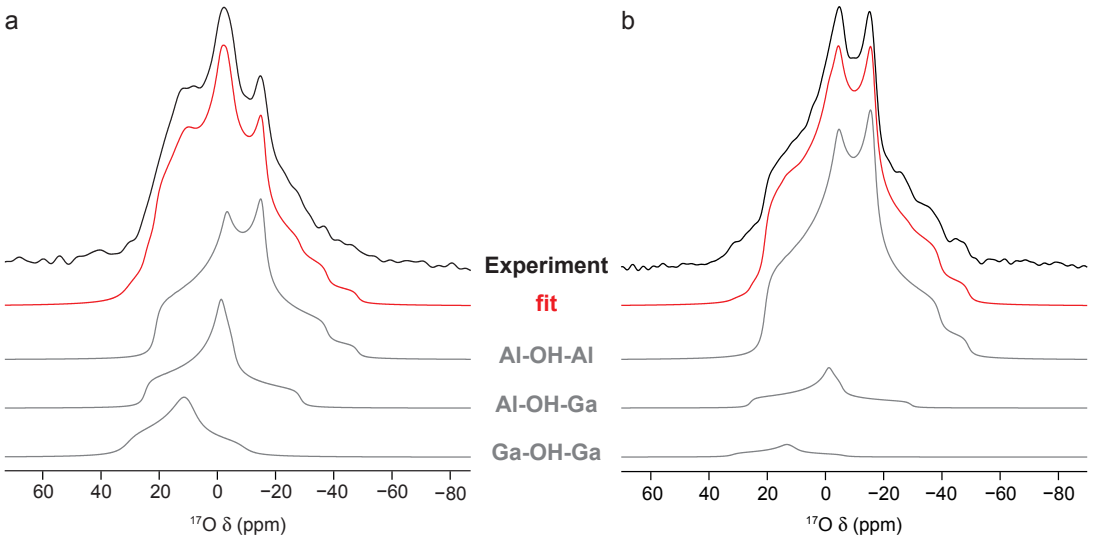

Figure 6.18 *Short flip angle ^{17}O (14.1 T, 20 kHz) MAS NMR spectra of calcined Al,Ga (a) (50:50, stoichiometric ratio) and (b) (80:20, stoichiometric ratio) MIL-53 (hydroxyl region only). From the top: experimental spectra, overall fits (red), Al-OH-Al, Al-OH-Ga and Ga-OH-Ga components.*

	Relative intensity (%)	
Stoichiometric ratios	Al:Ga (50:50)	Al:Ga (80:20)
Al/Al	58(1)	88(1)
Ga/Ga	16(1)	3(1)
Al/Ga	26(1)	9(1)
Actual Al:Ga ratios	70:30	92:8

Table 6.6 *Relative proportions of the bridging hydroxyl oxygen species (Al-**O**H-Al, Ga-**O**H-Ga and Al-**O**H-Ga) and the actual Al:Ga ratios, as determined from the short flip angle ^{17}O MAS NMR spectra in Figure 6.18, for the calcined mixed-metal MIL-53 samples.*

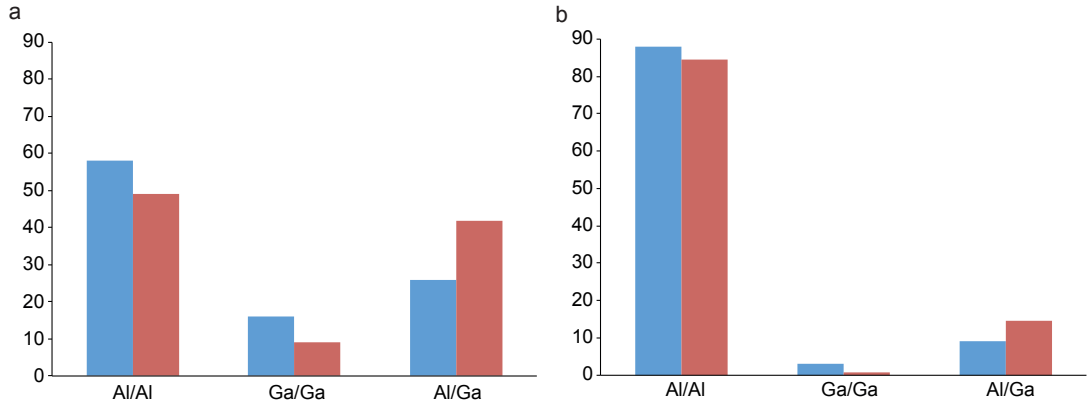

Figure 6.19 *Bar plot of the actual (blue) and calculated random (red) cation distribution of the bridging Al-OH-Al, Ga-OH-Ga and Al-OH-Ga in calcined Al,Ga (a) (50:50, stoichiometric ratio) and (b) (80:20, stoichiometric ratio).*

Hydration of the mixed-metal samples resulted in the ^{17}O MAS NMR spectra shown in Figure 6.20, where a behaviour consistent with that described for hydrated Al MIL-53 and Ga MIL-53 is observed. Also in this case, ^{17}O MQMAS NMR spectra resolved the two different resonances underneath the carboxylate lineshape with average NMR parameters, listed in Table 6.7, consistent with those reported in Table 6.2.

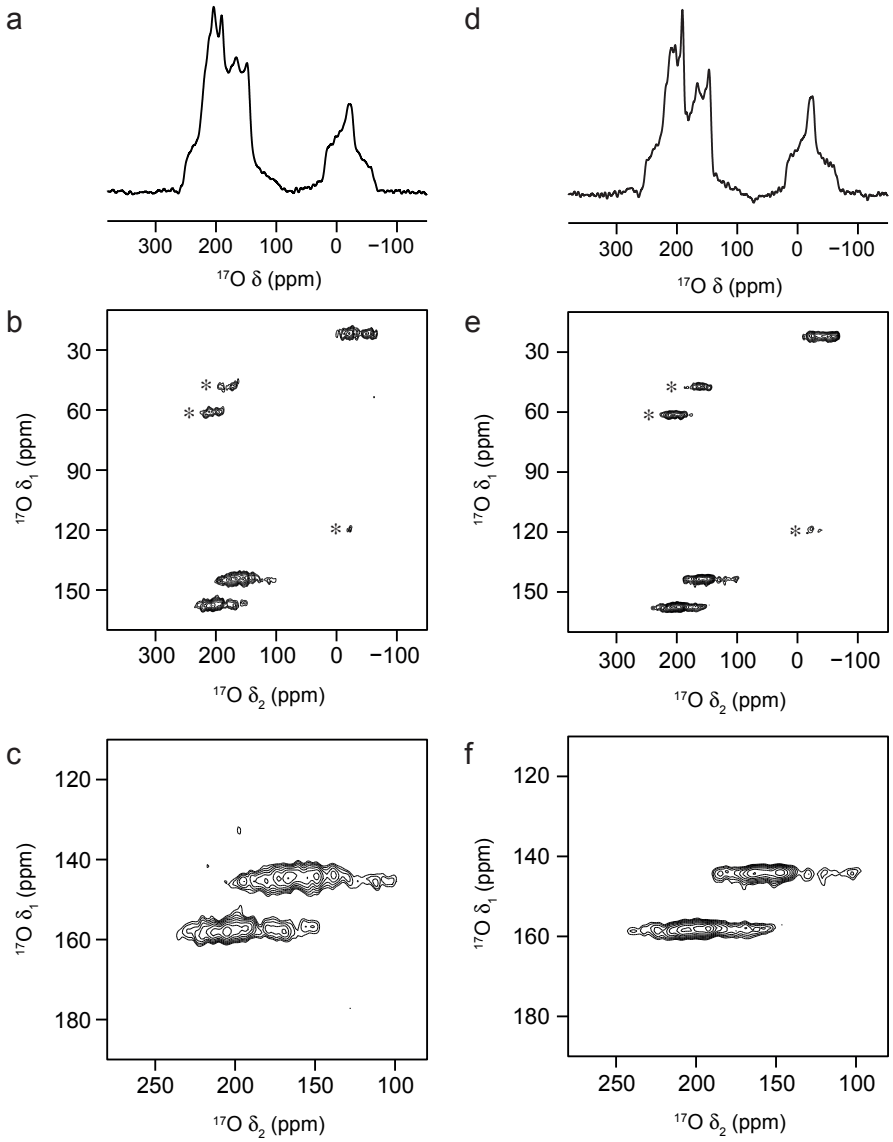

Figure 6.20 *^{17}O (14.1 T, 20 kHz) (a,d) spin echo MAS and (b,e) z-filtered 3QMAS NMR spectra, with expansions of the carboxylate regions (c,f), shown after a shearing transformation, of calcined hydrated Al,Ga (a,b,c) (50:50, stoichiometric ratio) and (d,e,f) (80:20, stoichiometric ratio) MIL-53. Asterisks denote spinning sidebands.*

O species	δ_{iso} (ppm)	P_Q / MHz
Calcined, hydrated Al,Ga (50:50) MIL-53		
carboxylate 1	253(3)	8.0(3)
carboxylate 2	225(3)	8.5(3)
hydroxyl	12(3)	7.2(3)
Calcined, hydrated Al,Ga (80:20) MIL-53		
carboxylate 1	256(3)	7.8(3)
carboxylate 2	224(3)	8.6(3)
hydroxyl	10(3)	7.5(3)

Table 6.7 *Average NMR parameters obtained from the ^{17}O MQMAS NMR spectra in Figure 6.20. Parameters are average values as a result of disorder in the hydrated samples.*

Upon dehydration a peculiar breathing behaviour was observed with a mix of narrow-pore and large-pore forms obtained, as introduced earlier in Section 5.2. Figures 6.21 and 6.22 show the ^{1}H, ^{17}O, ^{1}H-^{13}C CP and ^{27}Al MAS NMR spectra for the different stages of the breathing process of the materials with 50:50 and 80:20 nominal compositions, respectively. The corresponding PXRD patterns are shown in Figures 5.5 and 5.6. The ^{1}H and ^{27}Al MAS NMR spectra in Figures 6.21d and 6.22d show that upon dehydration the expected reversible transition to the spectrum of the calcined form is achieved. Specifically, ^{1}H MAS NMR spectra revert to the two main signals (from the hydroxyls and linkers) characteristic of the calcined form and ^{27}Al lineshapes show a change in C_Q from a value of ~10.7 MHz, characteristic of the hydrated form, to a value of ~8.3 MHz, characteristic of the calcined form.[7] However, the ^{17}O MAS NMR spectra of the dehydrated forms do not revert to give the lineshapes seen in the calcined form and ^{1}H-^{13}C CP MAS NMR spectra show the presence of resonances resulting from both the large- and narrow-pore forms in the carboxylate and aromatic regions, as highlighted by the green boxes in Figures 6.21d and 6.22d. The relative amount of this narrow-pore (empty) form is lower in the dehydrated sample with nominal composition 80:20 compared to the sample with nominal composition 50:50, as already highlighted in Figure 5.7. This is expected since the presence of the narrow-pore (empty) form in dehydrated mixed-metal samples is linked to both the greater thermodynamic stability of Ga MIL-53 in its

narrow-pore form up to 200 °C[6] and the non-uniform distribution of the two metals in different crystallites. The structural distortion present in the narrow-pore structure of dehydrated samples (on the basis of Pawley fits given in Table 5.4) is confirmed by the ^{1}H-^{13}C CP MAS NMR spectra in Figures 6.21d and 6.22d. Indeed, a slight shift is observed in the positions of the ^{13}C resonances between the narrow-pore structures of the hydrated and dehydrated states, as highlighted by the blue dashed lines in Figures 6.21c-d and 6.22c-d. This shift is more evident in the carboxylate region most likely because of the absence of hydrogen bonding to water in the dehydrated narrow-pore form. Traces of this distorted empty narrow-pore form can also be observed in the ^{1}H-^{13}C CP MAS NMR spectra in Figures 6.21b and 6.22b (as shown by the blue dashed lines), probably suggesting that a small amount of the MOF structure, most likely richer in Ga, survives the calcination process in its narrow-pore form.[6] However, detection of this narrow-pore form in the corresponding ^{17}O MAS and MQMAS NMR spectra of the calcined samples proved challenging, probably because of the very small amounts present. The large-pore form does not seem affected during this unusual breathing behaviour, comparing the calcined and dehydrated states of both compositions, as highlighted by the red dashed lines in Figures 6.21b and 6.21d and 6.22b and 6.22d.

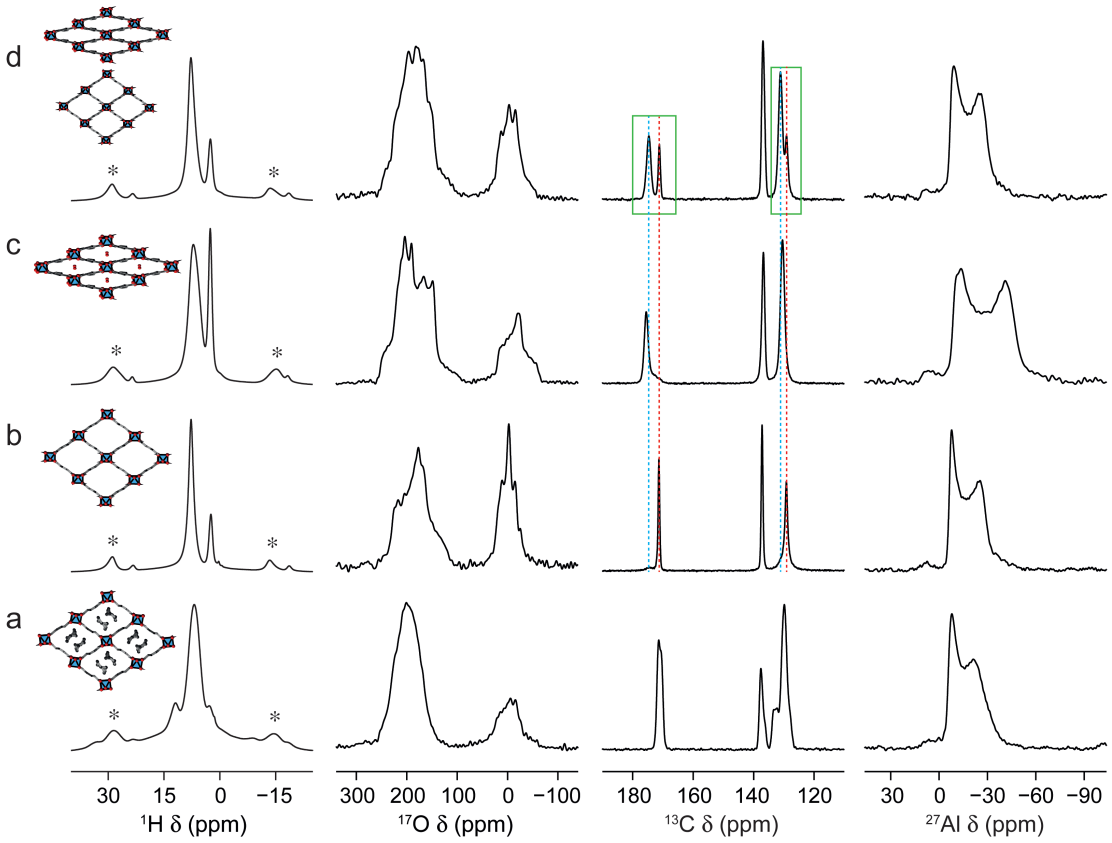

Figure 6.21 *^{1}H (14.1 T, 12.5 kHz), ^{17}O (14.1 T, 20 kHz), ^{1}H-^{13}C CP (14.1 T, 12.5 kHz), short flip angle ^{27}Al (14.1 T, 16 kHz) MAS NMR spectra and schematic structures of Al,Ga (50:50, nominal composition) in its (a) as-made, (b) calcined open-pore, (c) hydrated closed-pore and (d) dehydrated mixed-pore forms. Asterisks denote spinning sidebands. Green boxes in (d) highlight the carboxylate and aromatic regions where the coexistence of the closed- and open-pore forms is seen. The positions of the closed- and open-pore forms in both regions in (d) are highlighted by the blue and red dashed lines, respectively, and can be compared to the positions of resonances in (b) and (c).*

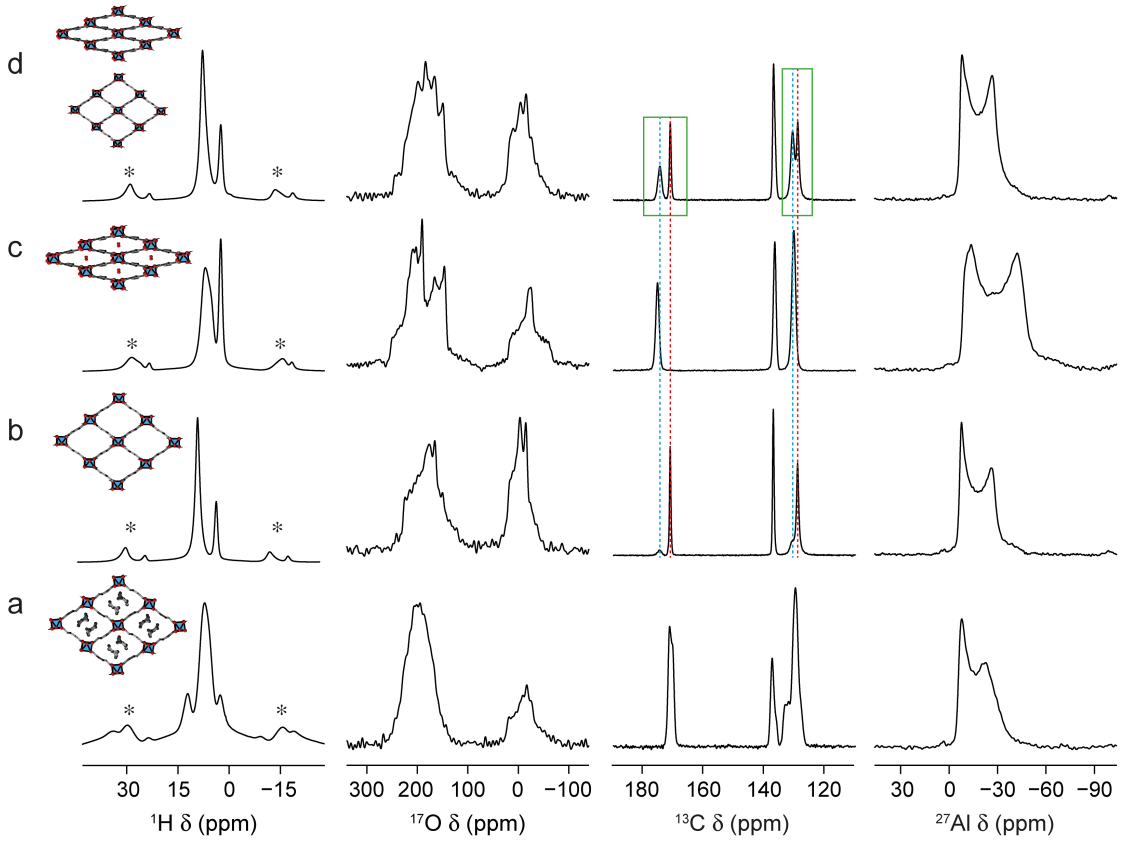

Figure 6.22 *^{1}H (14.1 T, 12.5 kHz), ^{17}O (14.1 T, 20 kHz), ^{1}H-^{13}C CP (14.1 T, 12.5 kHz), short flip angle ^{27}Al (14.1 T, 16 kHz) MAS NMR spectra and schematic structures of Al,Ga (80:20, nominal composition) in its (a) as-made, (b) calcined open-pore, (c) hydrated closed-pore and (d) dehydrated mixed-pore forms. Asterisks denote spinning sidebands. Green boxes in (d) highlight the carboxylate and aromatic regions where the coexistence of the closed- and open-pore forms is seen. The positions of the closed- and open-pore forms in both regions in (d) are highlighted by the blue and red dashed lines, respectively, and can be compared to the positions of resonances in (b) and (c).*

The coexistence of the large- and narrow-pore (empty) forms in the dehydrated mixed-metal Al,Ga MIL-53 samples with both nominal compositions was further investigated by recording ^{17}O MAS and MQMAS NMR spectra, as shown in Figure 6.23. In both cases, a splitting is still present in the carboxylate region, but a difference is observed in the position of the resonance at highest chemical shift compared to the respective samples in the hydrated state, as highlighted by the red dashed lines in Figures 6.23c and 6.23f. This confirms that these narrow-pore conformations are not identical in the hydrated and dehydrated forms, most likely because of the distorted nature of the narrow-pore structure without water molecules. The corresponding NMR parameters are given in Table 6.8. By comparison to values in Table 6.7, it can be seen that the difference in δ_{iso} of the carboxylate 1 species between hydrated and dehydrated samples of both nominal compositions is nonetheless quite small, considering the experimental error. It should be noted that the carboxylate oxygen signal from the large-pore form in the dehydrated samples is overlapped with the second carboxylate resonance from the narrow-pore form. The persistence of the splitting in the carboxylate resonances can be related to the different sets of distances between hydroxyl and carboxylate oxygens across the narrow-pore (empty) structure even with no water molecules present, as confirmed by the geometry-optimised structures shown in Figure 6.8. The ^{17}O MAS NMR spectrum in Figure 6.23a is slightly different to that reported in Figure 6.21d because different batches of the same nominal composition were analysed.

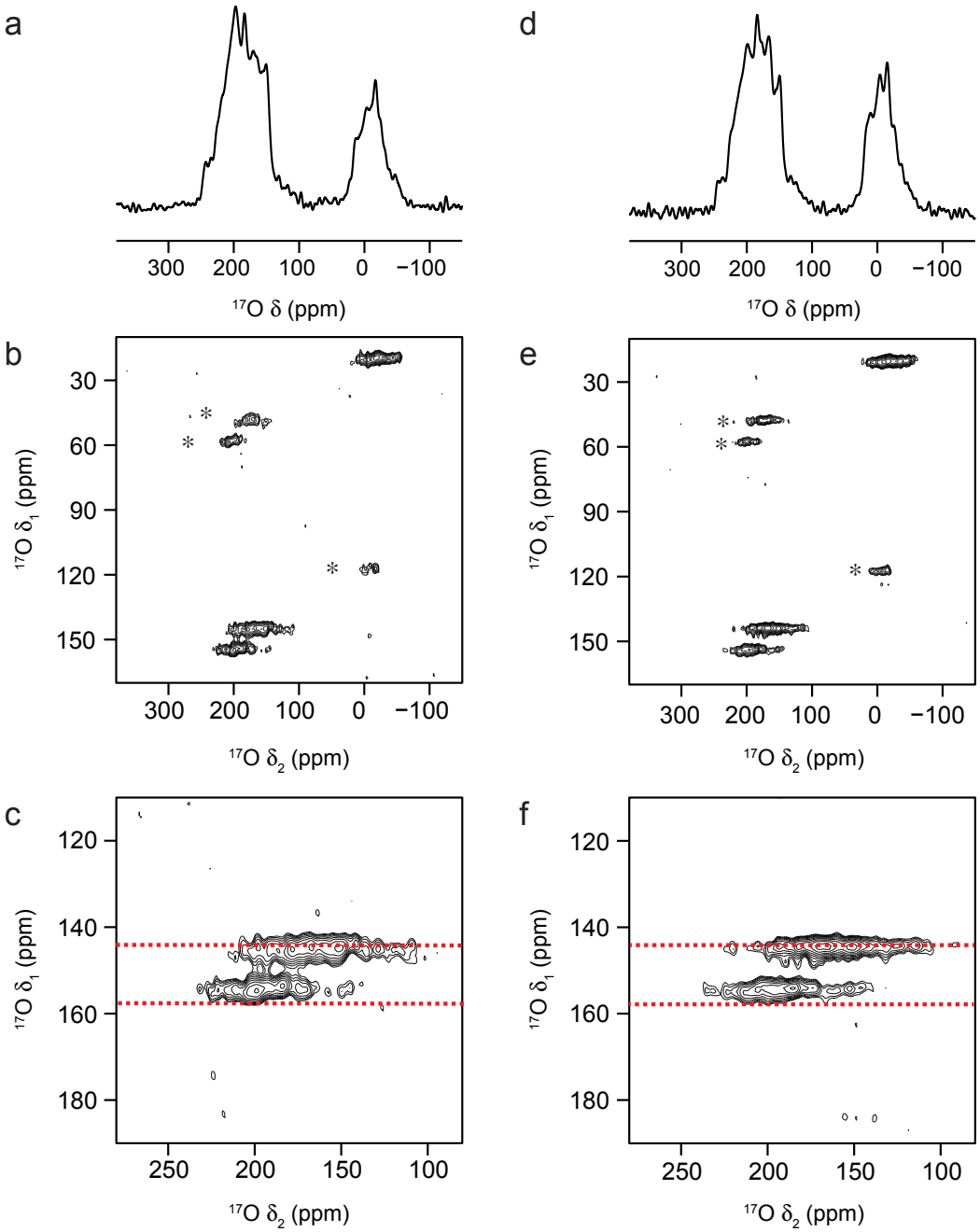

Figure 6.23 *^{17}O (14.1 T, 20 kHz) (a,d) spin echo MAS and (b,e) z-filtered 3QMAS NMR spectra, with expansions of the carboxylate regions (c,f), shown after a shearing transformation, of calcined hydrated and subsequently dehydrated Al,Ga (a,b,c) (50:50, stoichiometric ratio) and (d,e,f) (80:20, stoichiometric ratio) MIL-53. In the expansions of the carboxylate regions, the positions of the resolved carboxylate sites for the corresponding hydrated structures are highlighted by the red dashed lines. Asterisks denote spinning sidebands.*

O species	δ_{iso} (ppm)	P_Q / MHz
Dehydrated Al,Ga (50:50) MIL-53		
carboxylate 1	251(3)	7.5(3)
carboxylate 2	230(3)	7.9(3)
hydroxyl	16(3)	6.1(3)
Dehydrated Al,Ga (80:20) MIL-53		
carboxylate 1	249(3)	7.8(3)
carboxylate 2	224(3)	8.6(3)
hydroxyl	17(3)	6.1(3)

Table 6.8 *Average NMR parameters obtained from the ^{17}O MQMAS NMR spectra in Figure 6.23.*

6.3 NMR investigation of ^{17}O-enriched Sc-based terephthalate MOFs

As introduced in Section 5.1, when $Sc(NO_3)_3$ was used in DGC syntheses a small-pore MOF was obtained, $Sc_2(BDC)_3$, instead of Sc MIL-53. In addition to the XRD characterisation already presented in Section 5.2, ^{1}H, ^{13}C and ^{45}Sc MAS NMR spectra were recorded on the calcined MOF, as shown in Figure 6.24. Specifically, the ^{1}H-^{13}C CP MAS NMR spectrum in Figure 6.24a contains two main groups of resonances. Aromatic carbons can be found between 120 and 140 ppm, with quaternary carbons at higher shift, and carboxylate carbons between 160 and 180 ppm. The further fine structure observed can be attributed to the presence of two crystallographically distinct terephthalate linkers (in a 2:1 ratio) in this structure, in agreement with previous work.[1] The ^{1}H MAS NMR spectrum in Figure 6.24b shows a single resonance at ~7 ppm, assigned to aromatic protons of the linker,[1] confirming the absence of hydroxyl groups. A single ^{45}Sc resonance characterised by a narrow lineshape is seen in Figure 6.24c, consistent with the presence of isolated ScO_6 octahedra.[1] When ^{17}O-enriched water was used in the DGC synthesis it was possible to acquire ^{17}O MAS NMR spectra of the resulting ^{17}O-enriched $Sc_2(BDC)_3$. In both ^{17}O MAS and MQMAS NMR spectra in Figures 6.25a-b only the presence of the carboxylate resonances can be observed, without any signals attributable to hydroxyls, in agreement with the structure of this material. However, Figure 6.25b

shows that the ^{17}O MQMAS NMR spectrum does not resolve the two ^{17}O resonances expected in the carboxylate region resulting from the presence of two distinct linker molecules, suggesting these are very similar. The corresponding NMR parameters, determined from the position of the center of gravity of the resonance, are given in Table 6.9, showing that P_Q values are similar to those obtained for carboxylate species in Al and Ga MIL-53 materials, but that δ_{iso} is significantly different.

In order to ^{17}O enrich the Sc MIL-53 structure, a combined solvothermal and steaming procedure was optimised as described in Section 5.1, obtaining the "intermediate" phase of Sc MIL-53 with water molecules exchanged in the pores during steaming. The resulting ^{17}O spin echo, ^{1}H-^{17}O CP MAS and ^{17}O MQMAS NMR spectra are shown in Figures 6.25c-d for the batch of Sc MIL-53 that was steam enriched (see Figure 5.11). It is possible to observe the successful ^{17}O enrichment (estimated to be ~25% by comparison to previous materials) in both the hydroxyl (centered at ~120 ppm) and the carboxylate (centered at ~220 ppm) sites, along with the presence of traces of water at ~−13 ppm. The corresponding NMR parameters for the ^{17}O MQMAS NMR spectrum in Figure 6.25d are given in Table 6.9. The carboxylate parameters are similar for the two Sc-based MOFs, whereas the hydroxyl sites of Sc MIL-53 have different parameters to those of the corresponding Al and Ga MIL-53 materials. In addition, Figure 6.26 shows the ^{1}H, ^{1}H-^{13}C CP and ^{45}Sc MAS NMR spectra of Sc MIL-53 ^{17}O enriched by steaming. The ^{1}H-^{13}C CP MAS NMR spectrum in Figure 6.26a shows a number of carboxylate and aromatic resonances, suggesting many different environments for the linker molecules probably resulting from the presence of water in the pores.[1,20] The ^{1}H MAS NMR spectrum in Figure 6.26b shows resonances that, by comparison to Figure 6.2b, can be assigned to protons from the bridging hydroxyl groups at 2.4 ppm and aromatic protons from the linker molecules at 6.9 ppm. The third resonance can be related to incorporated water at 0.75 ppm.[1] In the ^{45}Sc MAS NMR spectrum shown in Figure 6.26c a broad quadrupolar signal from Sc MIL-53 with $\delta_{iso} \approx 60$ ppm, $C_Q \approx 17$ MHz and $\eta_Q \approx 0.3$ is seen, resulting from unresolved distinct Sc species (expected to be present in the structure) with similar NMR parameters.[1,20] In addition to this quadrupolar signal, a sharp resonance at ~1 ppm can be noticed. This resonance is assigned to the competing phase $Sc_2(BDC)_3$, which was found as an impurity in

some solvothermal syntheses of Sc MIL-53 (see PXRD patterns shown in Figure 5.11). As discussed in Section 5.2, these promising preliminary steaming results highlight the need for further optimisation of the synthetic and steaming procedures to avoid the possible presence of other phases as impurities from synthesis or possible phase transitions during steaming, but offer interesting future possibilities for isotopic enrichment.

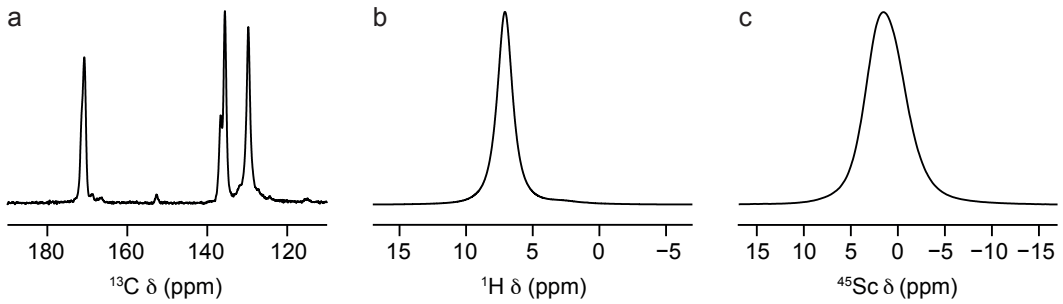

Figure 6.24 *(a) ^{1}H-^{13}C (14.1 T, 12.5 kHz) CP, (b) ^{1}H (14.1 T, 12.5 kHz) spin echo and (c) ^{45}Sc (14.1 T, 20 kHz) MAS NMR spectra of calcined $Sc_2(BDC)_3$.*

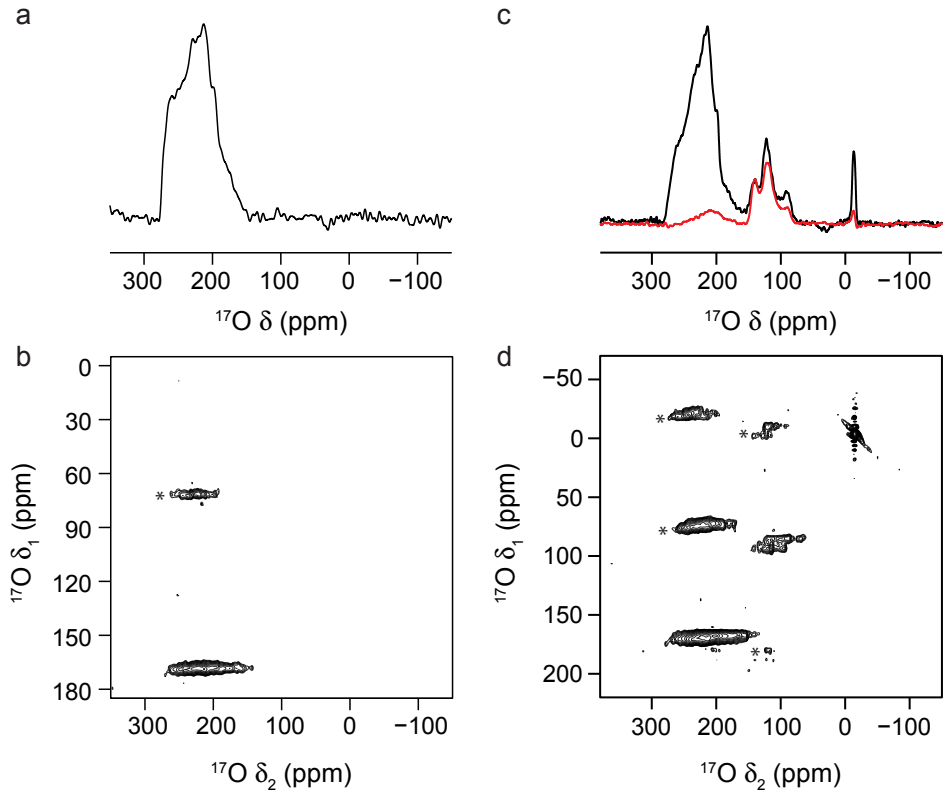

Figure 6.25 *^{17}O (14.1 T, 20 kHz) (a,c) spin echo MAS and (b,d) z-filtered 3QMAS NMR spectra, shown after a shearing transformation, of (a,b) calcined $Sc_2(BDC)_3$ and (c,d) as-made steamed Sc MIL-53. In (c), the ^{1}H-^{17}O (14.1 T, 20 kHz) CP MAS NMR spectrum (with a contact time of 1000 μs) is shown overlaid in red. Asterisks denote spinning sidebands.*

O species	δ_{iso} (ppm)	P_Q / MHz
Calcined $Sc_2(BDC)_3$		
carboxylate	273(3)	8.1(3)
Steamed (hydrated) Sc MIL-53		
carboxylate	272(3)	8.1(3)
hydroxyl	143(4)	6.0(4)

Table 6.9 *Average NMR parameters obtained from the ^{17}O MQMAS NMR spectra in Figure 6.25.*

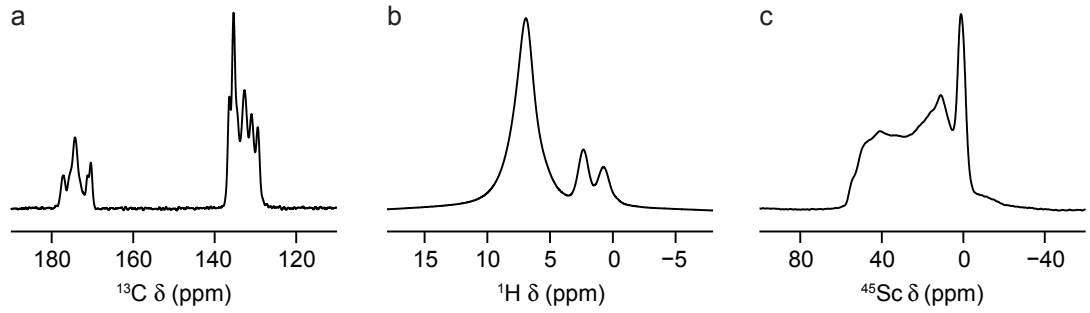

Figure 6.26 *(a) ^{1}H-^{13}C (14.1 T, 12.5 kHz) CP, (b) ^{1}H (14.1 T, 12.5 kHz) and (c) short flip angle ^{45}Sc (14.1 T, 20 kHz) MAS NMR spectra of as-made steamed Sc MIL-53.*

When $Sc(NO_3)_3$ and $Al(NO_3)_3$ were mixed in DGC conditions to synthesise a mixed-metal (Sc,Al) MIL-53, a mixed-phase material (containing $Sc_2(BDC)_3$ and Al MIL-53) was obtained instead. As already shown in Figure 5.9, XRD analysis confirmed the coexistence of the two separate compounds with the combined presence of peaks from the two pure phases. This most likely rules out any significant cation substitution in either phase. The ^{1}H-^{13}C CP, ^{1}H, ^{45}Sc and ^{27}Al MAS NMR spectra in Figure 6.27 confirmed the presence of a phase mixture. In particular, the ^{1}H-^{13}C CP MAS NMR spectrum in Figure 6.27a shows clear resolution of two ^{13}C resonances at 135.6 and 137.2 ppm, corresponding to the quaternary aromatic carbons in $Sc_2(BDC)_3$ and Al MIL-53, respectively. The ^{1}H MAS NMR spectrum in Figure 6.27b confirms the presence of hydroxyls groups from the MIL-53 phase at 2.2 ppm. The ^{45}Sc MAS NMR spectrum is very similar to that shown in Figure 6.24c, confirming Sc is entirely in the "BDC" phase. The ^{27}Al MAS NMR spectrum in Figure 6.27d shows the characteristic quadrupolar lineshape of calcined Al MIL-53

along with two additional resonances at ~8 and ~70 ppm, probably resulting from an Al_2O_3-based[21] impurity in the sample.

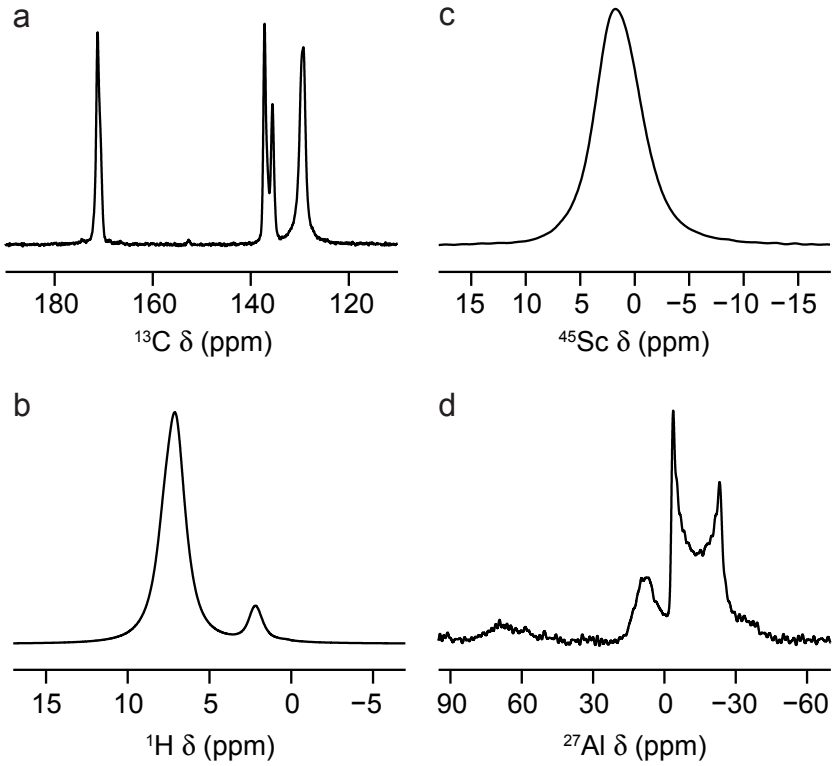

Figure 6.27 *(a) ^{1}H-^{13}C (14.1 T, 12.5 kHz) CP, (b) ^{1}H (14.1 T, 12.5 kHz) spin echo, (c) ^{45}Sc (14.1 T, 20 kHz) and (d) short flip angle ^{27}Al (14.1 T, 16 kHz) MAS NMR spectra of calcined mixed-phase $Sc_2(BDC)_3$ and Al MIL-53.*

When ^{17}O-enriched water was used in the DGC synthesis starting from $Sc(NO_3)_3$ and $Al(NO_3)_3$, the corresponding ^{17}O MAS and MQMAS NMR spectra were recorded and are shown in Figures 6.28a-b, confirming the presence of signals very similar to those found for the two separate phases. Resolution of the carboxylate oxygen sites from the $Sc_2(BDC)_3$ and Al MIL-53 phases is observed and a resonance in the hydroxyl region can be assigned to hydroxyls from the Al MIL-53 phase. Upon hydration of this ^{17}O-enriched mixed-phase material, the ^{17}O MAS and MQMAS NMR spectra in Figures 6.28c-d were recorded. In the carboxylate region, in addition to the resonance from $Sc_2(BDC)_3$, resolution of the two resonances belonging to hydrated Al MIL-53 is seen, consistent with the previously presented behaviour of ^{17}O-enriched MIL-53 compounds upon hydration (as in Figure 6.6). The corresponding NMR parameters are reported in Table 6.10 and are consistent with parameters previously reported in Tables 6.1, 6.2 and 6.9. An additional resonance

centered at ~58 ppm can be noticed in the ^{17}O MAS and MQMAS NMR spectra in Figure 6.28 for both the calcined and hydrated forms of the sample. The origin and assignment of this resonance is still under investigation, but could be related to the presence of an ^{17}O-enriched Al_2O_3-based[22] impurity in the sample, in agreement with the additional peaks seen in Figure 6.27d.

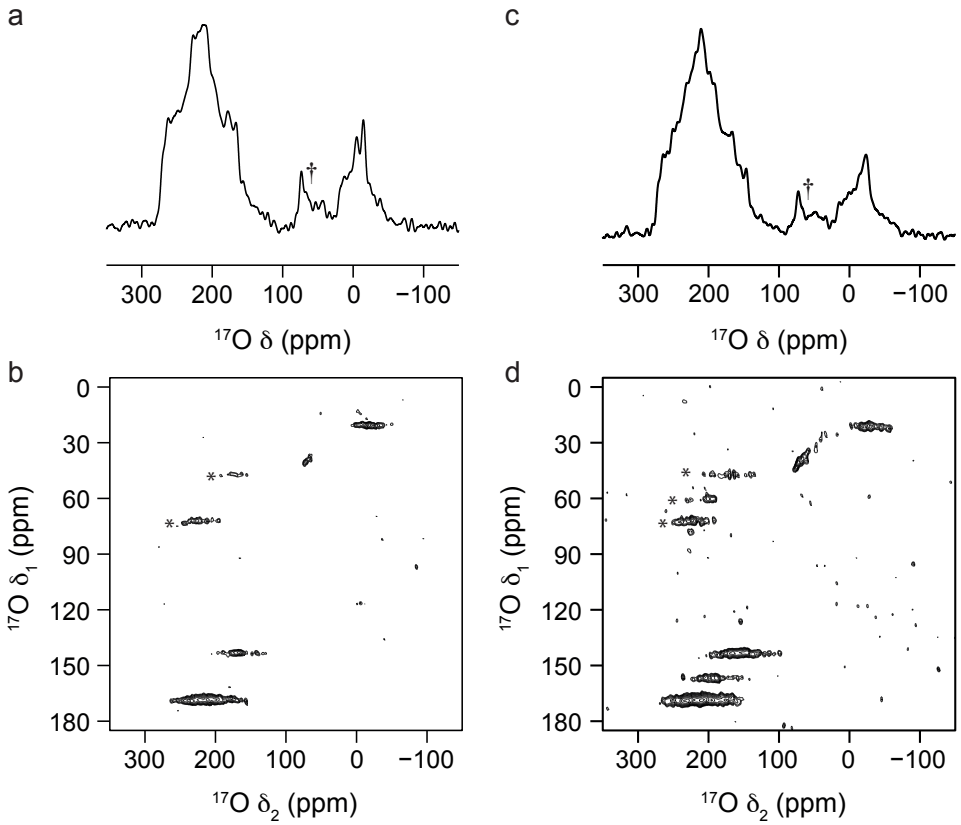

Figure 6.28 *^{17}O (14.1 T, 20 kHz) (a,c) spin echo MAS and (b,d) z-filtered 3QMAS NMR spectra, shown after a shearing transformation, of mixed-phase (a,b) calcined and (c,d) rehydrated $Sc_2(BDC)_3$ and Al MIL-53. Asterisks denote spinning sidebands and † denotes the unknown resonance.*

O species	δ_{iso} (ppm)	P_Q / MHz
Calcined mixed-phase $Sc_2(BDC)_3$ and Al MIL-53		
carboxylate ("BDC" phase)	272(3)	8.2(3)
carboxylate (MIL-53 phase)	226(4)	8.1(4)
hydroxyl (MIL-53 phase)	18(4)	6.1(5)
Rehydrated mixed-phase $Sc_2(BDC)_3$ and Al MIL-53		
carboxylate ("BDC" phase)	274(3)	8.0(3)
carboxylate 1 (MIL-53 phase)	253(4)	7.9(4)
carboxylate 2 (MIL-53 phase)	223(4)	8.5(4)
hydroxyl (MIL-53 phase)	16(4)	6.6(5)

Table 6.10 *Average NMR parameters obtained from the ^{17}O MQMAS NMR spectra in Figure 6.28.*

6.4 DNP NMR results for ^{17}O-enriched Al MIL-53

^{17}O-enriched Al MIL-53 samples were also characterised using DNP NMR spectroscopy, in collaboration with Dr Subhradip Paul at the UK DNP MAS NMR Facility in Nottingham, to investigate the structural interactions of the porous framework with impregnating radical solutions and resulting potential signal enhancements for ^{17}O NMR spectroscopy. Initially, ^{1}H-^{13}C CP experiments were performed to obtain a better understanding of the effect of the radical solution chosen on the framework. Ideally, radical solutions should provide unpaired electrons as polarisation sources and promote the formation of a frozen matrix without affecting the structure or the chemistry of the analysed compound. However, considering the breathing nature of the MOF under analysis, the polarity of the solvent chosen for impregnation could be expected to affect the pore conformation of the framework. For this reason, calcined ^{17}O-enriched Al MIL-53 samples were impregnated with three different types of radical solutions: 20 mM TOTAPOL in 90/10 v/v D_2O/H_2O, 20 mM AMUPOL in 60/30/10 v/v/v glycerol-d_8/D_2O/H_2O and 18 mM TEKPol in TCE, as described in Section 2.4.3. The corresponding ^{1}H-^{13}C CP MAS NMR spectra are shown in Figure 6.29.

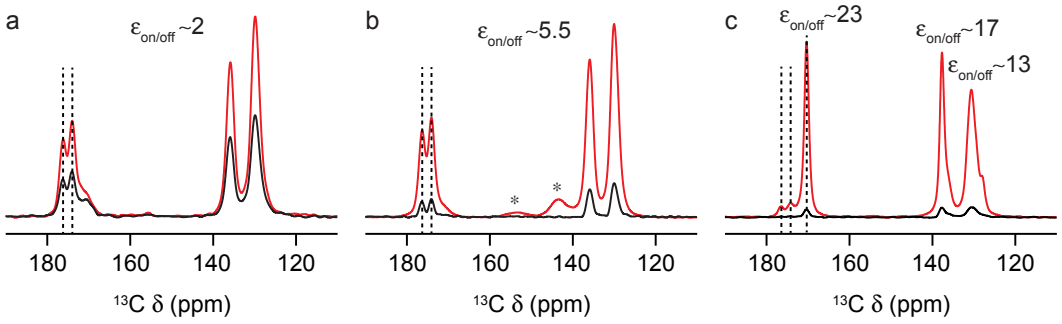

Figure 6.29 *^{1}H-^{13}C CP (14.1 T, 12.5 kHz, ~100 K) MAS NMR spectra of calcined ^{17}O-enriched Al MIL-53 impregnated with the (a) TOTAPOL, (b) AMUPOL and (c) TEKPol solutions described in the main text. Red and black spectra were acquired with and without microwave irradiation (with filament current at 110 mA), respectively. All spectra were acquired with 5 ms contact time, averaging 8 transients and with recycle intervals of (a) 42, (b) 70 and (c) 70 s based on ^{13}C polarisation build-up times measured on each sample. Asterisks denote spinning sidebands resulting from the glycerol signal outside of the range shown in (b). Dashed lines highlight changes the in the position of peaks in the region 160-180 ppm.*

Different enhancement ($\varepsilon_{on/off}$) values can be seen in Figure 6.29 depending on the type of impregnating solution used. Furthermore, there are significant differences in the position and number of ^{13}C resonances, primarily in the carboxylate region, in all three spectra in Figure 6.29. In the case of Figures 6.29a-b, where water-based radical solutions were used for the impregnation of the sample, two main peaks are observed at 176 and 174 ppm, whereas in Figure 6.29c, where a TCE radical solution was used for the impregnation of the sample, a single peak at 170 ppm appears dominant with two minor peaks at 176 and 174 ppm. On the basis of the previous investigation (see Section 6.1), the different positions observed for the ^{13}C resonances of Al MIL-53 impregnated with different radical solutions suggest that different pore conformations could be present. In particular, when water-based TOTAPOL or AMUPOL solutions are used, resonances belonging to the narrow-pore form are observed, as shown in Figures 6.29a-b. While at room temperature only one resonance is normally observed for the carboxylate group at 175 ppm (as in Figures 6.9c, 621c-6.22c), the splitting observed in Figures 6.29a-b could be related to the low temperature (~100 K) at which DNP NMR spectra were recorded. In these conditions, it is possible that any dynamics will be removed/restricted yielding the two resonances observed at 176 and 174 ppm, probably resulting from the two possible hydrogen-bonding arrangements predicted using DFT for water molecules in the pores (as in Figure 6.7). On the other hand, when TEKPol/TCE radical solutions are used, only one major peak at 170 ppm is observed in Figure 6.29c, in agreement with the presence of the large-pore conformation, as shown in Figure 6.3b for calcined Al MIL-53. This indicates that different solvents used for radical solutions affect the structure of the framework analysed, triggering conformational changes and affecting the position and the intensity of the resonances observed. Indeed, higher enhancement ($\varepsilon_{on/off}$) values were obtained when using TEKPol/TCE solutions. This suggests that the large-pore conformation, present when using this solution, provides better conditions for polarisation transfer compared to the narrow-pore conformation obtained from water-based impregnations. For all samples, the long polarisation build-up times observed (42-70 s) indicate that the biradical molecules are most likely located outside the pores. However, it should be noted that inconsistent enhancements ($\varepsilon_{on/off}$) values were obtained when impregnations of

calcined Al MIL-53 with TEKPol/TCE solutions were repeated (in identical experimental conditions) to test the reproducibility of the enhancement values obtained. This is still under investigation, but could be ascribed to different diffusion and matrix-formation processes occurring within the MOF framework every time the impregnation procedure is performed and the sample is cooled to ~100 K. On the basis of the ^{13}C investigation described so far, the pore conformation of the MOF framework is expected to be affected by the radical solution chosen. Since ^{17}O NMR spectroscopy has been shown to be sensitive to changes in conformations of MIL-53 MOFs, as described in Section 6.1, an ^{17}O DNP NMR investigation was carried out focusing on the carboxylate region, more sensitive to conformational changes. Direct ^{17}O DNP experiments were attempted first, to avoid spectral editing by indirect DNP through ^{1}H-^{17}O CP, but no enhancement was observed, even when a field sweep was performed. Subsequently, ^{1}H-^{17}O CP experiments were carried out optimising the conditions of ^{1}H-^{17}O polarisation transfer to maximise the intensity of the carboxylate sites. For these experiments, 20 mM AMUPOL in 60/30/10 v/v/v glycerol-d_8/D_2O/H_2O and 20 mM TEKPol in TCE solutions were used to impregnate calcined ^{17}O-enriched Al MIL-53 samples and, as shown in Figure 6.30, enhancement ($\varepsilon_{on/off}$) values of 2-3 were obtained. However, different lineshapes can clearly be observed in the carboxylate (and hydroxyl) region in Figures 6.30a-b, confirming the conformational changes detected by ^{13}C NMR spectroscopy when different impregnating solutions are used. A better signal build-up with time was observed in the case of the sample impregnated with the AMUPOL solution, as shown in Figure 6.30a, possibly because of the more proton-rich environment provided by the radical solution.

Overall, the preliminary data obtained from this ^{13}C and ^{17}O indirect DNP NMR investigation of ^{17}O-enriched Al MIL-53 highlight that the choice of impregnating solution can significantly affect the conformation of the MOF and therefore the spectra acquired, providing useful information for future DNP NMR investigations of these frameworks.

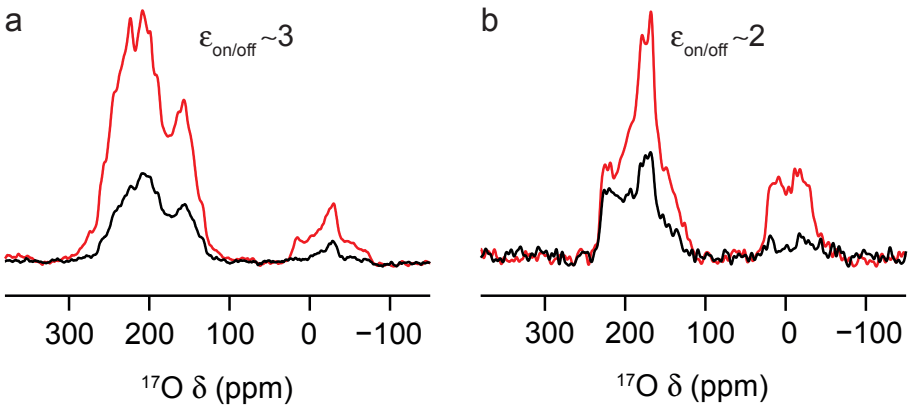

Figure 6.30 *^{1}H-^{17}O CP (14.1 T, 12.5 kHz, ~100 K) MAS NMR spectra of calcined ^{17}O-enriched Al MIL-53 impregnated with the (a) AMUPOL and (b) TEKPol solutions described in the main text. Red and black spectra were acquired with and without microwave irradiation (with filament current at 110 mA), respectively. All spectra were acquired with 10 ms contact time and a recycle interval of 70 s. Spectra are the result of averaging (a) 32 transients and (b) 160 transients.*

6.5 References

1 J. P. S. Mowat, S. R. Miller, A. M. Z. Slawin, V. R. Seymour, S. E. Ashbrook and P. A. Wright, *Micropor. Mesopor. Mater.*, 2011, **142**, 322–333.

2 R. W. Schurko, *Acc. Chem. Res.*, 2013, **46**, 1985–1995.

3 Y. Zhang, B. E. G. Lucier, V. V. Terskikh, R. Zheng and Y. Huang, *Solid State Nucl. Magn. Reson.*, 2017, **84**, 118–131.

4 P. He, B. E. G. Lucier, V. V. Terskikh, Q. Shi, J. Dong, Y. Chu, A. Zheng, A. Sutrisno and Y. Huang, *J. Phys. Chem. C*, 2014, **118**, 23728–23744.

5 P. He, J. Xu, V. V. Terskikh, A. Sutrisno, H.-Y. Nie and Y. Huang, *J. Phys. Chem. C*, 2013, **117**, 16953–16960.

6 C. Volkringer, T. Loiseau, N. Guillou, G. Férey, E. Elkaïm and A. Vimont, *Dalton Trans.*, 2009, 2241–2249.

7 T. Loiseau, C. Serre, C. Huguenard, G. Fink, F. Taulelle, M. Henry, T. Bataille and G. Férey, *Chem. Eur. J.*, 2004, **10**, 1373–1382.

8 C. Lieder, S. Opelt, M. Dyballa, H. Henning, E. Klemm and M. Hunger, *J. Phys. Chem. C*, 2010, **114**, 16596–16602.

9 G. Ortiz, G. Chaplais, J.-L. Paillaud, H. Nouali, J. Patarin, J. Raya and C. Marichal, *J. Phys. Chem. C*, 2014, **118**, 22021–22029.

10 S. J. Clark, M. D. Segall, C. J. Pickard, P. J. Hasnip, M. J. Probert, K. Refson and M. C. Payne, *Z. Kristallogr*., 2005, **220**, 567−570.

11 C. J. Pickard and F. Mauri, *Phys. Rev. B,* 2001, **63**, 245101.

12 J. P. Perdew, K. Burke and M. Ernzerhof, *Phys. Rev. Lett*., 1996, **77**, 3865–3868.

13 A. Tkatchenko and M. Scheffler, *Phys. Rev. Lett.*, 2009, **102**, 073005.

14 H. J. Monkhorst and J. D. Pack, *Phys. Rev. B*, 1976, **13**, 5188–5192.

15 C. Pickard and F. Mauri, in *Calculation of NMR and EPR Parameters: Theory and Applications*, Eds. M. Kaupp, M. Buhl and V. G. Malkin, Wiley-VCH, Weinheim, 2004, pp. 265–278.

16 J. R. Yates, C. J. Pickard and F. Mauri, *Phys. Rev. B*, 2007, **76**, 024401.

17 S. E. Ashbrook and D. McKay, *Chem. Commun.,* 2016, **52**, 7186–7204.

18 S. Sturniolo, T. F. G. Green, R. M. Hanson, M. Zilka, K. Refson, P. Hodgkinson, S. P. Brown and J. R. Yates, *Solid State Nucl. Magn. Reson*., 2016, **78**, 64–70.

19 Q. Liu, H. Cong and H. Deng, *J. Am. Chem. Soc.*, 2016, **138**, 13822–13825.

20 J. P. S. Mowat, V. R. Seymour, J. M. Griffin, S. P. Thompson, A. M. Z. Slawin, D. Fairen-Jimenez, T. Düren, S. E. Ashbrook and P. A. Wright, *Dalton Trans.*, 2012, **41**, 3937–3941.

21 K. J. D. MacKenzie and M. E. Smith, in *Multinuclear Solid-State NMR of Inorganic Materials*, Elsevier Science Ltd., 2002, Chapter 5.

22 K. J. D. MacKenzie and M. E. Smith, in *Multinuclear Solid-State NMR of Inorganic Materials*, Elsevier Science Ltd., 2002, Chapter 6.

Conclusions

7 Conclusions and future work

In this work, experimental results have been presented regarding the optimised synthetic pathways, cost-effective isotopic enrichment and solid-state characterisation of two classes of microporous solids, zeolites and MOFs.

Chapters 3 and 4 described the investigation of the synthesis, isotopic enrichment and solid-state NMR characterisation of zeolites derived from the ADOR process. On the basis of the results presented, it was possible to conclude that the successful synthesis of isotopically enriched IPC-2 and IPC-2P was achieved and new insights into the hydrolytic rearrangement process were obtained. Isotopic enrichment in ^{29}Si was introduced at the assembly stage (i.e., during the synthesis of the parent Ge-UTL zeolite), whereas isotopic enrichment in ^{17}O was introduced at the disassembly stage (i.e., by using $H_2{}^{17}O$ during hydrolysis). By XRD and *in situ*/*ex situ* solid-state NMR investigation of the ADOR process in different volume and acidity conditions, mechanistic insights were obtained regarding the evolution of the process with time. Depending on the acidity, silica rearrangement was shown to occur at different rates, affecting the structural outcome of the ADOR process as a whole. The observation of both hydrolysis and rearrangement was carried out by monitoring the evolution of the ADOR process in successful *in situ* NMR experiments. The sensitivity of the ADOR process to experimental conditions was demonstrated when using a lower volume of hydrolysis to enable economic isotopic enrichment. In these conditions, variations in reaction rates and the products obtained at each step of the process, compared to standard higher-volume conditions, were observed, highlighting the potential fine control of the reaction progression that may be possible. In these low-volume conditions, the hydrolysis to IPC-1P never goes to completion before the organisation step dominates, leading to the identification of a modified ADOR mechanism and the formation of the defective structure IPC-2P*. Both ^{29}Si and ^{17}O NMR spectroscopy proved to be of crucial importance for the study of hydrolysis and rearrangement in these conditions, showing that these processes occur over much longer time than seen by diffraction, where a constant d_{200} spacing is observed throughout the reaction times tested. ^{29}Si MAS NMR spectra, through a

consideration of the Q^4/Q^3 intensities, showed that hydrolysis is the dominant process for the first ~12 h, with subsequent rearrangement occurring up to ~48 h. However, ^{17}O MAS NMR spectra of ^{17}O-enriched hydrolysed zeolites showed changes of the spectral lineshapes up to 30 days after synthesis, reflecting a low level of ongoing hydrolytic cleavage even at room temperature, most likely resulting from small amounts of residual acidity between the layers.

The presence of 2-4 water molecules, depending on the storage and reaction conditions, for every hydroxyl species in the interlayer region was determined using ^{2}H MAS NMR spectra of deuterated $^{29}Si/^{17}O$-enriched zeolites after a careful investigation of the optimum experimental conditions for deuteration of isotopically enriched samples. Two main signals were observed in ^{17}O MAS NMR spectra of ^{17}O-enriched zeolites and attributed to the chemical environments known to be present in hydrolysed layered zeolites: Si-O-Si and Si-OH (along with H_2O). ^{17}O MQMAS, ^{1}H-^{17}O CP (at ~100 K and room temperature) and spin-locking experiments recorded at multiple fields provided information on the spectral lineshapes of the different components, enabling their relative proportions in the sample to be determined as ~8:1 for Si-^{17}O-Si:Si-^{17}OH, on the basis of a quantitative ^{17}O MAS NMR spectrum. Such a proportion of Si-O-Si species enriched in ^{17}O, even hypothesising a faster back-exchange of Si-OH groups, is unexpectedly high and suggests that ^{17}O enrichment is reaching the first layers of tetrahedral units in the bulk of the structure. This suggests a much more extensive rearrangement occurs during hydrolysis, with ^{17}O not only confined to the hydrolysed interlayer region, but also substantially incorporated in the bulk of the layers of IPC-2P, a hypothesis confirmed by high-field heteronuclear ^{17}O-^{29}Si correlation experiments. Overall, isotopic enrichment of these materials not only enabled a more detailed spectroscopic investigation but also provided new insight into the ADOR mechanism, shedding light on possible ways in which new zeolite structures could be targeted in the future.

The indirect ^{17}O DNP NMR investigation carried out on hydrolysed zeolites derived from the ADOR process was unsuccessful as no signal enhancement was observed. The reasons for this experimental observation could be related to inefficient processes occurring during the formation of the frozen matrix or at the stage of

polarisation transfer from ^{1}H to ^{17}O. Even if the latter process has been shown to be more efficient in the neat solid at the low temperature typical of DNP experiments, its efficiency might still not be sufficient to enable the observation of significant enhancements on the timescale and under the conditions of the DNP NMR experiments carried out. In addition, problems related to the incorporation of the radical solution with the sample in the frozen matrix or possible absorption/interference of microwave radiation cannot be ruled out. In light of these preliminary results, further investigation could be performed by direct ^{17}O DNP NMR experiments, which would avoid the need for a ^{1}H-^{17}O polarisation transfer. However, these experiments are quite challenging and time consuming as they require a field sweep to be performed.

Studies of post-synthesis heteroatom incorporation led to the successful alumination of Ge-UTL resulting in the presence of catalytic activity for the final aluminated material, with both octahedrally and tetrahedrally coordinated Al sites detected. Different exchange procedures were tested on aluminated Ge-UTL samples (with and without prior heat treatment) at 80 °C and at room temperature using concentrations of NH_4Cl from 0.06 to 0.6 M. The final values of NO produced were shown to be affected by the heat treatment of the starting material and the experimental conditions of ion-exchange, with the lowest and highest concentrations of NH_4Cl resulting in higher NO production for exchange procedures carried out at room temperature. Attempts to study the influence of Al incorporation in the Ge-UTL framework on the ADOR process were unsuccessful due to the difficulties encountered during the assembly and disassembly stages. The presence of the competing STF phase was almost always observed in the final products obtained from the autoclave synthesis of Ge-UTL when an Al source was added to the reaction mixture, regardless of changes in temperature, reaction time and pH of the reaction gel. Possible changes in the Al source and SDA used might benefit the phase selectivity of this reaction. In addition, a rapid loss of Al from the framework was observed in the typical conditions used for the hydrolysis of Ge-UTL. This hampered the study of the possible role of Al in the ADOR process, highlighting the need for further investigation of different pathways for efficient Al incorporation, potentially at the organisation stage.

Future work on the study of the mechanism of the ADOR process will involve hydrolytic reactions carried out in different conditions to achieve a better insight into the influence of experimental variables, such as temperature, acidity and time. Starting from different Ge loadings of the parent UTL zeolite could also provide useful information on the hydrolytic mechanism of removal of Ge from the structure. Reactions performed with ^{17}O-enriched water at different temperatures could enable the study of the mechanism of rearrangement of ^{17}O atoms within the structure, potentially resulting in different levels of overall and site-specific ^{17}O incorporation. Using the protocol implemented for low-volume hydrolyses, different parent zeolites could be investigated and ^{17}O enriched, extending the ADOR process to new structures and investigating potentially different mechanisms. On the basis of the feasibility study and initial results shown in this work for the *in situ* investigation, variations in acidity conditions and temperatures, as well as in the nature of the starting framework, could highlight the evolution of different processes/species in hydrolysed/rearranged layered materials. This investigation, at present carried out monitoring ^{29}Si, ^{1}H and ^{2}H NMR spectra, could be extended to ^{17}O NMR, obtaining information on the dynamics and incorporation of this nucleus in the structure (using $H_2{}^{17}O$) while the reaction is in progress.

Regarding the incorporation of heteroatoms in the Ge-UTL structure, the post-synthesis alumination procedure presented could be further optimised, in conjunction with ion-exchange protocols, to maximise the catalytic activity of the final aluminated zeolites. Moreover, the possible integration of post-synthesis Al incorporation with the ADOR process could offer the intriguing possibility of targeting new catalytically active zeolite frameworks.

Chapters 5 and 6 presented a synthetic, structural and NMR spectroscopic investigation of mixed-metal terephthalate MOFs. Using the atom-efficient and cost-effective DGC synthesis, Al, Ga and mixed-metal MIL-53 materials were successfully ^{17}O enriched. Mass spectrometry shows that samples ^{17}O enriched by DGC were characterised by enrichment levels between 11-21% (with an estimated cost of €750 per g of as-made MOF). Since DGC syntheses containing Sc resulted in the formation of the small-pore MOF $Sc_2(BDC)_3$, Sc MIL-53 was successfully ^{17}O-enriched using a novel post-synthetic steaming procedure, where the solvothermally

pre-synthesised sample is heated with $H_2{}^{17}O$ vapour. This procedure can potentially provide a cost- and atom-efficient pathway to isotopically enriched MOFs, removing the need to significantly adapt previously optimised synthetic methods. ^{17}O MAS spectra of MIL-53 resolved resonances from carboxylate and hydroxyl sites and proved to be very sensitive both to changes in pore structure (e.g., upon hydration) and cation substitution. ^{17}O MQMAS spectra of hydrated samples enabled resolution of two types of ^{17}O carboxylate sites. These inequivalent ^{17}O carboxylate species were shown to result from structural distortions of the pores upon narrowing, on the basis of DFT calculations carried out for literature structures of hydrated Al and Ga MIL-53. The predicted narrow-pore structures are characterised by two short and two long contacts between the carboxylates and the bridging hydroxyls, with water molecules found to preferentially bridge the shorter OH···O contact through hydrogen-bonding interactions. For both Al and Ga forms of MIL-53 the models resulting from optimised literature structures had very similar DFT energies. High-resolution ^{17}O NMR spectroscopy, involving the use of MQMAS and DOR experiments, proved the presence not only of Al-OH-Al and Ga-OH-Ga units, but also of hydroxyl groups bridging between one Al and one Ga center, confirming the formation of a mixed-metal material and ruling out the possibility of the presence of a simple two-phase mixture. The actual Al:Ga proportion and distribution of the two metals in mixed-metal samples were also determined. The Al:Ga ratio obtained from quantitative ^{17}O NMR spectroscopy was different to that of the initial synthetic mixture. Indeed, integration of the different hydroxyl resonances yielded Al:Ga ratios of 70:30 and 92:8 for the nominal compositions 50:50 and 80:20, respectively. A complementary XRD and EDX investigation confirmed these values. In addition, the spectroscopic investigation highlighted that Ga is not randomly distributed in the material, with a preferential clustering of like atoms. Interestingly, no thermal decomposition was observed upon incorporation of Al in Ga MIL-53, suggesting that mixing metal centers could improve the thermal stability and therefore widen the possible applications of this material. Moreover, an unusual breathing behaviour was observed upon dehydration of mixed-metal samples, unlike the two single-metal materials, where dehydration leads to an open-pore form in Al MIL-53 and closed-pore form in Ga MIL-53. In the case of both nominal compositions, dehydration

produced a mix of closed- and open-pore forms, most likely reflecting the adoption of different conformations for different crystallites depending on their particular Al:Ga ratios. This finding offers a future potential for dual-adsorption behaviour for guest molecules in mixed-metal MIL-53 materials, if the distribution and proportion of cations can be targeted synthetically. Overall, using DGC and a novel steaming method, this work shows that cost-effective and atom-efficient enrichment of MOFs is possible and that high-resolution ^{17}O NMR spectra are sensitive to the structural forms of the framework and the presence of guest molecules.

The direct ^{17}O DNP NMR investigation carried out on ^{17}O-enriched Al MIL-53 MOFs was unsuccessful as no signal enhancement was observed. The indirect ^{13}C and ^{17}O DNP NMR study performed on the same compounds proved the presence of different conformations of the breathing framework depending on the polarity of the radical solution used. However, the enhancement values were not repeatable, most likely as a result of variable rates of diffusion of the radical solution in the porous sample and possible variations in the freezing process affecting the formation of the frozen matrix.

Future work on the study of Al, Ga and Sc single- and mixed-metal terephthalate MOFs and their ^{17}O enrichment will involve further optimisation of the steaming procedure and its comparison with the DGC approach. Indeed, the repeatability of the overall and site-specific ^{17}O enrichment, as well as cation distribution, could be affected by the synthetic route chosen for isotopic enrichment. The systematic optimisation of steaming conditions and solvothermal synthetic routes for MIL-53 MOFs with various metal centers will be required to widen the applicability of the steaming ^{17}O-enrichment approach to study cation disorder and its effects on the physical and chemical properties of MOFs. Only a preliminary investigation was undertaken in this work for Sc MIL-53, with difficulties encountered during the synthetic and steaming processes owing to the structural instability of the framework under steaming and the presence of impurities in the solvothermal product. Different proportions of cation mixing during solvothermal and/or DGC syntheses could also be investigated to probe possible changes in the thermal behaviour of the final mixed-metal materials in view of future applications.

In conclusion, this work shows that, since good levels of enrichment can be achieved at a reasonable cost through optimised synthetic pathways, ^{17}O NMR spectroscopy should be an invaluable tool for the study of zeolites and MOFs.

Appendix A. Primary and secondary chemical shift references

The chemical shifts of the reference compounds used in this thesis are reported in Table A1.[1-2]

Nucleus	Compound	δ_{iso} (ppm)
$^{1/2}$H	$(CH_3)_4Si$	0.00
	L-alanine	8.5 ($N\mathbf{H}_3$)
	$C_2O_4D_2 \cdot 2D_2O$	16.5 ($CO_2\mathbf{D}$)
^{13}C	$(CH_3)_4Si$	0.00
	L-alanine	20.5 ($\mathbf{C}H_3$)
^{17}O	H_2O	0.00
^{27}Al	1 M $Al(NO_3)_{3\ (aq)}$	0.00
	Aluminium tris(acetylacetonate)	0.00[a]
^{29}Si	$(CH_3)_4Si$	0.00
	Octakis(trimethylsiloxy)silsesquioxane	11.5 ($O\mathbf{Si}(CH_3)_3$)
^{45}Sc	0.2 M $ScCl_{3\ (aq)}$	0.00[b]

[a] Practically relevant reference points are the left-hand horn of the quadrupolar lineshape (−1.1 ppm at 14.1 T) and the center of gravity (−4.2 ppm at 9.4 T).

[b] $LaScO_3$ was used as a solid secondary reference with the most intense peak in the spectrum at 162.91 ppm (14.1 T).[2]

Table A1 *Primary and secondary chemical shift references used in this work.*

References

1 K. J. D. MacKenzie and M. E. Smith, in *Multinuclear Solid-State NMR of Inorganic Materials*, Elsevier Science Ltd., 2002.

2 K. E. Johnston, *PhD Thesis*, University of St Andrews, 2010.

Appendix B. Additional ^{17}O experimental NMR parameters (Chapter 4)

Additional experimental NMR parameters for the ^{17}O spectra shown in Chapter 4 are given in Table B1. B_0 field strengths and MAS rates are given in the captions.

Figure	Experiment	Transients	Recycle interval / s	Processed increments	Increment / μs
Figure 4.10b	MAS	19912-22880	1		
Figure 4.11a	MAS	9216	3		
Figure 4.11b(black)	MAS	6832	3		
Figure 4.11b(red)	MAS	2048	3		
Figure 4.12c	MAS	33968	1		
Figure 4.12d	3QMAS	1536	1	50	50
Figure 4.13(red)	CP	10240	1		
Figure 4.13(blue)	CP	10240	1		
Figure 4.14a(red)	CP	254312	1		
Figure 4.14b(black)	MAS	1024	1		
Figure 4.14b(red)	CP	112682	0.5		
Figure 4.16	spin-lock	7600	1		
Figure 4.17(black)	CP	12288	4.3		

Figure 4.17(red)	CP	12288	1		
Figure 4.18(black)	MAS	1024	1		
Figure 4.18(red)	MAS	1024	1		
Figure 4.19a	MAS	1024	1		
Figure 4.19b	3QMAS	384	1	32	50
Figure 4.19c	3QMAS	1944	1	40	50
Figure 4.20a	MAS	21624	1		
Figure 4.20b	3QMAS	1944	1	40	50
Figure 4.20d	MAS	1024	1		
Figure 4.20e	3QMAS	384	1	32	50
Figure 4.21a	MAS	1024	1		
Figure 4.21b	D-HMQC	2560	1	18	25
Figure 4.21c	D-HMQC	2560	1	18	25
Figure 4.23	MAS	34424	1		

Table B1 *Additional experimental NMR parameters for the ^{17}O NMR spectra shown in Chapter 4.*

Appendix C. Additional ^{17}O experimental NMR parameters (Chapter 6)

Additional experimental NMR parameters for the ^{17}O spectra shown in Chapter 6 are given in Table C1. B_0 field strengths and MAS rates are given in the captions.

Figure	Experiment	Transients	Recycle interval / s	Processed increments	Increment / μs
Figures 6.1a-b,d-e	spin echo	4096	1		
Figure 6.1b(red)	CP	2048	1		
Figure 6.1e(red)	CP	4096	1		
Figure 6.1c	3QMAS	792	0.7	150	12.5
Figure 6.1f	3QMAS	960	0.75	154	10.0
Figures 6.6a,c	spin echo	4096	1		
Figure 6.6b	3QMAS	816	0.7	200	12.5
Figure 6.6d	3QMAS	1416	0.7	80	16.7
Figures 6.13a-d	spin echo	6114	1		
Figures 6.14a,c	spin echo	4096	1		
Figure 6.14b	3QMAS	936	0.7	134	12.5
Figure 6.14d	3QMAS	552	0.7	144	12.5
Figures 6.15a-d	3QMAS	480-576	0.75	100-120	12.5
Figure 6.16a	DOR	4552	1		
Figure 6.16b	DOR	5744	1		
Figure 6.16c	DOR	81920	1		
Figure 6.16d	DOR	57344	1		
Figure 6.17a(black)	DOR	6584	1		
Figure 6.17b(black)	DOR	12120	1		

Figures 6.17c/d(black)	DOR	73728	1		
Figures 6.17c/d(green)	DOR	62552	1		
Figures 6.17e/f(red)	DOR	10312	1		
Figures 6.17e/f(green)	DOR	22544	1		
Figure 6.18a	MAS	21504	2		
Figure 6.18b	MAS	34608	2		
Figures 6.20a,d	spin echo	4096	1		
Figures 6.20b-c	3QMAS	576	0.7	140	12.5
Figures 6.20e-f	3QMAS	480	0.7	180	12.5
Figures 6.21a-d	spin echo	4096	1		
Figures 6.22a-d	spin echo	4096	1		
Figures 6.23a,d	spin echo	4096	1		
Figures 6.23b-c	3QMAS	480	0.7	150	12.5
Figures 6.23e-f	3QMAS	888	0.7	170	12.5
Figures 6.25a,c	spin echo	4096	1		
Figure 6.25c(red)	CP	5632	1		
Figure 6.25b	3QMAS	720	0.7	150	12.5
Figure 6.25d	3QMAS	720	0.75	120	10.0
Figures 6.28a,c	spin echo	4096	1		
Figure 6.28b	3QMAS	816	0.7	180	12.5
Figure 6.28d	3QMAS	672	0.7	144	12.5

Table C1 *Additional experimental NMR parameters for the ^{17}O NMR spectra shown in Chapter 6.*

Appendix D. Structures of "ADORable" zeolites

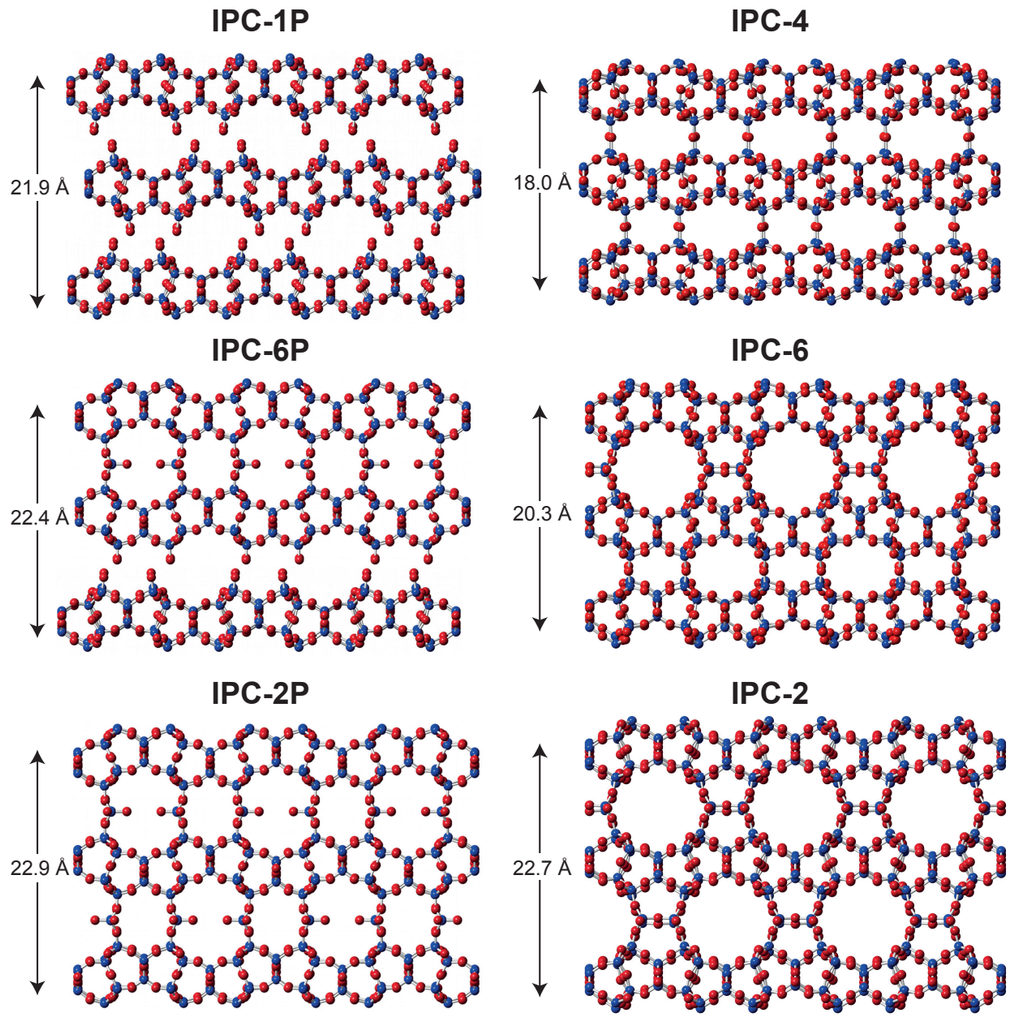

Figure D1 *Structures of IPC-1P, IPC-6P and IPC-2P and their reassembled counterparts IPC-4, IPC-6 and IPC-2, respectively. The values of* $2d_{200}$ *are highlighted for each structure.*[1]

References

1 S. A. Morris, G. P. M. Bignami, Y. Tian, M. Navarro, D. S. Firth, J. Čejka, P. S. Wheatley, D. M. Dawson, W. A. Slawinski, D. S. Wragg, R. E. Morris and S. E. Ashbrook, *Nature Chem.*, 2017, **9**, 1012–1018.